JSCSEN 89(3)291-442(2024)

ISSN 1820-7421(Online)

Journal of the Serbian Chemical Society

VOLUME 89

No 3

BELGRADE 2024

Available on line at

www.shd.org.rs/JSCS/

The **Journal of the Serbian Chemical Society** (formerly Glasnik Hemijskog društva Beograd), one volume (12 issues) per year, publishes articles from the fields of chemistry. The **Journal** is financially supported by the **Ministry of Education, Science and Technological Development of the Republic of Serbia.**

Articles published in the **Journal** are indexed in **Clarivate Analytics products: Science Citation Index-Expanded™** – accessed *via* **Web of Science®** and **Journal Citation Reports®**.

Impact Factor announced on 28 June, 2023: **1.000; 5-year Impact Factor**: **1.100**.

Articles appearing in the **Journal** are also abstracted by: **Scopus, Chemical Abstracts Plus (CAplus℠), Directory of Open Access Journals, Referativnii Zhurnal (VINITI), RSC Analytical Abstracts, EuroPub, Pro Quest** and **Asian Digital Library.**

Publisher:	**Serbian Chemical Society**, Karnegijeva 4/III, P. O. Box 36, 1120 Belgrade 35, Serbia tel./fax: +381–11–3370–467, E-mails: **Society** – shd@shd.org.rs; **Journal** – jscs@shd.org.rs Home Pages: **Society** – http://www.shd.org.rs/, **Journal** – http://www.shd.org.rs/JSCS/
Internet Service:	Contents, Abstracts and full papers (from Vol 64, No. 1, 1999) are available in the electronic form at the Web Site of the **Journal** (http://www.shd.org.rs/JSCS/).
Former Editors:	**Nikola A. Pušin** (1930–1947), **Aleksandar M. Leko** (1948–1954), **Panta S. Tutundžić** (1955–1961), **Miloš K. Mladenović** (1962–1964), **Đorđe M. Dimitrijević** (1965–1969), **Aleksandar R. Despić** (1969–1975), **Slobodan V. Ribnikar** (1975–1985), **Dragutin M. Dražić** (1986–2006).
Editor-in-Chief:	BRANISLAV Ž. **NIKOLIĆ**, Serbian Chemical Society (E-mail: jscs-ed@shd.org.rs)
Deputy Editor:	DUŠAN **SLADIĆ**, Faculty of Chemistry, University of Belgrade
Sub editors:	
Organic Chemistry	DEJAN **OPSENICA**, Institute of Chemistry, Technology and Metallurgy, University of Belgrade JÁNOS **CSANÁDI**, Faculty of Science, University of Novi Sad
Biochemistry and Biotechnology	OLGICA **NEDIĆ**, INEP – Institute for the Application of Nuclear Energy, University of Belgrade
Inorganic Chemistry	BILJANA **GLIŠIĆ**, Faculty of Science, University of Kragujevac
Theoretical Chemistry	IVAN **JURANIĆ**, Serbian Chemical Society
Physical Chemistry	LJILJANA **DAMJANOVIĆ-VASILIĆ**, Faculty of Physical Chemistry, University of Belgrade
Electrochemistry	SNEŽANA **GOJKOVIĆ**, Faculty of Technology and Metallurgy, University of Belgrade
Analytical Chemistry	RADA **BAOŠIĆ**, Faculty of Chemistry, University of Belgrade
Polymers	BRANKO **DUNJIĆ**, Faculty of Technology and Metallurgy, University of Belgrade
Thermodynamics	MIRJANA **KIJEVČANIN**, Faculty of Technology and Metallurgy, University of Belgrade
Chemical Engineering	TATJANA **KALUĐEROVIĆ RADOIČIĆ**, Faculty of Technology and Metallurgy, University of Belgrade
Materials	RADA **PETROVIĆ**, Faculty of Technology and Metallurgy, University of Belgrade
Metallic Materials and Metallurgy	ANA **KOSTOV**, Mining and Metallurgy Institute Bor, University of Belgrade
Environmental and Geochemistry	VESNA **ANTIĆ**, Faculty of Agriculture, University of Belgrade
History of and Education in Chemistry	DRAGICA **TRIVIĆ**, Faculty of Chemistry, University of Belgrade
English Language Editors:	LYNNE **KATSIKAS**, Serbian Chemical Society VLATKA **VAJS**, Serbian Chemical Society JASMINA **NIKOLIĆ**, Faculty of Technology and Metallurgy, University of Belgrade
Technical Editors:	VLADIMIR **PANIĆ**, Institute of Chemistry, Technology and Metallurgy, University of Belgrade, MARIO **ZLATOVIĆ**, Faculty of Chemistry, University of Belgrade
Journal Manager & Web Master:	MARIO **ZLATOVIĆ**, Faculty of Chemistry, University of Belgrade
Office:	VERA **ĆUŠIĆ**, Serbian Chemical Society

Editorial Board

From abroad: **R. Adžić**, Brookhaven National Laboratory (USA); **A. Casini**, University of Groningen (The Netherlands); **G. Cobb**, Baylor University (USA); **D. Douglas**, University of British Columbia (Canada); **G. Inzelt**, Etvos Lorand University (Hungary); **J. Kenny**, University of Perugia (Italy); **Ya. I. Korenman**, Voronezh Academy of Technology (Russian Federation); **M. D. Lechner**, University of Osnabrueck (Germany); **S. Macura**, Mayo Clinic (USA); **M. Spiteller**, INFU, Technical University Dortmund (Germany); **M. Stratakis**, University of Crete (Grecce); **M. Swart**, University de Girona (Cataluna, Spain); **G. Vunjak-Novaković**, Columbia University (USA); **P. Worsfold**, University of Plymouth (UK); **J. Zagal**, Universidad de Santiago de Chile (Chile).

From Serbia: **B. Abramović**, **V. Antić**, **R. Baošić**, **V. Beškoski**, **J. Csanadi**, **Lj. Damjanović-Vasilić**, **A. Dekanski**, **V. Dondur**, **B. Dunjić**, **M. Đuran**, **B. Glišić**, **S. Gojković**, **I. Gutman**, **B. Jovančićević**, **I. Juranić**, **T. Kaluđerović Radoičić**, **L. Katsikas**, **M. Kijevčanin**, **A. Kostov**, **V. Leovac**, **S. Milonjić**, **V.B. Mišković-Stanković**, **O. Nedić**, **B. Nikolić**, **J. Nikolić**, **D. Opsenica**, **V. Panić**, **M. Petkovska**, **R. Petrović**, **I. Popović**, **B. Radak**, **S. Ražić**, **D. Sladić**, **S. Sovilj**, **S. Šerbanović**, **B. Šolaja**, **Ž. Tešić**, **D. Trivić**, **V. Vajs, M. Zlatović**.

Subscription: The annual subscription rate is **150.00 €** including postage (surface mail) and handling. For Society members from abroad rate is **50.00 €**. For the proforma invoice with the instruction for bank payment contact the Society Office (E-mail: shd@shd.org.rs) or see JSCS Web Site: http://www.shd.org.rs/JSCS/, option Subscription.

Godišnja pretplata: Za članove SHD: **2.500,00 RSD**, za penzionere i studente: **1000,00 RSD**, a za ostale: **3.500,00 RSD**:za organizacije i ustanove: **16.000,00 RSD**. Uplate se vrše na tekući račun Društva: **205-13815-62**, poziv na broj **320**, sa naznakom "pretplata za JSCS".

Nota: Radovi čiji su svi autori članovi SHD prioritetno se publikuju.

Odlukom Odbora za hemiju Republičkog fonda za nauku Srbije, br. 66788/1 od 22.11.1990. godine, koja je kasnije potvrđena odlukom Saveta Fonda, časopis je uvršten u kategoriju međunarodnih časopisa (**M-23**). Takođe, aktom Ministarstva za nauku i tehnologiju Republike Srbije, 413-00-247/2000-01 od 15.06.2000. godine, ovaj časopis je proglašen za publikaciju od posebnog interesa za nauku. **Impact Factor** časopisa objavljen 28. juna 2023. godine je **1,000**, a petogodišnji **Impact Factor 1,100**.

Journal of the Serbian Chemical Society
JSCS-info@shd.org.rs • www.shd.org.rs/JSCS

J. Serb. Chem. Soc. Vol. 89, No. 3 (2024)

CONTENTS*

Published by the Serbian Chemical Society
Karnegijeva 4/III, P.O. Box 36, 11120 Belgrade, Serbia
Printed by the Faculty of Technology and Metallurgy
Karnegijeva 4, P.O. Box 35-03, 11120 Belgrade, Serbia

* For colored figures in this issue please see electronic version at the Journal Home Page: http://www.shd.org.rs/JSCS/

Journal of the Serbian Chemical Society
JSCS@tmf.bg.ac.rs • www.shd.org.rs/JSCS
J. Serb. Chem. Soc. *89* (3) 291–303 (2024)
JSCS–5721
Original scientific paper
Published 29 March 2024

Synthesis, computational and pharmacological evaluation of novel *N*-{4-[2-(4-aryl-piperazin-1-yl)ethyl]phenyl}-arylamides

DEANA B. ANDRIĆ[1]*#, SLADJANA DUKIĆ-STEFANOVIĆ[2], MIHAJLO J. KRUNIĆ[3#], IVANA I. JEVTIĆ[3#], JELENA Z. PENJIŠEVIĆ[3#], VLADIMIR B. ŠUKALOVIĆ[3#] and SLAĐANA KOSTIĆ-RAJAČIĆ[3#]

[1]*University of Belgrade, Faculty of Chemistry, Department of Organic Chemistry, Studentski trg 12-16, 11158 Belgrade, Serbia,* [2]*Helmholtz-Zentrum Dresden-Rossendorf, Institute of Radiopharmaceutical Cancer Research, Department of Neuroradiopharmaceuticals, Research site Leipzig, Germany and* [3]*University of Belgrade, ICTM – Department of Chemistry, Njegoševa 12, 11000 Belgrade, Serbia*

(Received 6 September, revised 1 October, accepted 11 October 2023)

Abstract: Serotonin, or 5-hydroxytryptamine (5-HT), is a biogenic amine most noted as a neurotransmitter, an activator of the utmost subtype family of G-protein-coupled receptors (GPCR). Drugs targeting 5-HT1A and other 5-HT receptors treat central nervous system diseases such as schizophrenia and depression. Recent advances in serotonin receptor structure research gave us several crystal 5-HT1A receptor structures, most notably 5-HT1A bound to the antipsychotic drug aripiprazole (Abilify®). This discovery prompted us to evaluate a series of newly synthesized ligands for serotonergic activity since those arylpiperazine derivatives share minimal general structure with aripiprazole. The results of molecular docking analysis of unsubstituted starting substances encouraged us to propound further modifications of the tail and head parts of the parent molecules to maximize receptor binding affinity. Intrigued by the results of molecular analysis, all foreseen derivatives were synthesized. The pharmacological activity of all nine (**5a** and **6a** are synthesized previously) compounds was assessed by the *in vitro* tests and *in silico* pharmacokinetics predictions for the most promising candidates. All tested ligands have improved affinity compering to parent compounds (**10a** and **11a**), **8b** and **9b** expressed the best pharmacological profile with an improved binding affinity toward serotonin 5-HT1A receptors (*K*i 12.1 and 4.8 nM, respectively).

Keywords: 5-HT1A; aripiprazole; arylpiperazines; molecular docking; binding assay.

* Corresponding author. E-mail: deanad@chem.bg.ac.rs
# Serbian Chemical Society member.
https://doi.org/10.2298/JSC230906076A

INTRODUCTION

Serotonin (5-HT) mediates a plethora of physiological effects through at least 14 different receptor subtypes: 13 belong to the G-protein-coupled or seven transmembrane-spanning receptor family, and only one is a ligand-gated ion channel. Based on molecular, pharmacological and functional criteria, 5-HT receptors have been classified into seven discrete families (5-HT1-7).[1] The 5-HT1A receptors are connected with mood disorders (anxiety, depression), cognition and pain modulation. After decades of research in this field, there is continuing interest in developing new chemical entities capable of 5-HT1A receptor activation or blockade.[2] 5-HT1A receptors are also a promising target for alleviating extrapyramidal side effects (EPS) and cognitive/affective disorders caused by either antipsychotic or Parkinson's disease therapy.[3]

N-Arylpiperazine-containing ligands are a large class of chemical compounds with various biological activities, such as antimicrobial, antiviral and anticancer properties and adrenergic and serotonin receptor inhibition.[4-8] Arylpiperazine derivatives are known to bind monoamine receptors, including 5-HT receptors. The general formula is Ar–piperazine–linker–terminal fragment, and suitable modifications of either Ar, linker or terminal segment, can lead to selective or nonselective compounds.[9] The high affinity of these systems to 5-HT receptors stems from the basic nitrogen atom of the piperazine, which can form strong interactions with the conserved acidic amino acids in the GPCR transmembrane domain of these proteins.[10] Chained arylpiperazines (CAPs) have established their position as favourable scaffolds for 5-HT1A receptor binding. Further CAP studies evaluated the length and flexibility of the alkyl chain at the *N*4. In contrast, the influence of introduced amide group is controversial. One study suggests that amide group can stabilize the ligand-receptor complex, whereas others suggest little or no impact on receptor binding.[11,12]

The design of CAPs became the standard approach in drug development, especially for diseases with complex pathophysiology. An aryl group attached to the nitrogen atom of piperazine is substituted phenyl or a heteroaromatic system. The other terminus often contains an amide or has an imide function, but it may be phenyl or another aromatic group. In many series of arylpiperazine ligands, the alkyl chain consists of two to four methylene units; however, groups other than methylene ones (heteroatoms, carbonyl, an amide fragment or multiple bonds) have also been introduced to the spacer. Therefore, investigations within active compounds consist of structural modifications of all the ligand fragments.[13]

In our study on the effect of the introduction of various moieties in *N*-{[2-(4--phenylpiperazin-1-yl)ethyl]phenyl}-arylamides on their binding affinity for the 5-HT1A receptor has been explored.[14] Results of that discovery inspired us to design a series of arylpiperazine derivatives.[15] The main focus of current modifications was on terminal amide moiety (introduction of hydroxyl group) and aryl-

piperazine part (introduction of 2,3-dichloro and methoxy groups) since proposed ligands share minimal general shape with aripiprazole (Fig. 1). Graph representation of the dissection of aripiprazole into four units crucial for the affinity towards 5-HT1A receptor and their incorporation into the structure of the newly synthesized compounds are: a) phenylpiperazine moiety plays a key role in binding at the active site; b) substitution of both electron-withdrawing and electron--donating groups at the ortho position and substitution of chloro group in the meta position of phenyl ring; c) two to five carbon spacer; d) amide group incurporated as part of the terminal fragment. After detailed molecular docking analysis, seven new *N*-{4-[2-(4-aryl-piperazin-1-yl)ethyl]phenyl}-arylamides (**5b** and **c**–**9b**) together with **5a** and **6a** (synthesised previously)[16] are subjected to pharmacological evaluation and *in silico* pharmacokinetics predictions for the most promising candidates.

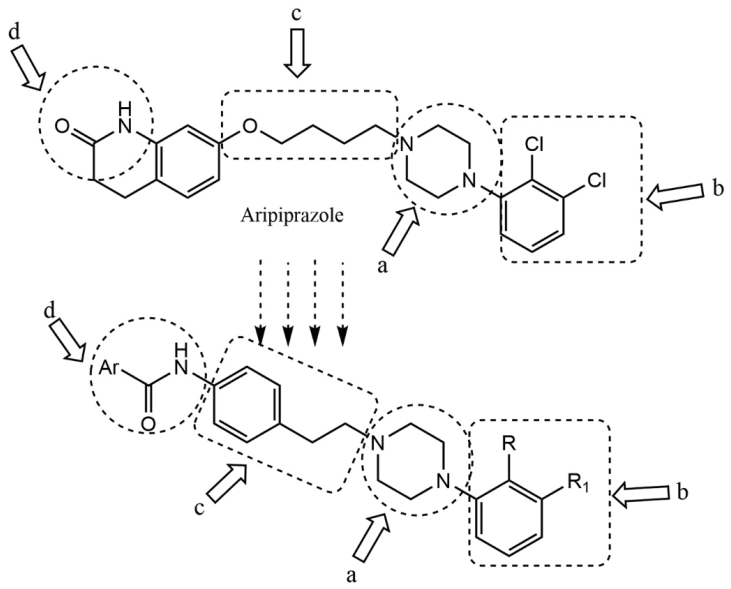

N-{4-[2-(4-aryl-piperazin-1-yl)ethyl]phenyl}-arylamides

Fig. 1. Rational design of novel arylpiperazines.

EXPERIMENTAL

General information

The reagents and solvents used in this work were obtained from Alfa Aesar or Sigma–Aldrich and used without further purification. Solvents were routinely dried over anhydrous Na_2SO_4 before evaporation. ^{1}H- and ^{13}C-NMR spectra were recorded on: ^{1}H-NMR (200 MHz) and ^{13}C-NMR (50 MHz), Gemini 2000 spectrometer; and ^{1}H-NMR (500 MHz) and ^{13}C-NMR (126 MHz), Bruker Avance III spectrometer. Chemical shifts (δ) are reported in ppm from tetramethylsilane (TMS) as an internal standard in deuterated chloroform ($CDCl_3$)

or dimethyl sulfoxide (DMSO-d_6); all coupling constants (J values) are reported in Hz; high-resolution mass spectra (HRMS) were obtained with a heated ESI (HESI)-LTQ Orbitrap XL spectrometer. Melting points were obtained by a Boetius PHMK apparatus (VEB Analytic, Dresden, Germany) at a heating rate of 4 °C/min and are uncorrected. IR spectra were recorded using a Thermo Scientific Nicolet 6700 Fourier-transform spectrometer operated in the ATR mode. For analytical thin-layer chromatography (TLC), Polygram SIL G/UV254 plastic-backed thin-layer silica gel plates were used (Macherey-Nagel, Germany).

Analytical and spectral data of the synthesized compounds are given in Supplementary material to this paper.

*General procedure for the synthesis of 2-(4-nitrophenyl)-1-(4-arylpiperazin-1-yl)ethane-1-ones (**2b** and **c**)*

Arylpiperazine (52 mmol), 4-nitrophenylacetic acid (**1**), (52 mmol) and Et_3N (57.2 mmol) were dissolved in 170 mL dry *N,N*-dimethylformamide (DMF). The obtained solution was cooled to 10 °C, and propylphosphonic acid anhydride (PPAA) solution (72.7 mmol, 50 % solution in DMF) was added dropwise, and the reaction mixture was stirred for 24 h at room temperature. The reaction was monitored by TLC. The reaction mixture was poured onto ice/water. The pH of the suspension was adjusted to 8 with a 10 % Na_2CO_3 solution (from the acidic range). The precipitate was filtrated, washed with water, and crystallized from acetone to give the expected product.

*General procedure for synthesis 1-(4-nitrophenethyl)-4-arylpiperazines (**3b** and **c**)*

To a suspension of **2b** or **2c** (46.1 mmol) in 300 mL dry tetrahydrofuran (THF), a diborane solution (1 M in THF, 118 mL, 118 mmol) was added dropwise at 0 °C. When the addition of diborane was completed reaction mixture was progressively heated. After the spontaneous boiling stop, the reaction mixture was refluxed for an additional 2 h. After cooling to room temperature, water (35 mL) was slowly added, followed by 5.5 M HCl (70 mL). The reaction mixture was refluxed for another 60 min and was left to cool down to 25 °C. The reaction mixture was evaporated, and the resulting fluid was treated with 10 % $NaHCO_3$ solution to pH 8. The product was extracted with ethyl acetate, washed with water and brine and evaporated. The resulting 4-nitrophenethyl-piperazines were purified by silica gel column chromatography using a gradient of methanol (0–5 %) in dichloromethane.

*General procedure for synthesis 4-(2-(4-arylpiperazin-1-yl)ethyl)anilines (**4b** and **c**)*

Raney/Ni (195 mg) was added, in portions, to a stirred mixture of hydrazine hydrate (32.5 mm), ethanol (26 mL), (6.5 mm) of compound **3b** or **3c** (6.5 mm), and 1,2-dichloroethane (12mL). Stirring was continued at room temperature until the mixture became colorless and then was heated at 50 °C for 40 min. The resulting mixture was filtrated through Celite, and the solvent was removed under reduced pressure. The resulting anilines were used for further synthesis without purification.

General procedure for synthesis N-*(4-(2-(4-phenylpiperazin-1-yl)ethyl)phenyl)arylamides (**5b** and **c**–**9b**)*

A solution of **4b** or **4c** (1.77 mmol), triethylamine (4.44 mmol, 0.62 mL), the corresponding carboxylic acid (1.77 mmol), and PPAA (1.95 mmol, 1.14 mL, 50 % solution in DMF) in dry DMF (10mL) was stirred at room temperature overnight. The mixture was poured into ice/water. Organic layers were separated and evaporated. The resulting *N*-{3-[2-(4-arylpiperazin-1-yl)ethyl]phenyl}arylamides were purified by silica gel column chromategraphy using a gradient of methanol (0–5 %) in dichloromethane.

Binding assays

The affinity of the synthesized compounds towards 5-HT1A was determined by radioligand competition binding assays. The assays were performed using crude cell membrane homogenates obtained from HEK cells stably transfected with human 5-HT1A receptor and the 5-HT1A specific radioligand [^{3}H]-8-OH-DPAT (obtained from PerkinElmer, NET929250UC). Membrane suspension was incubated with 1 nM [^{3}H]-OH-DPAT and various concentrations of the test compound in 25 mM Tris-HCl, pH 7.4 buffer containing 120 mM NaCl, 5 mM KCl at room temperature for 60 min. Non-specific binding was determined in the presence of 10 μM of serotonin. The reaction was terminated by rapid filtration using Whatman GF/B glass-fibre filters, pre-soaked in 0.3 % polyethyleneimine, and a 48-channel harvester (Biomedical Research and Development Laboratories, Gaithersburg, MD, USA) followed by washing four times with ice-cold Tris-HCl buffer. Filter-bound radioactivity was quantified by liquid scintillation counting. At least three separate experiments in triplicate were performed to determine inhibitory constant (*K*i) values. The data were analyzed by GraphPad Prism, version 4.1 (GraphPad Inc., La Jolla, CA, USA).

Absorption, distribution, metabolism, excretion and toxicity (ADMET) analysis

To predict absorption, distribution, metabolism and excretion (ADME) qualities of tested ligands, we used the SwissADME webserver (www.swissadme.ch).[17] Toxicology prediction was done through Pro Tox-II virtual lab server for the prediction of toxicities of small molecules (https://tox-new.charite.de/protox_II/index.php?site=home).[18] Ligand structures were provided as SMILES using ChemDraw.

Docking simulations

Docking simulations were done in Maestro Suite software.[19] 3D model of the 5-HT1A receptor with bound aripiprazole (PDB Code 7E2Z) was obtained from the GPCR database.[20] 2D structures of ligands were drawn in ChemDraw software and prepared for docking in Maestro software using default LigPrep procedures.

Induced fit docking (IFD) simulation using standard sampling protocol and default values, was carried out for prepared receptor model and selected ligands.[21] Bind site was defined, based on bound aripiprazole and centered on ASP 116 residue. The inner grid box was set to 10 Å ×10 Å ×10 Å and the outer box size according to the size of each tested ligand. Grid spacing was set to 1 Å. Obtained docking structures were examined and selected for further analysis based on the number of receptor-ligand interactions and calculated post docking MM–GBSA energy.

Molecular dynamics simulations

Molecular dynamics (MD) simulations were performed using the Schrodinger Desmond software package.[19] Docking poses selected for MD were prepared for simulation by embedding the protein–ligand complex into the POPC membrane bilayer using the Desmond system builder module. Protein was oriented in the membrane according to the data from the Orientations of Proteins in Membranes (OPM) server (http://opm.phar.umich.edu/). The entire system was solvated with a TIP3P explicit water model and neutralized *via* counter ions and salt solution of 0.15 M KCl. We used OPLS 2003 forcefield to calculate the interactions between all the atoms. For the calculation of the long-range Coulombic interactions, particle-mesh Ewald (PME) method was used, with the cut-off radius of 9 Å for the short-range van der Waals (VdW) and electrostatic interactions.

During the simulation, a constant temperature of 310 K and a pressure of 1.01235 bar were maintained, using the Nose–Hoover thermostat, and the Martyna Tobias Klein method.

100 ns MD simulation with 2.0 fs step for each complex was performed and the collected trajectory was used in the MD analysis to assess the docking pose and protein-ligand interactions stability.

RESULTS AND DISCUSSION

Chemistry

In Scheme 1, the general synthetic route towards modified derivatives (**5b** and **c**–**9b**) is presented. Briefly, acylation of the appropriate arylpiperazine by 4-nitrophenylacetic acid **1** afforded amides **2b** and **c**, which upon reduction by B_2H_6, provided corresponding amines **3b** and **c**. Further reduction of the nitro group in **3** with Ra/Ni, followed by *N*-acylation of **4** with aryl acids, yielded final products in high overall yields (59–73 %). All compounds were characterized spectroscopically.

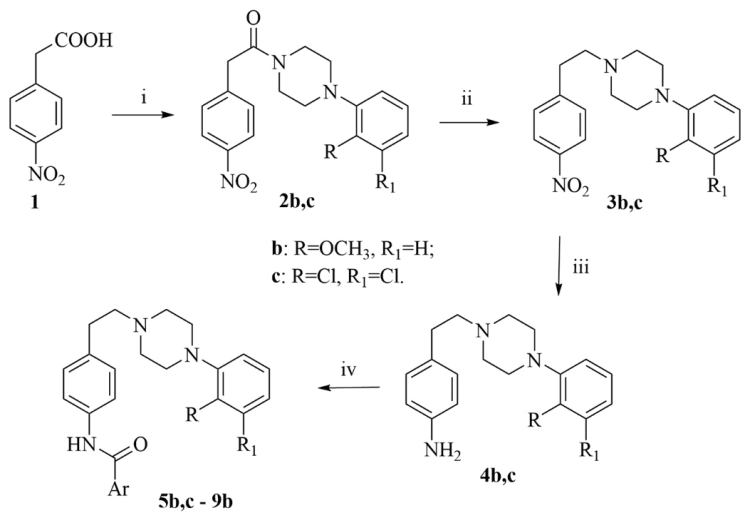

Scheme 1. Reagents and conditions for the synthesis: *i*) arylpiperazine, Et_3N, PPAA, DMF, r.t.; *ii*) B_2H_6, THF, 0 °C for 6 h, r.t. for 1 h, then reflux for 2 h; *iii*) Ra/Ni, NH_2NH_2, EtOH, 1,2-dichloroethane; *iv*) $ArCO_2H$, Et_3N, PPAA, DMF, r.t. ($ArCO_2H$: 2-hydroxynicotinic acid for the preparation of **5b** and **c**; 6-hydroxynicotinic acid for the preparation of **6b** and **c**; 2-(4-hydroxyphenyl)acetic acid for the preparation of **7b**; 3-hydroxybenzoic acid for the preparation of **8b**; 4-hydroxybenzoic acid for the preparation of **9b**).

Detailed spectral data for all synthesized compounds are given in the Supplementary material to this paper (Figs. S-1–S-22; for phenyl precursors and ligands **5a** and **6a**, please see ref. 14 and 16).

Biological evaluation

The affinity of the compounds, depicted in Table I, towards 5-HT1A was determined in radioligand competition binding assays using [^{3}H]-8-OH-DPAT.

As presented in Table I, all nine ligands (**5a**–**c**–**9b**) had an enhancement in affinity for 5-HT1A receptors compared to parent compounds (**10a** and **11a**). Scrutiny of the obtained experimental affinity values revealed that the most pronounced increase was recorded with ligand **9b**, followed by **8b**, **5b** and **7b**. For other ligands, the enhancement of the affinity is from temperate to slight (compared to hydroxy ligand **11a**, the more active of the two parent compounds), and the decreasing order is **6b** > **5a** > **5c** > **6c** > **6a**. Analyzing the relationship between the experimental affinity values of the new ligands and aripiprazole, ligand **9b** stood out with affinity in the same range as a commercial drug.

TABLE I. 5-HT1A affinity for newly synthesized and parent compounds and commercial drug, aripiprazole; data for parent compounds **10a** and **11a** taken from Ref. 14; data for aripiprazole taken from Ref. 22

No.	Ar	R	R_1	*Ki*±*SEM* / nM
5a		H	H	182.3±7.0
5b		OCH_3	H	24.2±3.1
5c		Cl	Cl	392.6±9.2
6a	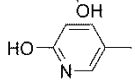	H	H	453.9±8.0
6b	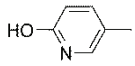	OCH_3	H	117.3±4.3
6c	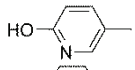	Cl	Cl	286.6±5.1
7b	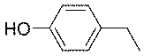	OCH_3	H	46.8±1.9
8b	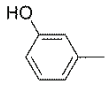	OCH_3	H	12.1±1.2
9b	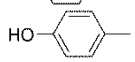	OCH_3	H	4.8±0.5
10a		H	H	2662
11a		H	H	575
Aripiprazole				5.6±0.8

The *Ki* values indicate that the influence of substitution on phenyl piperazine on the 5-HT1A receptors binding affinity is pronounced (compared to parent compounds **10a** and **11a**).

The introduction of 2,3-dichloro and methoxy group and hydroxyl group (regardless of the position) in the amide group led to an increase in the affinity of the 5-H1A receptor, especially pronounced in the case of ligands with sizeable affinity gains, **8b** and **9b**.

Docking simulations and molecular dynamics

Docking analysis was done using aripiprazole-bound 5-HT1A receptor-Gi protein complex receptor model (PDB: 7E2Z)[20] and selected ligands (Table I). Receptor binding site was determined using bound aripiprazole position. All ligands were protonated at physiological pH 7.4. Induced fit docking procedure using standard sampling procedure was carried out and results were sorted based on docking score and number of key receptor-ligand interactions.

5-HT1A receptor binding site can be divided into two distinctive parts. Orthosteric binding site (OBS) that is located deep inside the binding cavity, between transmembrane helices 3 and 5 and extended bind pocket (EBP) bordering extracellular space and formed in part by receptor extracellular loops. OBS is responsible for binding of arylpiperazine part of the ligand and correct ligand orientation in the receptor bind site.

Docking results and MD simulations of compounds **5a** and **6a** showed well-established pattern of aryl-piperazine binding to the 5-HT1A receptor. The aryl part of the ligand binds to the OBS inside the receptor binding cavity and the linker–terminal part fits into the EBP bordering extracellular space. Key interactions in the OBS, with Asp116 (salt bridge) and Phe361 and 362 (aromatic, edge-to-face, C–H···π), provide correct ligand orientation inside the receptor binding cavity and binding of linker–terminal part in the EBP.

Key interactions in the EBP depend on linker–terminal length, shape, size and flexibility, and can further amplify (or diminish) ligand affinity. In the case of compound **5a**, key interactions in the EBP are with Tyr96, Gln97, Asn386 and Asn387, while **6a** forms interaction with Tyr96 and Asn100 (for details, see the Supplementary material, Fig. S-22).

The introduction of 2-methoxy and 2,3-dichloro groups in the aryl part of starting compounds should lead to an increase in receptor affinity through the amplification of existing aromatic interactions with Phe361 and 362 and the establishment of new interactions with various amino acid residues in OBS.[23]

Experimental results show an increase in affinity in compounds **5b**, **6b** and **6c**, while compound **5c** had a slight affinity drop. Docking and MD results revealed that in the case of **5b**, **6b** and **6c**, original key interactions were preserved, and additional interactions were formed, with Gln97 and Asn386 (for **6b** and **c**) and Tyr390 (for **5b**). However, compound **5c** didn't perform as expected. Obviously, the addition of two chlorine atoms in the aryl part of the molecule and an intermolecular hydrogen bond in the linker–terminal fragment caused increased

ligand rigidity and size that led to a decrease in binding affinity (for details, see the Supplementary material, Figs. S-23 and S-24).

Since in both series (**5a**–**c** and **6a**–**c**), ligands with 2,3-dichloro substituent performed worse than expected, compared to 2-methoxy counterparts, the decision was to keep 2-methoxy moiety fixed for further synthesis, but to alter linker–terminal part, to obtain compounds with increased receptor affinity. With that in mind, compounds **7b**, **8b** and **9b** were synthesized and tested.

Molecular docking and dynamics gave us the following results. In the case of compound **8b**, we have key interactions with Asp116, Phe361, 362 and Cys120 in the OBS, together with Tyr96, Gln97 and Asn386 in the EBP. Interactions of **9b** formed in OBS are the same as **8b**. In the EBP, key interactions are with Tyr96, Gln97, Asn100 and Asn386 (Figs. 2 and 3). The indicated makes **9b** the best receptor affinity compound among newly synthesized compounds, followed by **8b** and **5b**. Compound **7b** shows a drop in affinity because the elongation of the linker-terminal part reached the maximum allowed length that can bind in EBP (for details, see the Supplementary material, Fig. S-25).

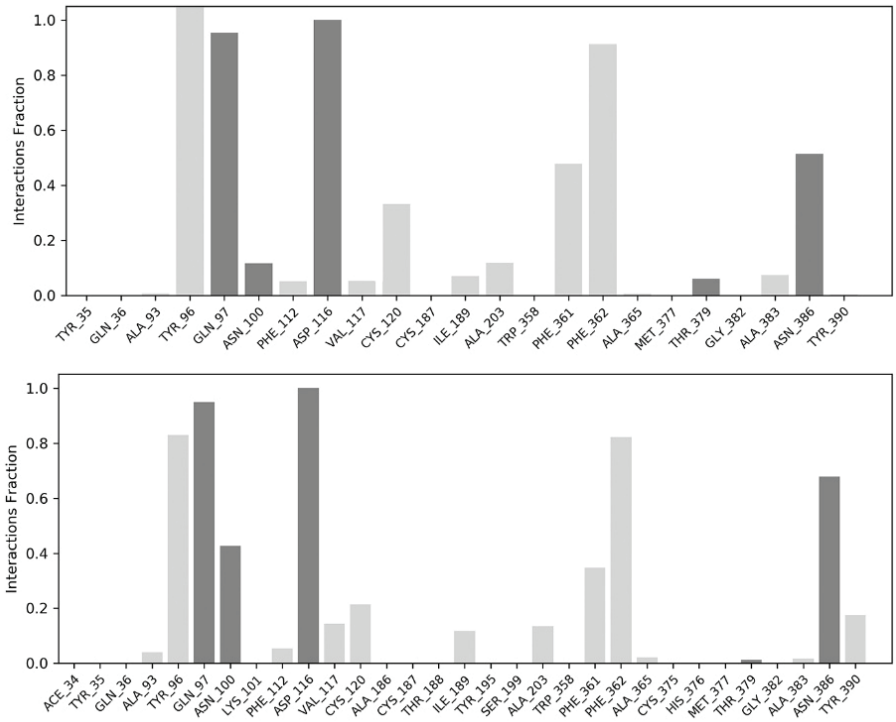

Fig. 2. Diagram of key receptor – **8b** (top) and **9b** (bottom) interactions observed during 100 ns molecular dynamics. Aromatic interactions are shown light gray, while hydrogen bonds are dark gray. Interactions maintained for 20 % or more of total MD time are considered crucial.

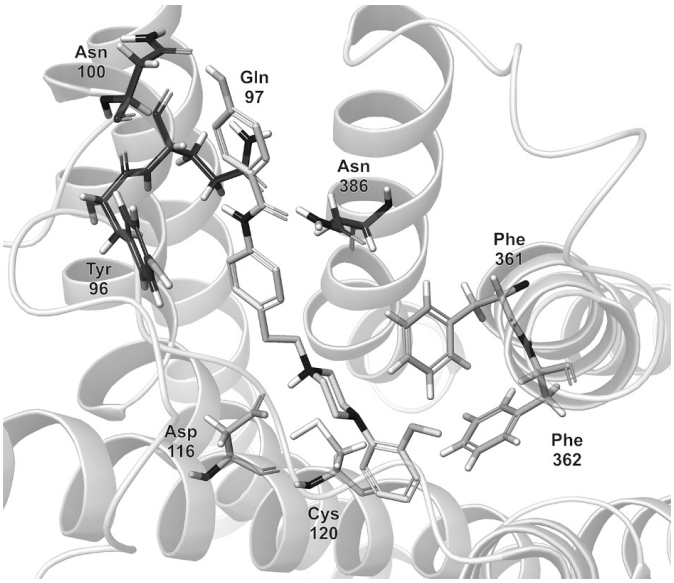

Fig. 3. 3D model of compound **9b** (light gray) docked into 5-HT1A bind site. Only key OBS (light gray) and EBP (dark gray) amino acid residues are shown for clarity.

ADMET prediction

Rejection of potential drugs at later stages of drug development may cause substantial financial loss; therefore, it is reasonable that pharmacokinetic studies have been highlighted as early predictors of important potential drug parameters. To account for these characteristics, we used ADMET prediction. Results of the most promising compounds, **8b** and **9b**, together with aripiprazole, are displayed (Fig. 4). Predicted ADME results are favorable and show no potential problems. Solubility, gastrointestinal absorption and crossing the blood–brain barrier (BBB) are on par with aripiprazole.

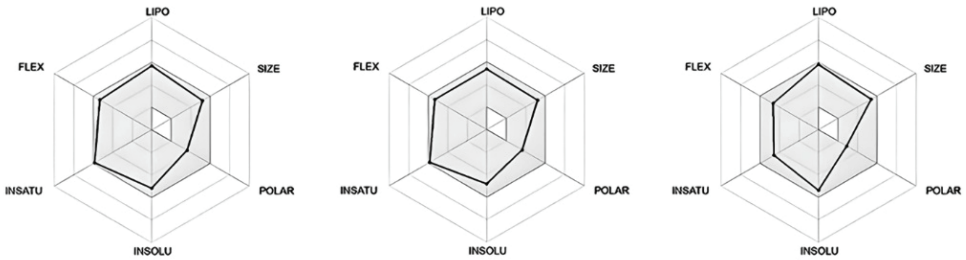

Fig. 4. Radar representation of ADME properties for compounds **8b** (left), **9b** (middle) and aripiprazole (right). For details, see the Supplementary material, Figs. S-26–S-28.

Toxicity calculations were negative for compound **9b**, but **8b** has a 0.6 chance of being immunotoxic. Compared to aripiprazole, this is not the reason for automatic exclusion as a potential drug candidate because aripiprazole shows the same result, with a greater probability (0.98, for details, see the Supplementary material, Figs. S-26–S-28).

CONCLUSION

In summary, we used computer-aided rational drug design to amplify the receptor affinity of starting compounds to levels comparable with aripiprazole. From nine tested *N*-{4-[2-(4-aryl-piperazin-1-yl)ethyl]phenyl}-arylamides, **9b** had *K*i = 4.7 nM, closely followed by **8b** (*K*i = 12.06nM). Both compounds are 2-OMe derivatives of the parent phenyl ligands with lower receptor affinity. Introduction of the 2-OMe group in the aryl part of the ligand strengthens aromatic interactions with Phe361 and 362 residues, establishing additional hydrogen bond with Cys120. The linker–terminal part of the compound is a material segment in obtaining high receptor affinity ligands because of the additional interaction with the key amino acid residues of EBP. According to our findings, Gln97 and Tyr96 are the key residues in EBP, shared between all tested compounds (and aripiprazole) and followed by Asn386 and Asn100. Flexible ligands had better affinity than rigid ones. The initial size of the compounds was well judged as elongation of the molecule in the case of **7b** caused a drop in affinity compared with **9b**. Predicted ADMET characteristics for both compounds show a preferable profile for drug candidates.

The results for the most active compound from series **9b** and aripiprazole (4.8 and 5.6 nM) suggest that the presented modification strategies resulted in candidates that confirm the effectiveness of the predictive-experimental correlation approach and in our opinion compound **9b** presents a good candidate for further testing.

SUPPLEMENTARY MATERIAL

Additional data and information are available electronically at the pages of journal website: https://www.shd-pub.org.rs/index.php/JSCS/article/view/12577, or from the corresponding author on request.

Acknowledgements. This work was supported by the Ministry of Science, Technological Development and Innovation of the Republic of Serbia (Grant No. 451-03-47/2023-01/ /200026, and for D. B. Andric Contract number: 451-03-47/2023-01/200168).

ИЗВОД

СИНТЕЗА, КОМПЈУТЕРСКА АНАЛИЗА И ФАРМАКОЛОШКА ЕВАЛУАЦИЈА НОВИХ *N*-{4-[2-(4-АРИЛПИПЕРАЗИН-1-ИЛ)ЕТИЛ]ФЕНИЛ}-АРИЛАМИДА

ДЕАНА Б. АНДРИЋ[1], СЛАЂАНА ДУКИЋ-СТЕФАНОВИЋ[2], МИХАЈЛО Ј. КРУНИЋ[3], ИВАНА И. ЈЕВТИЋ[3], ЈЕЛЕНА З. ПЕЊИШЕВИЋ[3], ВЛАДИМИР Б. ШУКАЛОВИЋ[3] и СЛАЂАНА КОСТИЋ-РАЈАЧИЋ[3]

[1]Универзитет у Београду, Хемијски факултет, Катедра за органску хемију, Студентски трг 12–16, 11158 Београд, [2]Helmholtz-Zentrum Dresden-Rossendorf, Institute of Radiopharmaceutical Cancer Research, Department of Neuroradiopharmaceuticals, Research site Leipzig, Germany и [3]Универзитет у Београду, ИХТМ – Центар за хемију, Његошева 12, 11000 Београд

Серотонин, 5-хидрокситриптамин (5-HT), је биогени амин који је најпознатији као неуротрансмитер, активатор највеће породице подтипова G-протеин-куплованих рецептора (GPCR). Лекови, чије су мете 5-HT1A и други 5-HT рецептори, се користе у лечењу болести централног нервног система, као што су шизофренија и депресија. Недавни напредак у истраживању структуре серотонинских рецептора се огледа у неколико кристалних 5-HT1A рецепторских структура, од којих је најзначајнија она код које је за 5-HT1A везан антипсихотични лек, арипипразол. Ово откриће нас је мотивисало да проценимо серотонергичку активност серије новосинтетизованих лиганада, пошто ти деривати арилпиперазина са арипипразолом деле минималну општу структуру. Резултати молекулске анализе пристајања несупституисаних лиганада подстакли су нас да предложимо даље модификације репа и делова главе полазних молекула, како би афинитет везивања за рецептор био израженији. Заинтригирани резултатима молекулске анализе, сви предвиђени деривати су и синтетисани. Фармаколошка активност свих девет једињења је процењена *in vitro* тестовима, док је за најперспективнија једињења урађено *in silico* фармакокинетичко предвиђање. Сва тестирана једињења имају побољшани афинитет у поређењу са полазним (**10a** и **11a**), док се **8б** и **9б** истичу најбољим фармаколошким профилом и афинитетом везивања према серотонинским 5-HT1A рецепторима (*K*i 12,06 и 4,78 nM).

(Примљено 6. септембра, ревидирано 1. октобра, прихваћено 10. октобра 2023)

REFERENCES

1. D. Hoyer, J. P. Hannon, G. R. Martin, *Pharmacol. Biochem. Behav.* **71** (2002) 533 (https://doi.org/10.1016/s0091-3057(01)00746-8)
2. P. M. Whitaker-Azmitia, *Neuropsychopharmacology* **21** (1999) 2S (https://doi.org/10.1016/S0893-133X(99)00031-7)
3. E. Lacivita, P. Di Pilato, P. De Giorgio, N. A. Colabufo, F. Berardi, R. Perrone, M. Leopoldo, *Expert Opin. Ther. Pat.* **22** (2012) 887 (https://doi.org/10.1517/13543776.2012.703654)
4. I. Malík, J. Csöllei, J. Jampílek, L. Stanzel, I. Zadražilová, J. Hošek, Š. Pospíšilová, A. Čížek, A. Coffey, *Molecules* **21** (2016) 1274 (https://doi.org/10.3390/molecules21101274)
5. Y. Chu, B. Raja Sekhara Reddy, V. Pratap Reddy Gajulapalli, K. Sudhakar Babu, E. Kim, S. Lee, *Bioorg. Med. Chem. Lett.* **30** (2020) 127613 (https://doi.org/10.1016/j.bmcl.2020.127613)
6. C. Wang, Z. Wang, M. Gao, Y. Li, Y. Zhang, K. Bao, Y. Wu, Q. Guan, D. Zuo, W. Zhang, *Bioorg. Chem*. **106** (2021) 104199 (https://doi.org/10.1016/j.bioorg.2020.104199)
7. R. O. Silva, A. S. de Oliveira, L. F. Nunes Lemesde, L. Camargo Nascente, P. Coelho do Nascimento Nogueira, E. R. Silveira, G. D. Brand, G. Vistoli, A. Cilia, E. Poggesi, M.

Buccioni, G. Marucci, M. L. Bolognesi, L. A. S. Romeiro, *Eur. J. Med. Chem*. **122** (2016) 601 (https://doi.org/10.1016/j.ejmech.2016.06.052)
8. R. R. Kumar, B. Sahu, S. Pathania, P. K. Singh, M. J. Akhtar, B. Kumar, *ChemMedChem* **16** (2021) 1878 (https://doi.org/10.1002/cmdc.202100045)
9. J. Staroń, R. Bugno, A. S. Hogendorf, A. J. Bojarski, *Expert Opin. Ther. Pat*. **28** (2018) 679 (https://doi.org/10.1080/13543776.2018.1514011)
10. P. Zaręba, P. Śliwa, G. Satała, P. Zajdel, G. Latacz, J. Jaśkowska, *Eur. J. Med. Chem*. **235** (2022) 114319 (https://doi.org/10.1016/j.ejmech.2022.114319)
11. K. Ostrowska, K. Młodzikowska, M. Głuch-Lutwin, A. Gryboś, A., Siwek, *Eur. J. Med. Chem*. **137** (2017) 108 (https://doi.org/10.1016/j.ejmech.2017.05.047)
12. E. Pindelska, M. A. Mogilnicki, J. Jaśkowska, I. D. Madura, *Cryst. Growth Des.* (2023) (https://doi.org/10.1021/acs.cgd.3c00438)
13. P. Kowalski, J. Jaśkowska, A. J. Bojarski, B. Duszyńska, A. Bucki, M. Kołaczkowski, *J. Heterocyclic Chem*. **48** (2011) 192 (https://doi.org/10.1002/jhet.526)
14. V. Sukalovic, A. E. Bogdan, G. Tovilovic, D. Ignjatovic, D. Andric, S. Kostic-Rajacic, V. Soskic, *Arch. Pharm. Chem. Life Sci*. **346** (2013) 708 (https://doi.org/10.1002/ardp.201300189)
15. J. Z. Penjišević, V. B. Šukalović, S. Dukic-Stefanovic, W. Deuther-Conrad, D. B. Andrić, S. V. Kostić -Rajačić, *Arab. J. Chem*. **16** (2023) 104636 (https://doi.org/10.1016/j.arabjc.2023.104636)
16. G. Tovilovic, N. Zogovic, L. Harhaji-Trajkovic, M. Misirkic-Marjanovic, K. Janjetovic, L. Vucicevic, S. Kostic-Rajacic, A. Schrattenholz, A. Isakovic, V. Soskic, V. Trajkovic, *ChemMedChem* **7** (2012) 495 (https://doi.org/10.1002/cmdc.201100537)
17. A. Daina, O. Michielin, V. Zoete, *Sci. Rep*. **7** (2017) 42717 (https://doi.org/10.1038/srep42717)
18. M. N. Drwal, P. Banerjee, M. Dunkel, M. R. Wettig, R. Preissner, *Nucleic Acids Res*. **42** (2014) W53 (https://doi.org/10.1093/nar/gku401)
19. *Schrödinger Release 2018-4, Maestro, Schrödinger*, LLC, New York, NY, 2018
20. P. Xu, S. Huang, H. Zhang, C. Mao, X. E. Zhou, X. Cheng, I. A. Simon, D-D. Shen, H-Y. Yen, C. V. Robinson, K. Harpsøe, B. Svensson, J. Guo, H. Jiang, D. E. Gloriam, K. Melcher, Y. Jiang, Y. Zhang, H. E. Xu, *Nature* **592** (2021) 469 (https://doi.org/10.1038/s41586-021-03376-8)
21. W. Sherman, H. S. Beard, R. Farid, *Chem. Biol. Drug Des*. **67** (2006) 83 (https://doi.org/10.1111/j.1747-0285.2005.00327.x)
22. D. A. Shapiro, S. Renock, E. Arrington, L. A. Chiodo, L-X. Liu, D. R. Sibley, B. L. Roth, R. Mailman, *Neuropsychopharmacology* **28** (2003) 1400 (https://doi.org/10.1038/sj.npp.1300203)
23. M. Sencanski, V. Sukalovic, K. Shakib, V. Soskic, L. Dosen-Micovic, S. Kostic-Rajacic, *Chem. Biol. Drug. Des*. **83** (2014) 462 (https://doi.org/10.1111/cbdd.12261).

Journal of the Serbian Chemical Society
JSCS@tmf.bg.ac.rs • www.shd.org.rs/JSCS
J. Serb. Chem. Soc. 89 (3) S102–S124 (2024) *Supplementary material*

SUPPLEMENTARY MATERIAL TO

Synthesis, computational and pharmacological evaluation of novel *N*-{4-[2-(4-aryl-piperazin-1-yl)ethyl]phenyl}-arylamides

DEANA B. ANDRIĆ[1]*, SLADJANA DUKIĆ-STEFANOVIĆ[2], MIHAJLO J. KRUNIĆ[3], IVANA I. JEVTIĆ[3], JELENA Z. PENJIŠEVIĆ[3], VLADIMIR B. ŠUKALOVIĆ[3] and SLAĐANA KOSTIĆ-RAJAČIĆ[3]

[1]*University of Belgrade, Faculty of Chemistry, Department of Organic Chemistry, Studentski trg 12-16, 11158 Belgrade, Serbia,* [2]*Helmholtz-Zentrum Dresden-Rossendorf, Institute of Radiopharmaceutical Cancer Research, Department of Neuroradiopharmaceuticals, Research site Leipzig, Germany and* [3]*University of Belgrade, ICTM – Department of Chemistry, Njegoševa 12, 11000 Belgrade, Serbia*

J. Serb. Chem. Soc. 89 (3) (2024) 291–303

TABLE OF CONTENTS

* Corresponding author. E-mail: deanad@chem.bg.ac.rs

1-(4-(2-methoxyphenyl)piperazin-1-yl)-2-(4-nitrophenyl)ethan-1-one (**2b**): Yield: 74%, oil. ^{1}H NMR (200 MHz, $CDCl_3$, δ): 8.25-8.15 (*m*, 2H, ArH), 7.50-7.41 (*m*, 2H, ArH), 7.09-6.84 (*m*, 4H, ArH), 3.87 (*s*, 5H, 3H OCH_3 and 2H CH_2), 3.83 (*d*, *J* = 5.1, 2H piperazine), 3.71-3.60 (*m*, 2H, piperazine), 3.06-2.95 (*m*, 4H, piperazine). ^{13}C NMR (50 MHz, $CDCl_3$, δ): 167.91, 152.12, 146.89, 142.67, 140.28, 129.90 (2C), 123.73 (3C), 120.00, 118.32, 111.25, 55.32, 50.75, 50.26, 46.23, 43.11, 40.94.

1-(4-(2,3-dichlorophenyl)piperazin-1-yl)-2-(4-nitrophenyl)ethan-1-one (**2c**): Yield: 74%, oil. ^{1}H NMR (200 MHz, $CDCl_3$, δ): 8.26-8.16 (*m*, 2H, ArH), 7.51-7.40 (*m*, 2H, ArH), 7.24-7.11 (*m*, 2H, ArH), 6.89 (*dd*, J_1 = 7.2, J_2 = 2.4, 1H, ArH), 3.86 (*d*, *J* = 6.7, 4H piperazine), 3.72-3.60 (*m*, 2H, CH_2), 2.98-2.89 (*m*,4H, piperazine). ^{13}C NMR (50 MHz, $CDCl_3$, δ): 168.88, 150.92, 148.10, 142.53, 134.23, 130.81 (2C), 127.60, 125.38, 123.88 (3C), 118.74, 52.03, 50.15, 46.27, 42.63, 40.27.

1-(2-methoxyphenyl)-4-(4-nitrophenethyl)piperazine (**3b**): Yield: 72%, oil. ^{1}H NMR (200 MHz, $CDCl_3$, δ): 8.21-8.10 (*m*, 2H, ArH), 7.44-7.35 (*m*, 2H, ArH), 7.08-6.84 (*m*, 4H, ArH), 3.87 (*s*, 3H, OCH_3), 3.13 (*t*, *J* = 4.9, 4H piperazine), 2.99-2.91 (*m*, 2H, CH_2), 2.82-2.65 (*m*, 6H, 4H piperazine and CH_2). ^{13}C NMR (50 MHz, $CDCl_3$, δ): 152.22, 148.36, 146.48, 141.12, 128.98 (2C), 124.14, 123.01 (2C), 120.96, 118.16, 111.13, 59.48, 55.29, 53.29 (2C), 50.54 (2C), 33.90.

1-(2,3-dichlorophenyl)-4-(4-nitrophenethyl)piperazine (**3c**): Yield: 72%, oil. ^{1}H NMR (200 MHz, $CDCl_3$, δ): 8.22-8.12 (*m*, 2H, ArH), 7.46-7.33 (*m*, 2H, ArH), 7.22-7.10 (*m*, 2H, ArH), 7.01-6.92 (*m*, 1H, ArH), 3.09 (*t*, *J* = 4.7, 4H piperazine), 2.99-2.92 (*m*, 2H, CH_2), 2.75-2.68 (*m*, 6H, 4H piperazine and CH_2). ^{13}C NMR (50 MHz, $CDCl_3$, δ): 151.14, 147.73, 146.54, 134.05 (2C), 129.54 (2C), 127.48, 124.67, 124.13 (2C), 118.60, 59.34, 53.17(2C), 52.03 (2C), 34.08.

4-(2-(4-(2-methoxyphenyl)piperazin-1-yl)ethyl)aniline (**4b**): Yield: 93%, oil. ^{1}H NMR (200 MHz, $CDCl_3$, δ): 7.07-6.81 (*m*, 6H, ArH), 6.68-6.56 (*m*, 2H, ArH), 3.86 (*s*, 3H, OCH_3), 3.14 (*s*, 4H, piperazine), 2.83-2.68 (*m*, 6H, 4H piperazine and CH_2), 2.66-2.57 (*m*, 2H, CH_2). ^{13}C NMR (50 MHz, $CDCl_3$, δ): 152.71, 144.46, 141.24, 131.00, 130.09 (2C), 123.38, 120.91, 118.14, 115.20 (2C), 103.92, 59.84, 54.48, 52.88 (2C), 51.00 (2C), 33.70.

4-(2-(4-(2,3-dichlorophenyl)piperazin-1-yl)ethyl)aniline (**4c**): Yield: 89%, oil. ^{1}H NMR (400 MHz, $CDCl_3$, δ): 8.18-8.12 (*m*, 2H, NH_2), 7.38 (*d*, *J* = 8.4, 2H, ArH), 7.29-7.21 (*m*, 2H, ArH), 6.93 (*d*, *J* = 8.2, 2H, ArH), 6.86 (*t*, *J* = 7.3, 1H, ArH), 3.28-3.16 (*m*, 4H, piperazine), 2.96-2.92 (*m*, 2H, CH_2), 2.76-2.61 (*m*, 6H, 4H piperazine and CH_2). ^{13}C NMR (101 MHz, $CDCl_3$, δ): 151.18, 148.23, 146.52, 129.54 (2C), 127.85 (2C), 123.64, 119.46 (2C), 116.09 (2C), 59.42, 53.54 (2C), 49.14 (2C), 33.43.

2-hydroxy-N-*(4-(2-(4-(2-methoxyphenyl)piperazin-1-yl)ethyl)phenyl)nicotinamide* (**5b**): Yield: 69%, oil. IR (ATR): 3257, 2933, 2832, 1673, 1593, 1239, 1115, 1022, 752, cm^{-1}. ^1H NMR (500 MHz, $CDCl_3$, δ): 8.71 (*d*, *J* = 9.4, 1H, ArH), 7.65 (*d*, *J* = 8.5, 1H, ArH), 7.57 (*d*, *J* = 8.5, 1H, ArH), 7.26-7.21 (*m*, 3H, ArH), 7.04-6.99 (*m*, 1H, ArH), 6.97-6.91 (*m*, 2H, ArH), 6.87 (*d*, *J* = 9.6, 1H, ArH), 6.59 (*t*, *J* = 6.8, 1H, ArH), 3.87 (*s*, 3H, OCH_3), 3.15 (*s*, 4H, piperazine), 2.88-2.66 (*m*, 8H, 4H piperazine and $2CH_2$). ^{13}C NMR (126 MHz, $CDCl_3$, δ): 163.70, 160.59, 151.61, 145.49, 139.81, 137.71, 136.34, 136.09, 129.15 (2C), 122.98, 121.86, 120.97, 120.67, 120.11, 118.21, 110.67, 108.08, 60.38, 54.94 (2C), 53.31 (2C), 50.43, 32.81. (+)ESI-HRMS *m/z*: calculated for $[C_{25}H_{28}N_4O_3+H^+]$ 433.22342, observed 433.22197.

N-*(4-{2-[4-(2,3-dichlorophenyl)piperazin-1-yl]ethyl}phenyl)benzamide* (**5c**): Yield: 88%, oil. IR (ATR): 3113, 2958, 2814, 1675, 1599, 1268, 1114, 961, 778, cm^{-1}. ^1H NMR (500 MHz, DMSO-d6, δ): 8.44 (*dd*, J_1 = 7.2, J_2 = 2.1, 1H, ArH), 7.78 (*dd*, J_1 = 6.2, J_2 = 2.3, 1H, ArH), 7.58 (*d*, *J* = 8.3, 2H, ArH), 7.28-7.25 (*m*, 2H, ArH), 7.21 (*d*, *J* = 8.1, 2H, ArH), 7.13-7.11 (*m*, 1H, ArH), 6.55 (*t*, *J* = 6.7, 1H, ArH), 2.97 (*s*, 4H piperazine), 2.72 (*t*, *J* = 7.8, 2H, CH_2), 2.60-2.55 (*m*, 6H, 4H piperazine and CH_2). ^{13}C NMR (126 MHz, DMSO-d6, δ): 162.95, 161.76, 151.60, 144.85, 140.41, 136.74, 136.23, 133.01, 129.56 (2C), 128.83, 126.40, 124.71, 120.52, 120.04, 119.95 (2C), 107.28, 60.00, 53.12 (2C), 51.32 (2C), 32.53. (+)ESI-HRMS *m/z*: calculated for $[C_{24}H_{24}Cl_2N_4O_2+H^+]$ 471.13491, observed 471.13342.

6-hydroxy-N-*(4-(2-(4-(2-methoxyphenyl)piperazin-1-yl)ethyl)phenyl)nicotinamide* (**6b**): Yield: 86%, oil. IR (ATR): 3118, 2944, 2814, 1673, 1539, 1238, 1133, 1028, 751, cm^{-1}. ^1H NMR (500 MHz, DMSO-d6, δ): 9.90 (*s*, 1H, OH), 8.17 (*d*, *J* = 2.7, 1H, ArH), 7.94 (*dd*, J_1 = 9.6, J_2 = 2.6, 1H, ArH), 7.58 (*d*, *J* = 8.5, 2H, ArH), 7.17 (*d*, *J* = 8.6, 2H, ArH), 6.93-6.89 (*m*, 2H, ArH), 6.84-6.82 (*m*, 2H, ArH), 6.38 (*d*, *J* = 9.7, 1H, ArH), 3.75 (*s*, 3H, OCH_3), 2.94 (*s*, 4H, piperazine), 2.71 (*t*, *J* = 7.8, 2H, CH_2), 2.56-2.52 (*m*, 6H, 4H piperazine and 2H CH_2). ^{13}C NMR (126 MHz, DMSO-d6, δ): 162.74, 152.93, 141.68, 139.72, 138.34, 137.34, 135.99, 129.12 (2C), 123.18, 121.91 (2C), 120.67 (2C), 119.53, 118.71, 113.03, 112.32, 60.27, 56.23, 53.36 (2C), 51.01 (2C), 32.58. (+)ESI-HRMS *m/z*: calculated for $[C_{25}H_{28}N_4O_3+H^+]$ 433.22342, observed 433.22182.

N-*(4-(2-(4-(2,3-dichlorophenyl)piperazin-1-yl)ethyl)phenyl)-6-hydroxynicotinamide* (**6c**): Yield: 92%, oil. IR (ATR): 3281, 2921, 2809, 1651, 1518, 1255, 1131, 790, cm^{-1}. ^1H NMR (500 MHz, DMSO-d6, δ): 9.90 (*s*, 1H, OH), 8.17 (*s*, 1H), 7.94 (*dd*, J_1 = 9.7, J_2 = 2.7, 1H, ArH), 7.58 (*d*, *J* = 8.2, 2H, ArH), 7.30-7.27 (*m*, 2H, ArH), 7.18 (*d*, *J* = 8.3, 2H, ArH), 7.12 (*dd*, J_1 = 6.8, J_2 = 2.9, 1H, ArH), 6.38 (*d*, *J* = 9.6, 1H, ArH), 3.35 (*s*, 4H, piperazine), 2.97 (*s*, 4H, piperazine), 2.71 (*t*, *J* = 7.7, 2H, CH_2), 2.60-2.55 (*m*, 2H, CH_2). ^{13}C NMR (126 MHz, DMSO-d6, δ): 162.74, 151.62, 139.71, 138.35, 137.72, 135.93, 132.42, 129.12 (2C), 128.84

(2C), 125.94, 124.72, 120.68 (2C), 119.97, 119.53, 113.03, 60.48, 53.14 (2C), 51.34 (2C), 32.56. (+)ESI-HRMS *m/z*: calculated for [$C_{24}H_{24}Cl_2N_4O_2$+H^+] 471.13491, observed 471.13327.

2-(4-hydroxyphenyl)-N-*(4-(2-(4-(2-methoxyphenyl)piperazin-1-yl)ethyl)-phenyl)acetamide* (**7b**): Yield: 91%, oil. IR (ATR): 3300, 2953, 2835, 1656, 1513, 1243, 1115, 1022, 754, cm^{-1}. ^{1}H NMR (500 MHz, DMSO-d6, δ): 10.00 (*s*, 1H, OH), 7.50 (*d*, *J* = 8.5, 2H), 7.14 (*dd*, J_1 = 13.6, J_2 = 8.5, 4H), 6.95-6.88 (*m*, 2H), 6.87-6.85 (*m*, 2H), 6.71 (*d*, *J* = 8.5, 2H), 3.76 (*s*, 3H, OCH_3), 3.48 (*s*, 2H, CH_2), 2.96 (*s*, 4H, piperazine), 2.72-2.65 (*m*, 2H, CH_2), 2.57 (*s*, 4H, piperazine), 2.55-2.51 (*m*, 2H, CH_2). ^{13}C NMR (126 MHz, DMSO-d6, δ): 169.84, 156.44, 152.38, 141.68, 137.63, 135.56, 130.37 (2C), 129.21 (2C), 126.60, 122.74, 121.25, 119.52 (2C), 118.30, 115.48 (2C), 112.32, 60.27, 55.71, 53.36 (2C), 50.43(2C), 42.92, 32.55. (+)ESI-HRMS *m/z*: calculated for [$C_{27}H_{31}N_3O_3$+H^+] 446.24382, observed 446.24189.

3-hydroxy-N-*(4-(2-(4-(2-methoxyphenyl)piperazin-1-yl)ethyl)phenyl)benz-amide* (**8b**): Yield: 75%, oil. IR (ATR): 3402, 2956, 2828, 1674, 1518, 1239, 1116, 1022, 750, cm^{-1}. ^{1}H NMR (500 MHz, DMSO-d6, δ): 10.10 (*s*, 1H, OH), 7.68 (*d*, *J* = 8.1, 2H, ArH), 7.38 (*d*, *J* = 7.6, 1H, ArH), 7.32-7.29 (*m*, 2H, ArH), 7.21-7.17 (*m*, 2H, ArH), 6.98-6.88 (*m*, 5H, ArH), 3.79 (*s*, 3H, OCH_3), 2.97 (*s*, 4H, piperazine), 2.75-2.70 (*m*, 2H, CH_2), 2.58-2.55 (*m*, 6H, 4H piperazine and 2H CH_2). ^{13}C NMR (126 MHz, DMSO-d6, δ): 167.43, 159.40, 154.00, 143.29, 139.13, 138.53, 137.68, 131.40, 130.72 (2C), 124.35, 122.86, 122.37 (2C), 121.16, 120.14, 119.91, 116.54, 113.93, 61.88, 57.95, 54.98 (2C), 52.05 (2C), 35.40. (+)ESI-HRMS *m/z*: calculated for [$C_{26}H_{29}N_3O_3$+H^+] 432.22817, observed 432.22637.

4-hydroxy-N-*(4-(2-(4-(2-methoxyphenyl)piperazin-1-yl)ethyl)phenyl)benz-amide* (**9b**): Yield: 69%, oil. IR (ATR): 3195, 2962, 2829, 1679, 1501, 1244, 1146, 1026, 747, cm^{-1}. ^{1}H NMR (500 MHz, DMSO-d6, δ): 10.09 (*s*, 1H, OH), 8.24 (*s*, 1H, ArH), 7.49 (*d*, *J* = 8.2, 2H, ArH), 7.18 (*d*, *J* = 8.4, 2H, ArH), 7.10 (*d*, *J* = 8.1, 1H, ArH), 6.94-6.87 (*m*, 6H, ArH), 3.76 (*s*, 3H, OCH_3), 2.96 (*s*, 4H, piperazine), 2.73-2.70 (*m*, 2H, CH_2), 2.58-2.53 (*m*, 6H, 4H piperazine and 2H CH_2). ^{13}C NMR (126 MHz, DMSO, δ): 164.49, 161.38, 153.99, 143.27, 138.18, 137.70, 131.57, 131.00 (2C), 124.36, 122.86 (2C), 121.15 (2C), 119.91 (2C), 119.68, 116.82, 113.93, 61.81, 57.32, 55.61 (2C), 52.85 (2C), 34.14. (+)ESI-HRMS *m/z*: calculated for [$C_{26}H_{29}N_3O_3$+H^+] 432.22817, observed 432.22709.

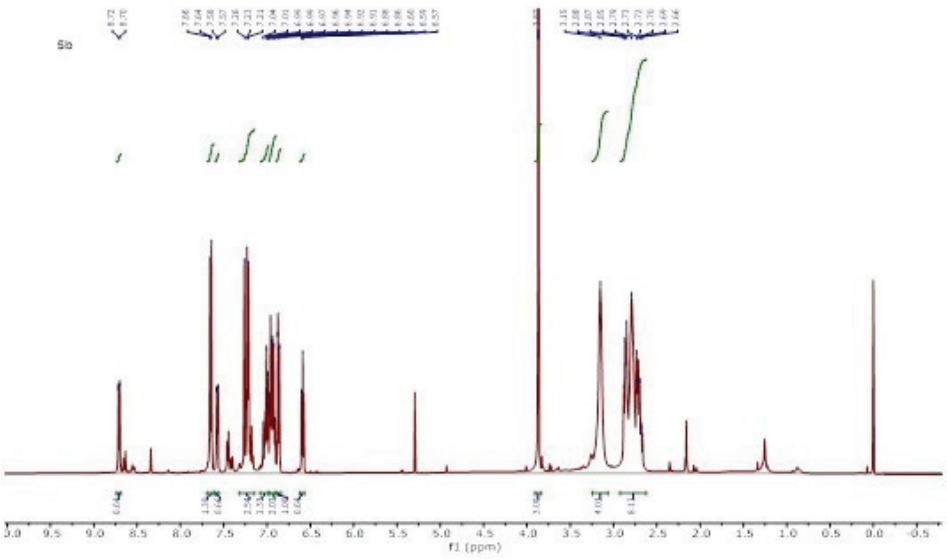

Fig. S-1. ^{1}H-NMR spectrum for 2-hydroxy-*N*-(4-(2-(4-(2-methoxyphenyl)piperazin-1-yl)ethyl)phenyl)nicotinamide (**5b**)

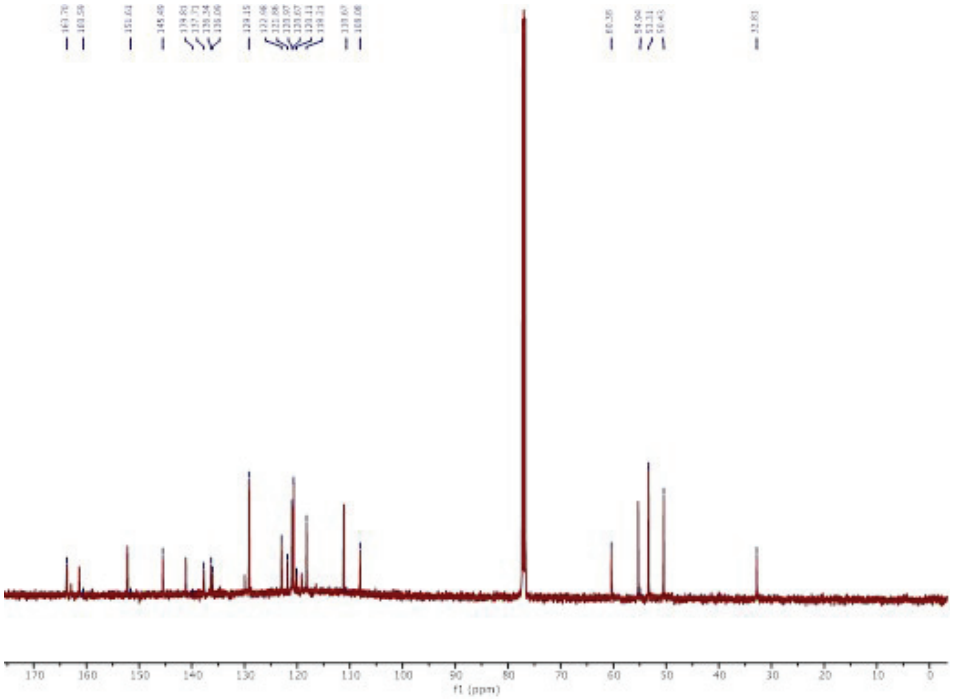

Fig. S-2. ^{13}C-NMR spectrum for 2-hydroxy-*N*-(4-(2-(4-(2-methoxyphenyl)piperazin-1-yl)ethyl)phenyl)nicotinamide (**5b**)

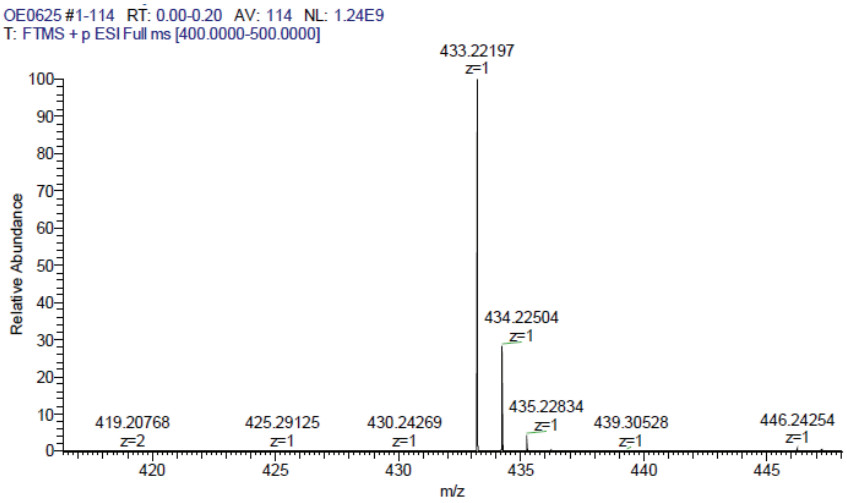

Exact mass	Observed mass	Observed ion type	Error (ppm)
433.22342	433.22197	$[M+H]^+$	3.35

Fig. S-3. HRMS spectrum for 2-hydroxy-*N*-(4-(2-(4-(2-methoxyphenyl)piperazin-1-yl)ethyl)phenyl)nicotinamide (**5b**)

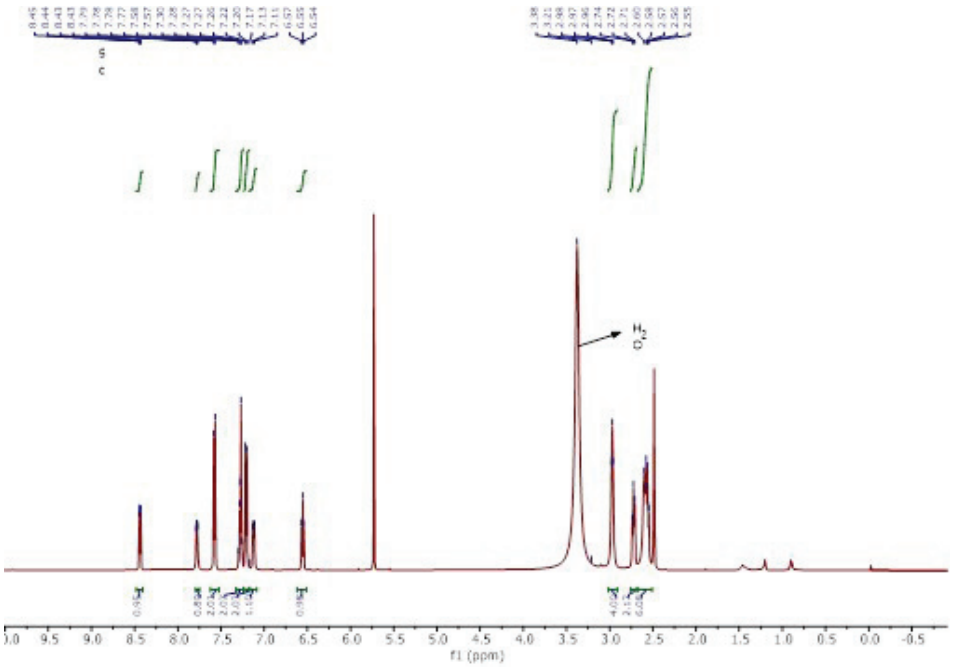

Fig. S-4. ^{1}H-NMR spectrum for *N*-(4-(2-(4-(2,3-dichlorophenyl)piperazin-1-yl)ethyl)phenyl)-2-hydroxynicotinamide (**5c**)

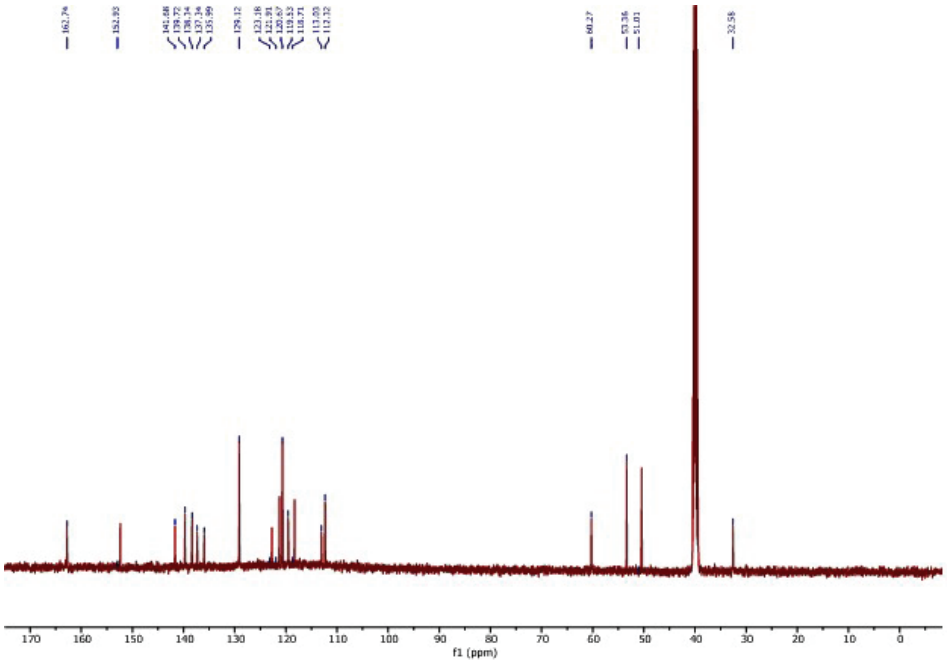

Fig. S-5. ^{13}C-NMR spectrum for *N*-(4-(2-(4-(2,3-dichlorophenyl)piperazin-1-yl)ethyl)phenyl)-2-hydroxynicotinamide (**5c**)

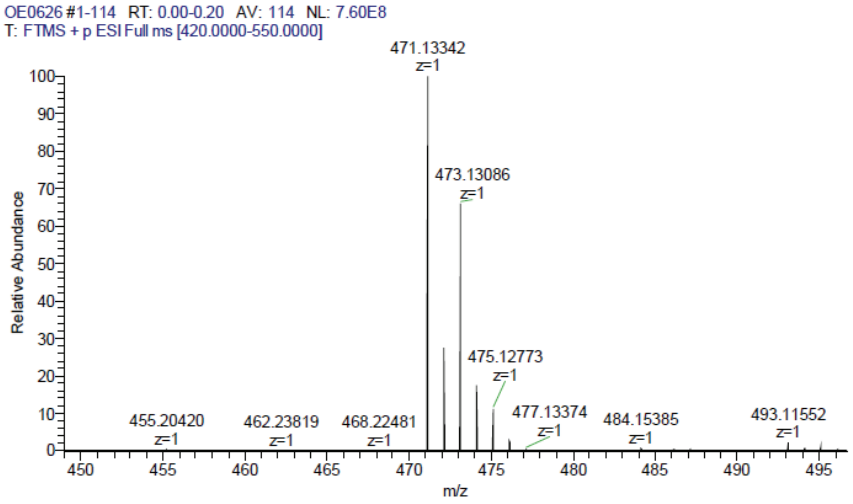

Exact mass	Observed mass	Observed ion type	Error (ppm)
471.13491	471.13342	$[M+H]^+$	3.16

Fig. S-6. HRMS spectrum for *N*-(4-(2-(4-(2,3-dichlorophenyl)piperazin-1-yl)ethyl)phenyl)-2-hydroxynicotinamide (**5c**)

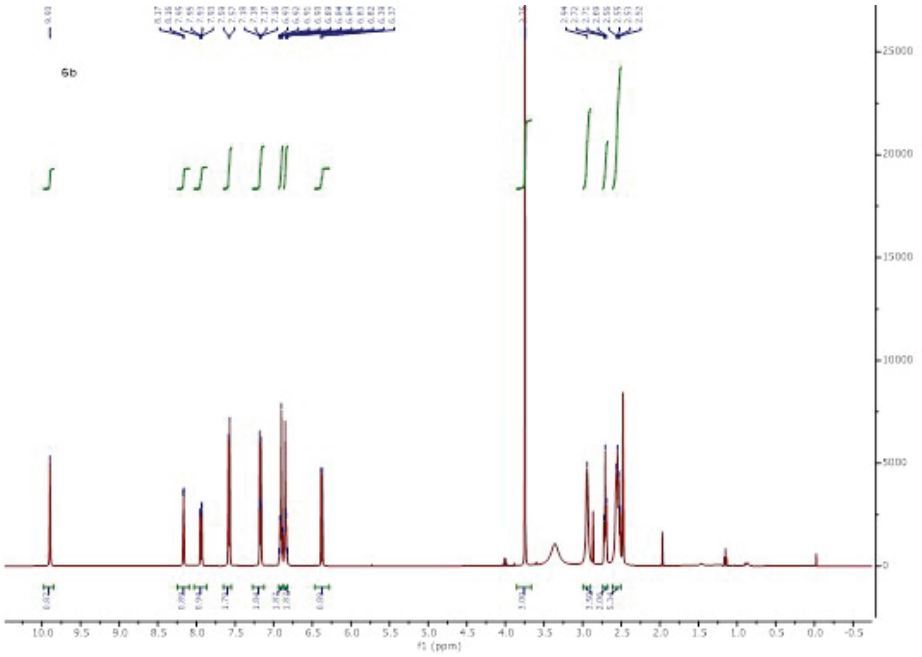

Fig. S-7. ^{1}H-NMR spectrum for 6-hydroxy-*N*-(4-(2-(4-(2-methoxyphenyl)piperazin-1-yl)ethyl)phenyl)nicotinamide (**6b**)

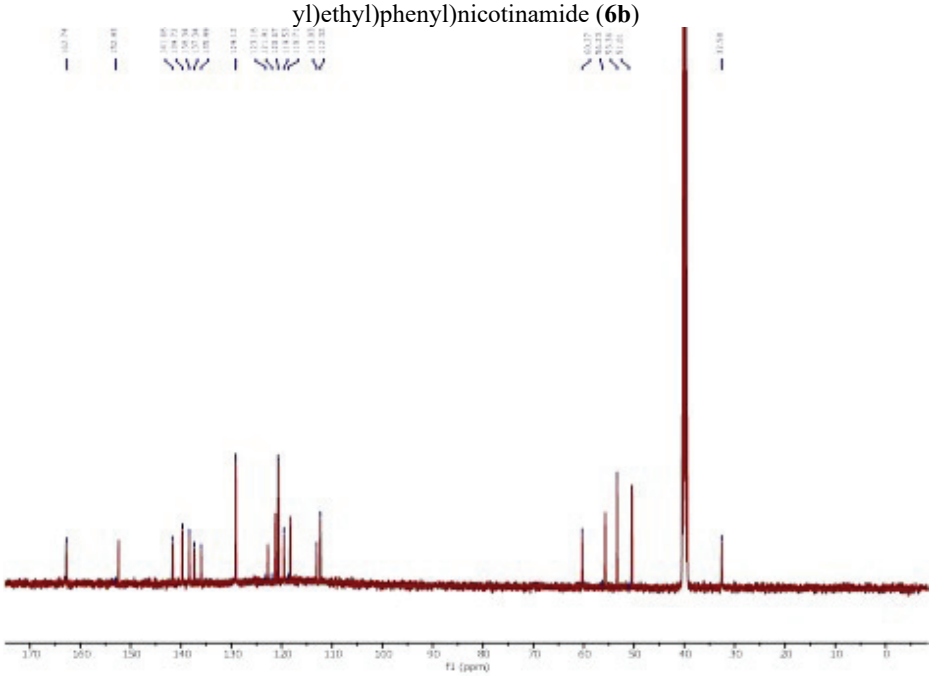

Fig. S-8. ^{13}C-NMR spectrum for 6-hydroxy-*N*-(4-(2-(4-(2-methoxyphenyl)piperazin-1-yl)ethyl)phenyl)nicotinamide (**6b**)

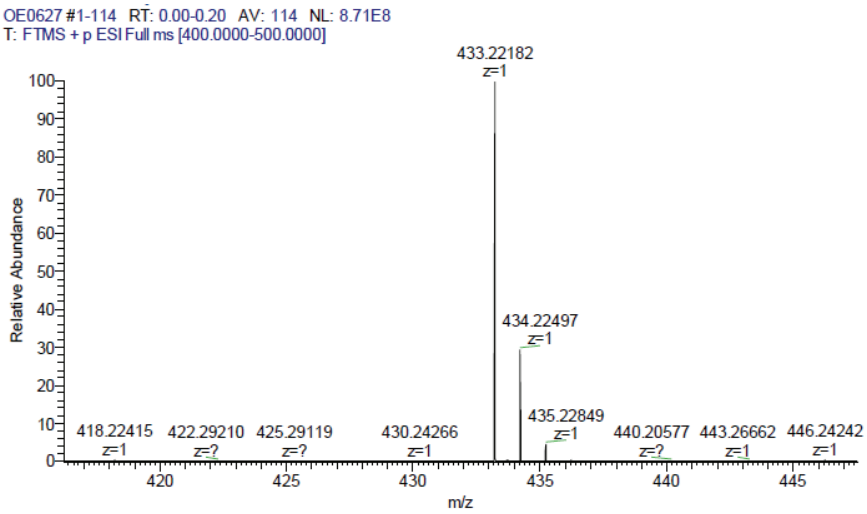

Exact mass	Observed mass	Observed ion type	Error (ppm)
433.22342	433.22182	$[M+H]^+$	3.69

Fig. S-9. HRMS spectrum for 6-hydroxy-*N*-(4-(2-(4-(2-methoxyphenyl)piperazin-1-yl)ethyl)phenyl)nicotinamide (**6b**)

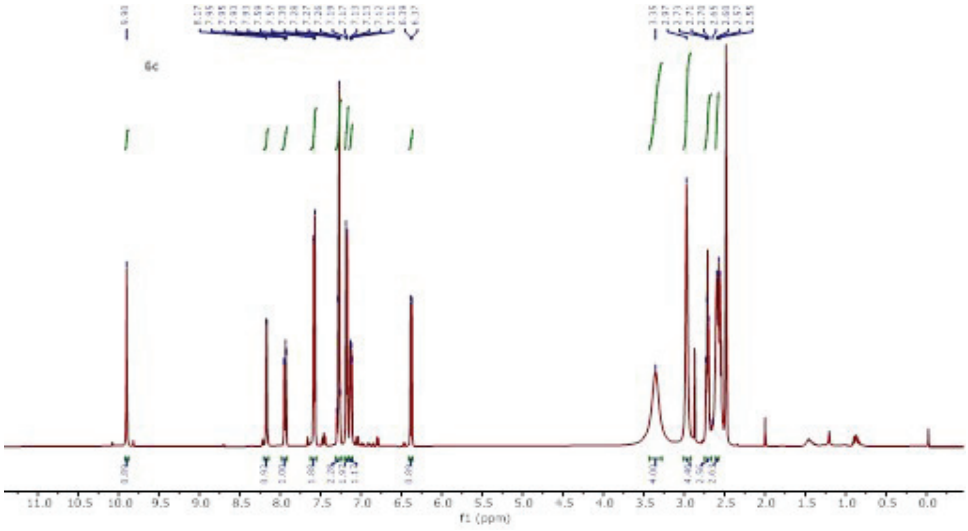

Fig. S-10. ^{1}H-NMR spectrum for *N*-(4-(2-(4-(2,3-dichlorophenyl)piperazin-1-yl)ethyl)phenyl)-6-hydroxynicotinamide (**6c**)

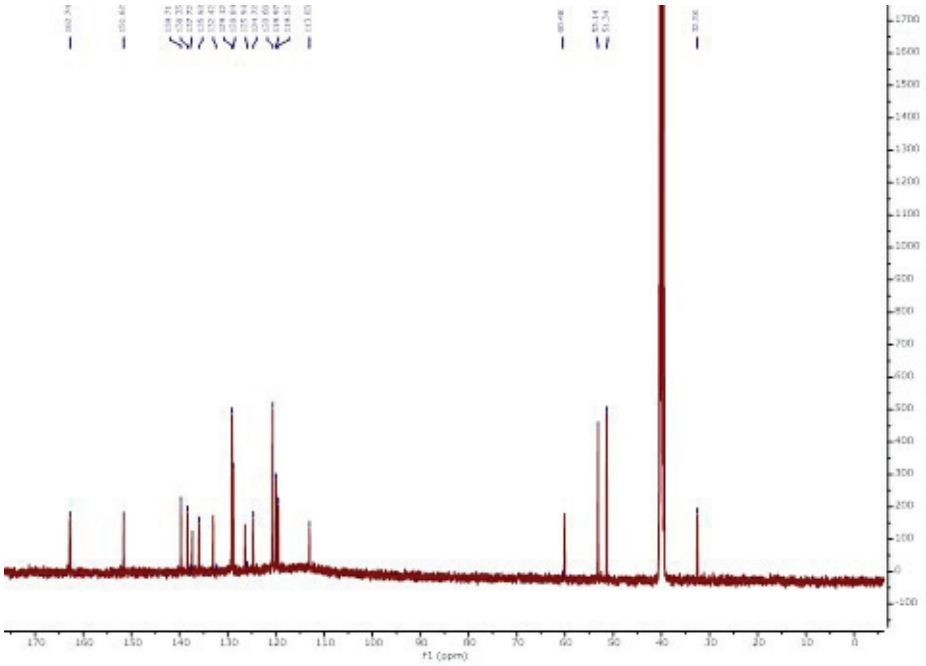

Fig. S-11. ^{13}C-NMR spectrum for *N*-(4-(2-(4-(2,3-dichlorophenyl)piperazin-1-yl)ethyl)phenyl)-6-hydroxynicotinamide (**6c**)

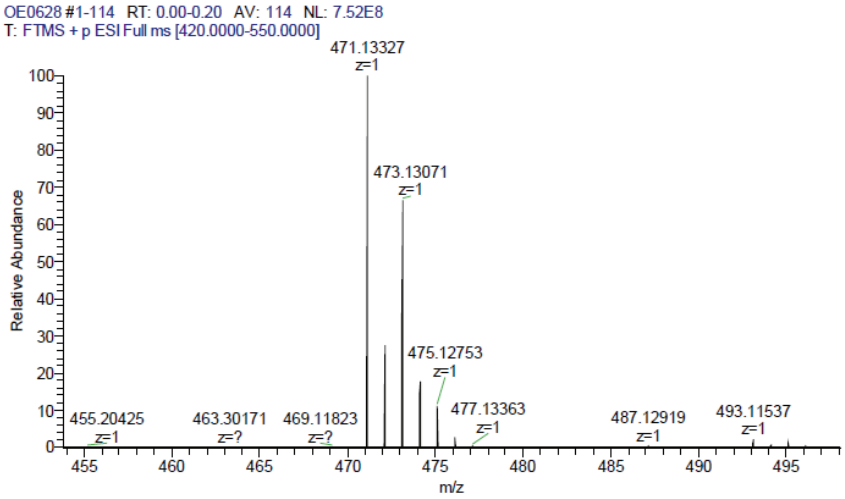

Exact mass	Observed mass	Observed ion type	Error (ppm)
471.13491	471.13327	$[M+H]^+$	3.48

Fig. S-12. HRMS spectrum for *N*-(4-(2-(4-(2,3-dichlorophenyl)piperazin-1-yl)ethyl)phenyl)-6-hydroxynicotinamide (**6c**)

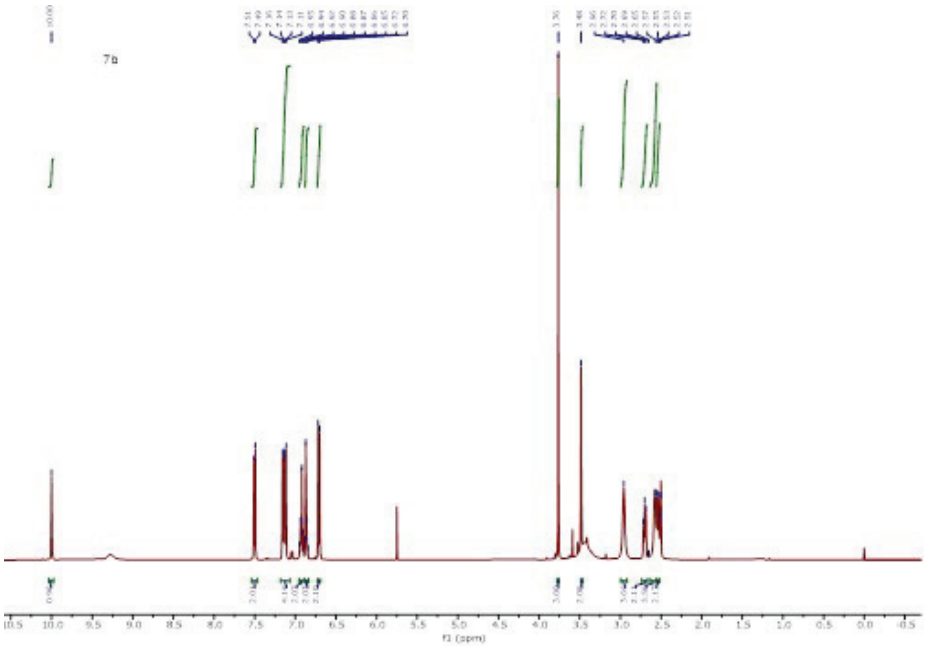

Fig. S-13. ^{1}H-NMR spectrum for 2-(4-hydroxyphenyl)-*N*-(4-(2-(4-(2-methoxyphenyl)piperazin-1-yl)ethyl)phenyl)acetamide (**7b**)

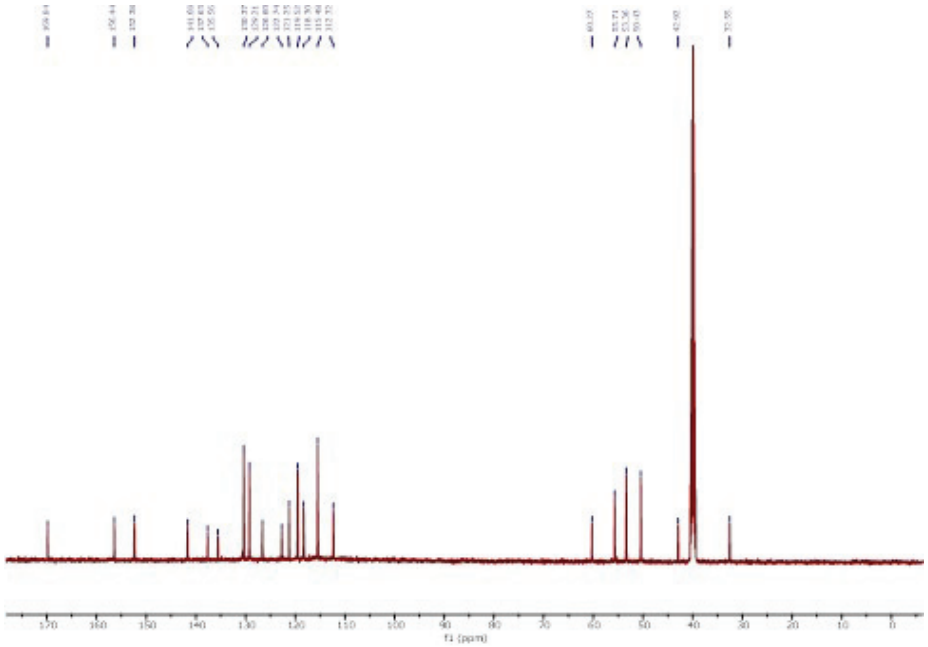

Fig. S-14. ^{13}C-NMR spectrum for 2-(4-hydroxyphenyl)-*N*-(4-(2-(4-(2-methoxyphenyl)piperazin-1-yl)ethyl)phenyl)acetamide (**7b**)

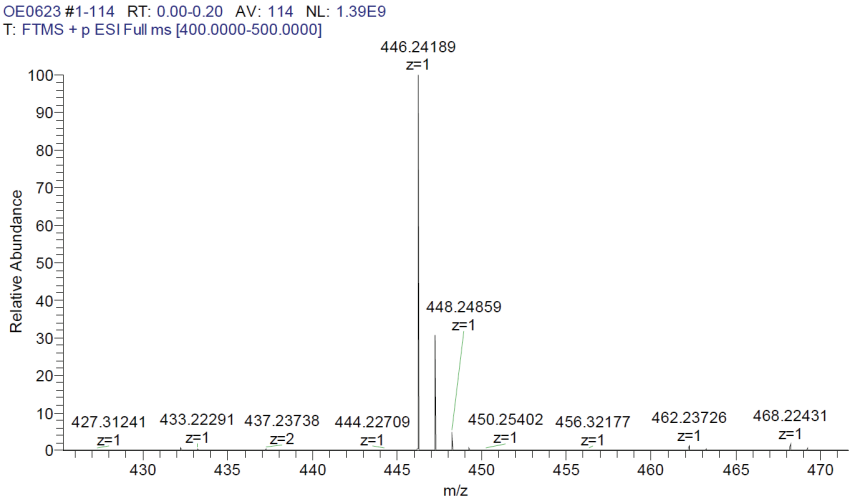

Exact mass	Observed mass	Observed ion type	Error (ppm)
446.24382	446.24189	$[M+H]^+$	4.32

Fig. S-15. HRMS spectrum for 2-(4-hydroxyphenyl)-*N*-(4-(2-(4-(2-methoxyphenyl)piperazin-1-yl)ethyl)phenyl)acetamide (**7b**)

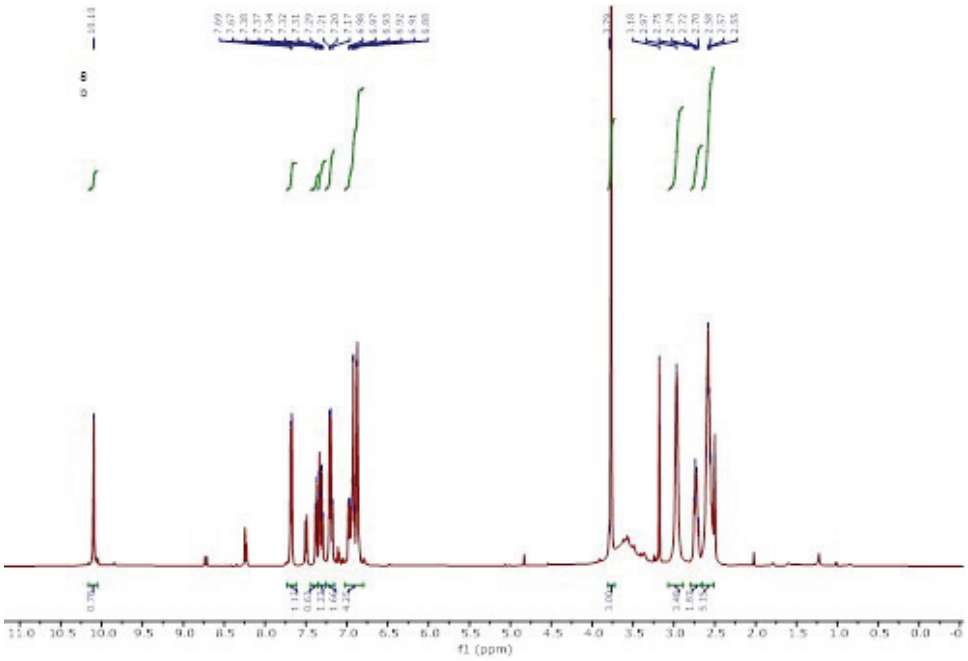

Fig. S-16. ^{1}H-NMR spectrum for 3-hydroxy-*N*-(4-(2-(4-(2-methoxyphenyl)piperazin-1-yl)ethyl)phenyl)benzamide (**8b**)

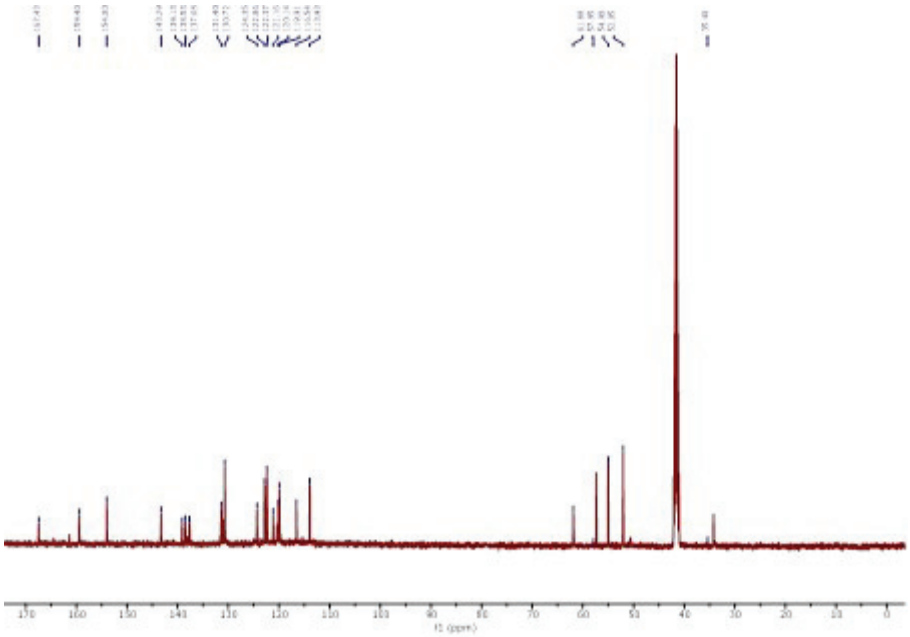

Fig. S-17. ^{13}C-NMR spectrum for 3-hydroxy-*N*-(4-(2-(4-(2-methoxyphenyl)piperazin-1-yl)ethyl)phenyl)benzamide (**8b**)

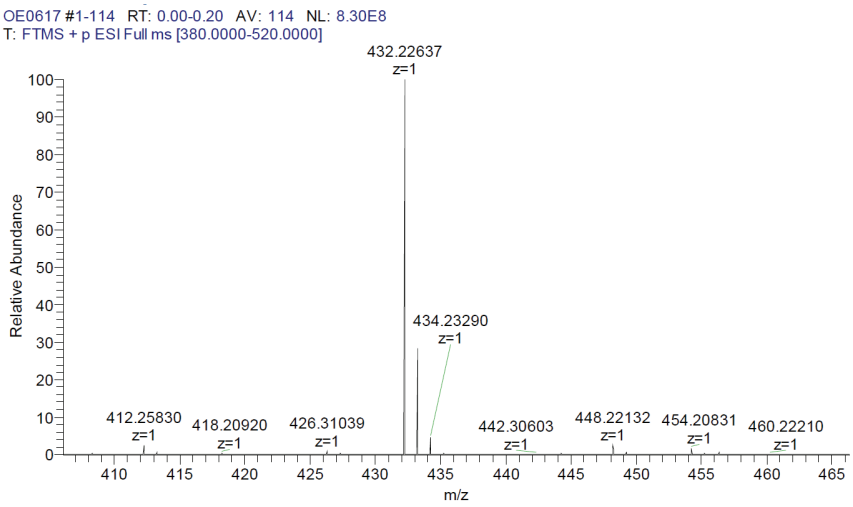

Exact mass	Observed mass	Observed ion type	Error (ppm)
432.22817	432.22637	$[M+H]^+$	4.16

Fig. S-18. HRMS spectrum for 3-hydroxy-*N*-(4-(2-(4-(2-methoxyphenyl)piperazin-1-yl)ethyl)phenyl)benzamide (**8b**)

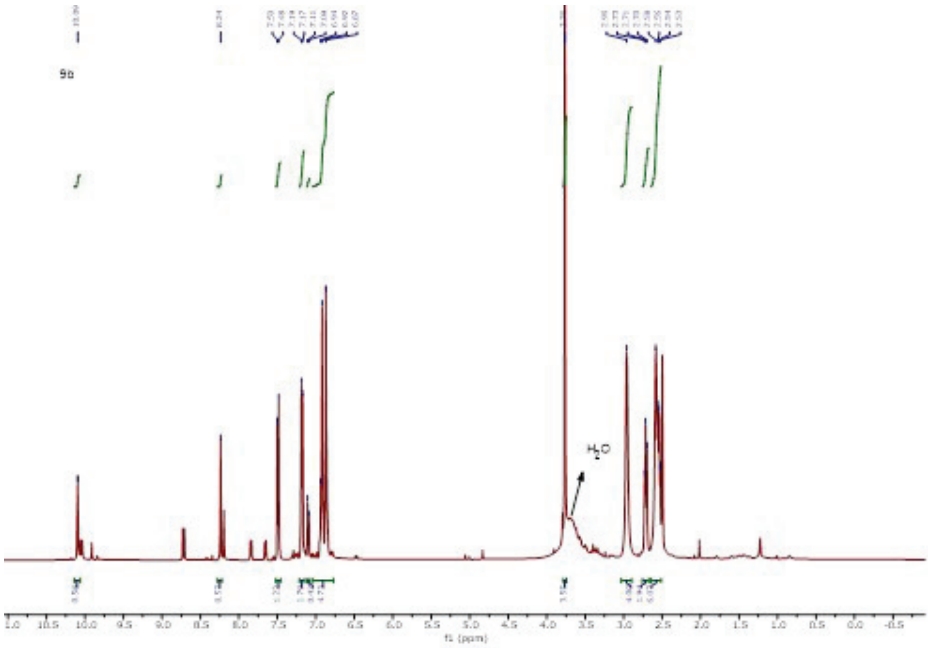

Fig. S-19. ^{1}H-NMR spectrum for 4-hydroxy-*N*-(4-(2-(4-(2-methoxyphenyl)piperazin-1-yl)ethyl)phenyl)benzamide (**9b**)

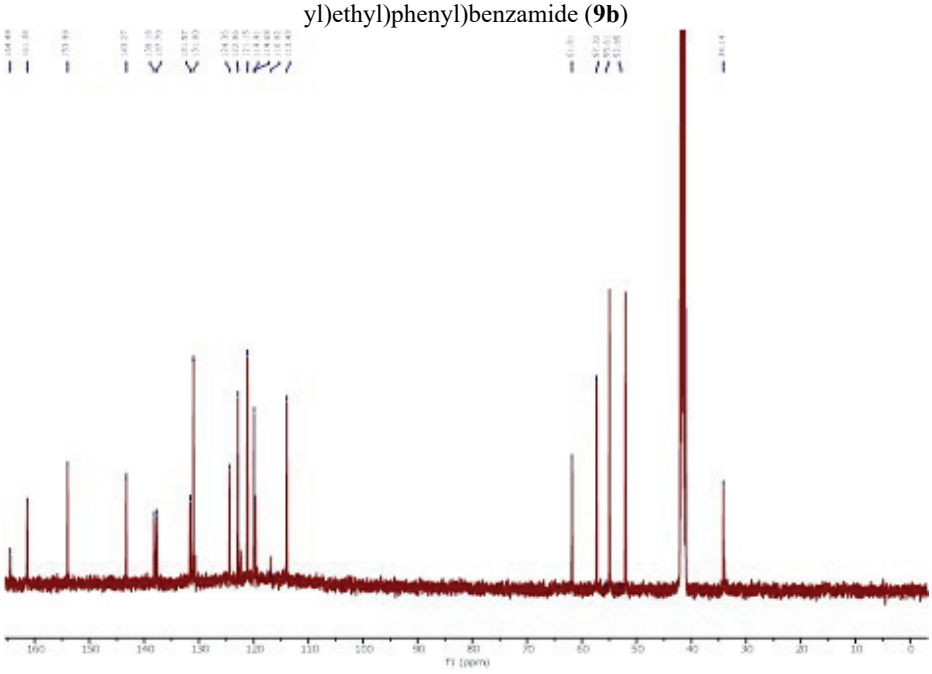

Fig. S-20. ^{13}C-NMR spectrum for 4-hydroxy-*N*-(4-(2-(4-(2-methoxyphenyl)piperazin-1-yl)ethyl)phenyl)benzamide (**9b**)

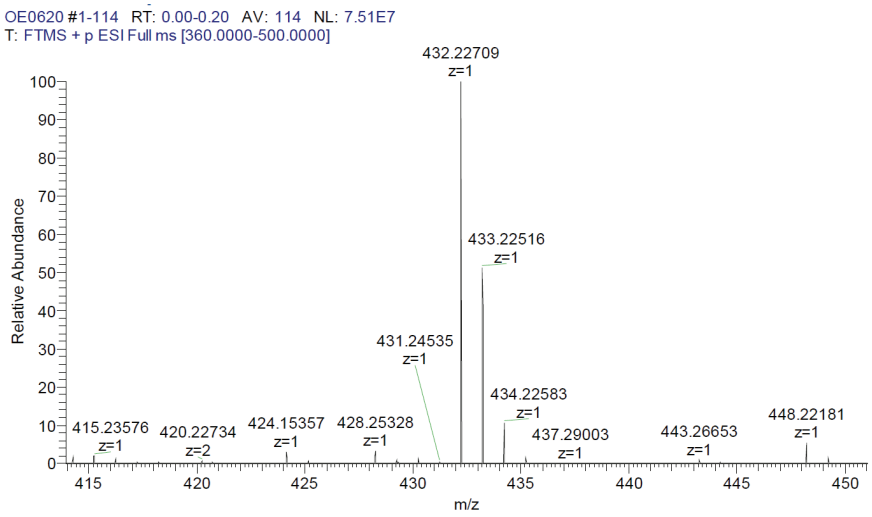

Exact mass	Observed mass	Observed ion type	Error (ppm)
432.22817	432.22709	$[M+H]^+$	2.50

Fig. S-21. HRMS spectrum for 4-hydroxy-*N*-(4-(2-(4-(2-methoxyphenyl)piperazin-1-yl)ethyl)phenyl)benzamide (**9b**)

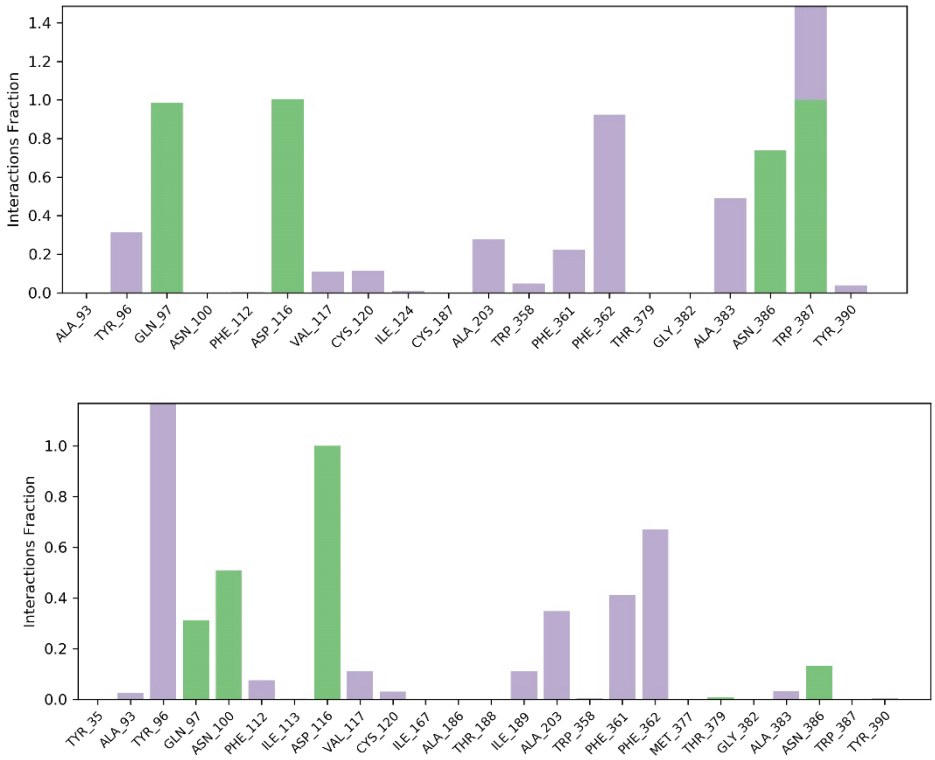

Fig. S-22. Diagram of key receptor – **5a** (top) and **6a** (bottom) interactions observed during 100ns molecular dynamics. Aromatic interactions are shown in violet, while hydrogen bonds are green. Interactions maintained for 20% or more of total MD time are considered crucial.

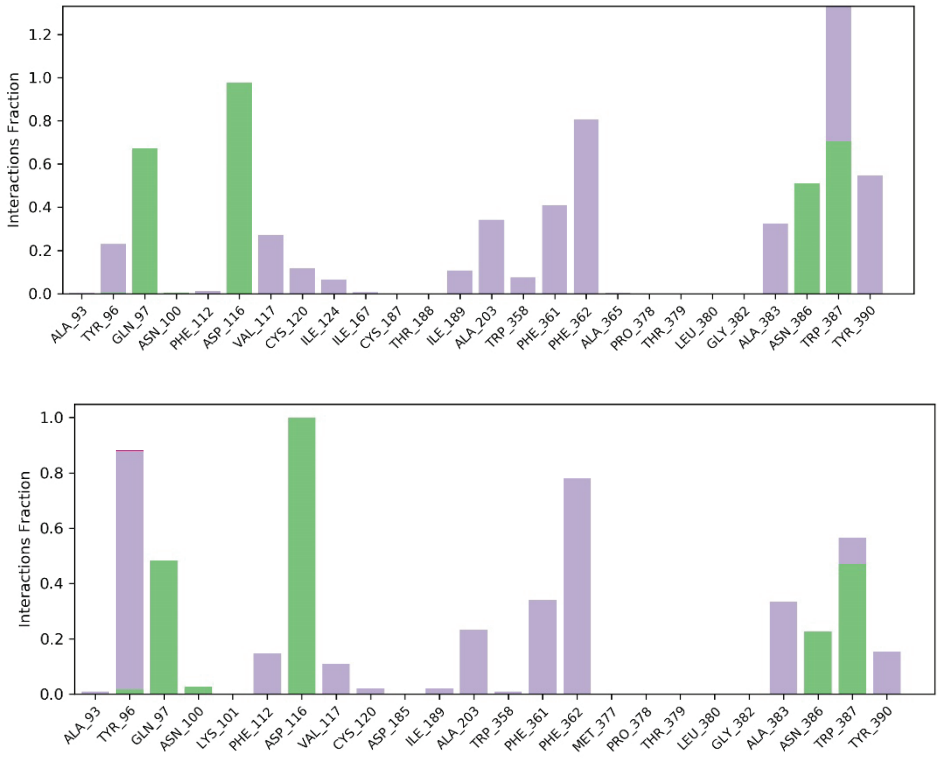

Fig. S-23. Diagram of key receptor – **5b** (top) and **5c** (bottom) interactions observed during 100ns molecular dynamics. Aromatic interactions are shown in violet, while hydrogen bonds are green. Interactions maintained for 20% or more of total MD time are considered crucial.

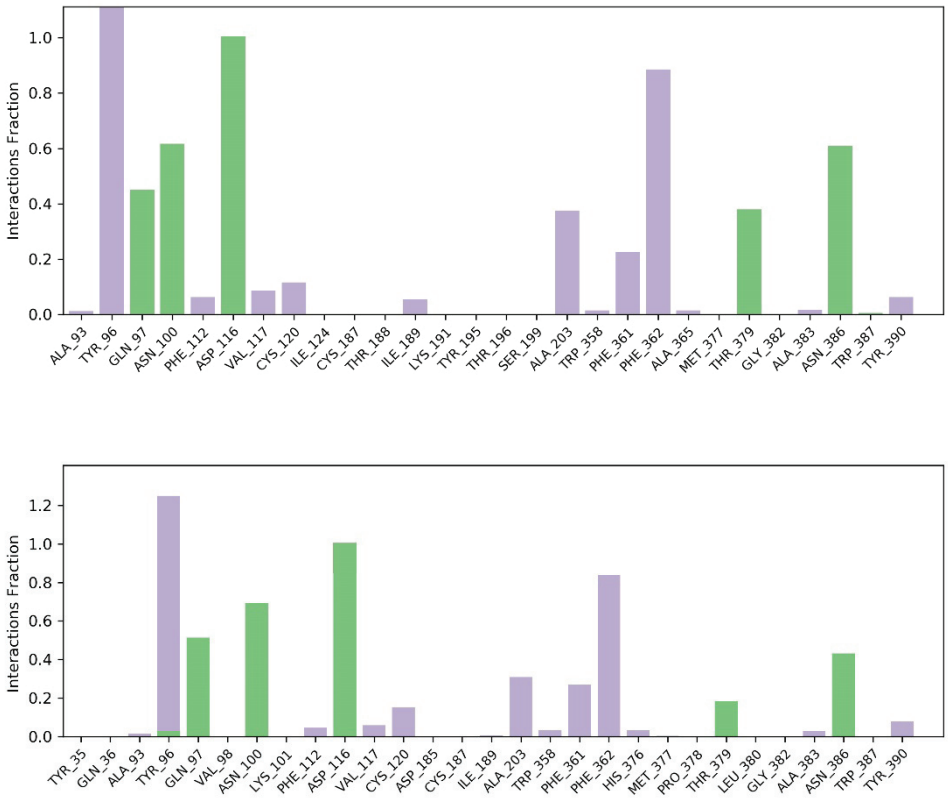

Fig. S-24. Diagram of key receptor – **6b** (top) and **6c** (bottom) interactions observed during 100ns molecular dynamics. Aromatic interactions are shown in violet, while hydrogen bonds are green. Interactions maintained for 20% or more of total MD time are considered crucial.

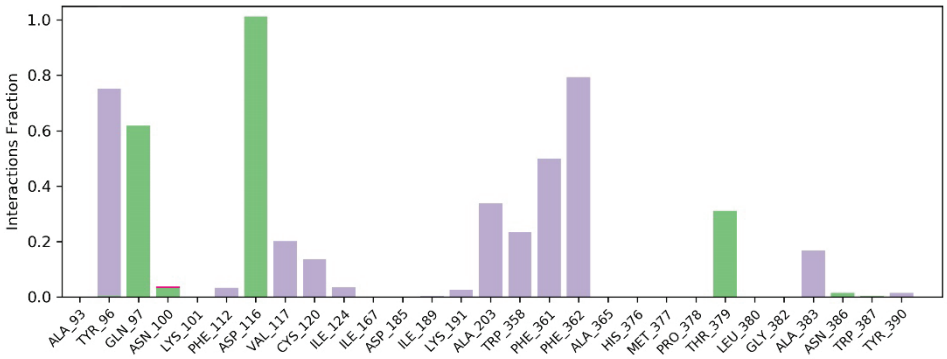

Fig. S-25. Diagram of key receptor – **7b** interactions observed during 100ns molecular dynamics. Aromatic interactions are shown in violet, while hydrogen bonds are green. Interactions maintained for 20% or more of total MD time are considered crucial.

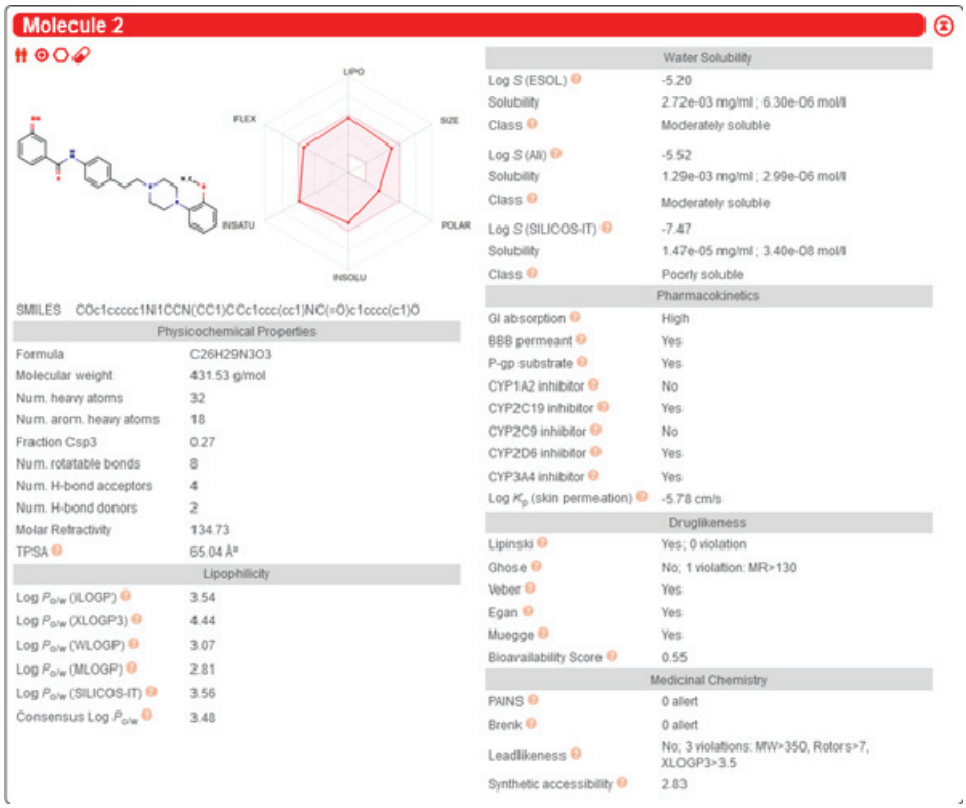

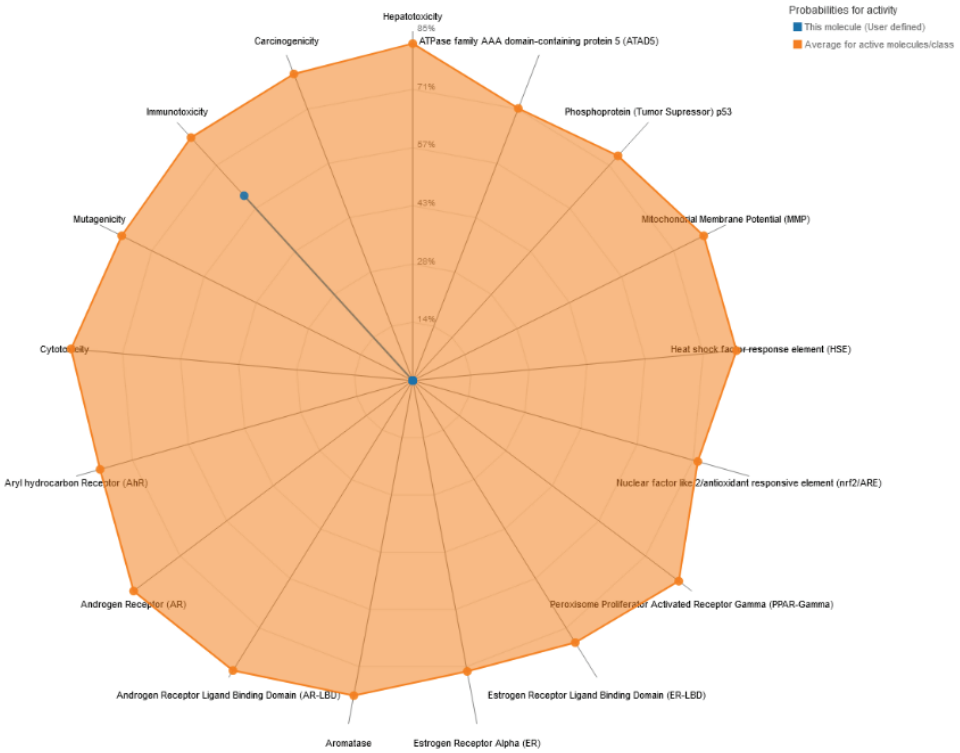

Fig. S-26. ADMET of 3-hydroxy-N-(4-(2-(4-(2-methoxyphenyl)piperazin-1-yl)ethyl)phenyl)benzamide (**8b**).

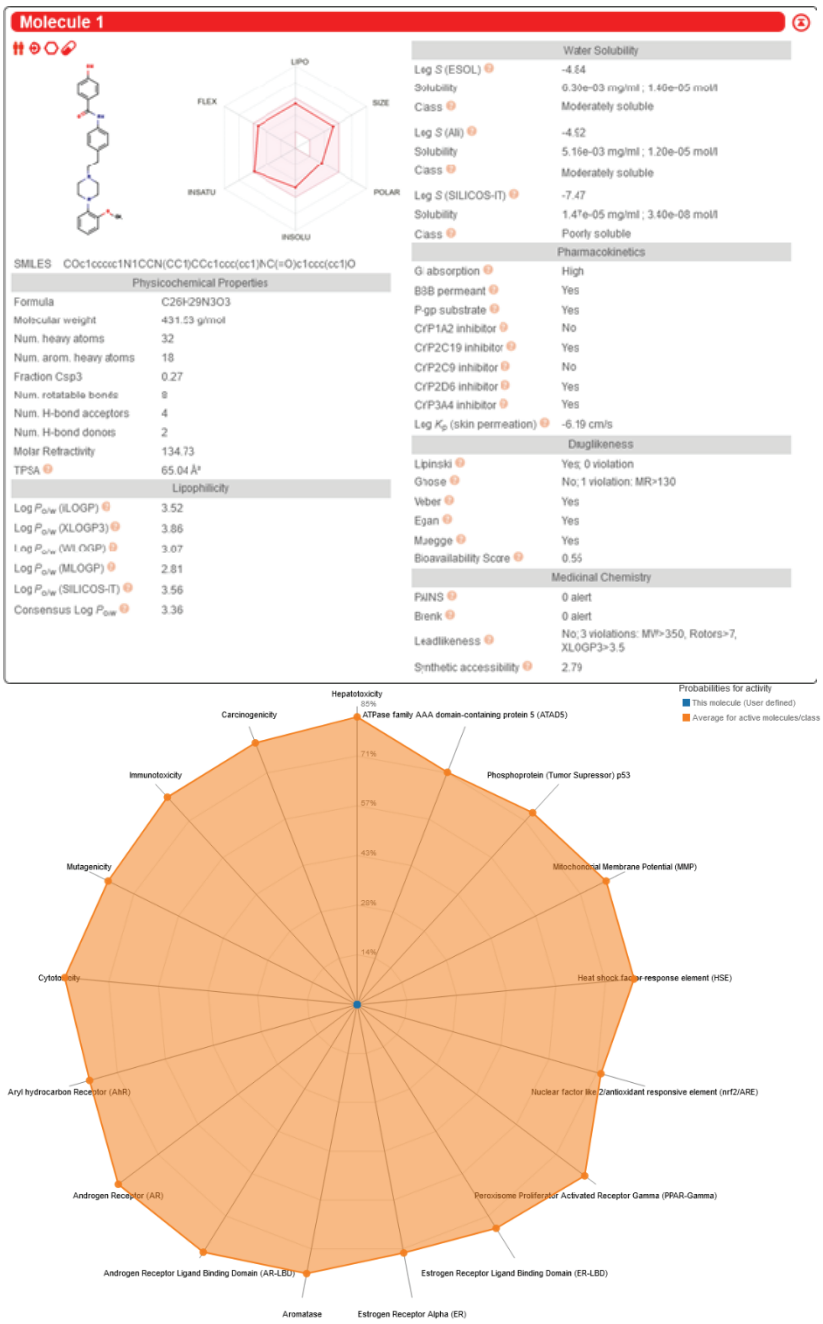

Fig. S-27. ADMET of 4-hydroxy-N-(4-(2-(4-(2-methoxyphenyl)piperazin-1-yl)ethyl)phenyl)benzamide (**9b**).

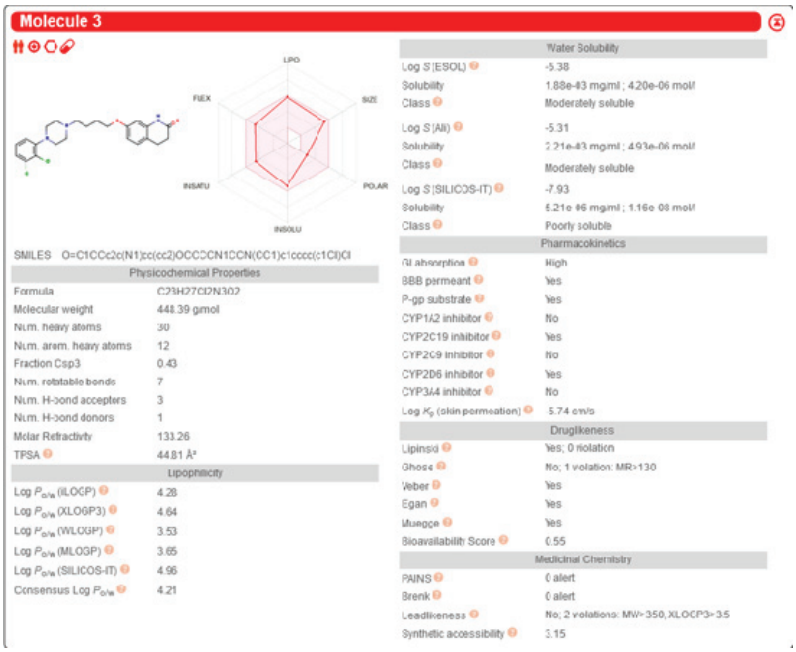

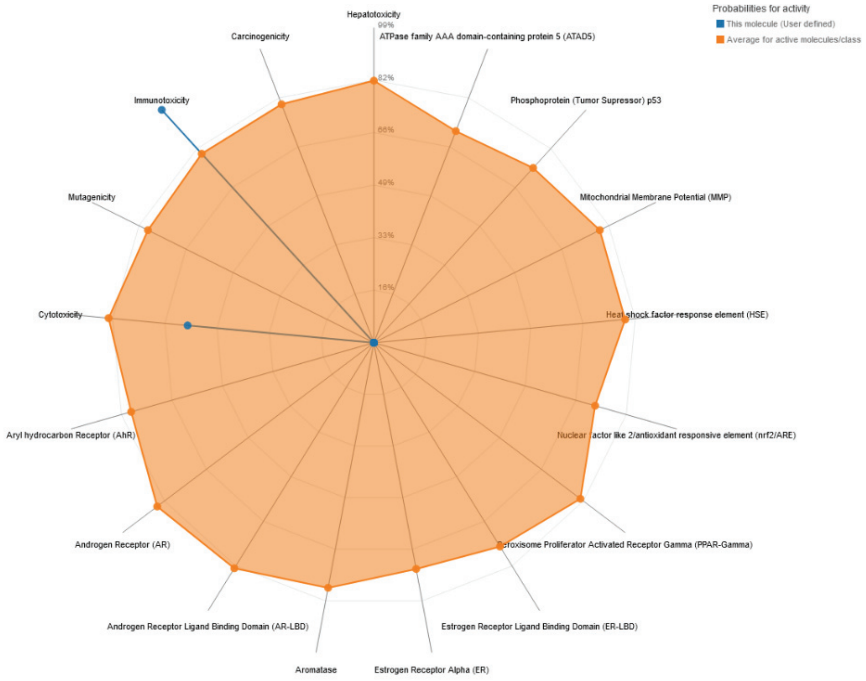

Fig. S-28. ADMET of aripiprazole.

Journal of the Serbian Chemical Society
JSCS@tmf.bg.ac.rs • www.shd.org.rs/JSCS
J. Serb. Chem. Soc. *89* (3) 305–320 (2024)
JSCS–5722
Original scientific paper
Published 24 March 2024

Breaking news: Empirical formulas, molar masses, biosynthesis reactions and thermodynamic properties of virus particles – Biosynthesis and binding of Omicron JN.1 variant of SARS-CoV-2

MARKO E. POPOVIĆ[1]*, MAJA STEVANOVIĆ[2] and MARIJA MIHAILOVIĆ[1#]

[1]*University of Belgrade, Institute of Chemistry, Technology and Metallurgy, Njegoševa 12, 11000 Belgrade, Serbia and* [2]*Inovation Centre of the Faculty of Technology and Metallurgy, University of Belgrade, Karnegijeva 4, 11120 Beograd, Serbia*

(Received 19 January, revised 31 January, accepted 20 February 2024)

Abstract: Breaking news are usually disturbing. Natural disasters, wars, epidemics, *etc*., are reported as breaking news. This paper reports a decreased danger of spreading of epidemics caused by the JN.1 variant, since analyses indicate that infectivity of the new variant is decreased compared to most earlier variants, which is confirmed by the number of cases (7500 daily in USA). Moreover, JN.1, despite the great number of mutations, has not been able to achieve the values of Gibbs energy change of biosynthesis (and thus virus multiplication rate) of the Hu-1 wild type. The research shows that infectivity and pathogenicity of the JN.1 variant has not reached worrying size, which means that there is no reason to expect the epidemiologic situation getting worse.

Keywords: biothermodynamics; Gibbs energy; immune evasion; infectivity; pathogenicity; virus time evolution.

INTRODUCTION

The year 2019 was at an end. On the social networks, several doctors from Wuhan warned about the appearance of a large number of infected people. Later, the new disease was named COVID-19. Breaking news in the media have alarmed the general public long before governments and health authorities reacted in most countries. After that, an overreaction occurred, with the enforcement of a lockdown, which was in some cases extreme. Fortunately, the scientific community reacted in a much more rational way. Very soon, it was discovered that the cause of the future pandemic is a virus from the *Coronaviridae* family, named SARS-CoV-2 Hu-1 variant. Molecular biologists have very soon reported the nucleic

* Corresponding author. E-mail: marko.popovic@ihtm.bg.ac.rs
# Serbian Chemical Society member.
https://doi.org/10.2298/JSC240119019P

acid sequences[1] and the protein sequences.[2] The virus morphology was known from before.[3]

SARS-CoV-2 belongs to RNA viruses.[4] RNA viruses exhibit a significant tendency towards mutation.[5] From 2019 to 2024, SARS-CoV-2 has mutated several dozen times.[6] The new variants of SARS-CoV-2 have suppressed the older variants and caused pandemic waves.[7] All the mutations of SARS-CoV-2 have been described and its genetic sequence, as well as the protein sequences of all the variants, have been reported.[8] As of January 4, 2024, during the COVID--19 pandemic, over 773 million cases have been reported with almost 7 million deaths.[9]

Except for researchers in the fields of molecular biology, virology, clinical medicine and immunology, the research was joined by scientists from the fields of biothermodynamics, chemistry, biochemistry and biophysics. Before 2019, it was known that a virus can be analysed as a chemical system[10] and processes that viruses perform as chemical reactions.[11] The empirical formula was known only for the poliovirus.[10]

Antigen–receptor binding is a process very similar to the protein ligand interactions.[12,13] Furthermore, the process of virus multiplication consists of polymerization of nucleotides into viral nucleic acids[14,15] and amino acids into viral proteins,[16] as well as self-assembly processes.[17] The Gibbs energy change is a measure of a driving force for these processes/reactions.[18,19]

The empirical formulas of SARS-CoV-2 variants have been reported in the literature.[20,21] The empirical formulas of viruses can be calculated with the atom counting method, based on their genetic sequences, protein sequences and morphology.[22,23] The results obtained with the atom counting method are in good agreement with experimental results.[22,23]

Based on the empirical formulas, it is possible to apply the Patel–Erickson model (Thornton's rule)[24,25] and Battley model[26] to calculate thermodynamic properties – enthalpy, entropy and Gibbs energy changes, including the driving force for chemical reactions involving viruses.[27–31] Thermodynamic properties of biosynthesis, including Gibbs energy change of biosynthesis – the driving force of virus multiplication, has been reported for major variants of SARS-CoV--2.[20,32] The biothermodynamic approach was also applied to study multiplication of the Ebola virus,[28] Mpox virus,[29] West Nile virus,[30] Rotavirus,[55] *etc*.

The virus–host interaction begins at the cell membrane with antigen–receptor binding, which allows a virus to enter its host cell.[13,33] The driving force of the antigen–receptor binding is related to Gibbs energy change of binding.[27,34–36] Moreover, the thermodynamic approach has also been applied to study the antigen–receptor binding of arboviruses,[35] HIV,[35] Ebola virus,[28] SARS-CoV,[13] *etc*.

Knowing the thermodynamic properties of virus particles and processes that comprise the viral life cycle is very important.[37] Based on the known thermos-

dynamic properties, it is possible to draw conclusions about the pathogenesis of viral infections[13,38,39] and epidemiology.[40]

During the COVID-19 pandemic, the appearance of new variants has often caused panic, first of all due to fear of change in infectivity and pathogenicity of the virus. The goal of this paper is to perform chemical and thermodynamic characterization of the new Omicron JN.1 variant, which has been spreading during December 2023 and January 2024, mostly in USA and Europe. Moreover, another goal is to predict the potential changes in the infectivity and the pathogenicity of the JN.1 variant, before the epidemiologic data arrive, in the moment when the epidemic wave reaches its maximum.

METHODS

Data sources

The genetic sequence of the Omicron JN.1 variant of SARS-CoV-2 was taken from GISAID, the global data science initiative.[41] It is labelled hCoV-19/Canada/ON-KHS-09219--v1/2023 and can be found under the accession number EPI_ISL_18615181. It was isolated on December 4, 2023, in the Canadian province Ontario. Thus, the findings of this study are based on the metadata associated with one sequence available on GISAID up to January 9, 2024, and accessible at https://doi.org/10.55876/gis8.240109xh (please see the Supplementary material for more details).

The protein sequences were taken from the NCBI database.[42] The sequence of the nucleocapsid phosphoprotein of SARS-CoV-2 was obtained under the accession number QIK50455.1. The sequence of the membrane protein of SARS-CoV-2 was obtained under the accession number QHR63293.1. The sequence of the spike glycoprotein of SARS-CoV-2 was obtained under the accession number QHR63290.2. The number of protein copies in the virus particle was taken from Neuman *et al.*[3] In a SARS-CoV-2 particle, there are 2368 copies of the nucleocapsid phosphoprotein, 1184 copies of the membrane protein and 222 copies of the spike glycoprotein.[3]

The dissociation equilibrium constant, K_d, of the Omicron JN.1 variant of SARS-CoV-2 was taken from.[43] It was measured by surface plasmon resonance at room temperature.[43]

Atom counting method

The empirical formulas, chemical formulas and macromolecular composition of the Omicron JN.1 variant of SARS-CoV-2 were obtained with the atom counting method, as described in the previous paper.[22] The atom counting method is a computational method for the calculation of empirical formulas of macromolecules and macromolecular assemblies, including virus particles.[22] The input of the program are genetic sequences, protein sequences and morphology.[22]

Patel–Erickson model

The Patel–Erickson model[24,25] was used to find the enthalpy of live matter (virus particle, nucleocapsid and nucleic acid). The Patel–Erickson model gives enthalpy of live matter based on its empirical formula.[24,25] First, from the empirical formula, the degree of reduction, E, is calculated:

$$E = 4n_C + n_H - 2n_O - 0n_N + 5n_P + 6n_S \quad (1)$$

where n_C, n_H, n_O, n_N, n_P and n_S are numbers of C, H, O, N, P and S atoms in the empirical formula, respectively.[24,25] Then, the degree of reduction is used to find the standard enthalpy change of combustion, $\Delta_C H^\ominus$, of live matter:[24,25]

$$\Delta_C H^\ominus(\text{bio}) = -111.14 \text{ kJ mol}^{-1} \times E \quad (2)$$

After that, $\Delta_C H^\ominus$ is used to find standard enthalpy change of formation, $\Delta_f H^o$, of live matter, with Hess's law:[25]

$$\Delta_f H^\ominus(\text{bio}) = n_C \Delta_f H^\ominus(CO_2) + (n_H/2)\Delta_f H^\ominus(H_2O) + (n_P/4)\Delta_f H^\ominus(P_4O_{10}) + \\ + n_S \Delta_f H^\ominus(SO_3) - \Delta_C H^\ominus \quad (3)$$

Battley model

The Battley model[26] was used to find the entropy of live matter (virus particles, nucleocapsids and nucleic acids). The Battley model gives entropy of live matter based on its empirical formula.[26] Standard molar entropy, $S_m^\ominus$, of live matter is obtained from the equation:

$$S_m^\ominus(\text{bio}) = 0.187 \Sigma_J (S_m^\ominus(J)/a_J) n_J \quad (4)$$

where $S_m^\ominus(J)$ is standard molar entropy of element J in its standard state elemental (pure) form, a_J number of atoms of element J in its standard state elemental form, and n_J is the number of atoms of element J in the empirical formula of live matter.[26] The standard entropy change of formation, $\Delta_f S^\ominus$, can be found as:[26]

$$\Delta_f S^\ominus(\text{bio}) = -0.813 \Sigma_J (S_m^\ominus(J)/a_J) n_J \quad (5)$$

The standard Gibbs energy change of formation, $\Delta_f G^\ominus$, of live matter is found from $\Delta_f H^\ominus$ and $\Delta_f S^\ominus$:

$$\Delta_f G^\ominus(\text{bio}) = \Delta_f H^\ominus(\text{bio}) - T\Delta_f S^\ominus(\text{bio}) \quad (6)$$

where T is temperature.[44]

Stoichiometry of biosynthesis reactions

Based on empirical formulas, the biosynthesis reactions were formulated with stoichiometry. The biosynthesis reactions are macrochemical equations that explain the conversion of nutrients into new live matter in metabolism[18] The general biosynthesis reaction of viruses has the form:[20,32,45]

$$(\text{Amino acid}) + CH_2O + O_2 + HPO_4^{2-} + HCO_3^- \rightarrow (\text{Bio}) + SO_4^{2-} + H_2O + H_2CO_3 \quad (7)$$

The nutrients for biosynthesis of virus live matter include: amino acids with the empirical formula $CH_{1.798}O_{0.4831}N_{0.2247}S_{0.022472}$ (source of energy, carbon, nitrogen and sulphur), carbohydrates with the empirical formula CH_2O (additional carbon and energy source), O_2 (electron acceptor), HPO_4^{2-} (source of phosphorus).[20,32,45] The main products of biosynthesis are new live matter (bio) with the empirical formula $C_{n\text{C}}H_{n\text{H}}O_{n\text{O}}N_{n\text{N}}P_{n\text{P}}S_{n\text{S}}$, SO_4^{2-} (excess sulphur removal) and H_2CO_3 (oxidized carbon removal).[20,32,45] Moreover, H^+ produced during biosynthesis are absorbed by the bicarbonate buffer made of HCO_3^- and H_2CO_3.[20,32,45]

Thermodynamic properties of biosynthesis

The thermodynamic properties of biosynthesis were calculated with Hess's law.[44] They were calculated by the application of Hess's law to the biosynthesis reactions and thermosdynamic properties of live matter. Thermodynamic properties of biosynthesis include the standard enthalpy of biosynthesis, $\Delta_{bs}H^\ominus$, the standard entropy of biosynthesis, $\Delta_{bs}S^\ominus$, and the standard Gibbs energy of biosynthesis, $\Delta_{bs}G^\ominus$.[18] They were found with the equations:

$$\Delta_{bs}H^{\ominus} = \Sigma_{Products}\nu\Delta_{f}H^{\ominus} - \Sigma_{Reactants}\nu\Delta_{f}H^{\ominus} \quad (8)$$

$$\Delta_{bs}S^{\ominus} = \Sigma_{Products}\nu S_{m}^{\ominus} - \Sigma_{Reactants}\nu S_{m}^{\ominus} \quad (9)$$

$$\Delta_{bs}G^{\ominus} = \Sigma_{Products}\nu\Delta_{f}G^{\ominus} - \Sigma_{Reactants}\nu\Delta_{f}G^{\ominus} \quad (10)$$

where ν represents a stoichiometric coefficient.[18,20,25,32,45]

Antigen–receptor binding

The interaction of a virus with its host cell begins at the host cell membrane.[46] There, the virus antigen binds to the host cell receptor.[46] The antigen–receptor binding is a chemical process similar to protein ligand binding.[12,34] The antigen–receptor binding can be represented with the chemical reaction:

$$(An) + (Re) \rightleftarrows (An–Re) \quad (11)$$

where (An) is the free virus antigen, (Re) free host receptor and (An–Re) the antigen–receptor complex.[12,34] The dissociation equilibrium constant, K_d, is given by the equation:

$$K_d = \frac{[An][Re]}{[An-Re]} \quad (12)$$

where [An] is the concentration of the free virus antigen, [Re] the concentration of the free host receptor and [An–Re] the concentration of the antigen–receptor complex.[12,34] From K_d, the binding equilibrium constant, K_B, can be determined:[12,34]

$$K_B = \frac{1}{K_d} = \frac{[An-Re]}{[An][Re]} \quad (13)$$

Based on K_B, it is possible to calculate standard Gibbs energy change of binding, $\Delta_B G^{\ominus}$:[12,34]

$$\Delta_B G^{\ominus} = -RT\ln K_B \quad (14)$$

RESULTS AND DISCUSSION

Table I gives the empirical formulas of the virus particle, nucleocapsid and nucleic acid of the Omicron JN.1 variant of SARS-CoV-2, which were determined for the first time in this research. Table II gives chemical formulas of the entire virus particle, nucleocapsid and nucleic acid of the Omicron JN.1 variant of SARS-CoV-2. Table III gives the macromolecular composition of the virus particle, nucleocapsid and nucleic acid of the Omicron JN.1 variant. Table IV presents the thermodynamic properties of live matter of the virus particle, nucleocapsid and nucleic acid of the Omicron JN.1 variant of SARS-CoV-2. Table V gives the biosynthesis stoichiometries of the virus particle, nucleocapsid and nucleic acid of the Omicron JN.1 variant. Table VI presents the thermodynamic properties of biosynthesis of the virus particle, nucleocapsid and nucleic acid of the Omicron JN.1 variant of SARS-CoV-2. Table VII shows the thermodynamic properties of antigen-receptor binding of the Omicron JN.1 variant of SARS-CoV-2.

In May 2023, WHO has declared the end of the COVID-19 pandemic.[47] Unfortunately, SARS-CoV-2 has not understood that the pandemic is finished, probably because it obeys the laws of biology, chemistry and physics, and not the

laws of WHO. SARS-CoV-2 Omicron variant has continued its path as time goes by, acquiring new mutations. Thus, in summer, autumn and winter, several new variants have appeared, which were analysed in the literature.[21,32] The laws of biology, chemistry and physics have a supremacy over all other laws, while the fight for survival is the most fundamental law of all living organisms. The newest variant Omicron JN.1 began the development of its epidemic wave in the United States (5000 to 15000 new cases daily) and Europe (3000 to 5000 new cases daily), during the last several weeks. The epidemic wave from December 2023 and January 2024 is of much lower intensity than the pandemic waves caused by the Hu-1, Delta and earlier Omicron variants.[9] The appearance of JN.1, like those of previous variants have caused panic in the general population and the media. The scientific community has reacted very soon, reporting the nucleic acid sequence of the new variant (GISAID ID: EPI_ISL_18615181).[41] The published data represent an excellent basis for the further research, but do not inform enough about the changed infectivity, the pathogenicity and the immune evasion. To obtain a quantitative picture of potential changes, it is necessary to have quantitative data, based on which it is possible to assess the changes in infectivity, the pathogenicity and the potential immune evasion.

TABLE I. Empirical formulas and molar masses of empirical formulas of the virus particle, nucleocapsid and nucleic acid of Omicron JN.1 variant of SARS-CoV-2. Empirical formulas have the general form $C_{nC}H_{nH}O_{nO}N_{nN}P_{nP}S_{nS}$, where *n*C, *n*H, *n*O, *n*N, *n*P and *n*S are numbers of C, H, O, N, P and S atoms in the empirical formula, respectively

Name	C	H	O	N	P	S	*Mr* / g C-mol^{-1}
Virus particle	1	1.6390	0.2841	0.2300	0.006439	0.003765	21.75
Nucleocapsid	1	1.5710	0.3431	0.3124	0.006004	0.003349	23.75
Nucleic acid	1	1.2299	0.7397	0.3863	0.105318	0.000000	33.76

TABLE II. Chemical formulas and molar masses of entire virus particle, nucleocapsid and nucleic acid of Omicron JN.1 variant of SARS-CoV-2. Chemical formulas have the general form $C_{mC}H_{mH}O_{mO}N_{mN}P_{mP}S_{mS}$, where *m*C, *m*H, *m*O, *m*N, *m*P and *m*S are numbers of C, H, O, N, P and S atoms in the chemical formula, respectively

Name	C	H	O	N	P	S	*Mr*(tot) / MDa
Virus particle	1.01E+07	1.66E+07	2.87E+06	2.32E+06	6.51E+04	3.80E+04	219.7
Nucleocapsid	4.95E+06	7.78E+06	1.70E+06	1.55E+06	2.97E+04	1.66E+04	117.6
Nucleic acid	2.82E+05	3.47E+05	2.09E+05	1.09E+05	2.97E+04	0.00E+00	9.5

TABLE III. Macromolecular composition of the virus particle, nucleocapsid and nucleic acid of Omicron JN.1 variant of SARS-CoV-2. Contents of all macromolecular constituents are expressed as mass fractions in %

Name	RNA	DNA	Proteins	Lipids	Carbohydrates
Virus particle	4.3	0.0	77.0	17.2	1.5
Nucleocapsid	8.1	0.0	91.9	0.0	0.0
Nucleic acid	100.0	0.0	0.0	0.0	0.0

TABLE IV. Thermodynamic properties of live matter of virus particles, nucleocapsids and nucleic acid of Omicron JN.1 variant of SARS-CoV-2

Name	$\Delta_f H^{\ominus}$ / kJ C-mol^{-1}	$S_m^{\ominus}$ / J C-mol^{-1} K^{-1}	$\Delta_f G^{\ominus}$ / kJ C-mol^{-1}
Virus particle	–64.43	30.70	–24.63
Nucleocapsid	–75.40	32.47	–33.31
Nucleic acid	–173.12	37.98	–123.90

TABLE V. Biosynthesis stoichiometry of the virus particle, nucleocapsid and nucleic acid of Omicron JN.1 variant of SARS-CoV-2. The general biosynthesis reaction has the form: (Amino acid) + CH_2O + O_2 + HPO_4^{2-} + HCO_3^- → (Bio) + SO_4^{2-} + H_2O + HCO_3^- + H_2CO_3. (Amino acid) denotes the empirical formula of amino acids and (Bio) denotes the empirical formula of live matter

Name	Reactants					→	Products				
	Amino acid	CH_2O	O_2	HPO_4^{2-}	HCO_3^-		Bio	SO_4^{2-}	H_2O	HCO_3^-	H_2CO_3
Virus particle	1.0236	0.0105	0.0000	0.0064	0.0256	→	1	0.0192	0.0674	0.0000	0.0597
Nucleocapsid	1.3903	0.0000	0.4925	0.0060	0.0438	→	1	0.0279	0.0550	0.0000	0.4341
Nucleic acid	1.7190	0.0000	1.0650	0.1053	0.0000	→	1	0.0386	0.3306	0.1334	0.5856

TABLE VI. Thermodynamic properties of biosynthesis of virus particles, nucleocapsids and nucleic acids of Omicron JN.1 variant of SARS-CoV-2

Name	$\Delta_{bs}H^{\ominus}$ / kJ C-mol^{-1}	$\Delta_{bs}S^{\ominus}$ / J C-mol^{-1} K^{-1}	$\Delta_{bs}G^{\ominus}$ / kJ C-mol^{-1}
Virus particle	–4.80	6.94	–6.94
Nucleocapsid	–232.88	–37.48	–221.74
Nucleic acid	–484.11	–98.20	–456.07

TABLE VII. Thermodynamic properties of antigen–receptor binding of Omicron JN.1 variant of SARS-CoV-2; the K_d value was taken from literature[43]

Virus	Variant	Interaction	K_d / M	K_B / M^{-1}	$\Delta_B G^{\ominus}$ / kJ mol^{-1}
SARS-CoV-2	Omicron JN.1	RBD with ACE2	1.45E–08	6.90E+07	–44.74

The infectivity of any virus or virus variant depends on its antigen–receptor binding affinity. In essence, the antigen receptor binding represents a purely chemical interaction similar to protein–ligand interactions. The driving force for this reaction is Gibbs energy change of binding.[34] This is why in the essence of affinity there is the value of Gibbs energy change of binding. The virus variant characterized by a more negative Gibbs energy change exhibits a greater affinity. Consequently, the increased affinity implies a greater infectivity, due to the greater rate of antigen–receptor binding and the faster entry rate of viruses into host cells. If in the same moment two virus variants appear in the same host, they compete for the receptors and the variant characterized by a more negative Gibbs energy change of binding will exclude the other variant or variants from the organism/population.[34,45]

The changes of Gibbs energy (change in thermodynamic properties) appear as a consequence of a change in chemical composition. The change in chemical

composition appears as a consequence of mutations. During mutations, there is the change in the sequence of nucleotides, which leads to the change in chemical composition. The empirical formula of the Hu-1 wild type is $CH_{1.6390}O_{0.2851}N_{0.2301}P_{0.0065}S_{0.0038}$,[48] while the empirical formula of the Omicron BA.1 variant is $CH_{1.6404}O_{0.2842}N_{0.2299}P_{0.0064}S_{0.0038}$,[48] which is different from that of JN.1 $CH_{1.6390}O_{0.2841}N_{0.2300}P_{0.006439}S_{0.003765}$ (Table I). The hydrogen content of the JN.1 variant is similar to that of the Hu-1 wild type, both of which are lower than that of the BA.1 variant. The oxygen content of the JN.1 variant is lower than those of Hu-1 and BA.1 variants. The nitrogen content of the JN.1 variant is between those of the Hu-1 and BA.1 variants. The phosphorus content of the JN.1 variant is similar to that of the BA.1 variant and lower than that of the Hu-1 variant. The sulphur content is similar for all three variants. Therefore, every variant of SARS-CoV-2 is characterized by a specific empirical formula, which can be used to identify the variant. This is in agreement with the result that the virus particles can be identified with single particle ICP-MS.[49]

Empirical formulas have been determined for other viruses: West Nile virus $CH_{1.7651}O_{0.2609}N_{0.1469}P_{0.019712}S_{0.003745}$[30] and Poxviruses $CH_{1.5876}O_{0.3008}N_{0.2538}P_{0.00223}S_{0.00554}$.[29] The empirical formula of JN.1 variant of SARS-CoV-2 is $CH_{1.6390}O_{0.2841}N_{0.2300}P_{0.006439}S_{0.003765}$ (Table I). The hydrogen content of the JN.1 variant is lower than that of the West Nile virus and higher than that of the Poxviruses. The oxygen content of the JN.1 variant is lower than that of poxviruses and higher than that of West Nile virus. The nitrogen content of the JN.1 variant is lower than that of Poxviruses and higher than that of the West Nile virus. The phosphorus content of the JN.1 variant is lower than that of West Nile virus and higher than that of Poxviruses. The sulphur content of the JN.1 variant is higher than those of the West Nile virus and Poxviruses. Therefore, every virus species is characterized by a specific empirical formula.

The chemical formula of the entire virus particle of the Omicron JN.1 variant of SARS-CoV-2 is $C_{1.01\times10^7}H_{1.66\times10^7}O_{2.87\times10^6}N_{2.32\times10^6}P_{6.51\times10^4}S_{3.80\times10^4}$, which has a molar mass of 219.7 MDa (Table II). The chemical formula of the West Nile virus is $C_{1.54\times10^6}H_{2.71\times10^6}O_{4.01\times10^5}N_{2.26\times10^5}P_{3.03\times10^4}S_{5.76\times10^3}$,[30] while that of the poliovirus is $C_{332652}H_{492388}O_{131196}N_{98245}P_{7501}S_{2340}$.[10] The virus particle of the JN.1 variant is composed of a much larger number of atoms than those of the West Nile virus and poliovirus. This is in agreement with the larger size of the SARS-CoV-2 virus particle $(90\ nm)^3$ than those of the West Nile virus (50 nm)[50] and poliovirus (30 nm).[51]

The biosynthesis reaction of the virus particle of Omicron JN.1 variant is:

$$1.0236CH_{1.798}O_{0.4831}N_{0.2247}S_{0.022472} + 0.0105CH_2O + 0.0064HPO_4^{2-} + 0.0256HCO_3^- \rightarrow CH_{1.6390}O_{0.2841}N_{0.2300}P_{0.006439}S_{0.003765} +$$

$$0.0192SO_4^{2-} + 0.0674H_2O + 0.0597H_2CO_3 \quad (15)$$

where $CH_{1.798}O_{0.4831}N_{0.2247}S_{0.022472}$ is the empirical formula of amino acids and $CH_{1.6390}O_{0.2841}N_{0.2300}P_{0.006439}S_{0.003765}$ is the empirical formula of the JN.1 virus particle. The biosynthesis reaction of the nucleocapsid of Omicron JN.1 variant is

$$1.3903CH_{1.798}O_{0.4831}N_{0.2247}S_{0.022472} + 0.4925O_2 + 0.0060HPO_4^{2-} + 0.0438\ HCO_3^- \rightarrow CH_{1.5710}O_{0.3431}N_{0.3124}P_{0.006004}S_{0.003349} + 0.0279SO_4^{2-} + 0.0550H_2O + 0.4341H_2CO_3 \quad (16)$$

where $CH_{1.5710}O_{0.3431}N_{0.3124}P_{0.006004}S_{0.003349}$ is the empirical formula of the JN.1 nucleocapsid. The biosynthesis reaction of the nucleic acid of Omicron JN.1 variant is:

$$1.7190CH_{1.798}O_{0.4831}N_{0.2247}S_{0.022472} + 1.0650O_2 + 0.1053\ HPO_4^{2-} \rightarrow CH_{1.2299}O_{0.7397}N_{0.3863}P_{0.105318} + 0.0386\ SO_4^{2-} + 0.3306\ H_2O + 0.1334HCO_3^- + 0.5856\ H_2CO_3 \quad (17)$$

where $CH_{1.2299}O_{0.7397}N_{0.3863}P_{0.105318}$ is the empirical formula of the JN.1 nucleic acid.

Based on the empirical formulas, thermodynamic properties can be calculated, with the Patel–Erickson model[24,25] and Battley model.[26] The Gibbs energy change of biosynthesis of microorganisms represents the driving force for microorganism multiplication.[18,19,34,45] By multiplying inside host cells, a virus leads to its damage in several ways. One of them is the lytic cycle.[46] Less obvious, but still realistic way of damage of the host cells is competition for resources. Namely, a virus hijacks the host cell metabolic machinery, making it function for the virus multiplication completely, while the synthesis of host cell building blocks is inhibited. Thus, since the reparatory mechanisms become ineffective, with time there is damage of the host cell. According to the phenomenological equations, the reaction rate (in this case rate of virus multiplication) depends on the Gibbs energy change of biosynthesis. A greater multiplication rate leads to greater damage of the host cell. Thus, virus pathogenicity is greater if Gibbs energy change of biosynthesis of the virus is more negative.

It is obvious that the infectivity and the pathogenicity depend on thermodynamic properties – Gibbs energy change of binding and Gibbs energy change of biosynthesis, respectively. Furthermore, the binding of antibodies to virus antigens also represents a chemical reaction, similar to protein–ligand interactions.[12,34] Thus, the driving force for the antigen–antibody binding reaction is the Gibbs energy change of the antigen–antibody binding and the antigen–antibody binding rate, according to the phenomenological equations, depends on it. Therefore, two different molecules – antibody and receptor – bind to the same substrate – antigen – and the reactions are competitive. This means that the reaction char-

acterized with a more negative Gibbs energy change will have an advantage. Macroscopically, if the Gibbs energy change of the reaction of antigen–antibody binding is more negative than the Gibbs energy change of the antigen–receptor binding, then the virus will be inactivated and removed from the host organism and will not lead to the development of a disease. On the other hand, if the Gibbs energy change of antigen–receptor binding is more negative than the Gibbs energy change of the antigen–antibody binding, then there will be immune evasion.

In this research, Gibbs energy change of binding was determined for the first time for the Omicron JN.1 variant of SARS-CoV-2, which is given in Table VII. Gibbs energy changes of binding have been determined for other variants of SARS-CoV-2: Hu-1 wild type –43.43 kJ mol^{-1},[48] Delta B.1.617 variant –43.38 kJ mol^{-1},[48] and Omicron BA.2 variant –51.50 kJ mol^{-1}.[52] Gibbs energy changes of binding of different variants of SARS-CoV-2 during its time evolution are shown in Fig. 1. Please notice that the JN.1 variant originates from the Omicron variant and has appeared by acquisition of mutations with the goal to survive. Obviously, the JN.1 variant has evolved towards less negative Gibbs energy change (which is not a rule observed during evolution of SARS-CoV-2). Indeed, SARS-CoV-2 has exhibited a tendency to evolve towards increase in infectivity and maintenance of pathogenicity.[53] The evolution of the JN.1 variant towards less negative Gibbs energy change of binding could be a consequence of extensive immunization by natural means or by vaccines. The decrease in Gibbs energy change of binding is a result of changed virus antigen structure. Since the changed antigen structure of the virus is different than those of the previous

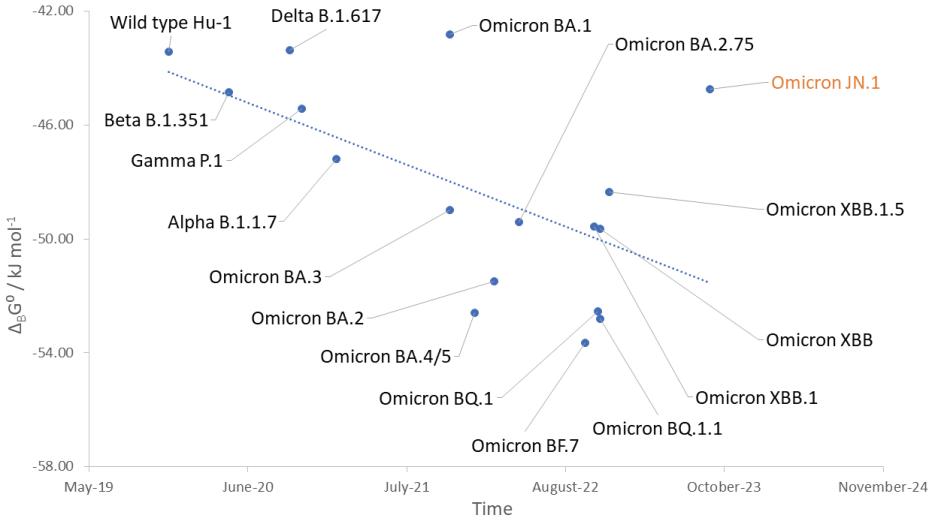

Fig. 1. Gibbs energy change of binding of different SARS-CoV-2 variants during the time evolution of the virus. $\Delta_B G^0$ represents standard Gibbs energy change of binding.

variants, it also binds with a lower affinity to highly specific host antibodies. The lower affinity of binding to antibodies provides immune evasion.

Development of vaccines based on virus variants in circulation is important in order to achieve greater specificity of the response antibodies to the virus and avoid antibody-dependent enhancement.[54] During the pandemic, SARS-CoV-2 developed a great number of mutations. These mutations allow some variants to avoid immune response. Thus, it is important for vaccines to follow the time evolution of SARS-CoV-2.

Infectivity does not depend only on the rate of entry of virus particles into host cells and immune response. The process of infection is much more complex and includes concentration of viruses at the site of entry into host organism (infective inoculum) expressed in number of infectious particles per mL. The concentration of infectious particles is much lower in an open space. This is why the possibility of infection in an open space is much lower. The lower the volume of a closed space, the greater the concentration and the possibility of infection. Furthermore, infectivity also depends on diffusion through nose mucosa and furin cleavage.[13] Due to complexity of the process of infection and the arguments in favour of a stronger immune response of the host organism, it seems that we can be optimistic regarding the epidemic spreading of SARS-CoV-2 variants, with the consciousness that the virus will continue to adapt during the evolution process in the future.

Pathogenicity of viruses depends on the degree of damage that a virus causes during infection. The degree of damage depends on the multiplication rate of the virus. The multiplication rate is, according to the phenomenological equations, dependent on the driving force of multiplication – Gibbs energy change of biosynthesis. Gibbs energy change of biosynthesis of the Omicron JN.1 variant is –221.74 kJ C-mol^{-1}. Gibbs energies changes of biosynthesis of different SARS--CoV-2 variants are given in Fig. 2. Gibbs energies change of biosynthesis of other SARS-CoV-2 variants are: Hu-1 wild type –222.2 kJ C-mol^{-1},[21] Omicron BA.2 –221.22 kJ C-mol^{-1},[52] Omicron XBB.1.5 Kraken –221.22 kJ C-mol^{-1},[34] Omicron XBB.1.16 Arcturus –221.19 kJ C-mol^{-1},[32] and Omicron EG.5 Eris –221.75 kJ C-mol^{-1}.[21] From this we can conclude that Gibbs energy change of biosynthesis has changed very little and that pathogenicity of SARS-CoV-2 variants has remained similar during evolution. This is in agreement with the predictions of theory of evolution, that organisms will evolve towards maintenance of the species. An increase in pathogenicity would lead to a greater number of lethal cases, which would as a consequence lead to lower possibility for the virus to survive.

In the basis of all biological processes performed by viruses, including the life cycle, the infection and the damage to host cells, are physical and chemical processes. This is why mechanistic models are useful for the better understanding

of mechanisms through which biological, physical and chemical processes occur and indicate the ways in which we can influence the course of the pandemic. At the very beginning of the COVID-19 pandemic, there were many misleading information. It was not clear what are the paths of the transmission of COVID-19 infection. Due to this, use of gloves was introduced, even though the primary path of transmission is not fecal-oral, but respiratory. In some countries, money was replaced by contactless payment, even though the transmission by indirect contact is almost impossible. Moreover, the extensive lockdown was enforced in almost all countries, even though it is clear that in the respiratory infections maintenance of distance and avoidance of small closed spaces (*e.g.*, elevators, toilets) should be effective in the avoidance of infections like COVID-19, especially with the extensive application of face masks. In the moment when the mechanistic models were developed and in parallel epidemiological measures and especially vaccines, the fight against the pandemic became much more efficient. However, the damage to production and logistics that could have been avoided has already been made. Moreover, a lot of time was needed for the population to understand that the application of facial masks is a very effective method for the suppression of pandemic, since it decreases the size of infectious inoculum. However, first of all thanks to the scientific community, the number of new cases of COVID-19 has been significantly decreased and the end of the pandemic was declared.

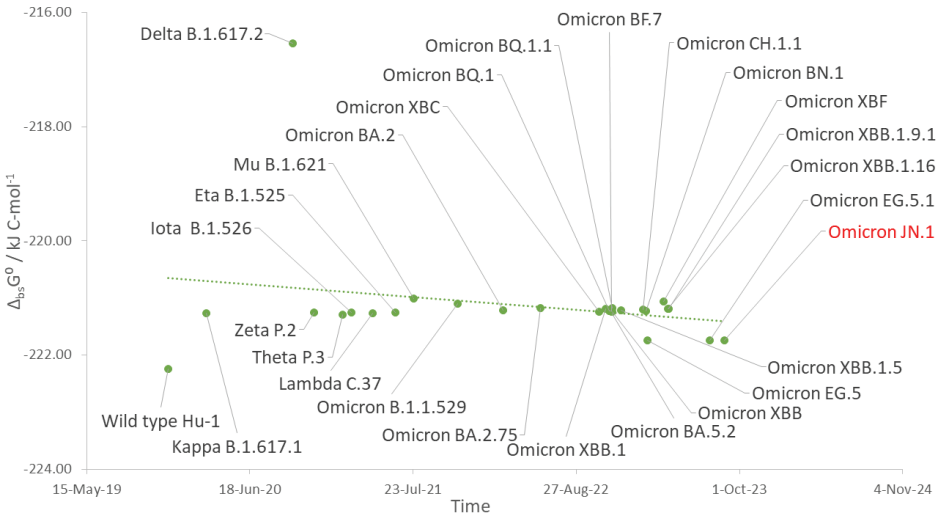

Fig. 2. Gibbs energies change of biosynthesis of different SARS-CoV-2 variants during the time evolution of the virus. $\Delta_{bs}G^0$ represents standard Gibbs energy change of biosynthesis.

CONCLUSIONS

The COVID-19 pandemic might be over. However, the new variants of SARS-CoV-2 are appearing quite frequently. Omicron JN.1 is the last in a sequence of variants. The mechanistic models allow the prediction that the Omicron JN.1 variant can cause a new epidemic wave, with a lower amplitude in the number of new infections (decreased infectivity) and a smaller number of casualties. The smaller number of casualties is a consequence of a smaller number of infected people with the unchanged pathogenicity of the Omicron JN.1 variant. This process is also contributed by the process of immunization. It seems that the need for the active immunization will be necessary for a long period. Moreover, the development of new vaccines will be needed, which will be based on some of the newer variants, due to the acquisition of a larger number of mutations in the new variants.

SUPPLEMENTARY MATERIAL

Additional data and information are available electronically at the pages of journal website: https://www.shd-pub.org.rs/index.php/JSCS/article/view/12786, or from the corresponding author on request.

Acknowledgements. We gratefully acknowledge all data contributors, i.e., the Authors and their Originating laboratories responsible for obtaining the specimens, and their Submitting laboratories for generating the genetic sequence and metadata and sharing *via* the GISAID Initiative, on which this research is based. This work was supported by the Ministry of Science, Technological Development and Innovation of the Republic of Serbia (Grant No. 451-03-47/2023-01/200026).

ИЗВОД

УДАРНЕ ВЕСТИ: ЕМПИРИЈСКЕ ФОРМУЛЕ, МОЛАРНЕ МАСЕ, РЕАКЦИЈЕ БИОСИНТЕЗЕ И ТЕРМОДИНАМИЧКЕ ОСОБИНЕ ВИРУСНИХ ЧЕСТИЦА: БИОСИНТЕЗЕ И ВЕЗИВАЊА OMICRON JN.1 ВАРИЈАНТЕ SARS-COV-2

МАРКО Е. ПОПОВИЋ[1], МАЈА СТЕВАНОВИЋ[2] и МАРИЈА МИХАИЛОВИЋ[1]

[1]Универзитет у Београду, Институт за хемију, технологију и металургију, Његошева 12, 11000 Београд и [2]Иновациони центар Технолошко–металуршког факултета, Универзитет у Београду, Карнегијева 4, 11120 Београд

Ударне вести су обично узнемирујуће. О природним катастрофама, ратовима, епидемијама, итд. се извештава као о ударним вестима. У овом раду је приказано смањење опасности од ширења епидемија изазваних варијантом JN.1, јер анализе показују да је инфективност нове варијанте слабија у односу на већину ранијих варијанти, што потврђује и број случајева (7500 дневно у САД). Штавише, JN.1 упркос великом броју мутација није успео да постигне вредности промене Гибсове енергије биосинтезе (а самим тим и стопе размножавања вируса) дивљег типа Hu.1. Истраживање показује да инфективност и патогеност варијанте JN.1 није достигла забрињавајућу величину, што значи да нема разлога за очекивање погоршање епидемиолошке ситуације.

(Примљено 19. јануара, ревидирано 31. јануара, прихваћено 20. фебруара 2024)

REFERENCES

1. H. Wang, X. Li, T. Li, S. Zhang, L. Wang, X. Wu, J. Liu, *Eur. J. Clin. Microb. Infect. Dis.* **39** (2020) 1629 (https://doi.org/10.1007/s10096-020-03899-4)
2. Y. Huang, C. Yang, Xf. Xu, W. Xu, S.-W. Liu, *Acta Pharmacol. Sin.* **41** (2020) 1141 (https://doi.org/10.1038/s41401-020-0485-4)
3. B. W. Neuman, M. J. Buchmeier, *Adv. Vir. Res.* **96** (2016) 1 (https://doi.org/10.1016/bs.aivir.2016.08.005)
4. M. Pal, G. Berhanu, C. Desalegn, V. Kandi, *Cureus* **12** (2020) e7423 (https://doi.org/10.7759/cureus.7423)
5. S. Duffy, *PLoS Biology* **16** (2018) e3000003 (https://doi.org/10.1371/journal.pbio.3000003)
6. P. V. Markov, M. Ghafari, M. Beer, K. Lythgoe, P. Simmonds, N. I. Stilianakis, A. Katzourakis, *Nat Rev Microbiol* **21** (2023) 361 (https://doi.org/10.1038/s41579-023-00878-2)
7. G. Campi, A. Perali, A. Marcelli, A. Bianconi, *Sci. Rep.* **12** (2022) 18108 (https://doi.org/10.1038/s41598-022-22816-7)
8. W. T. Harvey, A. M. Carabelli, B. Jackson, R. K. Gupta, E. C. Thomson, E. M. Harrison, C. Ludden, R. Reeve, A. Rambaut, *COVID-19 Genomics UK (COG-UK) Consortium*, *S. J. Peacock, D. L. Robertson*, *Nat. Rev. Microbiol.* **19** (2021) 409 (https://doi.org/10.1038/s41579-021-00573-0)
9. *WHO COVID-19 dashboard*, https://data.who.int/dashboards/covid19/cases?n=c (Accessed on Jan. 4, 2024)
10. E. Wimmer, *EMBO Reports* **7** (2006) S3 (https://doi.org/10.1038/sj.embor.7400728)
11. S. K. Thaker, J. Ch'ng, H.R. Christofk, *BMC Biol.* **17** (2019) 59 (https://doi.org/10.1186/s12915-019-0678-9)
12. X. Du, Y. Li, Y.L. Xia, S.M. Ai, J. Liang, P. Sang, X.L. Ji, S.Q. Liu, *Internat. J. Mol. Sci.* **17** (2016) 144 (https://doi.org/10.3390/ijms17020144)
13. M. Popovic, J. H. Martin, R. J. Head, *Heliyon* **9** (2023) e17174 (https://doi.org/10.1016/j.heliyon.2023.e17174)
14. A. V. Pinheiro, P. Baptista, J. C. Lima, *Nucl. Acids Res.* **36** (2008) e90 (https://doi.org/10.1093/nar/gkn415)
15. T. Dodd, M. Botto, F. Paul, R. Fernandez-Leiro, M. H. Lamers, I. Ivanov, *Nature Commun.* **11** (2020) 5379 (https://doi.org/10.1038/s41467-020-19165-2)
16. W. H. Wang, A. Thitithanyanont, S. F. Wang, *Viruses* **14** (2022) 1650 (https://doi.org/10.3390/v14081650)
17. R. D. Cadena-Nava, M. Comas-Garcia, R. F. Garmann, A. L. Rao, C. M. Knobler, W. M. Gelbart, *J. Virology* **86** (2012) 3318 (https://doi.org/10.1128/JVI.06566-11)
18. U. Von Stockar, in: *Biothermodynamics: the role of thermodynamics in Biochemical Engineering*, U. von Stockar, ed., EPFL Press, Lausanne, 2013, pp. 475–534
19. U. von Stockar, J. Liu, *Biochim. Biophys. Acta* **1412**(1999) 191 (https://doi.org/10.1016/s0005-2728(99)00065-1)
20. M. Popovic, M. Pantović Pavlović, M. Pavlović, *Microb. Risk Anal.* **24** (2023) 100263 (https://doi.org/10.1016/j.mran.2023.100263)
21. M. E. Popović, M. Pantović Pavlović, M. Popović, *Microb. Risk Anal.* **25** (2023) 100280 (https://doi.org/10.1016/j.mran.2023.100280)
22. M. Popovic, *Comp. Biol. Chem.* **96** (2022) 107621 (https://doi.org/10.1016/j.compbiolchem.2022.107621)

23. M. Popovic, V. Tadić, M. Mihailović, *J. Biomol. Struct. Dyn.* (2023) (https://doi.org/10.1080/07391102.2023.2256880)
24. S. A. Patel, L. E. Erickson, *Biotechnol. Bioeng.* **23** (1981) 2051 (https://doi.org/10.1002/bit.260230910)
25. E. H. Battley, *Thermochim. Acta* **309** (1998) 17 (https://doi.org/10.1016/S0040-6031(97)00357-2)
26. E. H. Battley, *Thermochim. Acta* **326** (1999) 7 (https://doi.org/10.1016/S0040-6031(98)00584-X)
27. M. Popovic, *Vaccines* **10** (2022) 2112 (https://doi.org/10.3390/vaccines10122112)
28. M. Popovic, *Microb. Risk Anal.* **22** (2022) 100236 https://doi.org/10.1016/j.mran.2022.100236
29. M. Popovic, *Thermal Sci.* **26** (2022) 4855 (https://doi.org/10.2298/TSCI220524142P)
30. M. Popovic, M. Popovic, G. Šekularac, *Microb. Risk Anal.* **25** (2023) 100281 (https://doi.org/10.1016/j.mran.2023.100281)
31. B. Şimşek, M. Özilgen, F. Ş. Utku, *Energy Storage* **4** (2021) e298 (https://doi.org/10.1002/est2.298)
32. M. E. Popovic, M. Mihailović, S. Pavlović, *Microb. Risk Anal.* **25** (2023) 100273 (https://doi.org/10.1016/j.mran.2023.100273)
33. M. S. Maginnis, *J. Mol. Biol.* **430** (2018) 2590 (https://doi.org/10.1016/j.jmb.2018.06.024)
34. M. Popovic, *Microbiol. Res.* **270** (2023) 127337 (https://doi.org/10.1016/j.micres.2023.127337)
35. P. Gale, *Microb. Risk Anal.* **15** (2020) 100104 (https://doi.org/10.1016/j.mran.2020.100104)
36. P. Gale, *Microb. Risk Anal.* **16** (2020) 100140 (https://doi.org/10.1016/j.mran.2020.100140)
37. R. J. Head, E. R. Lumbers, B. Jarrott, F. Tretter, G. Smith, K. G. Pringle, S. Islam, J. H. Martin, *Pharmacol. Res. Persp.* **10** (2022) e00922 (https://doi.org/10.1002/prp2.922)
38. U. Lucia, G. Grisolia, T. S. Deisboeck, *Atti Accad. Peloritana Pericolanti* **99** (2021) A3 (https://doi.org/10.1478/AAPP.992A3)
39. M. Özilgen, B. Yilmaz, *Int. J. Energy Res.* **45** (2021) 1157 (https://doi.org/10.1002/er.5883)
40. U. Lucia, T. S. Deisboeck, G. Grisolia, *Front. Phys.* **8** (2020) 274 (https://doi.org/10.3389/fphy.2020.00274)
41. S. Khare, C. Gurry, L. Freitas, M. B. Schultz, G. Bach, A. Diallo, N. Akite, J. Ho, R. T. C. Lee, W. Yeo, GISAID Core Curation Team, S. Maurer-Stroh, *China CDC Weekly* **3** (2021) 1049 (https://doi.org/10.46234/ccdcw2021.255)
42. E. W. Sayers, E. E. Bolton, J. R. Brister, K. Canese, J. Chan, D. C. Comeau, R. Connor, K. Funk, C. Kelly, S. Kim, T. Madej, A. Marchler-Bauer, C. Lanczycki, S. Lathrop, Z. Lu, F. Thibaud-Nissen, T. Murphy, L. Phan, Y. Skripchenko, T. Tse, J. Wang, R. Williams, B. W Trawick, K. D Pruitt, S.T. Sherry, *Nucl. Acids Res.* **50** (2022) D20 (https://doi.org/10.1093/nar/gkab1112)
43. S. Yang, Y. Yu, Y. Xu, F. Jian, W. Song, A. Yisimayi, P. Wang, J. Wang, J. Liu, L. Yu, X. Niu, J. Wang, Y. Wang, F. Shao, R. Jin, Y. Wang, Yunlong, *Lancet Infect. Diseases* (2023) S1473 (https://doi.org/10.1016/S1473-3099(23)00744-2)
44. P.W. Atkins, J. de Paula, *Physical Chemistry for the Life Sciences*, 2nd ed., W. H. Freeman and Company, London, 2011 (ISBN-13: 978-1429231145)

45. M. Popovic, *Microb. Risk Anal.* **24** (2023) 100260 (https://doi.org/10.1016/j.mran.2023.100260)
46. S. Riedel, J.A. Hobden, S. Miller, S.A. Morse, T.A. Mietzner, B. Detrick, T.G. Mitchell, J.A. Sakanari, P. Hotez, R. Mejia, *Jawetz, Melnick and Adelberg's Medical Microbiology*, 28th ed., McGraw-Hill, New York, 2019 (ISBN-13: 978-1260012026)
47. *End of the Federal COVID-19 Public Health Emergency (PHE) Declaration*, https://www.cdc.gov/coronavirus/2019-ncov/your-health/end-of-phe.html (Accessed on Jan. 7, 2024)
48. M. Popovic, *Microb. Risk Anal.* **22** (2022) 100217 (https://doi.org/10.1016/j.mran.2022.100217)
49. C. Degueldre, *Talanta* **228** (2021) 122211 (https://doi.org/10.1016/j.talanta.2021.122211)
50. M. A. Martín-Acebes, J.C. Saiz, *World J. Virol.* **1** (2012) 51 (https://doi.org/10.5501/wjv.v1.i2.51)
51. M. M. Mehndiratta, P. Mehndiratta, R. Pande, *Neurohospitalist* **4** (2014) 223 (https://doi.org/10.1177/1941874414533352)
52. M. Popovic, *Virology* **575** (2022) 36 (https://doi.org/10.1016/j.virol.2022.08.009)
53. M. Popovic, *Microb. Risk Anal.* **22** (2022) 100232 (https://doi.org/10.1016/j.mran.2022.100232)
54. J.A. Tetro, *Microbes Infect*. **22** (2020) 72 (https://doi.org/10.1016/j.micinf.2020.02.006)
55. M. E. Popović, G. Šekularac, M. Mihailović, *Microb. Risk Anal.* **26** (2024) 100291 (https://doi.org/10.1016/j.mran.2024.100291).

Journal of the Serbian Chemical Society
JSCS@tmf.bg.ac.rs • www.shd.org.rs/JSCS
J. Serb. Chem. Soc. 89 (3) S125 (2024) *Supplementary material*

SUPPLEMENTARY MATERIAL TO

Breaking news: Empirical formulas, molar masses, biosynthesis reactions and thermodynamic properties of virus particles – Biosynthesis and binding of Omicron JN.1 variant of SARS-CoV-2

MARKO E. POPOVIĆ[1]*, MAJA STEVANOVIĆ[2] and MARIJA MIHAILOVIĆ[1]

[1]*University of Belgrade, Institute of Chemistry, Technology and Metallurgy, Njegoševa 12, 11000 Belgrade, Serbia and* [2]*Inovation Centre of the Faculty of Technology and Metallurgy, University of Belgrade, Karnegijeva 4, 11120 Beograd, Serbia*

J. Serb. Chem. Soc. 89 (3) (2024) 305–320

DATA AVAILABILITY

GISAID Identifier: EPI_SET_240109xh
doi: https://doi.org/10.55876/gis8.240109xh

All genome sequences and associated metadata in this dataset are published in GISAID's EpiCoV database. To view the contributors of each individual sequence with details such as accession number, Virus name, Collection date, Originating Lab and Submitting Lab and the list of Authors, visit https://doi.org/10.55876/gis8.240109xh.

Data Snapshot:

- EPI_SET_240109xh is composed of 1 individual genome sequences.
- The collection dates range from 2023-12-04 to 2023-12-04;
- Data were collected in 1 country and territories;
- All sequences in this dataset are compared relative to hCoV-19/Wuhan/ /WIV04/2019 (WIV04), the official reference sequence employed by GISAID (EPI_ISL_402124). Learn more at https://gisaid.org/WIV04.

* Corresponding author. E-mail: marko.popovic@ihtm.bg.ac.rs

Journal of the Serbian Chemical Society
JSCS@tmf.bg.ac.rs • www.shd.org.rs/JSCS
J. Serb. Chem. Soc. *89* (3) 321–334 (2024)
JSCS–5723
Original scientific paper
Published 24 March 2024

PCR-based detection of alkane monooxygenase genes in the hydrocarbon and crude oil-degrading *Acinetobacter* strains from petroleum-contaminated soils

AYŞE EREN, FATMA MATPAN BEKLER and KEMAL GÜVEN*

Department of Molecular Biology and Genetics, Faculty of Science, Dicle University, 21280 Diyarbakır, Turkey

(Received 7 July, revised 8 August, accepted 18 August 2023)

Abstract: Bacterial strains D11, E1 and E2 isolated from petroleum-contaminated soils were found to be members of *Acinetobacter* genus revealed by 16S rRNA gene sequence analysis and phenotypic characteristics. After incubation for 5 days, about 43, 9 and 12 % of total petroleum hydrocarbons of crude oil were degraded by strains D11, E1 and E2, respectively, and determined by GC–MS analysis. Moreover, about 70 and 76 % of single hydrocarbon hexadecane was degraded by the strains D11 and E1 after 3 days of short incubation time, respectively, while the strain E2 degraded about 48 % of single hydrocarbon pentadecane. By using PCR-based method, gene sequences of the strains D11 and E2 showed similarity to alkane 1-monooxygenases from *Acinetobacter* sp. BUU8 *alkM* with 93.06 and 92.72 %, respectively, while the sequence similarity of strain E1 was 95.84 % to *Acinetobacter* sp. 826659. The present study of hydrocarbon biodegradation by *Acinetobacter* strains may provide a good advantage in bioremediation process.

Keywords: petroleum-degradation; bacteria; GC–MS analysis; *alkM* gene.

INTRODUCTION

There is a continuous great concern about petroleum hydrocarbons causing pollution in the environment, produced from various anthropogenic activities, such as accidental petroleum spills during transport and refining of oil products, industrial discharge and leakage from underground tanks.[1,2] Toxic oil products are known to pose a serious threat to marine habitats, fishery and human health, leading to an imbalance in the ecosystem and thus harming the wildlife which takes years or even decades to recover.[3,4] Aliphatic *n*-alkanes, formed by the reduction of organic material during the geochemical formation of petroleum, are hydrocarbons found in crude and refined oils.[5]

* Corresponding author. E-mail: kemalg@dicle.edu.tr
https://doi.org/10.2298/JSC230707053E

A greater amount of aliphatic alkanes is released into the environment and thus the bioavailability and toxicity of *n*-alkanes vary according to the chain length.[6] Since crude oil and its products are biodegradable, bioremediation for cleaning up oil-contaminated sites is considered as an efficient and cost-effective technique compared to chemical and physical treatments. Recently, bioremediation of oil-contaminated sites has been an important task for scientists, carrying out many studies using pure culture or mixed bacterial consortia which degrade petroleum hydrocarbons.[4,7,8] In the environmental biotechnology using biodegradation and bioremediation processes, various kinds of microorganisms including bacteria and fungi have been employed.[9] The bacteria using hydrocarbons as a carbon source and energy for their growth have been studied in detail, such as *Alcaligenes*, *Bacillus*, *Corynebacterium*, *Pseudomonas*, *Methylomonas*, *Micrococcus*, *Methylobacterium*, *Nocardia*, *Rhodococcus*, *Achromobacter*, *Acinetobacter*, *Arthrobacter*, *Flavobacterium*, *etc*. Members of these groups have been evaluated for usage in bioremediation processes.[10–13] Among these, biodegradation studies have been also focused on *Acinetobacter* species such as *Acinetobacter baylyi* ADP1,[14,15] *Acinetobacter* sp. MUB1,[16] *Acinetobacter oleivorans*,[17] *Acinetobacter* sp. LS-1,[18] *A. baumannii*[19] and *Acinetobacter johnsoni.*[20] As identified in *Acinetobacter*, alkane monooxygenases encoded by the *alkM* gene and composed of alkane hydroxylase (*alkM*), rubredoxin (*RubA*) and rubredoxin reductase (*RubB*) are key enzymes that catalyze the terminal oxidation of *n*-alkanes to alcohols.[14–16,21–23]

In this study, we aimed to study and characterise *Acinetobacter* strains isolated from petroleum-contaminated sites in Batman province of Turkey and to evaluate the hydrocarbon biodegradation potential of the isolated bacterial strains.

EXPERIMENTAL

Collection of samples

The samples were collected from petroleum-contaminated soils around the petroleum wells (Southern Raman1. and 237. petroleum stations). The crude oil used in the experiments was obtained from Batman petroleum refinery. The Basal medium (BM) contained per L: phosphate buffer (5.0 mL), magnesium sulphate (3.0 mL), calcium chloride (1.0 mL), ferric chloride (1.0 mL), as well as 1.0 mL mineral elements solution containing $ZnSO_4 \cdot H_2O$, $MnSO_4$ and $(NH_4)_6MoO_{24} \cdot 4H_2O$. Filtered crude oil (1 %) was transferred to the BM by using a 0.2 mm pore size filter as the energy source. The petroleum-contaminated soils (1 g) around the petroleum wells were transferred into BM in the presence of crude oil (1 %) and then incubated in a shaking water bath at 120 rpm at 30 °C for 5 days. After incubation, aliquots (1 mL) from each sample were transferred to freshly prepared BM plus crude oil (1 %) for preparing subculture. Following two subculture cycles, the microorganisms were let to grow on solid medium (nutrient broth agar) for 5 days of incubation. The morphological appearance of the colonies growing on the plates was examined and different colonies were selected and retransferred to BM in the presence or absence of crude oil for 5 days. The isolated strains

were characterized as colonies with different morphologies for petroleum hydrocarbon degradation and utilising hydrocarbons for the carbon and energy source.

Morphological, biochemical and physiological characteristics

Gram staining was carried out by the method of Dussault. [24] The temperature range of 10–45 °C was used for growth in liquid medium, whereas the pH range tested was 4.0–12.0. The initial pH of media was adjusted with acidic and basic solutions. Urease activity testing was carried out as described by Lányi.[25] Procedures described within Bergey *et al*.[26] and Claus and Berkeley,[27] were followed to determine different biochemical properties such as indole, oxidase, citritase, catalase and urease activity as well as motility of the studied isolates.

Preparation of genomic DNA extraction and 16S rRNA analyses

Bacterial cells (D11, E1 and E2) were cultured overnight in NB medium under optimum conditions. After incubation bacterial culture was centrifuged at 14,000 rpm for 10 min and bacterial pellet was resuspended in Tris-EDTA (TE) buffer. Genomic DNA was isolated from tested bacteria using protocol supplied by the manufacturer of the Bacterial Genomic DNA Extraction Kit. DNA concentrations were determined using a UV/Vis spectrophotometer (S60 Double Beam, Libra Biochrom). All DNA extracts were stored at –20 °C. 16S rRNA encoding genes were amplified by PCR from isolated chromosomal DNA (1 μL) using universal primers (27F and 1492R, Sentebiolab). PCR amplification was performed in PCR reaction mixture (25 μL) containing; primers (20 pmol for F and R), 0.3 mM dNTP's mixture and Taq DNA polymerase (2.5 U, Sigma) in the supplied buffer (10X, Sigma). The PCR temperature program used was: initial denaturation at 95 °C 5 min, 40 cycles of denaturing at 94 °C for 1 min, annealing at 55 °C for 1 min, and extension at 72 °C for 2 min and the final extension at 72 °C for 7 min, using thermal cycler (T100, BIO-RAD). Isolated chromosomal DNA samples and PCR products were subjected to analysis with agarose gel electrophoresis using 1 % of agarose gels containing red safe gel stain and visualized using a transilluminator (Wuv-M20, Daihan Scientific). PCR products were extracted from the gel using QIAquick gel extraction kit (QIAGEN).

Phylogenetic analysis

Sequence analysis of 16S rRNA gene sequences of hydrocarbon-degrading isolates was performed by BM Laboratory system (Ankara, Türkiye). Sanger Sequencing was performed in the Macrogen Netherlands laboratory using the ABI 3730XL Sanger sequencing instrument (Applied Biosystems, Foster City, CA) and the BigDye Terminator v3.1 cycle sequencing kit. Reads obtained with primers 27F and 1492R were contiguous using the CAP contig assembly algorithm in BioEdit software to generate a consensus sequence. The sequences of the 16S rRNA gene for all strains were determined (D11: 1407 bp, E1: 1383 bp; E2: 1393 bp). The Blast search tool on National Centre of Biotechnology (NCBI, http://www.ncbi.nlm.nih.gov) was used to compare and search for homology of these sequences in the GenBank database. The 16S rRNA gene similarities were retrieved from the database, determining most closely related strains. The Kimura-2 parameter algorithm Kimura[28] was used to calculate distance matrices. The phylogenetic tree was built using the neighbor-joining method according to Saitou and Nei.[29] The bootstrap consensus tree was set at 100 replicates to represent the evolutionary history of taxa. Evolutionary analyses were performed in MEGA11.[30] All strains were deposited in GenBank database.

PCR amplification of alkM gene

CLUSTALW, available from NCBI, was used to align all complete sequences of the *alkM*.[31] Consensus regions were used to design degenerate primers by identifying conserved regions in alkM nucleotide sequences. The purified DNA was screened by PCR to detect alkane degradation genes (*alkM*). Therefore, the*t alkM* gene was amplified using the primers *alkM*-F (5'-CCTGTCTCATTTGGCGCTCGTTCCTACAGG-3') and *alkM*-R (5'--GTGATGATCTGAATGTCGTTGTAACTGG-3'). PCR reactions mix (25 µL) were prepared containing 10X PCR Buffer with MgCl2 (Sigma), 0.5 µM primer *alkM*-F and *alkM*-R, dNTP's (0.2 mM of each, Sigma), Taq polymerase (0.05 U mL^{-1}, Sigma) and H_2O for PCR (Sigma). The amplification program consisted of a denaturation at 94 °C for 4 min, denaturing at 94 °C for 30 s (35 cycles), annealing at 55–65 °C for 1 min (using gradient), followed by extension at 72 °C for 7 min using a thermal cycler. PCR products were confirmed by running on 1.0 % agarose gel containing red safe staining and visualized using a transilluminator. For sequencing, PCR products were purified using gel extraction kit.

Detection of alkane monooxygenase gene alkM

PCR products of *alkM* gene from the strains were sequenced on both strands by the commercial services of Sentebio lab (Ankara, Türkiye). Analysis of PCR products was done by an automated genetic analyser and sequences were aligned and compared with other *alkM* sequences of *Acinetobacter* available in the GenBank database using the Clustal X program and all sequences were compared using a Blast search tool database[32] on NCBI. Phylogenetic trees of aligned sequences were constructed with MEGA11 software.[30] Nucleotide sequences were translated into amino acid sequences using the Transeq tool (on the website of the European Bioinformatics Institute) and compared directly with the Protein Database. Conserved areas within coding nucleotide sequences were analysed by CD-Search[33] while using the BLASTP tool on NCBI to check if sequenced *alkM* genes have conserved motifs. The *alkM* protein sequence was modelled by the SWISS-Model workspace (https://swissmodel.expasy.org). The Ramachandran plot was evaluated with Verify 3D and Procheck.[34]

Growth of bacterial strains in the presence of hydrocarbons and crude oil

A fresh culture of all strains grown in BM liquid medium for 24 h was obtained, followed by centrifugation and washing with BM. This process was repeated 3 times. Bacteria were then incubated in BM (25 mL) in the presence of crude oil (1 %) for 5 days and in single hydrocarbons (1 % hexane, heptane, octane, decane, pentadecane, hexadecane, toluene and squalene from Sigma) for 3 days under optimum growth conditions. Following incubation, the bacterial growth was determined by spectrophotometer at 600 nm. Each data point represents the mean of at least three experiments.

GC Analyses of degradation of crude oil and hydrocarbons by the strains

The determination of both crude oil and single n-alkanes degradation such as hexadecane and pentadecane by bacterial strains were performed by using gas chromatography–mass spectrometry (GC–MS). Bacterial cells precultured overnight in NB medium were transferred to a 100 mL Erlenmeyer flask containing 25 mL of BM in the presence of 1 % crude oil or *n*-alkanes and incubated under optimum conditions at 30 °C. Following incubation, the bacterial cells were removed, and petroleum hydrocarbons remaining in the BM were used for calculating the degradation ratio of single hydrocarbons and those within crude oil. Petroleum hydrocarbon fractions remaining in the culture medium after incubation time were analyzed by GC–MS with a flame ionization detector (FID, HP 6850, Hewlett Packard). Authentic stan-

dards were used to determine individual hydrocarbon fraction components by matching the retention times.

RESULTS AND DISCUSSION

Morphological, physiological and biochemical characteristics

Two bacterial strains designated as strains D11 and E2 were isolated from the petroleum station Southern Raman 237, while the strain E1 was isolated from Southern Raman1 in Batman province of Turkey, and all strains were found to degrade and use hydrocarbons within crude oil to grow (Fig. 1).

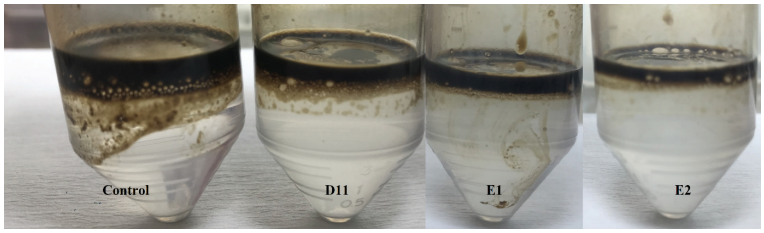

Fig. 1. Demonstration of growth and biodegradation by the strains D11, E1 and E2, compared to abiotic control at 1 % crude oil as carbon source.

The strain D11, E1 was Gram-negative, motile, coccobacilli, while E2 strain was Gram-negative, non-motile and coccobacilli (see Table S-I of the Supplementary material to this paper.). The comparison of phenotypic properties of the strain D11, E1 and E2 with some *Acinetobacter* strains in Table S-I reveal the similarities of both strains to each other and to other *Acinetobacter* species, phenotypically and biochemically, based on the results obtained. As Henrichsen[35] stated, the name "*Acinetobacter*" means "motile rod" and it has been noted in previous studies that a nonmotile phenotype is a common feature in this genus, but it was also noted that the motility of a few *A. calcoaceticus* strains was very conditional and observed. As D11 and E1 was found to be motile, there are several studies on *A. baylyi* and *A. gerneri*,[36] *Acinetobacter* sp. BT1A,[37] describing motile phenotypes of *Acinetobacter* members. As shown in Table I, all strains were gram-negative and aerobic. Moreover, the characteristics of oil--degrading strains D11, E1 and E2 were interestingly very similar of which the catalase, citrate and starch test results were clearly positive, whereas, oxidase, urea and indole test results were negative. The difference was that gelatine hydrolysis test was positive for E1, but negative for D11 and E2. The biochemical test results such as starch hydrolysis, catalase and citritase activities of D11, E1 and E2 strains were similarly positive as in most *Acinetobacter* species: positive starch hydrolysis also in *A. junii* strain VA2[38] and *Acinetobacter* sp. strain BT1A,[37] positive catalase and citritase activities also in *A. soli*, sp. Nov,[39] *Acinetobacter* strain USTB-X.[40] The growth values of strain D11 and E1 for the

temperature, pH and NaCI tolerance were found to be very close and observed to be 20–40 °C (optimum 35 °C), pH 5.0 and 10.0 (optimum pH 8.0–10.0 for D11, optimum pH 9.0–10.0 for E1) and tolerated up to 3 % NaCl, respectively. Moreover, the temperature and pH values for the strain E2 were also found to be 20––40 °C (optimum 35 °C), but pH growth range was 4.0–10.0 (a wide optimum range of 4.0–10.0), and tolerated up to 5 % NaCl. Compared with previous studies on other *Acinetobacter* species, the optimum pH values obtained were 8.0 for *A. soli*, sp. Nov,[39] and 8.5 for *Acinetobacter* sp. strain S2.[41] Similar temperature values as in the present study were reported as 20–40 °C for *Acinetobacter* strain USTB-X[40] and *A. junii* strain VA2.[38]

TABLE I. *alkM* Gene sequences and conserved domains within coding nucleotide sequences

Isolate	Related bacteria strains gene	Base pairs long	Nucleotides similarity, %	Description	Interval	*E*-value
D11	*Acinetobacter* sp. BUU8 (UniprotKB (A6N7F9)	651	93.06	The membrane fatty acid desaturase (Membrane_FADS)-like CD includes membrane FADSs, alkane	66–281 744–938	1.21×10^{-16} 2.15×10^{-19}
E1	*Acinetobacter* sp. 826659 (A0A013TK13)	471	95.84	The membrane fatty acid desaturase (Membrane_FADS)-like CD includes membrane FADSs, alkane	33–293 799–1542	2.00×10^{-20} 1.87×10^{-57}
E2	*Acinetobacter* sp. BUU8 (UniprotKB (A6N7F9)	448	92.72	The membrane fatty acid desaturase (Membrane_FADS)-like CD includes membrane FADSs, alkane	36–170	9.51×10^{-8}

Phylogenetic analysis

The amount of Genomic DNA isolated from D11, E1 and E2 strains was 25––71 μg/mL and each determined to be >10 kb in size on 1 % agarose gel. Reads obtained with primers 27F and 1492R were contiguous to form a consensus sequence. The contig of forward and reverse sequences, contig assembly algorithm (CAP) was used in BioEdit software to perform this process. The analysis of 16 S rRNA gene sequence revealed that the most similarity of the strain D11 (1407 bp) was to *A. pittii* (99.93 %) and E1 (1383 bp) to *A. pittii* (100 %), while the strain E2 (1393 bp) was similar to *A. calcoaceticus* (100 %), Fig. 2.

GenBank accession numbers of the sequences of the strains D11, E1, E2 are MT374264, MT374266 and MT374267, respectively. The tree was generated

using Blast program for sequence alignment and by the neighbor joining method using MEGA11 software. *Exiguobacterium* sp. (KM077136) was used as the outgroup.

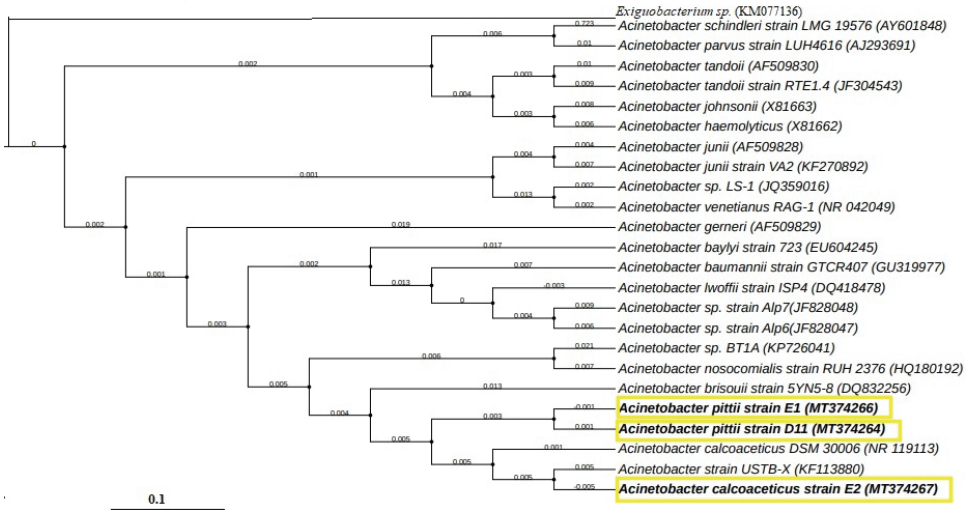

Fig. 2. The 16S gene sequence analysis of the strains D11, E1 and E2.

Detection of alkane monooxygenase gene alkM

The nucleotide and the predicted amino acid sequences for the *alkM* genes were compared using several databases as described in the previous section. The results of base pairs long and nucleotides similarity with related bacterial strains are presented in Table I.

Analysis of the derived amino acid sequences of alkane 1-monooxygenase from tested strains showed a high degree of similarity to that of other *Acinetobacter* strains. Conserved domains within coding nucleotide sequences were analysed with CD-Search using tool on NCBI. All sequences showed similarity the membrane fatty acid desaturase (accession no. cl00615) and the regions of the conserved domains of the tested strains are also given in the Table I. It was previously reported that members of *Acinetobacter* species possess many metabolic capabilities including degradation pathways.[42] For example, the biodegradation studies carried out on *Acinetobacter* species include: *A. baylyi* ADP1,[14,15] *Acinetobacter* sp. MUB1[16] and *A. oleivorans.*[17] *Acinetobacter* species isolated from petroleum contaminated sites have been reported to possess *n*-alkane degrading genes including alkane monooxgenase, alkane hydoxylase and dioxygenase genes which are the key enzymes of metabolic process in the remediation oil pollution,[18,19,22,23,43] Taking into account the amino acid sequences of the *alkM* protein from strains D11, E1 and E2, three-dimensional (3D) model was analysed

with SWISS-Model workspace through a comparative analysis of the Ramachandran Prochek software for each *alkM* protein model generated. Alignment of region linked to substrate specificity for the *alkM* from tested bacteria (D11, E1 and E2) and other related species (*A. baylyi* (O31250), *Acinetobacter* sp. SJ-2 (K4HWF9), *Acinetobacter* sp. BUU8 (A6N7F9), *Acinetobacter* sp. (Q9XBM0), *Acinetobacter* sp. 826659 (A0A013TK13), *A. calcoaceticus* (F0KMZ3), *Alkanindiges hydrocarboniclasticus* (A0A1S8CT34) was performed by using the UniprotKB server. Phylogenetic analysis of strains and related species was performed by the Neighbor joining method based on *alkM* gene sequences.

In Fig. S-1a–e of the Supplementary material, strain D11 (651 bp) sequences showed similarity to alkane 1-monooxygenase. Strain D11 sequences showed similarity to alkane 1-monooxygenase from *Acinetobacter sp.* BUU8 (UniprotKB (A6N7F9) with 93.06 %. The three-dimension (3D) model of alkane monooxygenase (*alkM*) of the *A. baylyi* (UniprotKB O31250) was used as reference.

The data shown by the Ramachandran graph (94.55 %) reveal the identity/similarity of primary, secondary and tertiary structures between the strain D11 and *A. baylyi* (UniprotKB O31250). Alkane monooxygenase gene sequences of strain E1 (471 bp) showed similarity to alkane 1-monooxygenase of *Acinetobacter* sp. 826659 (A0A013TK13) with 95.84 % and Ramachandran graph was found to be 83.33 % (Fig. S-2a–e of the Supplementary material).

In Fig. S-3a–e of the Supplementary material, strain E2 gene sequences (448 bp) showed similarity to alkane 1-monooxygenase from *Acinetobacter sp.* BUU8 (UniprotKB A6N7F9) with 92.72 % while the Ramachandran graph was 100 %. As van Beilen *et al.*[44] stated, many alkane hydroxylase homologues have been characterized in addition to *alkM* genes in studies conducted in *A. calcoaceticus* strains EB104, 69-VA and NCIMB 8250 and also *Acinetobacter* sp. 2769A related to *alkM* genes. Phylogenetic analysis of *alkM* amino acid sequences, in these studies, showed high sequence variation between them and clearly differentiated *alkM* genes from *alkB* genes. Therefore, most of these genes not found in *Acinetobacter* genus have been named *alkB* gene.

Growth of bacterial strains in the presence of crude oil and various hydrocarbons

The strains were tested by incubation in the presence of various short and long chain hydrocarbons and crude oil, namely hexane, heptane, octane, decane, pentadecane, hexadecane and squalene, as well as toluene cultivated in BM medium at 1 % concentrations under optimum conditions. As it can be seen in Fig. 3, the strains D11, E1 and E2 clearly use certain hydrocarbons as carbon and energy sources for growth on both 1 % crude oil and single hydrocarbons tested.

Fig. 3 also shows that the strains D11 and E1, significantly degrade hexadecane, among the aliphatic hydrocarbons tested. The strains also grow at low

rates on decane and pentadecane, but not in short chain hydrocarbons such as hexane, heptane or octane. However, the growth for strain E2 was remarkable in the presence of long chain hydrocarbon pentadecane, while the growth was relatively higher in hexadecane and squalene, compared to control. Sun *et al.*[45] reported that the aerobic degradation of *n*-alkanes by bacteria needs alkane monooxygenase encoded by *alkM* gene which catalyzes the terminal oxidation of *n*-alkanes to alcohols, suggesting that the transcription of *alkM* in bacterial strains directly influences the degradation of *n*-hexadecane.

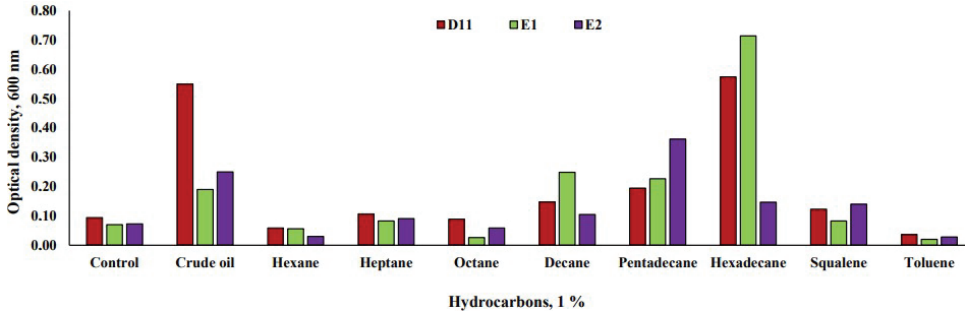

Fig. 3. Growth of strains D11 (red), E1 (green) and E2 (purple) in BM supplemented with crude oil (incubated for 5 days) and various hydrocarbons (incubated for 3 days) at 1% concentrations as carbon sources. Each data represents the mean of at least 3 different experiments

Degradation of crude oil and hydrocarbons by the strains determined by GC–MS analyses

Members of *Acinetobacter* sp. are capable of utilizing a broad range of *n*-alkanes with varying chain lengths (C10–C40) as a sole carbon source.[46] Furthermore, *Acinetobacter* species are dominant bacteria in most petroleum contaminated soils,[47,48] as well as in various environments including sea waters and sediments,[20,49] in waste waters[50] and in streams.[51]

Different degradation rates (%) of crude oil and alkane hydrocarbons by various *Acinetobacter* species are summarised in Table II, as well as the degradation results obtained in the present study. The remaining amount of hydrocarbons in the culture medium, analysed by GC–MS, were used for calculating degradation rates of crude oil and alkane hydrocarbons (1 %). The comparisons with the undegraded control showed that the strains D11, E1 and E2 degraded 43, 9 and 12 % of total petroleum hydrocarbons, respectively, within crude oil after short incubation time of only 5 days. The growth of the strains D11, E1 and E2 in the basal media with hexadecane or pentadecane was remarkable as shown in Fig. 3, and the gas chromatographic analysis of two single hydrocarbons were also carried out for each strain Fig. S-4a–e of the Supplementary material. Fig. S--4b shows that as much as 70 % of single hydrocarbon hexadecane (1 %) was

degraded by the strain D11, compared to abiotic control (Fig. S-4a), while 76 % of hexadecane was degraded by the strain E1 (Fig. S-4c). Moreover, as can be seen in Fig. S-4e, the strain E2 degraded about 48 % of single pentadecane (1 %) after 3 days of short incubation time, compared to abiotic control (Fig. S-4d).

TABLE II. The degradation of petroleum hydrocarbons by members of *Acinetobacter*

Isolate	Isolation of bacteria from	Substrate tested	Degradation rate %	Incubation time, days	Literature
Acinetobacter sp. strain Y9	Sea mud	C9–C22 *n*-alkanes from diesel oil (4 %)	53.28	7	Min *et al*.[23]
Acinetobacter sp. strain S2	Wastewaters	Diesel oil	50.62	7	Sawadogo *et al*.[41]
Acinetobacter sp. Strain BT1A	Crude-oil contaminated soil	Crude oil (1 %)	83	7	Acer *et al*.[37]
Acinetobacter baumannii MKS2	Crude-oil contaminated soil	Crude oil (1 %)	43	13	Muthukamalam et.al.[19]
Acinetobacter sp.	Crude-oil contaminated soil	Crude oil	75 (of C20, C21 and C22) 50 (of shorter chains)	7	Zheng *et al*.[52]
A. pittii H9-3	Crude-oil contaminated soil	Crude oil (1 %)	36.8	21	Wang *et al*.[43]
A. pittii strain D11	Crude-oil contaminated soil	Crude oil (1 %) Hexzadecane (1 %)	43 (c. oil) 70 (hexadecane)	5 3	Present study
A. pittii strain E1	Crude-oil contaminated soil	Crude oil (1 %) Hexzadecane (1 %)	9 (c. oil) 76 (hexadecane)	5 3	Present study
A. calcoaceticus strain E2	Crude-oil contaminated soil	Crude oil (1%) Pentadecane (1 %)	12 (c. oil) 48 (pentadecane)	5 3	Present study

There have been many studies reported in the literature related to biodegradation rates of hydrocarbons by various bacterial species. For example, Tapilatu *et al*.[53] reported that *Alcanivorax venustensis* strains and some other Gram-positive bacteria preferably degraded *n*-hexadecane (40–63 %), but other genera tested seemed to prefer *n*-heptadecane (8–44 %), after long time incubation of 30 days. Many other bacterial species isolated from contaminated sites were found to degrade oil hydrocarbons at varying degradation rates as: *Pseudomonas* sp. degraded 67.57 % of the oil (1 %) and *Micrococcus* sp. with 52.95 % after 25 days of incubation period.[54] *Pseudomonas* sp. had shown 49.93 % of diesel oil degradation in 20 days against 0.5 % of diesel.[55] Six isolated bacterial strains identified

as *P. alcaligenes* (HDB-6), *Bacillus thuringiensis*, *Pseudomonas alcaligenes* (HDB-4), *Pseudomonas mendocina*, *Bacillus flexus* and *Lysini bacillus* sp. were found to degrade between 37.88 and 54.01 % of crude oil after 14 days.[56] There have also been several studies on hydrocarbon biodegradation rates using *Acinetobacter* species. Throne-Holst *et al*.[46] determined that *Acinetobacter* strain can use carbon sources in the range of decane and tetracontane long-chain *n*-alkanes. Min *et al*.[23] reported that *Acinetobacter* strain Y9 degrades *n*-alkanes in the range of C9–C22 as sole carbon sources degrading 53.28 % in 7 days of incubation. *Acinetobacter* sp. BT1A was also found to degrade 83 % of 1 % crude oil in 7 days.[37] In more recent studies, various *A. baumannii* strains were found to degrade an average of 43 and 61% of oil alkanes, respectively.[19,57]

CONCLUSION

A wide variety of microorganisms including bacteria that can degrade hydrocarbons within petroleum were isolated from oil-contaminated soils. Bacteria are the most dominant microorganisms determined in microbial ecology degrading petroleum hydrocarbons. Among bacteria, *Acinetobacter* is recently found to be most common genera that is able to degrade hydrocarbons. The members of *Acinetobacter* species studied were found to biodegrade crude oil and sole hydrocarbons. Gene sequences of the strains D1, E1 and E2 showed similarity to alkane 1-monooxygenases from *Acinetobacter* sp. *alkM*. The present study seems to be effective in degrading *n*-alkanes in shorter incubation time and further microbial consortium studies, with the related strains, may provide a good advantage in bioremediation of oil-contaminated soil.

Acknowledgement. This study, a part of Ayse EREN's PhD project, was supported by Dicle University Scientific Research Projects Coordination Unit (Project no.: FEN.19.014).

SUPPLEMENTARY MATERIAL

Additional data and information are available electronically at the pages of journal website: https://www.shd-pub.org.rs/index.php/JSCS/article/view/12469, or from the corresponding author on request.

ИЗВОД

ДЕТЕКЦИЈА ГЕНА ЗА АЛКАН-МОНООКСИГЕНАЗУ У *ACINETOBACTER* СОЈУ КОЈИ РАЗЛАЖЕ УГЉОВОДОНИКЕ И СИРОВУ НАФТУ ПРИМЕНОМ PCR МЕТОДЕ НА ЗЕМЉИШТА КОНТАМИНИРАНА НАФТОМ

AYŞE EREN, FATMA MATPAN BEKLER и KEMAL GÜVEN

Department of Molecular Biology and Genetics, Faculty of Science, Dicle University, 21280 Diyarbakır, Turkey

Бактеријски сојеви D11, E1 и E2 изоловани из земљишта контаминираних нафтом су припадници *Acinetobacter* рода, што је утврђено секвенцирањем гена за 16S rRNA и фенотипском карактеризацијом. Након инкубације 5 дана, GC–MS анализом је утврђено да је око 43, 9, односно 12 % укупних угљоводоника из сирове нафте разложено соје-

вима D11, E1, односно E2, редом. Такође, око 70 и 76 % хексадекана је разложено сојевима D11 и E1 након 3 дана инкубације, док је сој E2 разложио око 48 % пентадекана. PCR методом генског секвенцирања утврђена је 93,06 %, односно 92,72 %, сличност гена за алкан-1-монооксигеназу сојева D11 и E2 са геном из *Acinetobacter* sp. BUU8 *alkM*, док је сличност секвенце соја E1 95,84 % са геном *Acinetobacter* sp.826659. Резултати ове студије биодеградације угљоводоника сојевима *Acinetobacter* могу наћи примену у поступку биоремедијације.

(Примљено 7. јула, ревидирано 8. августа, прихваћено 18. августа 2023)

REFERENCES

1. R. Bajagain, Y. Park, S. W Jeong, *Sci. Total Environ*. (2018) 1236 (https://doi.org/10.1016/j.scitotenv.2018.01.212)
2. S. J. Varjani, *Bioresour. Technol*. **223** (2017) 277 (http://dx.doi.org/10.1016/j.biortech.2016.10.037)
3. Z .Zhang, Z. Hou, C. Yang, C. Ma, F. Tao & P. Xu, *Bioresour. Technol*. **102** (2011) 4111 (https://dx.doi.org/10.1016/j.biortech.2010.12.064)
4. M. B. Yakubu, *Afr. J. Biotechnol*. **6** (2007) 2735 (https://doi.org/10.5897/AJB2007.000-2437)
5. K. Kloos, J. C. Munch, M. Schloter, *J.Microbiol. Methods* **66** (2006)486 (https://doi.org/10.1016/j.mimet.2006.01.014)
6. C. O. Gill,C. Ratledge, *J. Gen. Microbiol*. **72** (1972) 165 (https://doi.org/10.1099/00221287-72-1-165)
7. D. M. Al-Mailem, N. A. Sorkhoh, H. Al-Awadhi, M. Eliyas, S. S. Radwan, *Extremophiles* **14** (2010) 321 (https://doi.org/10.1007/s00792-010-0312-9)
8. F. Chaillan, A. Le Flèche, E. Bury,Y. Phantavong, P. Grimont, A. Saliot, J. Oudot, *Res. Microbiol*. **155** (2004) 587 (https://doi.org/10.1016/j.resmic.2004.04.006)
9. S. J. Varjani, D. P. Rana, A. K. Jain, S. Bateja, V. N. Upasani, *Int. Biodeterior. Biodegrad*. **103** (2015)116 (http://dx.doi.org/10.1016/j.ibiod.2015.03.030)
10. R. K. Jain, M. Kapur, S. Labana, B. Lal, P. Sarma, D. Mhattacharya, I. S.Thakur, *Curr. Sci*. **89** (2005) 101 (https://www.jstor.org/stable/24110436)
11. B. Thapa, A Kumar KC, A. Ghimire, *Kathmandu Univ. J. Sci. Eng. Technol*. **8** (2012) 164 (https://doi.org/10.3126/kuset.v8i1.6056)
12. W. Xia, H. Dong, C. Zheng, Q. Cui, P. He, Y. Tang, *RSC Adv.* **5** (2015) 102367 (https://doi.org/10.1039/C5RA17137G)
13. K. Sadighbayan, M. M. Assadi, A. Farazmand, A. R. Monadi, N. Aliasgharzad, H. Mobaiyen, Ramin Zadghaffari, *Adv. Biores*. **7** (2016) 57 (https://soeagra.com/abr/march_2016/11f.pdf)
14. A. Ratajczak, W. Geissdoerfer, W. Hillen, *Appl. Environ. Microbiol*. **64** (1998) 1175 (https://doi.org/10.1128/AEM.64.4.1175-1179.1998)
15. A. Ratajczak, W. Geissdoerfer, W. Hillen, *J. Bacteriol.* **180** (1998) 5822 (https://doi.org/10.1128/JB.180.22.5822-5827.1998)
16. S. Phrommanich, S. Suanjit, S. Upatham, S. V. Grams, M. Kruatrachue, P. Pokethitiyook, G. Korge, A. Hofmann, *Microbiol. Res*. **164** (2009) 486 (https://doi.org/10.1016/j.micres.2007.03.002)
17. J. Jung, E. L. Madsen, C. O. Jeon, W Park, *Appl. Environ. Microbiol*. **77** (2011) 7418 (https://doi.org/10.1128/AEM.05231-11)

18. H. Liu, J. Yao, Z. Yuan, Z. M. Yuan, Y. F. Shang, H. L. Chen, F. Wang, K. Masakorala, C. Yu, M. Cai, R. E. Blake, M. M. F. Choi, *Int. Biodeterior. Biodegrad.* **87** (2014) 52 (https://doi.org/10.1016/j.ibiod.2013.11.005)
19. S. Muthukamalam, S. Sivagangavathi, D. Dhrishya, S. S. Rani, *Braz. J. Microbiol.* **48** (2017) 637 (https://doi.org/10.1016/j.bjm.2017.02.007)
20. F. Bendadeche, M. B. B. Hamed, S. Ayad, *J. Environ. Eng. Sci.* (2019) 131 (https://doi.org/10.17265/2162-5298/2019.04.001)
21. W. Geissdoerfer, R. G. Kok, A. Ratajczak, K. J. Hellingwerf, W. Hillen, *J. Bacteriol.* **181** (1999) 4292 (https://doi.org/10.1128/jb.181.14.4292-4298.1999)
22. Y. Liu, A. Ding, Y. Sun, X. Xia, D. Zhang, *Front. Environ. Sci. Eng.* **12** (2018) 3 (https://doi.org/10.1007/s11783-018-1064-5)
23. S. Min, L. Qun, S. Xian-rong, H. Deng-yong, H. Ying, S. Zhan, W. Qing-Rong, *Afr. J. Microbiol. Res.* **6** (2012) 3936 (https://doi.org/10.5897/AJMR12.278)
24. H. P. Dussault, *J. Bacteriol.* **70** (1955) 484 (https://doi.org/10.1128/jb.70.4.484-485.1955)
25. B. Lányi, *Methods Microbiol.* **19** (1988) 1 (https://doi.org/10.1016/S0580-9517(08)70407-0)
26. D. H. Bergey, N. R. Krieg, J. G. Holt, *Bergey's manual of systematic bacteriology*, Williams and Wilkins Co, Baltimore, 1989
27. D. Claus, and C. W. Berkeley, in: *Bergey's manual of systematic bacteriology*, 1986, p. 1105
28. M. Kimura, *J. Mol. Evol.* **16** (1980) 111 (https://doi.org/10.1007/BF01731581)
29. N. Saitou, M. Nei, *Mol. Biol. Evol.* **4** (1987) 406 (https://doi.org/10.1093/oxfordjournals.molbev.a040454)
30. K. Tamura, G. Stecher, S. Kumar, *Mol. Biol. Evol.* **38** (2021) 3022 (https://doi.org/10.1093/molbev/msab120)
31. J. D. Thompson, D. G. Higgins,T. J. Gibson, *Nucleic Acids Res.* **22** (1994) 4673 (https://doi.org/10.1093/nar/22.22.4673)
32. S. F. Altschul, T. L. Madden, A. A. Schäffer, J. Zhang, Z. Zhang, W. Miller, D. J. Lipman, *Nucleic Acids Res.* **25** (1997) 3389 (https://doi.org/10.1093/nar/25.17.3389)
33. A. Marchler-Bauer, M. K. Derbyshire, N. R. Gonzales, S. Lu, F. Chitsaz, L. Y. Geer, S. H. Bryant, *Nucleic Acids Res.* **43** (2015) 222 (https://doi.org/10.1093/nar/gku1221)
34. R. A. Laskowski, M. W. MacArthur, D. S. Moss, J. M. Thornton, *Appl. Crystallogr.* **26** (1993) 283 (https://doi.org/10.1107/S0021889892009944)
35. J. Henrichsen, *Acta Pathol. Microbiol. Scand., B* **83** (1975) 179 (https://doi.org/10.1111/j.1699-0463.1975.tb00090.x)
36. Y. S. Kang, W. Park, *Environ. Microbiol.* **12** (2010) 1304 (https://doi.org/10.1111/j.1462-2920.2010.02175.x)
37. Ö. Acer, K. Güven, F. Matpan Bekler, R. Gül-Güven, *Bioremediat. J.* **20** (2016) 1 (https://doi.org/10.1080/10889868.2015.1096898)
38. Q. Zhang, D. Wang, M. Li, W. N. Xiang,V. Achal, *Front. Earth Sci.* **8** (2014) 58 (https://doi.org/10.1007/s11707-013-0415-6)
39. D. Kim, K. S. Baik, M. S. Kim, S. C. Park, S. S. Kim, M. S. Rhee, Y. S. Kwak, C. N. Seong, *J. Microbiol.* **46** (2008) 46 (https://doi.org/10.1007/s12275-008-0118-y)
40. H. Yuan, J. Yao, K. Masakorala, F. Wang, M. Cai, C. Yu, *Environ. Sci. Pollut.* **21** (2014) 2724 (https://doi.org/10.1007/s11356-013-2221-9)
41. A. Sawadogo, O. C. Harmonie, J. B. Sawadogo, A. Kaboré, A. S. Traoré, D. Dianou, *J. Environ. Prot.* **5** (2014)1183 (https://doi.org/10.4236/jep.2014.512115)

42. S. Yoshida, K. Tazaki, T. Minamikawa, *Phytochemistry* **14** (1975) 195 (https://doi.org/10.1016/0031-9422(75)85036-9)
43. Y. Wang, Q. Wang, L. Liu, *Int. J. Environ. Res. Public Health*. **16** (2019) 188 (https://doi.org/10.3390/ijerph16020188)
44. J. B van Beilen, Z. Li, W. A. Duetz, T. H. M. Smits, B. Witholt, *Oil Gas Sci. Technol.* **58** (2003) 427 (https://doi.org/10.2516/ogst:2003026)
45. J.-Q. Sun, L. Xu, Y.-Q.Tang, F.-M. Chen, X.-L. Wu, *Bioresour. Technol*. **123** (2012) 664 (https://doi.org/10.1016/j.biortech.2012.06.072)
46. M. Throne-Holst, A. Wentzel, T. E. Ellingsen, H. K. Kotlar, S. B. Zotchev, *Appl. Environ. Microbiol.* **73** (2007) 3327 (https://doi.org/10.1128/AEM.00064-07)
47. P. Anbu, M. J. Nouh, D. H. Kim, J. S. Seo, B. K. Hur, K. H. Min, *Afr. J. Biotechnol*. **10** (2011) 4147 (https://academicjournals.org/journal/AJB/article-full-text-pdf/467B98830582)
48. A. M. Tanase, R. Ionescu, I. Chiciudean, T. Vassu, I.S toica, *Int. Biodeterior. Biodegradation* **84** (2012) 150 (https://doi.org/10.1016/j.ibiod.2012.05.022)
49. D. Cerqueda-Garcíaa, J. Q. García-Maldonadob, L. Aguirre-Macedoc, U. García-Cruz, *Mar. Pollut. Bull*. **150** (2020) 110775 (https://doi.org/10.1016/j.marpolbul.2019.110775)
50. H. Li, X. L. Wang, B. Z. Mub, J. D. Gu, Y. D. Liu, K. F. Lin, S. G. Lu, Q. Lu, B. Z. Li, Y. Y. Li, X. M. Du, *Int. Biodeterior. Biodegradation* **76** (2013) 49 (https://doi.org/10.1016/j.ibiod.2012.06.007)
51. S. A. Adebusoye, M. O. Ilori, O. O. Amund, O. D. Teniola, S. O. Olatope, *World J. Microbiol. Biotechnol*. **23** (2007) 1149 (https://doi.org/10.1007/s11274-007-9345-3)
52. J. Zheng, J.*Q. Feng, L. Zhou, S. M. Mbadinga, J.-D. Gu, B.-Z. Mu, *World J. Microbiol. Biotechnol*. **34** (2018) 1 (https://doi.org/10.1007/s11274-018-2417-8)
53. Y. Tapilatu, M. Acquaviva, C. Guigue, G. Miralles, J. C. Bertrand, P. Cuny, *Lett. Appl. Microbiol.* **50** (2009) 234 (https://doi.org/10.1111/j.1472-765X.2009.02766.x)
54. T. Nikhil, V. Deepa, G.Rohan, B. Satish, *Int. J. Environ. Res*. **2** (2013) 48 (http://www.isca.me/IJENS/Archive/v2/i2/8.ISCA-IRJEvS-2012-092.pdf)
55. S. K. Panda, R. N. Kar, C. R. Panda, *Int. J. Environ. Sci*. **3** (2013) 1314 (https://doi.org/10.6088/ijes.2013030500001)
56. X. Tian, X. Wang, S. Peng, Z. Wang, R. Zhou, H. Tian, *Water Sci. Technol*. **78** (2019) 2626 (https://doi.org/10.2166/wst.2019.025)
57. I. Jerin, M. Rahi, T. Sultan, M. S. Islam, S. A. Sajib, K. M.H oque, M. A. Reza, *Arch. Microbiol*. **203** (2021) 5075 (https://doi.org/10.1007/s00203-021-02469-2).

Journal of the Serbian Chemical Society
JSCS@tmf.bg.ac.rs • www.shd.org.rs/JSCS
J. Serb. Chem. Soc. *89* (3) S126–S130 (2024) *Supplementary material*

SUPPLEMENTARY MATERIAL TO

PCR-based detection of alkane monooxygenase genes in the hydrocarbon and crude oil-degrading *Acinetobacter* strains from petroleum-contaminated soils

AYŞE EREN, FATMA MATPAN BEKLER and KEMAL GÜVEN*

Department of Molecular Biology and Genetics, Faculty of Science, Dicle University, 21280 Diyarbakır, Turkey

J. Serb. Chem. Soc. *89* (3) (2024) 321–334

Table S-I. The phenotypical characteristics of the strains D11, E1 and E2, in comparison with other *Acinetobacter* species

Characteristic	1	2	3	4	5	6	7	8	9	10	11
Cell shape	Cb	Cb	Cb	ND	B	Cb	B	C	B	Rs	Cb
Gram staining	-	-	-	-	-	-	-	-	-	-	-
Motility	+	+	-	-	-	-	ND	-	-	-	+
Oxygen requirement	A	A	A	ND	A	A	ND	ND	ND	ND	A
Growth temperature (°C)	20-40	20-40	20-40	ND	10-40	25-37	ND	25-45	20-40	30-39	10-45
Optimum Growth temperature (°C)	35	35	35	25-30	30	ND	28	30	30	36-37	30
Growth pH	5.0-10.0	5.0-10.0	4.0-10.0	ND	5.0-10.0	ND	ND	6.0-8.0	6.0-9.0	7.0-9.0	5.0-11.0
Optimum growth pH	8.0-10.0	9.0-10.0	4.0-10.0	7.0-8.0	6.0-8.0	ND	7.0	7.0	ND	8.5	5.0
Starch hydrolysis	+	+	+	-	-	ND	ND	ND	+	ND	+
Gelatin hydrolysis	-	+	-	-	ND	+	-	ND	+	ND	+
Oxidase	-	-	-	-	-	-	-	-	-	-	-
Catalase	+	+	+	+	+	+	+	+	+	+	+
Citrate	+	+	+	+	+	+	-	+	+	+	+
Urease	-	-	-	+	ND	ND	-	ND	ND	ND	+
Indole	-	-	-	-	-	ND	-	-	ND	-	-
NaCl resistance	3	3	5	3.5	0-5	ND	ND	ND	0-9	0-3	4

+ = positive; - = negative; ND= no data available; C=coccoid; Cb=coccobacil; Rs= short rod; B=bacil; A= aerobic; 1=Acinetobacter pittii strain D11, 2: Acinetobacter pittii E1 3=Acinetobacter calcoaceticus strain E2 , 4= Acinetobacter sp. strain ADH-1 (Cormack and Fraile 1997), 5 = Acinetobacter soli, sp. Nov. (Kim et al. 2008), 6= Acinetobacter beijerinckii, sp. Nov.,NIPH 838^T (Nemec et al. 2009), 7=Acinetobacter sp. strain RTE1.4 (Paisio et al. 2013), 8= Acinetobacter strain USTB-X (Yuan et al. 2014) ,9= Acinetobacter junii strain VA2 (Zhang et al. 2014), 10= Acinetobacter sp. strain S2 (Sawadogo et al. 2014), 11= Acinetobacter sp. strain BT1A (Acer et al. 2016).

* Corresponding author. E-mail: kemalg@dicle.edu.tr

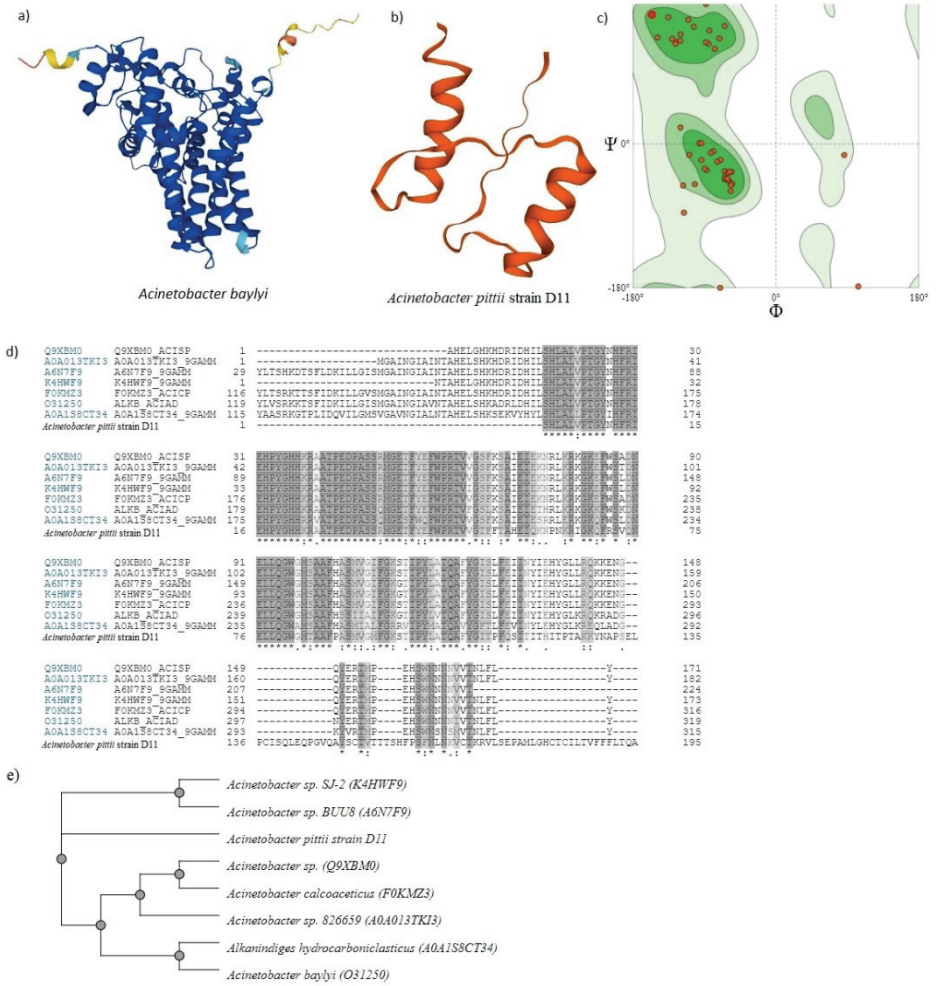

Figure S-1. 3-D models of *alkM* protein of *A. baylyi* (a) and strain D11 (b) generated by the Swiss-Model server (c) Graphs obtained by using the Ramachandran-Prochek software for each *alkM* protein model generated (d) Alignment of region linked to substrate specificity for the *alkM* from D11 and other related species by the UniprotKB server (e) Phylogenetic tree

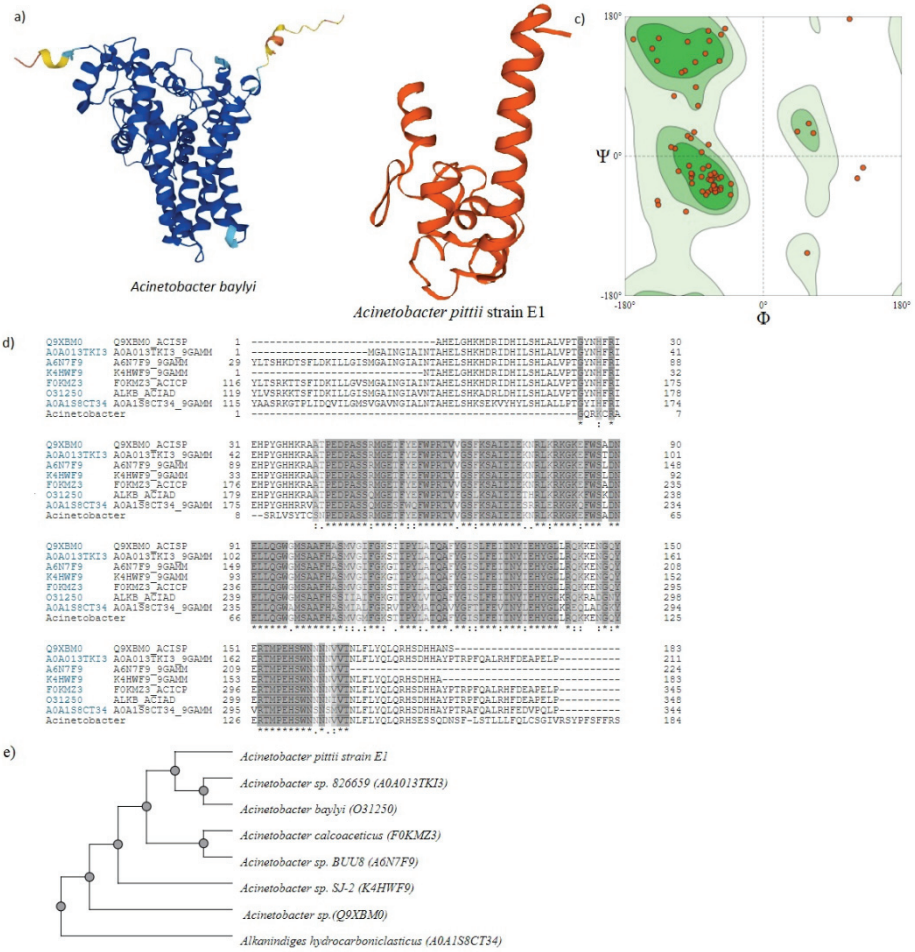

Figure S-2. 3-D models of *alkM* protein of *A. baylyi* (a) and strain E1 (b) generated by the Swiss-Model server (c) Graphs obtained by using the Ramachandran-Prochek software for each *alkM* protein model generated (d) Alignment of region linked to substrate specificity for the *alkM* from E1 and other related species by the UniprotKB server (e) Phylogenetic tree

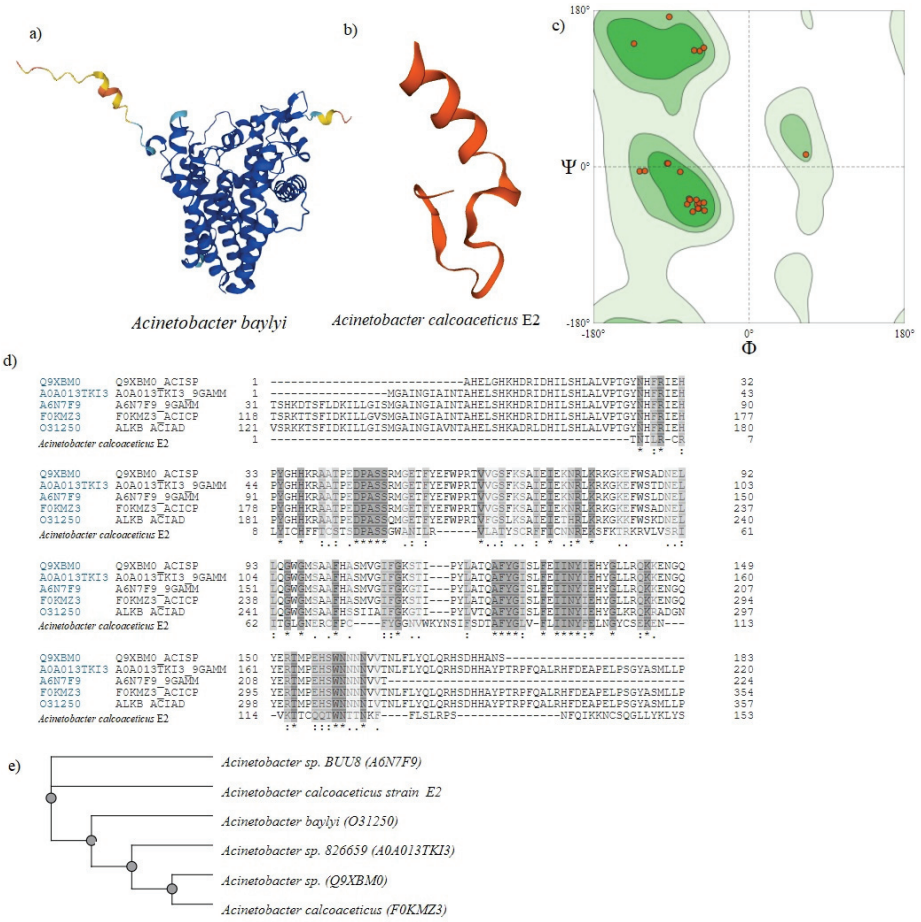

Figure S-3. 3-D models of *alkM* protein of *A. baylyi* (a) and strain E2 (b) generated by the Swiss-Model server (c) Graphs obtained by using the Ramachandran-Prochek software for each *alkM* protein model generated (d) Alignment of region linked to substrate specificity for the *alkM* from E2 and other related species by the UniprotKB server (e) Phylogenetic tree

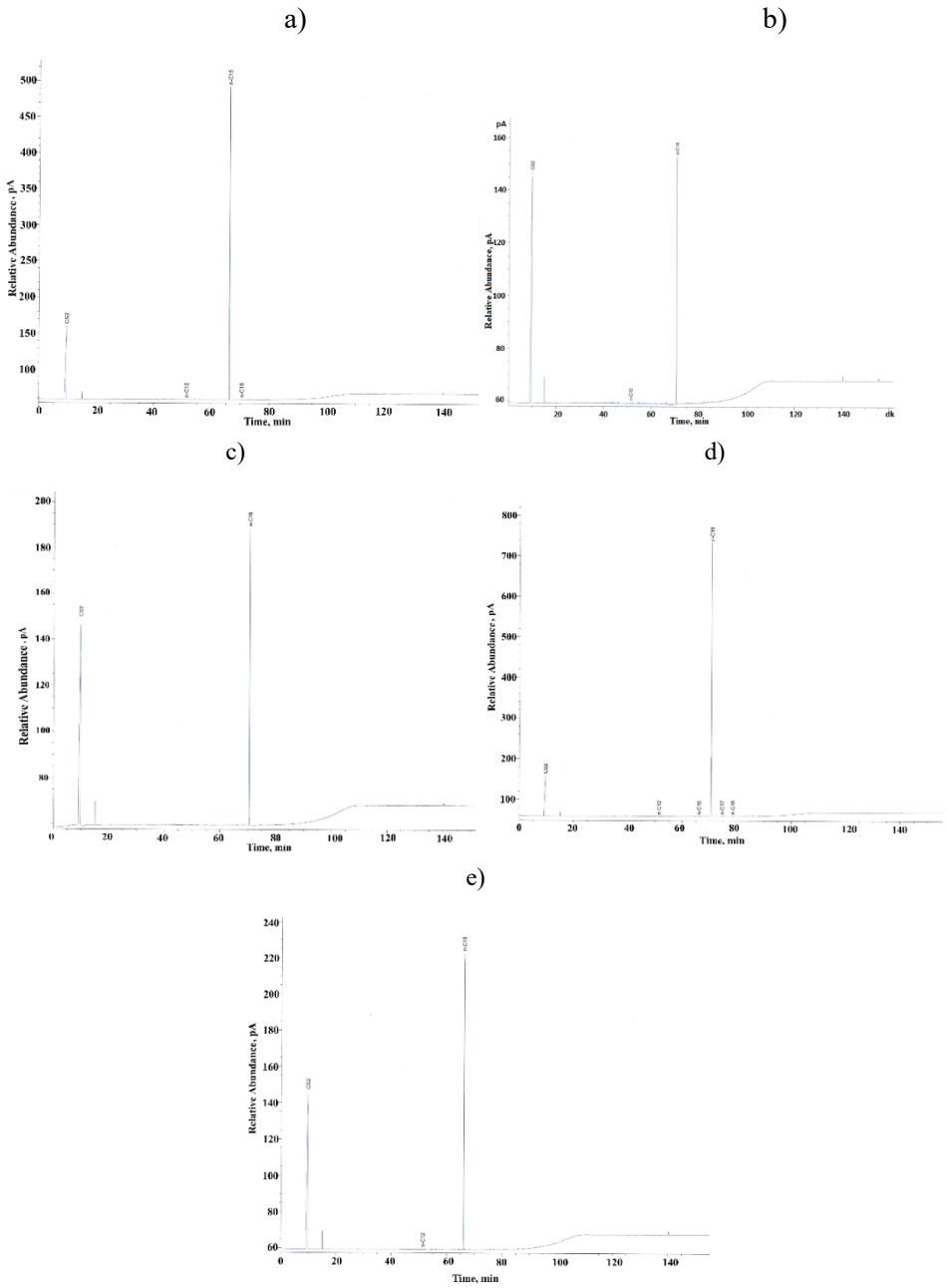

Figure S-4. a) Abiotic control of hexadecane b) Degradation of hexadecane by strain D11 c) Degradation of hexadecane by strain E1 d) Abiotic control of pentadecane e) Degradation of pentadecane by strain E2.

Journal of the Serbian Chemical Society
JSCS-info@shd.org.rs • www.shd.org.rs/JSCS
J. Serb. Chem. Soc. *88* (3) 335–348 (2024)
JSCS–5724
Original scientific paper
Published 24 March 2024

Exploring the properties of uranyl nicotinate: Synthesis, characterisation and thermal analysis

MILEICKSON APARECIDO DE ASSIS PIRES, CLAUDIO TEODORO DE CARVALHO and TIAGO ANDRÉ DENCK COLMAN*

Faculty of Exact Sciences and Technology – Federal University of Grande Dourados – UFGD, Dourados, Mato Grosso do Sul, Brazil

(Received 17 August, revised 1 September, accepted 21 September 2023)

Abstract: This study reports the successful synthesis and characterization of a uranyl nicotinate compound, $UO_2(C_6H_4NO_2)_2 \cdot 0.25H_2O$. The compound was synthesized using a metal 1:2 ligand ratio and water as the solvent. The average yield of the compound was 67 %. Thermogravimetric analysis revealed multiple stages of mass loss, including dehydration, nitrogen decomposition and UO_2^{2+} reduction. Fourier-transform infrared spectroscopy confirmed the coordination of the carboxylate group in the compound. Field emission gun scanning electron microscope analysis showed the particles with a regular oval shape. Energy-dispersive X-ray spectroscopy provided semi-quantitative data on the elemental composition of the compound. The major elements identified were uranium, carbon, oxygen and nitrogen. These results contribute to understanding the compound's synthesis, thermal behaviour, molecular composition, particle morphology and elemental composition. Further research can build upon these findings to explore potential applications and develop new compounds with tailored properties.

Keywords: coordination chemistry; actinides; thermoanalytical characterization.

INTRODUCTION

Nicotinic acid derivatives have been extensively studied in coordination chemistry due to their wide spectrum of coordinating modes. These derivatives, such as *N,N*-diethylnicotinamide (DENA), have shown potential as respiratory stimulants. Transition metal complexes with nicotinic acid derivatives and other biochemical-relevant molecules have displayed interesting physical and chemical properties, making them promising candidates for the applications in biological systems.[1]

* Corresponding author. E-mail: tiagocolman@ufgd.edu.br
https://doi.org/10.2298/JSC230817071A

Metal coordination chemistry plays a crucial role in the design and synthesis of novel compounds with desired properties.[2] Crystallography studies have provided valuable insights into the structures of metal complexes. The literature reports studies on the structure of similar compounds Sertçelik *et al.* and Hökelek *et al*.[3–6] Sertçelik *et al.* investigated a manganese complex with monodentate ligands, revealing the intramolecular and the intermolecular hydrogen bonds and π–π interactions.[4] In a related work, a copper complex displayed various hydrogen bonds and C–H···π interactions, adding to our understanding of transition metal complexes.[3] Hökelek *et al.* examined a cobalt complex, emphasizing hydrogen bonds and π–π contacts. They highlighted the significance of nicotinamide in transition metal complexes.[5] Sertçelik and collaborators also describe the structure of the polymeric compound $[Pb(C_{12}H_6N_2O_4)]_n$, the Pb(II) cation is positioned on a mirror plane. It forms *N,N′*-chelation with a 2-2′-bipyridine-5,5′--dicarboxylate (bpdc) anion and coordinates with six oxygen atoms from four carboxyl groups of bpdc anions.[6] Aşkın *et al.* presented a cobalt complex with some intriguing hydrogen bonds and ring motifs, discussing their potential applications in biological systems. The study underscores the relevance of benzoic acid derivatives in coordination chemistry.[7]

Actinide complexation has attracted significant attention due to the unique properties of actinide ions and their potential applications in various fields.[8] The coordination properties of actinide ions, such as uranyl, have been extensively studied.[9] Understanding the coordination environment of actinide complexes is essential for the development of new synthetic methodologies and designing ligands with improved coordination properties.[10]

Synthetic methodologies for the preparation of novel compounds have been the subject of intense research.[11] Microwave-assisted synthesis has emerged as a powerful tool for the rapid and efficient synthesis of various compounds, including metal complexes. This technique offers advantages such as shorter reaction times, higher yields, and improved selectivity.[2] Using the microwave-assisted synthesis, researchers have successfully prepared metal complexes with ligands such as 2-hydroxy-6-methylnicotinic acid.[2]

Ligand design is a critical aspect of coordination chemistry, as ligands play a crucial role in determining the coordination properties of metal complexes. The choice of the right ligand is essential for achieving the desired properties in metal complexes.[12] Distinct types of ligands, such as carbene ligands, imidazole derivatives and phosphine ligands, have been extensively studied for their coordination properties and applications in metal complexes.[12–14]

The coordination properties of metal complexes are influenced by factors such as ligand structure, metal centre, and coordination environment. Understanding the coordination properties of metal complexes is crucial for tailoring their properties for specific applications.[15] Metal–organic frameworks (MOFs)

are an example of coordination polymers that have attracted significant attention due to their unique structures and properties.[16] These frameworks are constructed from metal ions coordinated with organic ligands, and their properties can be fine-tuned by selecting the appropriate structural components.[15]

Research has delved into three-dimensional networks of uranium–carboxylate through covalent and hydrogen bonding. The combination of these bonds is crucial for stability.[17] Organic–inorganic frameworks with uranium and pyridine carboxylate ligands have also been studied, revealing the formation of three-dimensional structures and cation–cation interactions.[18] An organic–inorganic hybrid polymer containing uranyl, nicotinate and molybdate exhibited fluorescent properties. Uranyl, nicotinate and molybdate bonds form the structural basis.[19] Coordination of the uranyl ion with the oxidized calixpyrrole ligand demonstrated the stabilization of the U(VI) oxidation state, with the potential in catalysis and energy storage.[20] The studies by Arnold *et al.* and Kumar *et al.* are related in their investigation of uranyl dication and its reactivity, focused on the reduction and selective oxo group silylation of the uranyl dication. They demonstrated the disruption of the UO_2 bonding by manipulating the uranyl oxo within the molecular cleft, leading to the activation of the exo oxo group towards reductive silylation.[21] They also studied the uranyl dication and its reactivity, specifically in the context of heterobimetallic complexes. They reported the divergent synthesis of heterobimetallic complexes with the uranyl dication and redox-inactive metal cations, which allowed the modulation of the reduction potential of the uranyl ion.[22]

These studies have deepened the understanding of uranium–carboxylate three-dimensional networks and uranium-containing frameworks, highlighting their properties and potential applications. In this article, we will explore the coordination chemistry of nicotinic acid derivatives, the complexation of actinide ions, synthetic methodologies for compounds, ligand design and the coordination properties of metal complexes. In contrast to the existing literature, this study employs a straightforward synthesis route that eliminates the need for extended reaction times or hydrothermal reactors, for instance. Additionally, it extensively investigates the compound's characterisation, particularly focusing on thermoanalytical and microscopic methods. The understanding of these topics is crucial for the development of new synthetic methodologies and the design of novel compounds with tailored properties.

EXPERIMENTAL

Materials

The reagents used for the synthesis of coordination compounds were nicotinic acid (Sigma–Aldrich, purity >99 %), sodium hydroxide (Sigma–Aldrich, purity >99%), and ultrapure water.

Synthesis

The uranyl compound with nicotinic acid (HL) was synthesised with adjustments to the existing methodology in the literature.[23-28] The reaction is a solution of the ligands (diprotonated species derived from the acid) with the solutions prepared from uranyl nitrate.

The acid (2.5 mmol) was dissolved in 30 mL of ultrapure water and slowly neutralised with the drops of NaOH to achieve stoichiometric proportions, as reported in the literature, thereby generating the ligands. The metal solution was prepared by dissolving 1.25 mmol of the metal in 20 mL ultrapure water, maintaining a 1:2 ratio (metal:ligand). The pH of the solutions was adjusted to approximately 5 using a 0.010 mol L^{-1} NaOH solution.

The metal and ligand solutions were heated to 90 °C and slowly mixed dropwise. After the complete mixing, the solution was kept under agitation (100 rpm) and heating (90 °C) for 60 min. Subsequently, the solution was allowed to rest in an open container for evaporation and compound formation. Upon drying, the formed compound was washed with 100 mL of ultrapure water to remove impurities, byproducts, and/or unreacted excess reagents.

Thermal analysis – Simultaneous thermogravimetry and differential scanning calorimetry (TG-DSC)

The TG-DSC curves were obtained using a NETZSCH thermogravimetric analyser, STA 449 F3. It consists of a vertical mass comparator with a capacity of 70.00 µL, a silicon carbide furnace capable of operating in the temperature range of 30 to 1600 °C, and a thermocouple system controlled by Proteus® software. The thermocouples for the sample and reference are made of Pt/Pt–Rh 13 mass %, and the balance sensitivity is 0.2 µg. The system was calibrated according to the manufacturer's specifications. Masses close to 5 mg were used to analyse the samples, and an α-alumina (α-Al_2O_3) sample holder was employed. The purge gas flow (air) was set at 50 mL min^{-1}, with a heating rate of 10 °C min^{-1} and a temperature range of 30–1000 °C.[28-31]

Mid-infrared absorption spectroscopy with Fourier transform (FT-IR)

The infrared spectra were obtained using a Fourier transform infrared spectrophotometer (FT-IR), Nicolet iS10 FT-IR model. The instrument has a resolution of 4 cm^{-1} and can scan the region between 4000–600 cm^{-1} using an attenuated total reflectance (ATR) accessory with a germanium (Ge) crystal.[23,25-29,32]

High-resolution field emission scanning electron microscopy (FEG-SEM) with energy-dispersive X-ray spectroscopy (EDS)

The perimeter and surface area of the formed particles were observed by a MIRA 3 field emission scanning electron microscope (FEG-SEM, Tescan, Czech Republic) with an electron beam current of 15 kV at the field emission gun, generated by a tungsten filament lamp. The particles were previously arranged on a carbon tape and metalised with a 20 mA gold plasma for 150 s to enhance electron passage.[33,34] The analysis of the obtained results was performed with the assistance of ImageJ software.[35]

RESULTS AND DISCUSSION

Synthesis

To observe the distinct characteristics and the formations of compounds derived from metals with similar properties and ligands, the same synthesis pattern was used for all repetitions, with proportions (metal 1:2 ligand) and the use of water as the solvent and reaction medium. The solubility of the metal and the

residues generated at the end of the experiment were observed as relevant in this context.

The synthesis of uranyl coordination compounds was conducted using the corresponding nitrate. The precipitate was washed with distilled water and separated by decantation until the complete elimination of nitrate ions (qualitative test with diphenylamine/H_2SO_4 solution for nitrates).

The pH was maintained at 5 using NaOH throughout the synthesis process, and the temperature was kept around 80 °C for better precipitation. Yang and coworkers reported in their studies that the equilibrium constant for this complex is favourable in solutions with low pH and low L:M ratio (1:1 UO_2L^+), while for the proportions of 1:2 (UO_2L_2), there is a greater affinity for the solutions with higher pH and higher L:M ratio.[36] At the end of ligand addition, the addition of NaOH was also completed, and the pH of the solution with the precipitate stabilised between 2.5 and 3 for all repetitions, according to the observed chemical reaction scheme:

$$2NaC_6H_4NO_2 \xrightarrow[\text{pH 5/80 °C}]{H_2O} \underbrace{UO_2(C_6H_4NO_2)_2 \cdot 0.25H_2O}_{67\ \%} + 2Na^+ + 2NO_3^-$$

The syntheses of coordination compounds with nicotinate and UO_2^{2+} were successfully conducted, producing a significant precipitate for the planned analyses. The characteristic yellow coloration of uranyl compounds was observed (Fig. 1), with an average yield of 67 %.

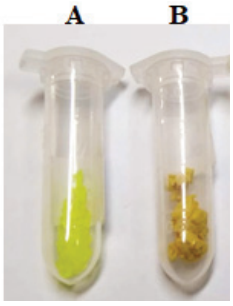

Fig. 1. Comparison of coloration between hexahydrated uranyl nitrate (A) and synthesized uranium nicotinate compound (B).

Thermal characterization: Calculation of molecular formula and theoretical mass loss

Fig. 2 presents the TG-DSC curves of the synthesised compound. A first mass loss is observed between 30–200 °C, accompanied by the endothermic peaks, which are attributed to the dehydration of the compound. This mass loss corresponds to a loss of $0.25H_2O$, which is adsorbed in the complex. The mass loss observed from the beginning of the TG analysis indicates that the water present in the compound is weakly bound.

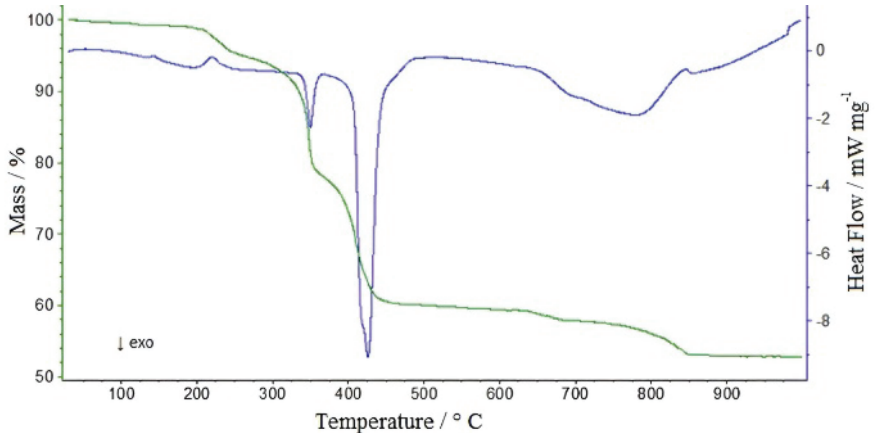

Fig. 2. TG-DSC Curves of $UO_2(C_6H_4NO_2)_2 \cdot 0.25H_2O$, mass 5.2548 mg.

The following calculations were performed to determine the molecular formula and the amount of water present in the compound, about the corresponding theoretical values: UO_2= 270.03 g mol^{-1}; $C_6H_4NO_2$ = 122.11 g mol^{-1}; initial mass = 5.2548 mg; anhydrous mass = 5.1896 mg; experimental residue (TG) = 52.83 %:

$$UO_2(C_6H_4NO_2)_2 \cdot nH_2O \rightarrow UO_2(C_6H_4NO_2)_2 + nH_2O\uparrow:$$
$$514.23:18.02n = 5.1896:0.0652$$
$$n \cong 0.25$$

These calculations were based on the initial and final masses of the compound, allowing the determination of the proportion of each element and the amount of water present. The experimental residue obtained in the TG analysis was 52.83 %. These pieces of information provide a more precise understanding of the composition and the thermochemical characteristics of the synthesised compound, contributing to its characterisation and the understanding of thermal properties. It is important to emphasize that these calculations are complementary to the experimental analyses and help confirm the molecular formula and the presence of water in the compound.

In the second stage of mass loss, the decomposition of nitrogen present in nicotinate is suggested. Based on similar compounds reported in the literature,[26–28] the release of NH_3 is possible to happen at this stage. The stoichiometric calculations support this hypothesis, as the calculated 6.52 % loss closely matches the experimental loss of 5.89 %. These calculations are based on the anhydrous mass obtained in the first stage of the experiment.

Mass: $UO_2(UO_2(C_6H_4NO_2)_2$ = 507,85 g mol^{-1}; NH_3 = 17 g mol^{-1}

$$514.23:2.17 = 5.1896:X$$
$$X = 0{,}3431 \text{ mg}$$

$$\Delta m = 100 \times 0.3475/5.2548 = 6.52\ \%$$

From the third stage to the fifth stage of mass loss, the oxidation of the remaining organic matter and the release of gaseous products during the thermal decomposition are observed.[26,27] Between the fourth and fifth stages of compound decomposition, the formation of a carbonized residue and a carbonate derivative takes place. The compounds were heated until reaching the temperature of the formation of this intermediate, as indicated by the corresponding TG--DSC curves. The test performed with a diluted hydrochloric acid solution, followed by heating of the solution, revealed the presence of the carbonized residue (black solid) and the carbonate derivative, observed through the release of bubbles attributed to the formation of CO_2. This composition stage is considered slow and corresponds to the fifth stage. The last mass loss occurs around 920 °C, and this stage can be attributed to the reduction of UO_2^{2+}, from the oxidation state of 6+ to the formation of UO_2, with an oxidation state of 4+, as the final residue (calculated as 52.06 %, experimentally observed as 52.83 %).

$$UO_2(C_6H_4NO_2)_2 \cdot 0.25H_2O \rightarrow UO_2 + 0.25\ H_2O\uparrow + 2C_6H_4NO_2\uparrow$$

$$518.74:270.03 = 100:X$$

$$X = 52.06\ \%$$

The slightly exothermic enthalpy after the dehydration of uranium nicotinate can be explained by the possible chelation involving the amino nitrogen. This is because the amino nitrogen is less hydrated compared to the carboxylate group, requiring less energy for nitrogen dehydration.[28]

The anhydrous compound remained stable up to 200 °C. The thermal decomposition of the anhydrous compound occurred in five consecutive stages, from the second to the fourth stage, observed at all heating rates, with peaks respectively at 210–220 °C, 340–350 °C and 420–430 °C. For the fifth and sixth stages, higher heating rates are more suitable for observing the mass loss.

Infrared spectroscopy

Fig. 3 presents the Fourier-transform infrared (FT-IR) spectrum in the mid--infrared region of the synthesized complex.

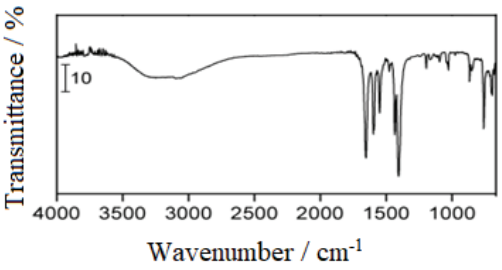

Fig. 3. FT-IR Spectrum of: $UO_2(C_6H_4NO_2)_2 \cdot 0.25H_2O$.

The carboxylate displays two bands: an intense band corresponding to the asymmetric stretching (nas) is observed between 1650 and 1550 cm^{-1}, and a weaker band related to the symmetric stretching (n_s) is observed around 1400 cm^{-1}.[37]

In the case of sodium nicotinate, $Na(C_6H_4NO_2)$, the medium-intensity band at 1566 cm^{-1} and the strong band at 1402 cm^{-1} are attributed to the asymmetric and symmetric frequencies of the carboxylate group, as described in the literature.[27,28]

The analysis of the frequencies of the bands $n_{as}(COO^-)$ at 1543 cm^{-1} and $n_s(COO^-)$ at 1428 cm^{-1} present in the spectrum of the synthesised compound suggests that coordination occurs through the carboxylate group.[27,28,38,39] The calculated values of Δn ($n_{as}(COO^-) - n_s(COO^-)$) for the synthesized compounds are lower than those of the sodium salt (sodium salt Δn = 166 cm^{-1}, the synthesized compound Δn = 115 cm^{-1}), indicating that the coordination of the carboxylate group occurs through a bridging and/or chelating structure. The characteristic bands of the U=O stretch are observed at 930 and 1018 cm^{-1} in the synthesized coordination compound with the significant suppression in its intensity and displacement to lower wavelengths, when compared with uranyl nitrate hexahydrate, which presents these bands at 940 and 1025 cm^{-1} corroborating previous observations in the literature.[40]

Field emission gun scanning electron microscope (FEG-SEM)

Fig. 4 depicts the micrograph of the synthesized compound, captured using a field emission gun scanning electron microscope (FEG-SEM), with a magnification of 55,000 times.

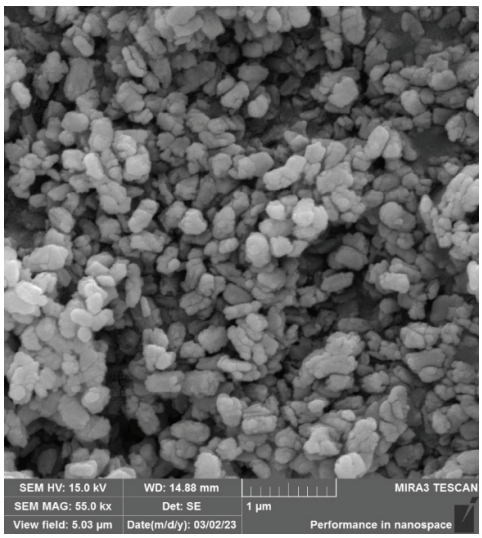

Fig 4. Field emission gun scanning microscopy image of $UO_2(C_6H_4NO_2)_2 \cdot 0.25H_2O$ samples at a magnification of 55,000×.

The analysis of the micrograph reveals that the particles formed exhibit a remarkable regularity in their size and possess an oval shape.

To quantitatively characterize the particles, the histograms illustrating the distribution of the particle perimeter and surface area observed in Fig. 5. The analysis of the data reveals an average particle perimeter of 830 nm and an average surface area of 42.243 nm^2. The obtained data conform to the Gaussian distribution, which provides a statistical description of the particle size distribution based on the perimeter and surface area measurements.

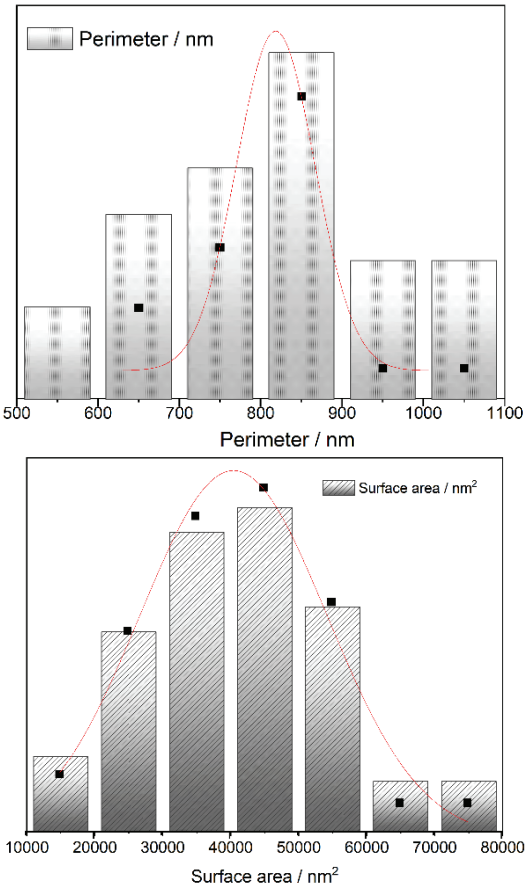

Fig. 5. Histograms and Gaussian distribution curves for the surface area and perimeter of the synthesized particles.

The Gaussian distribution equation for the particle perimeter and surface area can be described as follows:

$$f(x) = \frac{1}{\sigma\sqrt{2\pi}} \exp\left(-\frac{1}{2}\left(\frac{x-y}{\sigma}\right)^2\right) \quad (1)$$

The data obtained from the analysis of the images of the synthesised compound in the ImageJ software were subjected to the following equation: $y = y_0 + (A/(w\times\text{sqrt}(p/2)))\times\exp(-2((x-xc)/w)^2)$. This equation was used to determine the density through the Gaussian distribution of the synthesised particles. The data used to determine the Gaussian distribution are shown in Table I.

TABLE I. Data for Gaussian distribution of the particle perimeter and surface area

Parameter	Surface area	Perimeter
y_0	0.7872±1.50616	5.9202±1.1932
xc	40592.76361±1091.42289	818.37458±36.67738
w	27480.11962±4492.42048	96.53167±98.2148
A	440661.65893±108329.07045	1358.94276±428.49344
Reduced chi-sqare	1.24207	3.97615
R-square (*COD*)	0.97177	0.8965
Adj. *R*-square	0.94354	0.74125

These Gaussian distribution equations provide a mathematical representation of the particle size characteristics observed in the synthesised compound, facilitating a comprehensive understanding of the distribution and the variability of particle sizes within the sample.

The results obtained through EDS analysis reveal a uniform distribution of detected elements in the sample in significant quantities, as evidenced by the elemental distribution map presented in Fig. 6.

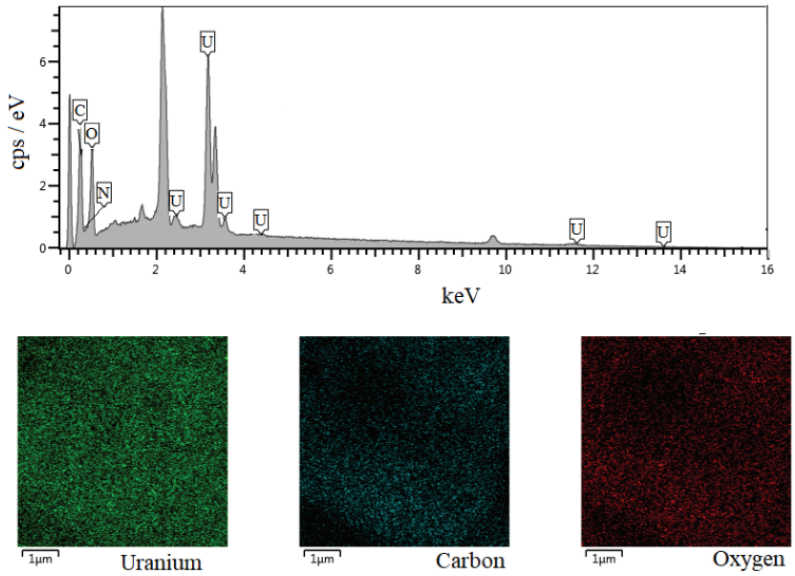

Fig. 6. Dispersive X-ray spectrum and elemental mapping of $UO_2(C_6H_4NO_2)_2\cdot 0.25H_2O$ sample.

The EDS technique enabled the semi-quantitative determination of the composition of the synthesised compound. Uranium was identified as the most predominant element, representing 46.12 % of the mass, followed by carbon at 27.02 %, oxygen at 21.77 %, and nitrogen at 5.09 %. It is important to note that small variations in the percentage values are acceptable, as EDS is unable to quantify hydrogen, which, according to theoretical calculations performed for the synthesised compound, accounts for approximately 2 % of the sample. These results confirm the presence of the expected elements and provide a solid foundation for the understanding of the chemical composition of the synthesised compound.

CONCLUSION

In conclusion, this study successfully synthesised and characterised a uranyl nicotinate compound, $UO_2(C_6H_4NO_2)_2 \cdot 0.25H_2O$. The synthesis process followed a consistent pattern using a metal 1:2 ligand ratio with water as the solvent and reaction medium. The yield of the compound averaged 67 %, indicating the efficient synthesis.

Fourier-transform infrared (FT-IR) spectroscopy confirmed the presence of characteristic bands corresponding to the asymmetric and symmetric stretching frequencies of the carboxylate group. The calculated values of Δn ($n_{as}(COO^-)$ – – $n_s(COO^-)$) indicated a lower value compared to the sodium salt reference, suggesting a bridging and/or chelating coordination structure for the carboxylate group in the synthesised compound.

The field emission gun scanning electron microscope (FEG-SEM) analysis revealed the morphology of the synthesised particles, displaying a regular oval shape. The quantitative analysis of the particle size distribution showed an average particle perimeter of 830 nm and an average surface area of 42,243 nm^2, indicating a relatively uniform particle size within the sample.

The energy-dispersive X-ray spectroscopy (EDS) analysis provided semi--quantitative data on the elemental composition of the synthesised compound. Uranium was identified as the most predominant element, followed by carbon, oxygen, and nitrogen. Although hydrogen could not be quantified by EDS, the theoretical calculations estimated its presence at approximately 2 % in the compound.

These findings contribute to the comprehensive understanding of the synthesised uranyl nicotinate compound, including its synthesis yield, thermal behaviour, molecular composition, particle morphology, and elemental composition. The insights gained from this study can serve as a basis for further research in the field of inorganic chemistry, enabling the exploration of potential applications and the development of novel compounds with tailored properties.

Acknowledgments. This work is financially supported by the National Council for Scientific and Technological Development of Brazil (CNPq Process n°: 402435/2022-2) and by the

Financing Agency for Studies and Projects of Brazil (FINEP contract 04.13.0448.00/2013); the authors would like to thank the Group for Thermoanalytical Studies on Food, Drugs and Chemicals (dgp.cnpq.br/dgp/espelhogrupo/8922309087083951).

ИЗВОД

ИСПИТИВАЊЕ СВОЈСТАВА УРАНИЛ-НИКОТИНАТА: СИНТЕЗА, КАРАКТЕРИЗАЦИЈА И ТЕРМАЛНА АНАЛИЗА

MILEICKSON APARECIDO DE ASSIS PIRES, CLAUDIO TEODORO DE CARVALHO и TIAGO ANDRÉ DENCK COLMAN

Faculty of Exact Sciences and Technology – Federal University of Grande Dourados – UFGD, Dourados, Mato Grosso do Sul, Brazil

У овом раду описана је синтеза и карактеризација уранил-никотината, $UO_2(C_6H_4NO_2)_2{\cdot}0{,}25H_2O$. У синтези овог једињења метал и лиганд су реаговани у 1:2 молском односу у води као растварачу. Једињење је добијено у приносу од 67 %. Термогравиметријска анализа је показала да испитивано једињење постепено губи масу, што укључује дехидратацију, разлагање азота и редукцију UO_2^{2+}. На основу инфра-црвене спектроскопије потврђено је да је карбоксилна група у овом једињењу координована. Методом скенирајуће електронске микроскопије нађено је да су испитиване честице правилног овалног облика. Применом енергетски дисперзивне рендгенске спектроскопије нађено је да једињење садржи уранијум, угљеник, кисеоник и азот. Добијени резултати су од значаја за синтезу, термичка својства, састав, молекулску структуру и облик честица испитиваног једињења. Поред тога, приказани резултати могу бити од значаја за потенцијалну примену овог типа једињења.

(Примљено 17. августа, ревидирано 1. септембра, прихваћено 21. септембра 2023)

REFERENCES

1. G. Ş. Aşkın, H. Necefoğlu, G. Yılmaz Nayir, R. Çatak Çelik, T. Hökelek, *Acta Crystallogr., E* **71** (2015) 561 (https://doi.org/10.1107/S2056989015008270)
2. S. K. Verma, N. Bhojak, *Int. J. Chem. Phys. Sci.* **7** (2018) 67 (https://doi.org/10.30731/ijcps.7.2.2018.67-74)
3. M. Sertçelik, N. Delibas, H. Necefoğlu, T. Hökelek, *Acta Crystallogr., E* (2012) (https://doi.org/10.1107/s1600536812028814)
4. M. Sertçelik, B. Tercan, E. Şahin, H. Necefoğlu, T. Hökelek, *Acta Crystallogr., E* (2009) (https://doi.org/10.1107/s1600536809006047)
5. T. Hökelek, F. Yılmaz, B. Tercan, M. Sertçelik, H. Necefoğlu, *Acta Crystallogr., E* (2009) (https://doi.org/10.1107/s1600536809033200)
6. M. Sertçelik, N. Çaylak Delibaş, S. Çevik, H. Necefoğlu, T. Hökelek, *Acta Crystallogr., E* **68** (2012) m1196 (https://doi.org/10.1107/S1600536812035647)
7. G. Ş. Aşkın, H. Necefoğlu, S. Özkaya, R. Çatak Çelik, T. Hökelek, *Acta Crystallogr., E* **72** (2016) 888 (https://doi.org/10.1107/S2056989016008689)
8. G. Ş. Aşkın, H. Necefoğlu, A. M. Tonbul, N. Dilek, T. Hökelek, *Acta Crystallogr., E* **71** (2015) 479 (https://doi.org/10.1107/S2056989015006490)
9. V. A. Cocalia, M. P. Jensen, J. D. Holbrey, S. K. Spear, D. C. Stepinski, R. D. Rogers, *Dalton Transactions* (2005) 1966 (https://doi.org/10.1039/b502016f)

10. M. A. Degli-Esposti, P. J. Smolak, H. Walczak, J. Waugh, C.-P. Huang, R. F. DuBose, R. G. Goodwin, C. A. Smith, *J. Exp. Med.* **186** (1997) 1165 (https://doi.org/10.1084/jem.186.7.1165)
11. A. S. Ojo, S. Mamman, P. O. Ukoha, *J. Appl. Phys. Sci. Int.* (2022) 1 (https://doi.org/10.56557/japsi/2022/v14i17456)
12. D. Munz, *Organometallics* **37** (2018) 275 (https://doi.org/10.1021/acs.organomet.7b00720)
13. S.-S. Chen, *CrystEngComm* **18** (2016) 6543 (https://doi.org/10.1039/C6CE01258B)
14. H.-Z. Duan, C. Hu, Y.-L. Li, S.-H. Wang, Y. Xia, X. Liu, J. Wang, Y.-X. Chen, *J. Am. Chem. Soc.* **144** (2022) 22831 (https://doi.org/10.1021/jacs.2c09683)
15. K. Otake, H. Kitagawa, *Small* **17** (2021) 2006189 (https://doi.org/10.1002/smll.202006189)
16. P.-F. Yao, Y. Tao, H.-Y. Li, X.-H. Qin, D.-W. Shi, F.-P. Huang, Q. Yu, X.-X. Qin, H.-D. Bian, *Cryst. Growth Des.* **15** (2015) 4394 (https://doi.org/10.1021/acs.cgd.5b00724)
17. S. Dalai, M. Bera, A. Rana, D. S. Chowdhuri, E. Zangrando, *Inorg. Chim. Acta* **363** (2010) 3407 (https://doi.org/10.1016/j.ica.2010.06.043)
18. P. Thuéry, *Inorg. Chem. Commun.* **12** (2009) 800 (https://doi.org/10.1016/j.inoche.2009.06.021)
19. X. Kong, Y. Ren, L. Long, R. Huang, L. Zheng, *Inorg. Chem. Commun.* **10** (2007) 894 (https://doi.org/10.1016/j.inoche.2007.03.023)
20. G. T. Kent, J. Murillo, G. Wu, S. Fortier, T. W. Hayton, *Inorg. Chem.* **59** (2020) 8629 (https://doi.org/10.1021/acs.inorgchem.0c01224)
21. P. L. Arnold, D. Patel, C. Wilson, J. B. Love, *Nature* (2008) (https://doi.org/10.1038/nature06467)
22. A. Kumar, D. Lionetti, V. W. Day, J. D. Blakemore, *J. Am. Chem. Soc.* (2020) (https://doi.org/10.1021/jacs.9b11903)
23. J. A. Teixeira, W. D. G. Nunes, T. A. D. Colman, A. L. C. S. do Nascimento, F. J. Caires, F. X. Campos, D. A. Gálico, M. Ionashiro, *Thermochim. Acta* **624** (2016) 59 (https://doi.org/10.1016/j.tca.2015.11.023)
24. F. O. Farias, A. C. Jasko, T. A. D. Colman, L. A. Pinheiro, E. Schnitzler, A. C. Barana, I. M. Demiate, *Braz. Arch. Biol. Technol.* **57** (2014) 821 (https://doi.org/10.1590/S1516-8913201402506)
25. F. X. Campos, A. L. C. S. Nascimento, T. A. D. Colman, D. A. Gálico, A. C. S. Carvalho, F. J. Caires, A. B. Siqueira, M. Ionashiro, *Thermochim. Acta* **651** (2017) 73 (https://doi.org/10.1016/j.tca.2017.03.002)
26. T. A. D. Colman, D. J. C. Gomes, F. J. Caires, O. T. Filho, R. de C. da Silva, M. Ionashiro, *J. Anal. Appl. Pyrolysis* **111** (2015) 132 (https://doi.org/10.1016/j.jaap.2014.11.021)
27. A. L. C. S. do Nascimento, F. J. Caires, T. A. D. Colman, D. J. C. Gomes, G. Bannach, M. Ionashiro, *Thermochim. Acta* **604** (2015) 7 (https://doi.org/10.1016/j.tca.2014.12.022)
28. T. A. D. Colman, D. J. C. Gomes, F. J. Caires, O. T. Filho, R. de C. da Silva, M. Ionashiro, *Thermochim. Acta* **591** (2014) 111 (https://doi.org/10.1016/j.tca.2014.06.013)
29. A. S. de Souza, B. Ekawa, C. T. de Carvalho, J. A. Teixeira, M. Ionashiro, T. A. D. Colman, *Thermochim. Acta* **683** (2020) 178443 (https://doi.org/10.1016/j.tca.2019.178443)

30. K. V. Tenório, J. A. Teixeira, L. M. de Campos Pinto, F. J. Caires, O. Treu-Filho, F. A. dos Santos, T. A. Denck Colman, A. Cuin, C. T. de Carvalho, *J. Rare Earths* **36** (2018) 1090 (https://doi.org/10.1016/j.jre.2018.03.019)
31. M. D. Colman, S. R. da S. Lazzarotto, M. Lazzarotto, F. A. Hansel, T. A. D. Colman, E. Schnitzler, *J. Anal. Appl. Pyrolysis* **119** (2016) 157 (https://doi.org/10.1016/j.jaap.2016.03.005)
32. J. A. Teixeira, W. D. G. Nunes, A. L. C. S. do Nascimento, T. A. D. Colman, F. J. Caires, D. A. Gálico, M. Ionashiro, *J. Anal. Appl. Pyrolysis* **121** (2016) 267 (https://doi.org/10.1016/j.jaap.2016.08.0060)
33. C. D. Bet, C. S. de Oliveira, T. A. D. Colman, R. Z. B. Bisinella, C. Beninca, L. G. Lacerda, A. P. Ramos, E. Schnitzler, *J. Therm. Anal. Calorim.* **138** (2019) 2733 (https://doi.org/10.1007/s10973-019-08374-7)
34. C. D. Bet, C. S. de Oliveira, T. A. D. Colman, M. T. Marinho, L. G. Lacerda, A. P. Ramos, E. Schnitzler, *Food Chem.* **264** (2018) 435 (https://doi.org/10.1016/j.foodchem.2018.05.021)
35. C. A. Schneider, W. S. Rasband, K. W. Eliceiri, *Nat. Methods* **9** (2012) 671 (https://doi.org/10.1038/nmeth.2089)
36. Y. Yang, J. Liu, Y. Sun, S. Hu, Y. Gao, Z. Zhang, S. Luo, L. Rao, *J. Chem. Thermodyn.* **113** (2017) 350 (https://doi.org/10.1016/j.jct.2017.07.002)
37. J. A. Teixeira, W. D. G. Nunes, A. L. C. S. do Nascimento, T. A. D. Colman, F. J. Caires, D. A. Gálico, M. Ionashiro, *J. Anal. Appl. Pyrolysis* **121** (2016) 267 (https://doi.org/10.1016/j.jaap.2016.08.006)
38. G. Deacon, *Coord. Chem. Rev.* **33** (1980) 227 (https://doi.org/10.1016/S0010-8545(00)80455-5)
39. F. X. Campos, A. L. C. S. Nascimento, T. A. D. Colman, D. A. Gálico, O. Treu-Filho, F. J. Caires, A. B. Siqueira, M. Ionashiro, *J. Therm. Anal. Calorim.* **123** (2016) 91 (https://doi.org/10.1007/s10973-015-4956-7)
40. M. A. Abu-Dalo, N. A. F. Al-Rawashdeh, I. R. Al-Mheidat, N. S. Nassory, *IOP Conf. Ser. Mater. Sci. Eng.* **92** (2015) 012023 (https://doi.org/10.1088/1757-899X/92/1/012023).

Journal of the Serbian Chemical Society
JSCS-info@shd.org.rs • www.shd.org.rs/JSCS
J. Serb. Chem. Soc. *89* (3) 349–365 (2024)
JSCS–5725
Original scientific paper
Published 31 March 2024

The cyanide, cyanate, thiocyanate ambident anions: Structure, topological analysis of electron density and homolytic oxidative coupling regioselectivity

ALEXEI N. PANKRATOV*

Division of Analytical Chemistry and Chemical Ecology, Institute of Chemistry, N. G. Chernyshevskii National Research Saratov State University, 83 Astrakhanskaya Street, Saratov 410012, Russia

(Received 25 September, revised 7 November, accepted 23 December 2023)

Abstract: At the B3LYP/6-311++G(3df,3pd) level of theory, the spatial and electronic structure of the cyanide, cyanate and thiocyanate ambident anions has been studied. By means of the natural bond orbital (NBO) analysis and the R. F. W. Bader's quantum theory "Atoms in Molecules" (QTAIM), the electron density delocalization and topological properties in the above anions have been investigated. The distribution of electron density (NBO, QTAIM) in the XCN^- (X = O, S) anions is reflected by the scheme $[X^{\bullet\bullet\bullet}C^{\bullet\bullet\bullet}N]^-$. The relative contribution of the hypothetical structure $X=C=N^-$ to the resonance hybrid $^-X–C\equiv N \leftrightarrow X=C=N^-$ is higher in the case of X = O. The degree of the C≡N or $C^{\bullet\bullet\bullet}N$ bond triple character and bond strength changes in the following series of anions: $CN^- > SCN^- > OCN^-$. The occupancy of the lone electron pair (LP) orbital of the nitrogen atom in the above anions is close to 2, and the LP orbital is sp-hybridized. Condensed K. Fukui functions for the electrophilic attack have been evaluated. Local hardness of the donor reaction centres: N > C (CN^-), O > N (OCN^-), N > S (SCN^-). The regioselectivity of the homolytic oxidative coupling reactions of CN^-, OCN^-, SCN^- has been substantiated.

Keywords: density functional theory (DFT); B3LYP; natural bond orbital (NBO) analysis; R.F.W. Bader's quantum theory "Atoms in Molecules" (QTAIM); electron density delocalization; hybridization; K. Fukui functions; radical dimerization.

INTRODUCTION

The dual reactivity of the ambident anions, such as cyanide CN^-, cyanate OCN^-, thiocyanate (rhodanide) SCN^-,[1–8] *etc.*, as ligands in coordination compounds[1–5,8] and nucleophiles, mainly in organic chemistry,[6–8] is an important theoretical problem.

* E-mail: PankratovAN@info.sgu.ru
https://doi.org/10.2298/JSC230925101P

The ambident reactivity is often treated by means of the Hard and Soft Acids and Bases (HSAB) principle.[1–8] However, the HSAB theory displayed itself as not always appropriate.

Free cyanide, CN^-, *e.g.*, is generally alkylated at carbon. N-attack is only observable in diffusion-controlled reactions with carbenium cations. Since isonitrile $RN^+{\equiv}C^- \leftrightarrow RN{=}C$ formation in reactions with $[Ag(CN)_2]^-$ is due to the change of the nucleophile, the explanation of these regioselectivities by the HSAB principle has to be abandoned.[9]

It has been shown that the cyanate anion, OCN^-, being an ambident nucleophile, may react with electrophiles either at the oxygen terminus, to yield alkyl cyanates $ROC{\equiv}N$, or at the nitrogen centre, to yield alkyl isocyanates $RN{=}C{=}O$. Equal amounts of alkyl cyanates and alkyl isocyanates were obtained, when secondary iodoalkanes were treated with silver(I) cyanate. The formation of *tert*-butyl isocyanate $(CH_3)_3CN{=}C{=}O$, along with 2-methylpropene $(CH_3)_2C{=}CH_2$ and cyanic acid, was also considered as an indication for concomitant O- and N-attack. The study also investigated the possibility of S_N1 reactions of cyanates proceeding with charge control to give alkyl cyanates.[10]

A kinetic study of SCN^- reaction with carbenium cations using laser flash photolysis and stopped-flow methods lead to the conclusion that the selectivities of the above reactions cannot be explained by the HSAB theory.[11]

For CN^-, both C- and N-coordination, and for OCN^-, both N- and O-bonding with metal cations is known.[12–15]

In accordance with the HSAB theory,[1–8] in the ambident SCN^-, donor sulphur atom is the reaction centre of a soft base, and the nitrogen atom is the centre of a hard/soft boundary base. Cations of ammonium (azanium), NH_4^+, alkaline (except in any case caesium) and alkaline earth metals, magnesium, aluminium are hard acids (Cs^+ is a soft acid), so they "gravitate" to the nitrogen atom of the thiocyanate. At the same time, thiocyanates of at least alkaline and alkaline earth elements have ionic crystal structures, and the ionic bond is non-directional, and therefore we can talk not about coordination in the literal sense, but about the mutual spatial orientation of metal or NH_4^+ and SCN^-, favourable potential or actual association of the metal or ammonium cation with the nitrogen atom of the thiocyanate anion.

The preferential orientation of the thiocyanate nitrogen atom in the direction of the lithium cation in solution finds a quantum chemical confirmation. The impact of the association of lithium cation with SCN^- n acetonitrile $CH_3C{\equiv}N$ on the vibrational spectrum has been studied in the B3LYP/6-31+G(d,p) approximation. The best agreement between experimental and calculated ionic association data was achieved taking into account the nonspecific solvation, oversolvation and solvability of ionic complexes within the framework of the polarizable continuum model (PCM) in a variant (IEF-PCM) based on the integral equation

formalism (IEF). The microstructures of the thiocyanate in a contact ion pair with lithium cation and ion-pair dimer and trimer in acetonitrile were established.[16]

The main continuum models of solvent accounting in quantum chemical computations are listed in the work.[17]

The formulae of the above mentioned thiocyanates are preferably written as NH_4NCS, LiNCS, NaNCS, KNCS, RbNCS, CsNCS, $Mg(NCS)_2$, $Ca(NCS)_2$, $Sr(NCS)_2$, $Ba(NCS)_2$, $Al(NCS)_3$.[12,15]

On the contrary, thiocyanates of copper(I), silver(I), mercury(II), lead(II) are characterized by the coordination of the metal ion to the sulphur atom: CuSCN, AgSCN, $Hg(SCN)_2$, $Pb(SCN)_2$ (Cu^+, Ag^+, Hg^{2+} – soft acids, Pb^{2+} – boundary acid).[12,15]

Soft acid Cd^{2+} behaves ambiguously. There is a $Cd(SCN)_2$ compound. However, in an aqueous solution of sodium tetrathiocyanocadmate, SCN^- is coordinated *via* sulphur ($Na_2[Cd(SCN)_4]$), and in methanol through nitrogen ($Na_2[Cd(NCS)_4]$). Coordination *via* nitrogen in the case of cadmium thiocyanates is also observed in the melt of KNCS.[12,15]

The lead(II) ion, which is borderline in hardness/softness, is coordinated by the sulphur atom: $Pb(SCN)_2$.[12,15] However, for the boundary acids, manganese(II), iron(II), cobalt(II), nickel(II), copper(II) and zinc ions, there is coordination at the nitrogen atom: $Mn(NCS)_2$, $Fe(NCS)_2$, $[Fe(NCS)_4]^{2-}$, $Co(NCS)_2$, $[Co(NCS)_4]^{2-}$, $Ni(NCS)_2$, $[Ni(NCS)_4]^{2-}$, $Cu(NCS)_2$, $[Cu(NCS)_4]^{2-}$ and $Zn(NCS)_2$.[12,15]

The soft acid Cs^+, like other alkali metal cations (hard acids), orients towards SCN^- with a preference for the nitrogen atom.[12,15]

Thus, the structure of metal thiocyanates cannot always be substantiated from the standpoint of a qualitative version of the HSAB concept. This is largely due to the boundary nature of the donor nitrogen atom as the reaction centre.

Iron(III), cobalt(III) and nickel(III) ions are hard acids and add SCN^- with the participation of its nitrogen atom, for example $Fe(NCS)_3$, $[Fe(NCS)_6]^{3-}$.[12,15]

Such a nature of the binding of SCN^- with highly charged cations such as Al^{3+}, Fe^{3+} and in general with metal ions – hard acids, can be due to a higher negative charge on the nitrogen atom of the thiocyanate anion, since the hard––hard (and hard-boundary to a large extent) interaction in the framework of a simple version of the perturbation theory[18] is treated as charge-controlled.[8]

The HSAB principle is usually expressed *via* the charge, electronegativity, size, polarizability, oxidation ability, energies of the frontier orbitals of an atom, ion, closed or open electronic shell molecule.[1–8] All the above characteristics directly or indirectly depend upon the electron density distribution in molecule, including the electronic delocalization and topological properties. The electronic distribution is significant regardless of whether it is considered within the framework of the HSAB theory or beyond.

CN^-, OCN^- and SCN^- are capable of undergoing chemical and electrochemical homolytic oxidative coupling (dimerization) with the intermediate appearance of the $^{\bullet}CN$, $OCN^{\bullet}$ and $^{\bullet}SCN$.

In particular, CN^- dimerizes upon interaction with acidified $S_2O_8^{2-}$, with copper(II) and gold(III).

CN^- reduces Cu^{2+} to Cu^+, oxidizing to cyanogen N≡C–C≡N, and binds copper(I) into complex anions, tricyanocuprate(I) $[Cu(CN)_3]^{2-}$ and tetracyanocuprate(I) $[Cu(CN)_4]^{3-}$, for example:

$$2Cu^{2+} + 4CN^- \rightarrow 2CuCN\downarrow + N{\equiv}C{-}C{\equiv}N,$$
$$CuCN\downarrow + 2CN^- \rightleftarrows [Cu(CN)_3]^{2-},$$

or in total:

$$2Cu^{2+} + 8CN^- \rightarrow 2[Cu(CN)_3]^{2-} + N{\equiv}C{-}C{\equiv}N$$

The above chemical reactions are used to mask the copper(II) ion in the analytical determination of other ions, to change the redox potential of the Cu(II)/Cu↓ conjugate redox pair in the separate electrolytic and polarographic determination of copper and other metals, *etc.*

Similarly, the interaction of gold(III) with CN^- includes the preliminary reduction of Au(III) to Au(I) followed by the formation of the dicyanoaurate(I) anion $[Au(CN)_2]^-$:

$$Au^{3+} + 3CN^- \rightarrow AuCN\downarrow + N{\equiv}C{-}C{\equiv}N,$$
$$AuCN\downarrow + CN^- \rightleftarrows [Au(CN)_2]^-,$$

or in total:

$$Au^{3+} + 4CN^- \rightarrow [Au(CN)_2]^- + N{\equiv}C{-}C{\equiv}N$$

Hydrocyanic acid or gaseous hydrogen cyanide HC≡N is oxidized to cyanogen N≡C–C≡N under the action of O_2 or air in the presence of a silver catalyst, NO_2 in the presence of calcium glasses, Cl_2 on activated carbon or quartz, when passing dry hydrogen cyanide over MnO_2 heated to 250 °C, as well as when interacting with H_2O_2 in the presence of copper(II) and iron(III) salts, with $Na_2S_2O_8$, MnO_2, PbO_2 in the 0.05 M H_2SO_4 medium, *etc.*[1,2,12,19]

The fact of the existence of oxocyanogen $(OCN)_2$ remains controversial. The formation of a colorless compound $(OCN)_2$, which is stable only at low temperature (down to −12 °C), has been reported by the exchange reaction of silver(I) cyanate with I_2.[12] There is an assumption that oxocyanogen can be obtained by the reaction of silver(I) cyanate with Br_2, but no conclusive evidence is provided. It has been shown that O=C=N–N=C=O is obtained in this and other similar reactions.[12,19] However, data on the anodic oxidation of cyanates in $CH_3C{\equiv}N$ cast doubt on the existence of $(OCN)_2$.[12]

Thiocyanogen N≡C–S–S–C≡N is obtained by mild oxidation of metal thiocyanates with an aqueous solution of Cl_2, with Br_2, I_2, MnO_2, copper(II) salts at a temperature of about 0 °C, $Pb(CH_3COO)_4$, as well as by electrochemical oxidation of SCN^-.[1,2,12]

Previously,[20–22] it has been shown that the regioselectivity of reactions of homolytic (radical) oxidative and reductive coupling (dimerization) of organic compounds of various classes is controlled by the spin density on atoms in the reaction intermediates (electroneutral radicals, radical cations, radical anions), calculated by *ab initio*, DFT, HMDFT and semi-empirical methods of quantum chemistry. In this case, such intermediates are •CN, OCN• and •SCN.

The aim of the present work consists in quantum chemical investigation of spatial, electronic structure of the cyanide, cyanate, thiocyanate ambident anions, including study of the electron density delocalization and topological properties, comparative local hardness of the donor reaction centres, as well as substantiation of regioselectivity of the homolytic oxidative coupling reactions of CN^-, OCN^- and SCN^-.

METHODOLOGY OF THEORETICAL RESEARCH

Quantum chemical computations (within the restricted (RHF) D. R. Hartree – V. A. Fock (HF) approach[23] for the closed-shell anions CN^-, OCN^-, SCN^- and unrestricted (UHF) D. R. Hartree – V. A. Fock (HF) approach[23] for •CN, •OCN, •SCN derived from the above anions by homolytic oxidative coupling) were carried out by means of the hybrid density functional theory (DFT) method[23-26] using the Gaussian 09W package[27] without any geometrical restrictions. Within the SCF, the hybrid B3LYP functional, which combines the three-parameter exchange functional by A. D. Becke[28,29] with the Chengteh Lee – Weitao Yang – R. G. Parr (LYP) correlation functional,[30] was applied. The computations were performed using "tight" convergence criteria.[30,31] The rather wide 6-311++G(3df,3pd)[32,33] basis set was used. Diffuse functions were included in order to treat the nonbonding (unshared, lone) electron pairs (LP) and blurred character of electron cloud in the anions properly. Harmonic vibrational frequencies were computed. All equilibrium structures without the imaginary frequencies correspond to the minima points on the potential energy surfaces. Requested convergence on *RMS* density matrix amounted 1×10^{-8} within 200 cycles, on *MAX* density matrix – 1×10^{-6}, and on energy – 1×10^{-6} Hartree (a.u). The initial geometries were generated by means of HyperChem Professional 8.0.10 software[34] and optimized by the PM3 method.[35,36]

The natural bond orbital (NBO) analysis[37-40] was performed by the NBO Version 3.1 program.[41]

To describe the electronic structure of molecules, the topological analysis of electron density by means of R. F. W. Bader's quantum theory "Atoms in Molecules" (QTAIM)[42-54] at the B3LYP/6-311++G(3df,3pd) level of theory was performed by the AIMAll Version 19.10.12 software[55] to calculate the charge density (ρ_b), Laplacian of the charge density ($\nabla^2\rho_b$), local electronic energy (h_e) in the saddle (which are indicators of binding) bond critical points (3, −1) and ellipticity (ε).

RESULTS AND DISCUSSION

By means of the DFT method at the B3LYP/6-311++G(3df,3pd) level of theory with the use of the NBO and QTAIM analysis, we have computed the spatial and electronic structure of the ambident CN^-, OCN^- and SCN^-.

In CN^-, the C≡N bond length is 1.171 Å. The calculation is in agreement with the experiment: a neutron diffraction study of KCN at room temperature gives a length of 1.16 Å for the C≡N bond.[15] The natural (one of the most objective, most consistent with chemical intuition) charge on carbon and nitrogen atoms is –0.236 and –0.764, respectively. The natural order (natural K. B. Wiberg index) of the C≡N bond is 2.854.

The values of the second-order perturbation energy $E(2)$, obtained as a result of the NBO analysis for CN^-, indicate that the main directions of electron density transfer are from the LP orbital of the nitrogen atom to the antibonding (loosening) J. R. Rydberg orbital of the carbon atom ($E(2)$ = 75.7 kJ mol^{-1}), from the core level of the nitrogen atom to the same J. R. Rydberg orbital ($E(2)$ = 26.1 kJ mol^{-1}) and from the LP orbital of the carbon atom to the antibonding J. R. Rydberg orbital of the nitrogen atom ($E(2)$ = 20.6 kJ mol^{-1}).

OCN^- and SCN^- have a linear structure.

In OCN^-, bonds have the following lengths: 1.224 (C$^{\bullet\bullet\bullet}$O) and 1.187 Å (C$^{\bullet\bullet\bullet}$N); the bond angle OCN is 180.000°. X-ray diffraction analysis of NaNCO gives a length of 1.21 Å for the C$^{\bullet\bullet\bullet}$O bond and 1.13 Å for the C$^{\bullet\bullet\bullet}$N bond. In this case, the linear structure of the anion is confirmed, but the low accuracy of the values of the bond lengths,[15] which nonetheless agree with our computation, is stipulated.

The natural charge on atoms in OCN^- is: –0.776 (O), 0.600 (C), –0.823 (N). The negative charge on the O- and N-atoms is almost the same, slightly higher on the nitrogen atom. The natural orders of bonds in OCN^- are: 1.493 (C$^{\bullet\bullet\bullet}$O) and 2.444 (C$^{\bullet\bullet\bullet}$N).

According to the results of our quantum chemical computation, the bond lengths in SCN^- are: 1.661 (C$^{\bullet\bullet\bullet}$S) and 1.172 Å (C$^{\bullet\bullet\bullet}$N), the SCN bond angle is 180.000°. In accordance with the data of X-ray diffraction analysis of NaNCS, KNCS,[15] the corresponding values are 1.65, 1.17 Å and 180°. The calculation agrees well with experiment.

The natural charge on the atoms is: –0.463 (S), 0.055 (C), –0.592 (N). The nitrogen atom is somewhat more negatively charged compared to the sulphur atom, which is consistent with the regioselectivity of the interaction of metal ions – hard G. N. Lewis acids with SCN^-. The natural orders of bonds in SCN^- are: 1.403 (C$^{\bullet\bullet\bullet}$S) and 2.608 (C$^{\bullet\bullet\bullet}$N).

Based on the charge distribution in the ambident CN^- and XCN^- (X = O, S), the negative charge of which is delocalized between the X and N atoms, it is expedient to write the minus sign at the nitrogen atom when depicting these anions.

For the entire set of C≡N, C⋮⋮N, C⋮⋮O and C⋮⋮S bonds in CN^-, OCN^- and SCN^-, the following trend is observed: the longer the bond, the smaller its natural order.

OCN^- and SCN^- have a number of energetically significant donor–acceptor interactions. However, the dominant contributions are:

– in OCN^-: electron transfer from two different LP orbitals of the oxygen atom to the antibonding π-orbital of the C⋮⋮N bond (each such transition has an energy effect $E(2) = 341.8$ kJ mol^{-1}), from the LP orbital of the nitrogen atom to the antibonding J. R. Rydberg orbital of the carbon atom ($E(2) = 75.3$ kJ mol^{-1}), from the LP orbital of the nitrogen atom to the antibonding σ-orbital of the C⋮⋮O bond ($E(2) = 71.5$ kJ mol^{-1}), from the orbital of the third LP of the oxygen atom to the antibonding σ-orbital of the C⋮⋮N bond ($E(2) = 69.0$ kJ mol^{-1}) and from the orbital of the same (third) LP orbital of the oxygen atom to the same J. R. Rydberg orbital ($E(2) = 63.2$ kJ mol^{-1});

– in SCN^-: transfer of electron density from two LP orbitals of the sulphur atom to the antibonding π-orbital of the C⋮⋮N bond with the same second-order perturbation energy contribution $E(2) = 169.5$ kJ mol^{-1}, from the LP orbital of the nitrogen atom to the antibonding J. R. Rydberg orbital of the carbon atom ($E(2) = 84.1$ kJ mol^{-1}), from the orbital of the third LP of the sulphur atom to the antibonding σ-orbital of the C⋮⋮N bond ($E(2) = 81.6$ kJ mol^{-1}) and from the LP orbital of the nitrogen atom to the loosening σ-orbital of the C⋮⋮S bond ($E(2) =$ $= 59.4$ kJ mol^{-1}).

It can be seen that in the donor–acceptor redistribution of the electron density in OCN^- and SCN^-, the orbitals of nonbonding electron pairs of the oxygen and sulphur atoms take an active part as donors, *i.e.*, the possibilities absent in CN^-, are realized.

To describe the electronic structure of the anions in more detail, we have carried out a topological analysis of the electron density using the QTAIM[42–54] at the B3LYP/6-311++G(3df,3pd) level of theory.

The electron density (ρ_b) in the bond critical points (BCP), the Laplacian of the electron density ($\nabla^2\rho_b$) in the BCP, the local electronic energy (h_e), which is estimated as the density (taken with the opposite sign) of the local kinetic energy in the form of Hamiltonian (Hamiltonian form of kinetic energy density) in the critical points (3, –1) and the ellipticity (ε) have been computed (Table I).

Comment. ρ_b – the value of the electron density in the bond critical point (3, –1); $\nabla^2\rho_b$ – second derivative of electron density (density Laplacian); h_e – local electronic energy in the bond critical point (3, –1). Units: e – atomic unit of charge (elementary charge) $e = 1.60219\times10^{-19}$ C); Bohr – atomic unit of length (the radius of the first Bohr orbit): 1 Bohr = 0.529177 Å = 5.29177×10^{-11} m); Hartree – atomic unit of energy: 1 Hartree = e^2 Bohr^{-1} = 627.5095 kcal mol^{-1} = $= 2.6255\times10^3$ kJ mol^{-1} = 27.212 eV = 2.1947×10^5 cm^{-1}.

TABLE I. Some properties of the bond critical points (3, –1)

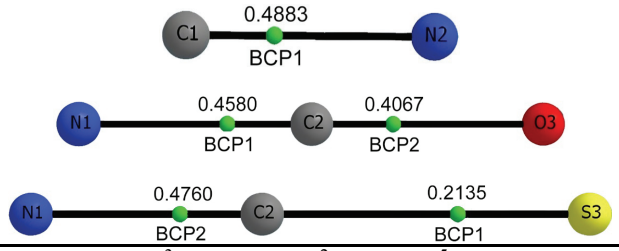

Bond	ρ_b / *e* Bohr^{-3}	$\nabla^2\rho_b$ /*e* Bohr^{-5}	h_e / Hartree Bohr^{-3}
		CN^-	
C≡N	0.488	–0.849	–0.951
		OCN^-	
C•••O	0.407	–0.510	–0.715
C•••N	0.458	–0.896	–0.827
		SCN^-	
C•••S	0.213	–0.132	–0.243
C•••N	0.476	–0.680	–0.905

According to the general pattern, the positive value of the electron density (ρ_b) in the bond critical point (BCP) and the negative value of the Laplacian of the electron density ($\nabla^2\rho_b$) in the BCP indicate the concentration of the electron charge in the internuclear region and its exhaustion in the direction of the nuclei, *i.e.*, the presence of strong covalent bond (shared interaction, in which the compression of the electron density along the bond line, directed to the critical point (3, –1), dominates).[42–54] A negative value of the local electronic energy (h_e) is a necessary criterion for a covalent bond (shared interaction).[43,54]

Fulfillment of the conditions $\rho_b > 0$, $\nabla^2\rho_b < 0$, $h_e < 0$ and sufficiently large absolute ρ_b, $\nabla^2\rho_b$, h_e values in the saddle (which are indicators of binding) critical points (3, –1) (Table I) show a high strength of all covalent bonds in CN^-, OCN^- and SCN^-, in accordance with the bonds lengths and natural orders (see above).

The position of BCP of an A–B bond shifts towards A and thus leaves more electron density for B if B is more electronegative than A.[42–54] As it can be seen from Table I, the aforesaid is confirmed for CN^-, OCN^- and SCN^-.

The ellipticity of all bonds in all three anions is essentially zero (according to our calculations, it is 10^{-15}–10^{-14}), which allows us to state the presence of a cylindrical symmetry of the electronic distribution in bonds.

According to our NBO and QTAIM analysis, in accordance with the criteria of natural charge on atoms, natural order and electron density (ρ_b) in the bond critical point (3, –1) it has been shown that in XCN^- (X = O, S) the C•••X bond is "one and a half", the C•••N bond carries a significant proportion of triple

bonding. The distribution of electron density (NBO, QTAIM) in XCN^- is reflected by the scheme $[X^{\bullet\bullet\bullet}C^{\bullet\bullet\bullet}\equiv N]^-$.

There is an electronic delocalization due to which there is a certain alignment of the negative charge on the X- and N-atoms, and not its significant predominance on the oxygen atom in the case of X = O and unconditional dominance on the nitrogen atom at X = S.

Herewith in OCN^-, the electronic distribution is more even compared to SCN^-: the $C^{\bullet\bullet\bullet}O$ bond is more "one and a half" than $C^{\bullet\bullet\bullet}S$ and the $C^{\bullet\bullet\bullet}\equiv N$ bond is more close to triple in the sulphur-containing anion.

One of the factors of more effective delocalization of electron density in OCN^- as compared to SCN^- is, apparently, the fact that the key donor–acceptor interaction for delocalization, namely the electron transfer from the LP orbital of the heteroatom X to the antibonding π-orbital of the $C^{\bullet\bullet\bullet}\equiv N$ bond, is energetically much more favorable for X = O compared to X = S. The remaining second-order perturbation energy $E(2)$ contributions noted above are basically comparable in magnitude and are less significant for the delocalization of the π-electron density.

If, on the basis of our quantum chemical computations by the molecular orbital method, we pass to a visual qualitative interpretation using the method of valence bonds, then OCN^- and SCN^- can be represented as resonance hybrids of two imaginary limiting canonical structures (X = O, S):

$$^-X–C\equiv N \leftrightarrow X=C=N^-$$

Wherein the relative contribution of the hypothetical structure $X=C=N^-$ to the hybrid is higher in the case of X = O.

The degree of the C≡N or $C^{\bullet\bullet\bullet}\equiv N$ bond triple character and bond strength changes in the following series: $CN^- > SCN^- > OCN^-$. The weakest $C^{\bullet\bullet\bullet}\equiv N$ bond (in OCN^-) is the longest.

As the results of the NBO analysis show (Table II), the occupancy of the LP orbital of the nitrogen atom in CN^-, OCN^- and SCN^- is close to 2, that is, the named orbital is practically not involved in the electron density delocalization.

TABLE II. Occupancy and hybrid state of the LP orbital of the nitrogen atom according to the NBO analysis

Anion	Occupancy	Hybridization character, %			
		s	p	d	f
CN^-	1.978	49.04	50.75	0.21	0.00
OCN^-	1.962	57.92	41.94	0.14	0.00
SCN^-	1.958	51.38	48.44	0.17	0.01

This orbital is sp-hybridized. The complementary (symbiotic) hard–hard interaction is largely electrostatic in nature, while the soft–soft interaction includes a significant covalent component.[8] The highest negative charge on the nitrogen

atom compared to other atoms of all the studied anions, on the one hand, and the wide possibility of nonbonding electrons showing donor properties, on the other hand, along with the parity contribution of 2s- and 2p-atomic orbitals to the LP orbital, providing favourable steric conditions of reactions with various (from the HSAB theory viewpoint) G. N. Lewis acids, in many respects predetermine the nitrogen atom character as an electron-donating centre, which is borderline in hardness/softness.

The interrelated concepts of hardness (softness) and electronegativity are becoming increasingly important in chemistry to implement a unified approach to two most important chemical problems – the construction of reaction barriers and molecular design, to explain regioselectivity and ambivalence (nucleophilic–electrophilic dichotomy),[56–58] to describe and model chemical bond, properties of molecules and crystals, intermolecular interactions,[59] solvation, extraction.[60,61]

The concept of electronegativity (including in connection with the HSAB), especially in the version of variable orbital electronegativity, turns out to be essentially the language of chemistry, thanks to which it is easily integrated into the general theory of systems. Indeed, the distinct periodicity of electronegativity and the contrast of properties emphasized by it (electropositive and electronegative elements, hard and soft acids and bases) underlie the nature of the chemical interaction and the emergence of new qualities as a result of the alignment of electronegativity (or electronic chemical potential), the repayment of opposites in the course of acid–base reactions, *etc.*[59]

Without focusing on theoretical premises, we note that global (absolute) hardness (η) is interpreted as the energy gap between the boundary molecular orbitals – the highest occupied (HOMO) and the lowest unoccupied (LUMO) ones:[8,62,63]

$$\eta = 0.5(E(\text{LUMO}) - E(\text{HOMO})) \quad (1)$$

where E(HOMO) and E(LUMO) are the energy values of HOMO and LUMO, respectively.

We have shown that in CN^-, the HOMO is a σ-orbital; in OCN^- and SCN^-, the HOMO level corresponds to two degenerate π-orbitals. In all three anions, the LUMO is a σ-type orbital.

To evaluate the local hardness of the electrophilic attack (h) of individual reaction centres of a molecular system, including N electrons, the condensed K. Fukui function (f_k^-) is used:[8,62–64]

$$f_k^- = q_k^N - q_k^{N-1} \quad (2)$$

where q_k^N and q_k^{N-1} is the charge on the atoms (natural one in our work) of the initial systems (in our case, CN^-, OCN^- and SCN^-) and radicals ($^\bullet$CN, OCN$^\bullet$ and $^\bullet$SCN) having the same arrangement of nuclei (*i.e.*, geometry), but a different number of electrons (N for anions and N–1 for radicals).

Local hardness (h) is calculated by the formula:[8,62,63,65]

$$h = f_k^- \eta \quad (3)$$

For anions, the B3LYP method unsatisfactorily conveys all parameters, the evaluation of which uses the HOMO and LUMO energy values, and the smaller the molecular system, the more pronounced the errors.[66] To ensure the correctness of the calculations, it is necessary either to take into account countercations (contradicting the purpose of this study, which requires consideration of isolated anions), or go[66] to the second-order Ch. Møller – M.S. Plesset perturbation theory (MP2)[67–70] level with a basis set of at least 6-311++G(d,p).[32,33]

However, K. Fukui's local indices (and, consequently, the charge characteristics of atoms) are calculated correctly.[66]

Thus, using the B3LYP method, we cannot reliably estimate the global (absolute) hardness (η) of the anions under study, but we are able to determine the relationship between the values of the local hardness of individual donor reaction centres.

Below are the f_k^- (Table III) values computed by us at the B3LYP/6--311++G(3df,3pd) and UB3LYP/6-311++G(3df,3pd) level of theory.

TABLE III. Condensed electrophilic K. Fukui functions (f_k^-)

Anion	Condensed electrophilic K. Fukui function			
	C	N	O	S
Geometry of radicals is fixed like anions				
CN^-	–0.655	–0.345	–	–
OCN^-	–0.021	–0.557	–0.422	–
SCN^-	0.077	–0.350	–	–0.727
Geometry of radicals is optimized				
CN^-	–0.657	–0.343	–	–
OCN^-	–0.058	–0.536	–0.406	–
SCN^-	0.094	–0.357	–	–0.737

Values close to each other were obtained both with the spatial structure of the radicals, the same as that of the anions, and with the optimized geometry of the radicals.

In CN^-, the local hardness of the nitrogen donor atom is higher compared to the carbon atom. In OCN^-, the oxygen atom is a slightly more hard donor centre than the nitrogen atom. In SCN^-, the sulphur atom is a softer centre than the N atom. Such results are consistent with known patterns[1–8] and explain many of the above examples of coordination in the formation of metal thiocyanates.[12,15]

As noted above, the homolytic oxidative coupling of CN^-, OCN^- and SCN^- is accompanied by $^{\bullet}CN$, $OCN^{\bullet}$ and $^{\bullet}SCN$ intermediates formation.

Table IV gives the R. S. Mulliken spin density, calculated at the UB3LYP/6--311++G(3df,3pd) level of theory, on atoms of •CN, OCN• and •SCN with optimized geometry.

TABLE IV. R. S. Mulliken spin density on atoms in •CN, OCN• and •SCN

Radical	Spin density on atom			
	C	N	O	S
•CN	0.889	0.111	–	–
OCN•	–0.122	0.764	0.358	–
•SCN	–0.144	0.384	–	0.760

The wave function in the unrestricted D. R. Hartree – V. A. Fock approach[19] used for computing the spin density, is not the $\hat{S}^2$ operator eigenfunction, and contains the admixed components of higher multiplicities. For avoiding the wave function spin contamination at the quantum chemical computations, we used the spin annihilating procedure.[19] As a result, the full spin S^2 after annihilation for •CN, OCN• and •SCN was 0.7501, that coincides with the value of 0.75 for the pure doublet state, characteristic for the radical particles with one uncoupled electron in the ground state.[19]

The latter fact testifies to the correct implementation of spin density as a reactivity index, alike the previous studies.[20–22] Then again, the above index has proved its predictive power even in the cases, in which the uncontaminated spin state is not provided.[71,72]

The significant predominance of the spin density on the carbon atom in •CN and on the sulphur atom in •SCN naturally explains the appearance of cyanogen N≡C–C≡N and thiocyanogen N≡C–S–S–C≡N during the oxidation of CN^- and SCN^-, respectively:[12,19]

$$CN^- \rightleftarrows {}^\bullet CN + \bar{e},$$
$$2{}^\bullet CN \rightleftarrows N{\equiv}C{-}C{\equiv}N;$$

$$SCN^- \rightleftarrows {}^\bullet SCN + \bar{e},$$
$$2SCN^\bullet \rightleftarrows N{\equiv}C{-}S{-}S{-}C{\equiv}N$$

For CN^-, the specified process of oxidative dimerization is also promoted by the higher stability of cyanogen N≡C–C≡N compared to the hypothetical products of C,N- and N,N-coupling, including quite labile bonds between the monomer units.

In OCN•, the excess of spin density on the nitrogen atom is much higher than on the oxygen centre. This testifies in favour of the possible emergence of an unstable product O=C=N–N=C=O:[12,19]

$$OCN^- \rightleftarrows OCN^\bullet + \bar{e},$$

$$2OCN^\bullet \rightleftarrows O{=}C{=}N{-}N{=}C{=}O.$$

CONCLUSION

The key features of the structure, some aspects of the ambident reactivity of CN^-, OCN^- and SCN^- have been substantiated, along with the above anions homolytic oxidative coupling behaviour.

We have used the B3LYP method since it is the most widely used, tested and well-proven DFT option. The results obtained are consistent with the known patterns and experimental data:

1. The calculated lengths of the C≡N, C$^{\bullet\bullet\bullet}$N, C$^{\bullet\bullet\bullet}$O and C$^{\bullet\bullet\bullet}$S bonds correspond to the experimental values. Calculations represent the linear structure of OCN^- and SCN^-.

2. In the series of CN^-, OCN^- and SCN^-, the values changes for the lengths and natural orders of the C≡N, C$^{\bullet\bullet\bullet}$N, C$^{\bullet\bullet\bullet}$O and C$^{\bullet\bullet\bullet}$S bonds are of an antibate character.

3. The bond critical points (3, –1) in CN^-, OCN^- and SCN^- are located closer to less electronegative atoms.

4. Local hardness of the donor reaction centres has been reproduced: N > C (in CN^-), O > N (in OCN^-), N > S (in SCN^-).

5. The regioselectivities of the homolytic oxidative coupling reactions have been explained and predicted. The oxidative dimerization of CN^- occurs as C,C-coupling, SCN^- undergoes S,S-coupling, and OCN^- would provide the product of N,N-dimerization.

Probably, results similar to those obtained in this work would be also provided by other functionals, as well as by methods of the hybrid meta density functional theory (HMDFT) and by advanced, sophisticated *ab initio* approaches (MP2, MP3, MP4 (including MP4SDTQ), MP5 (for $^\bullet$CN, OCN$^\bullet$ and $^\bullet$SCN), CISD, QCISD, QCISD(T), CCSD, CCSD(T), G1, G2, G2M, CASSCF, GVB-PP, *etc.*).

ИЗВОД

ЦИЈАНИДНИ, ЦИЈАНАТНИ, ТИОЦИЈАНАТНИ АМБИДЕНТНИ АНЈОНИ: СТРУКТУРА, ТОПОЛОШКА АНАЛИЗА ЕЛЕКТРОНСКЕ ГУСТИНЕ И РЕГОСЕЛЕКТИВНОСТ ХОМОЛИТИЧКОГ ОКСИДАТИВНОГ КУПЛОВАЊА

ALEXEI N. PANKRATOV

Division of Analytical Chemistry and Chemical Ecology, Institute of Chemistry, N. G. Chernyshevskii National Research Saratov State University, 83 Astrakhanskaya Street, Saratov 410012, Russia

На B3LYP/6-311++G(3df,3pd) нивоу теорије, проучавана је просторна и електронска структура цијанидног, цијанатног и тиоцијанатног јона. Помоћу анализе природних орбитала веза (NBO) и Р.Ф.В. Бејдерове квантне теорије “атома у молекулима” (QTAIM), испитиване су делокализација електронске густине и тополо-

шке особине горепоменутих анјона. Расподела електронске густине (NBO, QTAIM) у XCN^- (X = O, S) одражава се у шеми $[X\overset{\bullet\bullet\bullet}{\text{—}}C\overset{\bullet\bullet\bullet}{=}N]^-$. Релативни допринос хипотетичке структуре $X{=}C{=}N^-$ у резонанционом хибриду $^-X{-}C{\equiv}N \leftrightarrow X{=}C{=}N^-$ је виши у случају када је X = O. Удео C≡N или $C\overset{\bullet\bullet\bullet}{=}N$ карактера троструког везивања и степена јачине везе у анјонима мења се на следећи начин: $CN^- > SCN^- > OCN^-$. Насељеност орбитале слободног електронског пара (LP) на атому азота у горњим анјонима је близу 2, а LP орбитала је sp-хибридизована. Процењене су кондензоване К. Фукуијеве функције за електрофилни напад. Локална тврдоћа донорских реакционих центара је: N > C (CN^-), O > N (OCN^-), N > S (SCN^-). Поткрепљена је региоселективност реакција хомолитичког оксидативног купловања CN^-, OCN^- и SCN^-.

(Примљено 25. септембра, ревидирано 7. новембра, прихваћено 23. децембра 2023)

REFERENCES

1. J. E. House, *Inorganic Chemistry*, Academic Press (imprint of Elsevier Inc.), Amsterdam, 2008 (ISBN: 978-0-12-356786-4)
2. G. L. Miessler, P. J. Fischer, D. A. Tarr, *Inorganic Chemistry*, Pearson Education, Inc. (Pearson advanced chemistry series), Boston, MA, 2014 (ISBN-10: 0321811054; ISBN-13: 978-0-321-81105-9)
3. R. K. Sharma, *Text Book of Coordination Chemistry*, Discovery Publishing House, New Delhi, 2007 (ISBN-10: 81-8356-223-X; ISBN-13: 978-8183562232)
4. M. H. Najar, *A Comprehensive Guide to Coordination Chemistry, Spectra and Magnetism: Frontiers of Inorganic Chemistry*, LAP LAMBERT Academic Publishing, Saarbrücken, 2020 (ISBN-10: 6202516321; ISBN-13: 978-6202516327)
5. B. Weber, *Coordination Chemistry: Basics and Current Trends*, Springer Spektrum, Berlin, 2023 (https://doi.org/10.1007/978-3-662-66441-4)
6. *Theoretical Organic Chemistry*, C. Párkányi, Ed., Elsevier Science, Amstrdam, 2011 (ISBN: 978-0444546227)
7. P. Vogel., P. N. Houk, *Organic Chemistry: Theory, Reactivity and Mechanisms in Modern Synthesis*, Wiley-VCH Verlag GmbH, Weinheim, 2019 (ISBN: 978-3-527-81927-0)
8. R. G. Pearson, *Chemical Hardness: Applications from Molecules to Solids*, Wiley-VCH Verlag GmbH, Weinheim, 1997 (https://doi.org/10.1002/3527606173)
9. A. A. Tishkov, H. Mayr, *Angew. Chem. Int. Ed.* **44** (2005) 142 (https://doi.org/10.1002/anie.200461640)
10. H. F. Schaller, U. Schmidhammer, E. Riedle, H. Mayr, *Chem. – Eur. J.* **14** (2008) 3866 (https://doi.org/10.1002/chem.200800314)
11. R. Loos, Sh. Kobayashi, H. Mayr, *J. Amer. Chem. Soc*. **125** (2003) 14126 (https://doi.org/10.1021/ja037317u)
12. A. M. Golub, H. Kőhler, V. V. Skopenko, H. Boland, T. P. Lishko, V. M. Samoilenko, G. V. Tsintsadze, *Chemistry of Pseudohalides*, A. M. Golub, H. Kőhler, V. V. Skopenko, Eds., Elsevier Science Ltd, Amsterdam, 1986 (ISBN-10: 0444416269; ISBN-13: 9780444416261)
13. K. Nakamoto, *Infrared and Raman Spectra of Inorganic and Coordination Compounds: Part A: Theory and Applications in Inorganic Chemistry*, John Wiley & Sons, Inc., Hoboken, NJ, 2009 (https://doi.org/10.1002/9780470405840)

14. K. Nakamoto, *Infrared and Raman Spectra of Inorganic and Coordination Compounds: Part B: Application in Coordination, Organometallic, and Bioinorganic Chemistry*, John Wiley & Sons, Inc., Hoboken, NJ, 2009 (https://doi.org/10.1002/9780470405888)
15. A. F. Wells, *Structural Inorganic Chemistry*, Oxford Univ. Press, Oxford, 2012 (ISBN-10: 0199657637; ISBN-13: 978-0199657636)
16. G. P. Mikhailov, *J. Appl. Spectrosc.* **83** (2016) 339 (https://doi.org/10.1007/s10812-016-0305-2)
17. A. N. Pankratov, O. M. Tsivileva, *Current Phys. Chem.* **6** (2016) 210 (https://doi.org/10.2174/1877946806666160524154445)
18. F. M. Fernández, *Introduction to Perturbation Theory in Quantum Mechanics*, CRC Press, Inc., Boca Raton, FL, 2000 (https://doi.org/10.1201/9781420039641)
19. R. V. Selezenev, *Psevdogalogeny i ikh soedineniya Pseudohalogens and Their Compounds*, https://present5.com/psevdogalogeny-i-ix-soedineniya-selezenev-r-v/ (accessed 7th December 2023)
20. A. N. Pankratov, *J. Mol. Struct.: THEOCHEM* **315** (1994) 179 (https://doi.org/10.1016/0166-1280(94)03779-K)
21. A. N. Pankratov, A. N. Stepanov, *Croat. Chem. Acta* **70** (1997) 585 (ISSN: 0011-1643; e-ISSN: 1334-417X)
22. A. N. Pankratov, *J. Anal. Chem.* **77** (2022) 1063 (https://doi.org/10.1134/S106193482209009X)
23. I. N. Levine, *Quantum Chemistry*, Pearson, Boston, MA, 2014 (ISBN-10: 0321803450; ISBN-13: 978-0321803450)
24. W. Kohn, *Rev. Mod. Phys.* **71** (1999) 1253 (https://doi.org/10.1103/RevModPhys.71.1253)
25. W. Koch, M. C. Holthausen, *Chemist's Guide to Density Functional Theory*, Willey-VCH Verlag GmbH, Toronto, 2001 (https://doi.org/10.1002/3527600043)
26. S. F. Sousa, P. A. Fernandes, M. J. Ramos, *J. Phys. Chem., A* **111** (2007) 10439 (https://doi.org/10.1021/jp0734474)
27. *Gaussian 09, Revision E.01*, Gaussian, Inc., Wallingford, CT, 2013 https://gaussian.com (accessed 7th December 2023)
28. A. D. Becke, *Phys. Rev. A* **38** (1988) 3098 (https://doi.org/10.1103/physreva.38.3098)
29. A. D. Becke, *J. Chem. Phys.* **98** (1993) 5648 (https://doi.org/10.1063/1.464913)
30. Chengteh Lee, Weitao Yang, R. G. Parr, *Phys. Rev., B* **37** (1988) 785 (https://doi.org/10.1103/PhysRevB.37.785)
31. H. B. Schlegel, J. J. W. McDouall, in *Computational Advances in Organic Chemistry*, C. Ögretir, I. G. Csizmadia, Eds., Kluwer Academic, Dordrecht, 1991, pp. 167–185 (https://doi.org/10.1007/978-94-011-3262-6)
32. R. Krishnan, J. S. Binkley, R. Seeger, J. A. Pople, *J. Chem. Phys.* **72** (1980) 650 (https://doi.org/10.1063/1.438955)
33. A. D. McLean, G. S. Chandler, *J. Chem. Phys.* **72** (1980) 5639 (https://doi.org/10.1063/1.438980)
34. *HyperChem Professional 8.0*, Hypercube, Inc., Gainesville, FL, http://hypercubeusa.com/Products/HyperChemProfessional/tabid/360/Default.aspx; http://www.hypercubeusa.com/Products/HyperChemProfessional/tabid/360/Default.aspx (accessed 7th December 2023)
35. J. J. P. Stewart, *J. Comput. Chem.* **10** (1989) 209 (https://doi.org/10.1002/jcc.540100208)

36. J. J. P. Stewart, *J. Comput. Chem.* **10** (1989) 221 (https://doi.org/10.1002/jcc.540100209)
37. A. E. Reed, L. A. Curtiss, F. Weinhold, *Chem. Rev*. **88** (1988) 899 (https://doi.org/10.1021/cr00088a005)
38. A. V. Nemukhin, F. Weinhold, *Ros. Khim. Zh.* (*Zh. Ros. Khim. Obshchestva im. D. I. Mendeleeva* **38** (1994) 5 (ISSN: 0373-0247)
39. F. Weinhold, C. R. Landis, *Valency and Bonding: A Natural Bond Orbital Donor-Acceptor Perspective*, Cambridge Univ. Press, Cambridge, 2005 (https://doi.org/10.1017/CBO9780511614569)
40. I. Mayer*, Bond Orders and Energy Components: Extracting Chemical Information from Molecular Wave Functions*, CRC Press, Taylor & Francis Group, Boca Raton, FL, 2016 (https://doi.org/10.1201/9781315374895)
41. *NBO Version 3.1*, 1995, https://gaussian.com (accessed 7th December 2023)
42. R. F. W. Bader, in *Chemical Applications of Topology and Graph Theory: A Collection of Papers from a Symposium Held at the Univ. of Georgia. Athens, Georgia, USA, 18-22 April, 1983*, R. B. King, Ed., Elsevier Science Ltd, Amsterdam, 1983, pp. 40–56 (ISBN-10: 0444422447; ISBN-13: 978-0444422446)
43. D. Cremer, E. Kraka, *Croat. Chem. Acta* **37** (1984) 1259 (ISSN: 0011-1643; e-ISSN: 1334-417X)
44. R. F. W. Bader, *Acc. Chem. Res.* **18** (1985) 9 (https://doi.org/10.1021/ar00109a003)
45. R. F. W. Bader, *Pure Appl. Chem.* **60** (1988) 145 (https://doi.org/10.1351/pac198860020145)
46. R.F.W. Bader, *Chem. Rev.* **91** (1991) 893 (https://doi.org/10.1021/cr00005a013)
47. R. F. W. Bader, *Atoms in Molecules: A Quantum Theory*, Oxford Univ. Press, Clarendon Press, New York, 1994 (ISBN-10: 0198551681; ISBN-13: 978-0198551683)
48. R. F. W. Bader, P. L. A. Popelier, T. A. Keith, *Angew. Chem.* **106** (1994) 647 (https://doi.org/10.1002/ange.19941060605)
49. P. L. A. Popelier, *Atoms in Molecules: An Introduction*, Prentice Hall, London, 2000 (ISBN-10: 0582367980; ISBN-13: 978-0582367982)
50. P. L. A. Popelier, F. M. Aicken, S. E. O'Brien, in *Chemical Modelling: Applications and Theory. Vol. 1*, Ch. A. Reynolds, J. Tennyson, J. Ladik, P. Pyykko, R. I. Maurer, Th. E. Simos, S. Wilson, S. E. O'Brien, D. Pugh, P. L. A. Popelier, A. J. Richardson, H. Stoll, M. Springborg, F. M. Aicken, Eds., Roy. Soc. Chem., Cambridge, 2000, pp. 143–198 (ISBN 978-0854042548)
51. J. R. Mohallem, *Theor. Chim. Acta* **107** (2002) 372 (https://doi.org/10.1007/s00214-002-0345-y)
52. R. F. W. Bader, *Monatsh. Chem.* **136** (2005) 819 (https://doi.org/10.1007/s00706-005-0307-x)
53. R. F. W. Bader, *J. Phys. Chem., A* **111** (2007) 7966 (https://doi.org/10.1021/jp073213k)
54. I. S. Bushmarinov, K. A. Lyssenko, M. Yu. Antipin, *Russ. Chem. Rev.* **78** (2009) 283 (https://doi.org/10.1070/RC2009v078n04ABEH004017)
55. *Computational Chemistry Using the Quantum Theory of Atoms in Molecules* (*QTAIM*), *AIMAll Version 19.10.12*, http://aim.tkgristmill.com (accessed 7th December 2023)
56. S. V. Volovik, G. G. Dyadyusha, V. I. Staninets, *Regioselektivnost' i reaktsionnaya sposobnost' svobodnykh radikalov v protsessakh prisoedineniya i aromaticheskogo zameshcheniya*, V. D. Pokhodenko, Ed., Naukova Dumka, Kiev, 1988 (ISBN: 5-12-000209-9)

57. S. V. Volovik, V. I. Staninets, N. S. Zefirov, *Theor. Exp. Chem.* **26** (1990) 390 (https://doi.org/10.1007/BF00530251)
58. S. V. Volovik, V. I. Staninets, N. S. Zefirov, *Doklady Akad. Nauk Ros.* **330** (1993) 321 (ISSN: 0869-5652)
59. V. S. Urusov, *J. Struct. Chem.* **35** (1994) 101 (https://doi.org/10.1007/BF02578507)
60. A. M. Rozen, B. V. Krupnov, *Russ. Chem. Rev.* **65** (1996) 973 (https://doi.org/10.1070/RC1996v065n11ABEH000241)
61. E. P. Buchikhin, A. M. Chekmarev, N. A. Bobyrenko, *Russ. J. Inorg. Chem.* **55** (2010) 790 (https://doi.org/10.1134/s0036023610050219)
62. Weitao Yang, W. J. Mortier, *J. Amer. Chem. Soc.* **108** (1986) 5708 (https://doi.org/10.1021/ja00279a008)
63. M. V. Lebedev, *Semiconductors* **35** (2001) 1291 (https://doi.org/10.1134/1.1418074)
64. P. W. Ayers, R. G. Parr, *J. Amer. Chem. Soc.* **122** (2000) 2010 (https://doi.org/10.1021/ja9924039)
65. F. Méndez, J. L. Gázquez, *J. Amer. Chem. Soc.* **116** (1994) 9298 (https://doi.org/10.1021/ja00099a054)
66. M. E. Kletskii, O. N. Burov, N. S. Fedik, S. V. Kurbatov, *Chem. Heterocycl. Compounds* **52** (2016) 700 (https://doi.org/10.1007/s10593-016-1952-1)
67. M. Head-Gordon, J. A. Pople, M. J. Frisch, *Chem. Phys. Lett.* **153** (1988) 503 (https://doi.org/10.1016/0009-2614(88)85250-3)
68. O. Christiansen, *J. Chem. Phys.* **119** (2003) 5773 (https://doi.org/10.1063/1.1601593)
69. M. Del Ben, J. Hutter, J. VandeVondele, *J. Chem. Theory Comput.* **8** (2012) 4177 (https://doi.org/10.1021/ct300531w)
70. M. Ochi, Sh. Tsuneyuki, *Chem. Phys. Lett.* **621** (2015) 177 (https://doi.org/10.1016/j.cplett.2015.01.009)
71. I. A. Abronin, G. M. Zhidomirov, *Theor. Exp. Chem.* **12** (1976) 68 (https://doi.org/10.1007/BF00524932)
72. G. M. Zhidomirov, A. A. Bagatur'yants, I. A. Abronin, *Prikladnaya kvantovaya khimiya. Raschety reaktsionnoi sposobnosti i mekhanizmov khimicheskikh reaktsii*, Khimiya, Moscow, 1979.

Journal of the Serbian Chemical Society
JSCS@tmf.bg.ac.rs • www.shd.org.rs/JSCS
J. Serb. Chem. Soc. *89* (3) 367–382 (2024)
JSCS–5726
Original scientific paper
Published 31 March 2024

ADMET profiles of selected anabolic steroid derivatives

ANDREI BITANG[1], VIOREL BITANG[1], VLAD GROSU[2], ALECU CIORSAC[3] and ADRIANA ISVORAN[4]*

[1]*Department of Physical Education and Sports Performance, Faculty of Physical Education and Sport, "Aurel Vlaicu" University of Arad, Romania,* [2]*Mechatronics and Mechanical Engineering Department, Faculty of Automotive, Technical University of Cluj Napoca, Romania,* [3]*Department of Physical Education and Sport, University Politehnica Timisoara, Romania and* [4]*Department of Biology-Chemistry and Advanced Environmental Research Laboratories, West University of Timisoara, Romania*

(Received 3 August, revised 25 September, accepted 5 November 2023)

Abstract: There is control over steroids use and marketing, but also new compounds that mimic their effects, steroid derivatives, are being synthesized. They are frequently produced as dietary supplements intended to improve physical activity, and usually no information is provided regarding their composition, dosages, and efficacy or safety. In this study, a computational approach was used to evaluate the absorption, distribution, metabolism, excretion and toxicity (ADMET) profiles of several steroid derivatives: methasterone, methyl-1-testosterone, 4-hydroxytestosterone, methyldienolone, methyltrienolone and 19-nor-5-androstenedione. The following computational prediction tools were applied: admetSAR2.0, ADMETLab2.0, Endocrine Disruptome, PredSkin3.0. All investigated compounds showed good human intestinal absorption, are not able to penetrate the blood-brain barrier and inhibit cytochrome P450 enzymes involved in the metabolism of xenobiotics. These compounds have potential for skin sensitisation, induce reproductive toxicity and endocrine disruption, and have a low potential for hepatotoxicity and respiratory toxicity. It is important that the results of the study are known by those exposed at workplaces where these compounds are produced and packed as well as by consumers. These predictions can also guide the experimental evaluation of the possible toxicity of the investigated compounds, the results of which can be further used for purposes of regulating the use of these steroid derivatives.

Keywords: dietary supplements; steroid derivatives; skin sensitization; hepatotoxicity; reproductive toxicity.

* Corresponding author. E-mail: adriana.isvoran@e-uvt.to
https://doi.org/10.2298/JSC230803086B

INTRODUCTION

Some athletes, but also amateurs and even teenagers, interested in improving performance or body appearance, consume specific drugs that are usually represented by a form of steroids, as these drugs are intended to increase their muscle mass and strength. Synthetic anabolic androgenic steroids (AAS) are testosterone-derived compounds produced by pharmaceutical manufacturers and may be used by prescription for some related diseases. Even though the use of these compounds is controlled in many countries, they can be obtained through the Internet and there are also veterinary steroids often used by people to increase their physical performance.[1]

Due to the control of the use and marketing of steroids, new compounds that mimic their effects have been synthesized by similarity to androgenic steroids. These new compounds are known as steroid derivatives (SDs) or designer steroids. They are produced as dietary supplements by less reputable suppliers and are sold on the Internet or in fitness stores.[2] These supplements are designed as pharmaceutical compounds, but information on ingredients, dosages, companies, manufacturers is usually not provided.[3] Data from the literature show that dietary supplements are often contaminated with steroid derivatives or designer steroids.[4]

Published data have revealed numerous effects of AAS. They can help build muscle tissue, increase body mass and improve performance.[5] As toxicological effects of AAS are mentioned: carcinogenic, cardiovascular, cerebrovascular, dermal, endocrine, genito-urinary, genotoxic, hematological, hepatic, immunological, renal and reproductive effects.[6–8]

A concerning feature of the use of these compounds is that data on their efficacy and/or safety are usually not available. In this study, a computational approach is used to evaluate the toxicity of several SDs that are not approved for human use or are considered experimental drugs under certain circumstances: methasterone, methyl-1-testosterone, 4-hydroxytestosterone, methyldienolone, methyltrienolone and 19- nor-5-androstenedione.[9] These compounds were selected because they can be easily purchased on the Internet, and the online Drug Bank database (https://go.drugbank.com/, accessed in October 2023) does not contain information on their ADMET profiles. It was not possible to identify studies that strictly examine Internet sales of the investigated SDs. Information on the internet market for AAS is also scarce, but few recently published articles point out that AAS with controlled use are readily available for purchase, without a valid prescription, on the online market.[10,11] Websites only advertise the aesthetic and ergogenic benefits of use of these compounds and do not inform about the potential complications and adverse effects.[10] Moreover, social media platforms facilitate the supply of AAS and increase the accessibility of these compounds, which especially affect young people and less informed people.[12] In addition, literature data is limited in information regarding the toxicological

effects of the investigated SDs on humans. To our knowledge, this is the first computational study evaluating toxicokinetics of these compounds in humans.

METHOD

The SDs used in this study are presented in Table I. This table also contains, for each compound, the IUPAC (International Union of Pure and Applied Chemistry) name which was extracted from the PubChem database (www.pubchem.org, accessed January 2023),[13] the accession number in Drug Bank online (https://go.drugbank.com/, accessed January 2023) and known toxicological effects. As a control, this study considers oxymetholone, a synthetic AAS that is also a clinical drug used under controlled conditions since 1960.[14]

TABLE I. The compounds that are used in the present study: their common name, IUPAC name, accession number in Drug Bank online (when available), known toxicological effects

Common name	IUPAC name	Drug Bank accession number / status	Toxicological effects listed in Drug Bank
Methasterone	(2*R*,5*S*,8*R*,9*S*,10*S*,13*S*,14*S*,17*S*)-17--Hydroxy-2,10,13,17-tetramethyl--2,4,5,6,7,8,9,11,12,14,15,16-dodecahydro-1*H*-cyclopenta[*a*]phenanthren-3-one	Not found in Drug Bank	Not available
Methyl-1-testosterone	(5S,8*R*,9*S*,10*R*,13*S*,14*S*,17*S*)-17--Hydroxy-10,13,17-trimethyl--5,6,7,8,9,11,12,14,15,16-decahydro--4*H*-cyclopenta[*a*]phenanthren-3-one	DB01572 / prohibited doping compound	Not available
4-Hydroxytestosterone	(8*R*,9*S*,10*R*,13*S*,14*S*,17*S*)-4,17-dihydroxy-10,13-dimethyl--1,2,6,7,8,9,11,12,14,15,16,17-dodecahydrocyclopenta[*a*]phenanthren--3-one	DB01485 / experimental/ illicit	Hepatic metabolism, renal excretion
Methyldienolone	(8*S*,13*S*,14*S*,17*S*)-17-Hydroxy-13,17--dimethyl-1,2,6,7,8,11,12,14,15,16--decahydrocyclopenta[*a*]phenanthren-3-one	not found in Drug Bank	not available
Methyltrienolone	(8*S*,13*S*,14*S*,17*S*)-17-Hydroxy-13,17--dimethyl-1,2,6,7,8,14,15,16-octahydrocyclopenta[*a*]phenanthren-3--one	DB02998 / experimental	Not available
19-Nor-5-androstenedione	(8*R*,9*S*,10*R*,13*S*,14*S*)-13-methyl--1,2,4,7,8,9,10,11,12,14,15,16-dodecahydrocyclopenta[*a*]phenanthrene-3,17-dione	DB01443 / Experimental / Illicit	Not available
Oxymetholone	(2*Z*,5*S*,8*R*,9*S*,10*S*,13*S*,14*S*,17*S*)-17--hydroxy-2-(hydroxymethylidene)--10,13,17-trimethyl--1,4,5,6,7,8,9,11,12,14,15,16-dodecahydrocyclopenta[*a*]phenanthren-3-one	DB06412 Approved / Illicit	Carcinogenic, cardiotoxicity

In order to obtain the possible toxicity of these compounds on human organs, several computational tools have been used: admetSAR2.0,[15] ADMETLab2.0,[16] Endocrine Disruptome,[17] and Pred-Skin3.0.[18] These computational facilities were used because they are freely available and have been developed by recognized chemiformatics groups. In addition, they are based on models with a large amount of training data, are continuously updated, are robust, and the accuracy of predictions is at least 70 %. These computational facilities were developed to study drug candidates, but they have also been successfully used to predict the human and environmental toxicity of many types of compounds: chito-oligomers[19,20] and some of their water-soluble derivatives,[21] cosmetics,[22] phthalates,[23] oligomers of hydroxyalkanoates[24] and of lactic acid,[25] intensive sweeteners,[26] pesticides,[27-29] acyclic monoterpenes[30] and other steroids.[8] A brief description of each instrument used is presented in Table II.

TABLE II. Online tools used for predicting the absorption, distribution, excretion, metabolism and toxicity of the investigated designer steroids: SMILES – Simplified Molecular Input Line Entry System, CYPs – human cytochromes, NR – nuclear receptors

Online prediction tool	Predicted activity and the accuracy of prediction
ADMETSAR2.0: offers 22 qualitative classification models and 5 quantitative regression models that allow the user to compute the probability of an activity to be present (positive values) or absent (negative values); uses the SMILES formulas of investigated steroids as input data and outputs the probabilities of the predicted pharmacokinetics and toxicological effects.[15]	Gastrointestinal absorption (GI) (96.5 %); Blood brain barrier permeation (BBBP) (90.7 %); Plasma protein binding (PPB) (66.8 %); Substrate/inhibition of the P-glycoprotein (Pgps/Pgpi) (80.2 % / 86.1 %); Substrates (77.9 %) or inhibitors (85.5 %) of the human cytochromes (cyps); Carcinogenicity (89.6 %); Eye corrosion and/or irritation (94.9 %/96.3 %); Hepatotoxicity (83.3 %) Human Ether-a-go-go-Related Gene (herg) inhibition (80.4 %); Mutagenicity by Ames test (84.3 %).[15]
ADMETlab2.0 uses as entry data the SMILES formulas of the investigated steroids; outputs ADMET profiles of the investigated compound. The accuracy of the classification models is of minimum 80 % and most of the regression models have R^2>0.72.[16]	Intestinal absorption, Plasma protein binding, Volume of distribution, Clearance are predicted, P-glycoprotein binding, Blood brain barrier permeation, Binding to the human cyps, Cardiotoxicity, Hepatotoxicity, Mutagenicity, Carcinogenicity Nephrotoxicity, Skin sensitization.[16]
Endocrine Disruptome evaluates the interactions between the investigated steroids and 12 human NR; uses SMILES formulas as input data; delivers computed sensitivity coefficients associated to colour codes: green cells for compounds that do not affect the NR, yellow cells with low probability of affecting NR, orange cells for compounds with mean probability of affecting NR and red cells for compounds revealing a high probability of affecting NR. The accuracy of prediction is at least 78 %.[17]	Interactions with the following nuclear receptors: Androgen receptor (AR) (both agonistic and antagonistic interactions) Oestrogen receptors (ER) α and β Glucocorticoid receptor (GR) (both agonistic and antagonistic interactions) Liver X receptors (LXR) α and β Peroxisome proliferator activated receptors (PPAR) α, β/δ and γ Retinoid X receptor (RR) α Thyroid receptors (TR) α and β.[17]

TABLE II. Continued

Online prediction tool	Predicted activity and the accuracy of prediction
Pred-Skin 3.0 predicts the skin sensitization potential of chemicals; uses the SMILES formulas as input data; outputs the probability of compounds to illustrate or not skin sensitization potential; products a probability map allowing the illustration of the contribution of predicted fragment toward skin sensitization.[18]	Predictions based on five sensitization assays: *In vitro* (keratinosens and human Cell Line Activation Test, H-CLAT, accuracy 80 to 86 %) *In vivo* (murine local lymph node assay, LLNA, accuracy 70 to 84 %) *In chemico* (Direct Peptide Reactivity Assay, DPRA, accuracy 73 to 76 %) Human repeated insult patch (HRIPT) test (accuracy 70 %) Human maximization test (HMT, accuracy 84 %).[18]

RESULTS AND DISCUSSION

The physicochemical and structural properties of query compounds are typically used as descriptors by computational tools that predict chemical ADMET profiles. These properties and the 2D formulas of the investigated steroids were extracted from PubChem database[13] and are shown in Table III. This table also contains the 2D formula and physicochemical properties of oxymetholone, the AAS used as a control in this study.

The data presented in Table III show that all investigated SDs have quite similar physicochemical properties to those of oxymetholone: low molecular weights, low numbers of hydrogen bond donors and acceptors and reveal low hydrophobicity. These properties fulfil Lipinski's rule of five[31] and are common to orally administered drugs. This is confirmed by the ADMETLab2.0 tool results illustrating that these compounds satisfy Lipinski's rule (Table S-I of the Supplementary material to this paper). Methasterone and methyl-1-testosterone are considered potentially toxic because they do not meet Pfizer's rule.[32]

It should be noted that the major limiting point of the results of prediction tools based on classification models is the reliability of the predictions because computational models have limited domains of applicability. An applicability domain (AD) is defined as the area of physicochemical and/or structural space in which the model is expected to be exploitable, such as the predictions to be assumed to be reliable.[33] The admetSAR2.0 and ADMETLab2.0 prediction tools allow estimation of the prediction accuracy for each compound individually and specify whether the compound characteristics fall within the AD of the model (illustration in Fig. S-1 of the Supplementary material for 19-nor-5-androstenedione). In the cases of the investigated steroids, the predictions were within the range of applicability.

The absorption, distribution and excretion profiles of the investigated SDs obtained with the admetSAR2.0 and ADMETLab2.0 prediction tools are revealed in Table IV. The data presented in this table bring up quite similar values

obtained for the probabilities related to absorbtion, distribution and excretion profiles of the investigated SDs compared to the those obtained for the control, oxymetholone.

TABLE III. Steroids used in the present study, 2D formulas and their main physicochemical properties extracted from PubChem database;[13] *MW* – molecular weight, log *P* – partition coefficient, *HBD* – hydrogen bonds donors, *HBA* – hydrogen bonds acceptors, *tPSA* – topological polar surface area

Common name	2D formula	*MW* g mol^{-1}	log *P*	*HBD*	*HBA*	*tPSA* Å^2
Methasterone	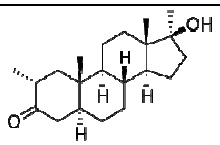	318.5	4.5	1	2	37.3
Methyl-1-testosterone	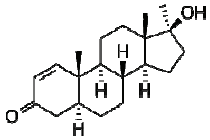	302.5	4.1	1	2	37.3
4-Hydroxytestosterone	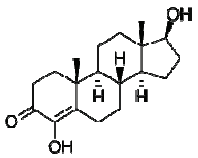	304.4	3.2	2	3	57.5
Methyldienolone	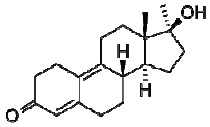	286.4	2.0	1	2	37.3
Methyltrienolone	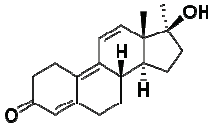	284.4	2.1	1	2	37.3
19-Nor-5-androstene-dione	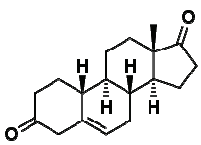	272.4	2.1	0	2	34.1
Oxymetholone	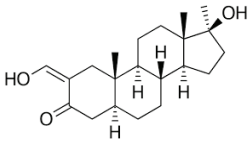	332.5	4.4	1	3	37.5

Predictions obtained using both admetSAR2.0 and ADMETLab2.0 reveal, for all SDs investigated, good human intestinal absorption. This result is in good

correlation with published data disclosing good intestinal absorption of oral steroids[27] in general and of oxymetholone in particular.[14]

Predictions obtained using admetSAR2.0 and ADMETLab2.0 also regarding the ability of SDs to be P-glycoprotein inhibitors are inconsistent, Table IV. ADMETLab2.0 predictions exhibit high probabilities for SDs to be inhibitors of this protein, while admetSAR2.0 predicts that SDs are not inhibitors of P-glycoprotein. This inconsistency may be due to the different models used by the two prediction tools to evaluate this effect. Testosterone is known to be an endogenous substrate of P-glycoprotein[34] and it is expected that its derivatives may also interact with this protein. Further experimental investigations are needed to evaluate the ability of the investigated compounds to inhibit P-glycoprotein.

TABLE IV. Absorption, distribution and excretion profiles of the investigated steroids obtained using admetSAR2.0 and ADMETLab2.0 prediction tools; the data represent the probabilities that the analysed compounds are involved in the following processes: *HIA* – human intestinal absorption, *BBBP* – blood brain barrier penetration, *P-gpi* – inhibitor of the P-glycoprotein, *P-gps* – substrate of the P-glycoprotein, *PPB* – plasma protein binding, *CL* – clearance

Steroid	admetSAR2.0				ADMETLab2.0					
	HIA	*P-gpi*	*P-gps*	*BBBP*	*HIA*	*P-gpi*	*P-gps*	*BBBP*	*PPB* %	*CL* / mL min^{-1} kg^{-1}
Methasterone	0.985	–0.662	–0.823	–0.271	0.982	0.600	0.000	–0.924	95.89	21.338
Methyl-1-testosterone	0.989	–0.732	–0.795	–0.350	0.995	0.974	0.000	–0.419	95.31	18.841
4-Hydroxytestosterone	0.986	–0.581	–0.925	–0.310	0.988	0.971	0.000	–0.484	90.74	18.459
Methyldienolone	0.993	–0.760	–0.819	–0.735	0.978	0.945	0.005	–0.050	87.92	7.716
Methyltrienolone	0.989	–0.845	–0.801	–0.735	0.927	0.997	0.022	–0.127	90.05	5.957
19-Nor-5-androstenedione	0.990	–0.718	–0.841	–0.262	0.992	0.939	0.001	–0.348	88.71	14.532
Oxymetholone	0.771	–0.754	–0.842	0.700	0.986	0.295	0.000	–0.152	66.54	19.616

The investigated SDs are not considered as being able to penetrate the blood brain barrier (BBB) through passive diffusion. This prediction seems to be in contradiction with expected ability of the AAS, due to their low molecular weight and lipophilic character, to penetrate the BBB through passive diffusion. However, even if AAS are known to strongly influence the central nervous system (CNS), the modality how they enter the CNS through the BBB is still poorly understood.[35]

All investigated SDs are able to bind to plasma proteins, but methasterone and methyl-1-testosterone emphasize high levels of plasma protein binding (more than 90 %). This limits their distribution from the blood to the tissues to be meta-

bolized and prolongs their half-life. The binding of several other steroids to plasma proteins has also been studied, and it has been observed that steroids, including oxymetholone, are transported in the blood by their binding to human serum albumin, sex hormone-binding globulin, and corticosteroid-binding globulin.[36]

Regarding metabolism, both prediction tools reveal that none of the SDs investigated in this study, nor the control oxymetholone, are considered cytochrome (CYP) inhibitors involved in xenobiotic metabolism (Tables S-II and S-III of the Supplementary material). Data obtained through *in vitro* experiments show that oxymetholone is able to bind weakly to CYP enzymes, but these interactions have no clinical significance, oxymetholone is not considered an inhibitor of CYPs, nor is it metabolized by these enzymes.[14] It means that investigated SDs do not interfere with drugs or endogenous compounds that are metabolized by these enzymes and do not cause unanticipated adverse reactions or therapeutic failures. Methasterone and methyl-1-testosterone reveal high probabilities of being substrates for CYP2C19, and there are reasonable probabilities for the other SDs to be substrates for CYP3A4. The predictions of the interactions of the investigated SDs with human CYPs are in good correlation with the known data revealing that testosterone is considered as one of the CYP3A4 substrates.[37] An experimental study highlighted that 17 steroids demonstrated strong interactions with CYP3A4 and moderate interactions with CYP2C9, CYP1A2 and CYP2D6.[38] Other steroids showed the ability to interact with CYP2C9 in a computational study.[8]

The prediction of some of the toxicological effects of the investigated SDs are revealed in Fig. 1 and Table S-IV of the Supplementary material.

Fig. 1 highlights that none of the investigated SDs can produce nephrotoxicity, cardiotoxicity through potassium channel inhibition (h-ERG), and the probabilities of producing hepatotoxic effects are usually low. Regarding the cardiotoxicity of AAS through potassium channel inhibition, there is a good correlation of the obtained predictions with the published information revealing the protective effect of steroids on the potassium channel.[39] Predictions regarding nephrotoxicity are not well correlated with literature data revealing that some AAS have been observed to induce or worsen acute and chronic kidney disease and glomerular toxicity.[40] Regarding hepatotoxicity, published data reveal that AAS may lead to hepatomegaly, liver adenomas, cholestatic hepatitis and hepatocellular carcinoma.[8] The high probability revealed by the ADMETLab2.0 tool that oxymetholone induces hepatotoxicity is in agreement with the known information that high doses of oxymetholone have resulted in hepatotoxicity.[14]

The data obtained show that it is possible that the investigated SDs have an impact on the respiratory system and may induce respiratory toxicity (respiratory sensitization, respiratory allergy, rhinitis, asthma).[41] This prediction is in good

correlation with published data revealing that ASA produced acute dyspnea and pulmonary haemorrhage.[42]

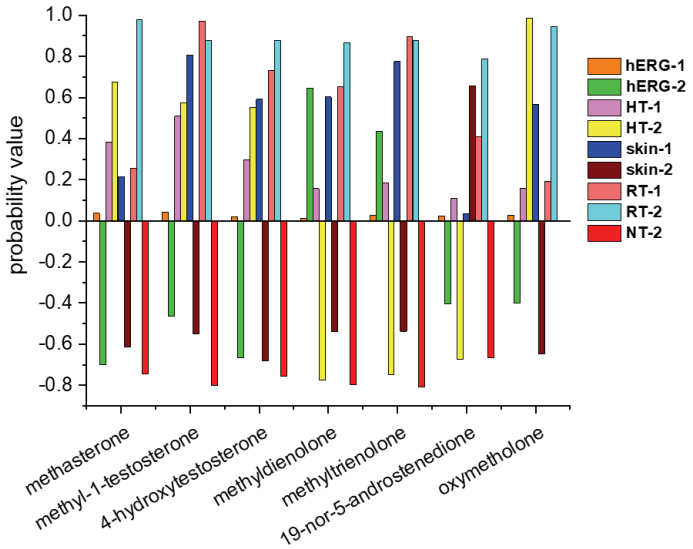

Fig. 1. Predictions regarding the cardiotoxicity (h-ERG), hepatotoxicity (HT), skin sensitization potential (skin), respiratory toxicity (RT) and nephrotoxicity (NT) obtained using ADMETLab2.0 (1) and admetSAR2.0 (2) tools. ADMETLab2.0 does not output information regarding nephrotoxicity.

There is an inconsistency in the predictions regarding the skin sensitization potential of these molecules: ADMETALab2.0 usually predict skin sensitization potential, but admetSAR2.0 predict non skin sensitization potential, with the exception of 19-nor-5-androstenedione that exposes a reasonable probability to produce skin sensitization. Due to this inconsistency, the ability of the investigated SD to produce skin sensitization is also investigated by using PredSkin3.0 prediction tool (see further).

The outcomes of the admetSAR2.0 tool indicate reproductive toxicity of all investigated SDs and high values for the probabilities of these compounds to affect the nuclear receptors (Fig. 2).

All investigated SDs reveal high probabilities to produce reproductive toxicity and to affect the nuclear receptors, excepting the peroxisome proliferators-activated protein (PPAR) gamma. Predictions obtained using ADMETLab2.0 tool also reveal probabilities with reasonable values that the SDs under consideration affect the binding domain of several nuclear receptors (Table S-V of the Supplementary material), excepting PPAR gamma. This result is in good correlation with published data reflecting that numerous synthetic steroids, are able to interact with the nuclear receptors.[42] A molecular docking study revealed that the

synthetic anabolic steroids methandrostenolone, oxandrolone, oxymetholone and stanozolol were able to bind to the human androgen receptor, oestrogen receptor alpha and thyroid receptor.[8]

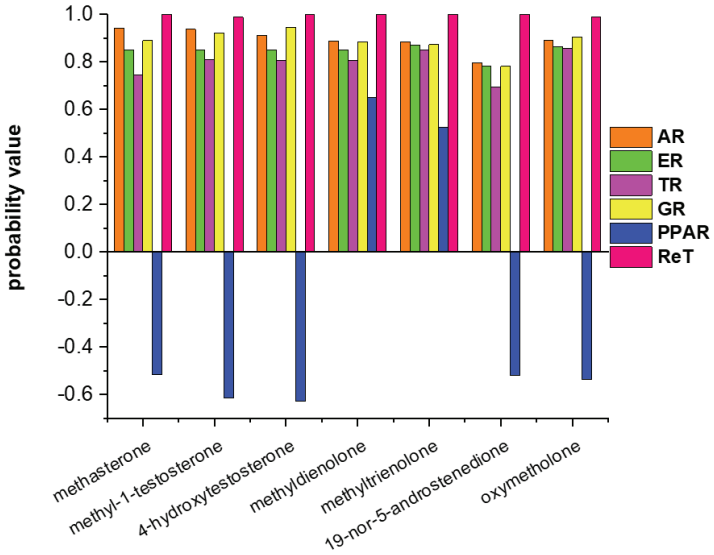

Fig. 2. Predicted values for the probabilities of the investigated steroids to produce reproductive toxicity (ReT) and to affect the nuclear receptors: AR – androgen receptor, ER – oestrogen receptor alpha, TR – thyroid receptor, GR – glucocorticoid receptor, PPAR– peroxisome proliferator-activated receptor gamma.

The Endocrine Disruptome computational tool was also used to obtain predictions regarding the interactions of the investigated SDs with the nuclear receptor, the results being revealed in Fig. 3.

All investigated SDs exhibit the potential for endocrine disruption. The most affected are androgen, oestrogen and thyroid receptors. Peroxisome proliferator-activated α, β and γ receptors are not affected or the possible effect is low. These predictions are in good correlation with those obtained using both ADMETLab2.0 and admetSAR2.0 tools. This result is also in line with literature data revealing the reproductive toxicity and endocrine-disrupting potential of numerous steroids, including oxymetholone.[6,8,42] It should be noted that AAS are expected to bind mainly to the androgen receptor, but their non-specific binding to the other nuclear receptors may be due to the fact that the nuclear receptors share a common spatial structure with a well-conserved ligand-binding domain.[43]

Predictions of the skin sensitization potential of the investigated SDs obtained using the PredSkin3.0 tool are revealed in Table V. Visualization of probability maps illustrating the contribution of different fragments to skin sen-

sitization, which was constructed based on human repeat insult patch and human maximization (HRIPT/HMT) models is revealed in Fig. 4.

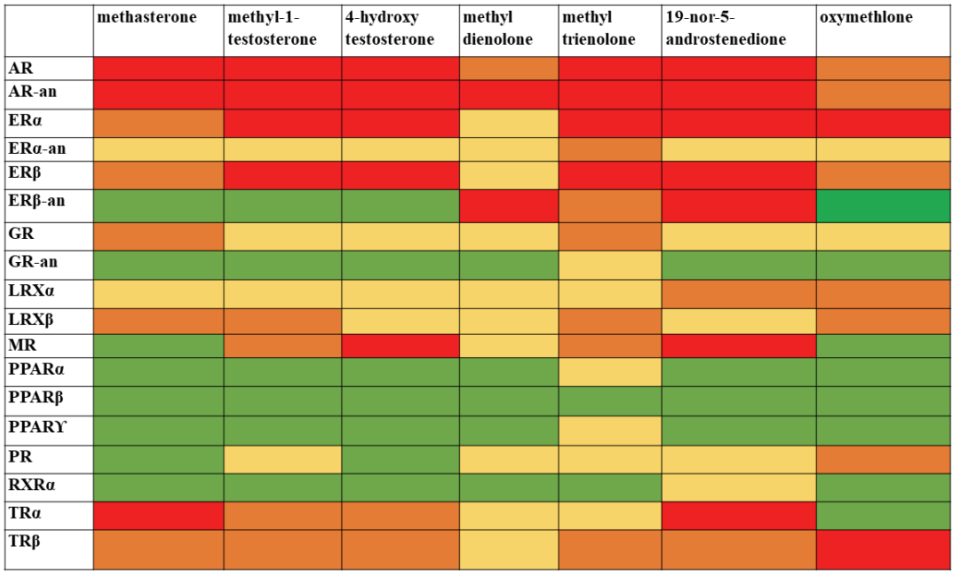

Fig. 3. Endocrine Disruptome predictions of steroid derivatives binding to nuclear receptors: androgen receptor (AR) both agonistic and antagonistic (an) interactions, oestrogen receptors (ER) α and β, glucocorticoid receptor (GR) both agonistic and antagonistic interactions (an), progesterone receptor (PR), liver X receptors (LXR) α and β, peroxisome proliferator activated receptors (PPAR) α, β and γ, retinoid X receptor (RXR) α, and thyroid receptors (TR) α and β. Red cells reveal high effect, orange grey cells reveal mean effect, yellow cells reveal low effect and green cells reveal no effect of the steroids derivatives on the nuclear receptors.

TABLE V. Predictions of the skin sensitization potential of the investigated steroid derivatives based on the following models: DPRA – direct peptide reactive assay, HRIPT/HMT human repeat insult patch and human maximization, KeratinoSens – activation of a cytoprotective pathway in keratinocytes, h-CLAT – human cell line activation test, LLNA – local lymph node assay. The sign ”+” indicates skin sensitization potential and the sign ”–” indicates the absence of skin sensitization potential

Steroid	DPRA	HRIPT/HMT	KerationoSens	h-CLAT	LLNA	Bayesian outcome
Methasterone	+	+	–	+	–	+
Methyl-1-testosterone	+	+	+	+	+	+
4-Hydroxytestosterone	+	+	–	+	–	+
Methyldienolone	+	+	–	+	–	+
Methyltrienolone	+	+	+	+	–	+
19-Nor-5-androstenedione	+	+	–	+	+	+
Oxymetholone	+	+	+	+	–	+

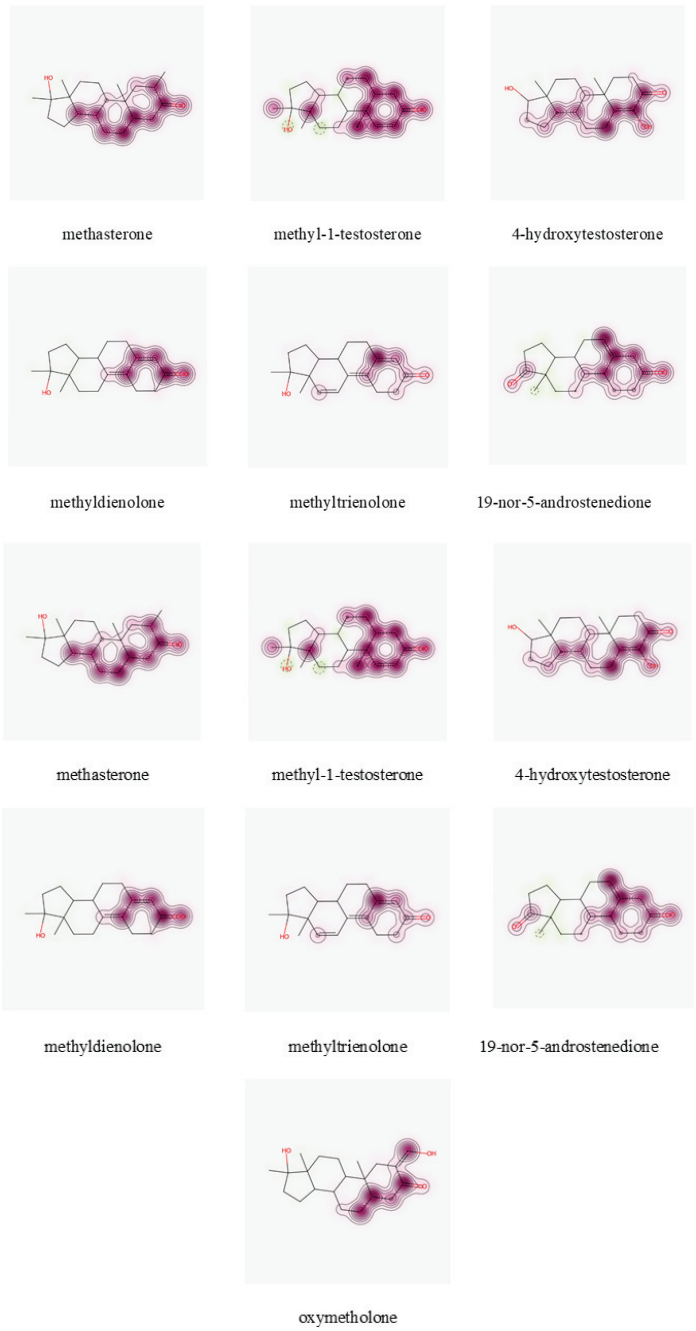

Fig. 4. Visualization of the probability maps illustrating the contribution of various fragment (magenta regions) toward skin sensitization, build based on the human repeated insult patch and human maximization (HRIPT/HMT) models for the investigated steroids derivatives.

The data presented in Table V and Fig. 4 highlight that all investigated SDs have skin sensitization potential. This prediction is in good correlation with the literature data that emphasize several skin effects of AAS use: acne, epidermoid cysts, folliculitis, furunculosis, oily skin and hair, seborrheic dermatitis, *etc*.[44]

Predictions obtained in this study for the SDs do not always correlate with literature data that were obtained for numerous AAS. A possible reason of the mismatch is the fact that the obtained predictions do not take into account the amount of the chemical compound that was ingested (this being a common week point of the *in silico* prediction tools), whereas many of the published papers, highlighting the toxicological effects, mention the high doses of AAS. However, both predictions and published data emphasize the need to implement clinical studies on the potential of the SDs, investigated in this study, to produce toxicological effects before they are approved for human use.

CONCLUSION

The investigated SDs reveal good human intestinal absorption, the inability to penetrate the blood–brain barrier by passive diffusion, and the ability to bind to cytochromes involved in xenobiotic metabolism as substrates or inhibitors. Methasterone and methyl-1-testosterone show high levels of plasma protein binding and moderate clearance. The toxicity evaluation reveals that the investigated SDs can be harmful to human health, causing a diversity of side effects: respiratory toxicity, endocrine disruption, reproductive toxicity, and skin sensitization.

These findings are important for both practitioners and consumers of dietary supplements, especially for the supplements that are intended to enhance physical activity. Potential toxicity should be considered, as many dietary supplements contain designer steroids, which are sometimes not labelled as ingredients and are easily bought on the Internet without any controls. Considering all these adverse effects, consumers should be warned about using either steroid derivatives or dietary supplements that may contain them.

SUPPLEMENTARY MATERIAL

Additional data and information are available electronically at the pages of journal website: https://www.shd-pub.org.rs/index.php/JSCS/article/view/12525, or from the corresponding author on request.

ИЗВОД

ADMET ПРОФИЛИ ОДАБРАНИХ ДЕРИВАТА АНАБОЛИЧКИХ СТЕРОИДА

ANDREI BITANG[1], VIOREL BITANG[1], VLAD GROSU[2], ALECU CIORSAC[3]и ADRIANA ISVORAN[4]

[1]Department of Physical Education and Sports Performance, Faculty of Physical Education and Sport, "Aurel Vlaicu" University of Arad, Romania, [2]Mechatronics and Mechanical Engineering Department, Faculty of Automotive, Technical University of Cluj Napoca, Romania, [3]Department of Physical Education and Sport, University Politehnica Timisoara, Romania и [4]Department of Biology-Chemistry and Advanced Environmental Research Laboratories, West University of Timisoara, Romania

Постоји контрола употребе и трговања стероидима, али такође су синтетисани нови стероидни деривати, једињења која опонашају њихов ефекат. Они се често производе као дијетески суплементи који треба да поправе физичку активност, а обично се не дају информације у погледу састојака, дозе, и ефикасности или безбедности. У овој студији се користи рачунарски приступ да би се проценили ADMET профили неколико стероидних деривата: метастерона, метил-1-тестостерона, 4-хидрокситестостерона, метилдиенолона, метилтриенолона, 19-нор-5-андростендиона. Примењена су следећа оруђа за рачунарско предвиђање: admetSAR2.0, ADMETLab2.0, Endocrine Disruptome, PredSkin3.0. Сва истраживана једињења су показала добру апсорпцију у људској утроби, не могу да прођу баријеру између крви и мозга, и инхибирају ензиме цитохрома P450 који су укључени у метаболизам ксенобиотика. Ова једињења имају потенцијал за сензибилизацију коже, да индукују токсичност у репродукцији и ендокрине поремећаје, те имају низак потенцијал за тровање крви и дисајних органа. Резултати ове студије треба да буду познати онима који су изложени на радним местима где се ова једињења праве и пакују, те потрошачима. Ова предвиђања могу такође усмеравати експериментално процењивање могуће токсичноости испитиваних једињења, чији резултати се могу даље користити у сврху регулисања ових стероидних деривата.

(Примљено 3. августа, ревидирано 25. септембра, прихваћено 5. новембра 2023)

REFERENCES

1. National institute for Drug Abuse, *Steroids and Other Appearance and Performance Enhancing Drugs (APEDs) Research Report 2018* (https://nida.nih.gov/download/815/steroids-other-appearance-performance-enhancing-drugs-apeds-research-report.pdf?v=b864e9e791bbde96f1c35024bc52084f, accessed on February 2023)
2. R. Kazlauskas, *Handb. Exp. Pharmacol.* **195** (2010) 155 (https://doi.org/10.1007/978-3-540-79088-4_7)
3. N. Fabresse, I. Larabi, A. Knapp, C. Mayer, J. Alvarez, *Toxicol. Anal. Clin.* **31** (2019) S52 (https://doi.org/10.1016/j.toxac.2019.03.074)
4. L. M. Lorenz, V. M. Toomey, A. C. Lanzarotta, R. A. Flurer, T. M. Falconer, *Drug. Test. Anal.* **11** (2019) 1109 (https://doi.org/10.1002/dta.2589)
5. A. Grönbladh, E. Nylander, M. Hallberg, *Brain. Res. Bull.* **126** (2016) 127 (https://doi.org/10.1016/j.brainresbull.2016.05.003)
6. A. A. Ciorsac, I. Popescu, A. Isvoran, *Rom. J. Phys.* **60** (2015) 1112 (https://rjp.nipne.ro/2015_60_7-8/RomJPhys.60.p1112.pdf)
7. R. Solimini, M. C. Rotolo, L. Mastrobattista, C. Mortali, A. Minutillo, S. Pichini, R. Pacifici, I. Palmi, *Eur. Rev. Med. Pharmacol. Sci.* **21** (2017) 7 (https://www.europeanreview.org/article/12427)

8. M. Roman, D. L. Roman, V. Ostafe, A. Ciorsac, A. Isvoran, *Pharm. Res.* **35** (2018) 41 (https://doi.org/10.1007/s11095-018-2353-1)
9. D. S. Wishart, C. Knox, A. C. Guo, S. Shrivastava, M. Hassanali, P. Stothard, Z. Chang, J. Woolsey, *Nucleic Acids Res.* **34** (2006) D668 (https://doi.org/10.1093/nar/gkj067)
10. K. Nyssanbayeva, V. Abdulla, Y. Semenova, M. Bakasheva, D. Sagoe, N. Glushkova, *Subst. Use Misuse* (2023) (https://doi.org/10.1080/10826084.2023.2257317)
11. L. Turnock, N. Gibbs, *Perform. Enhanc. Health* **11** (2023) 100251 (https://doi.org/10.1016/j.peh.2023.100251)
12. L. Cox, N. Gibbs, L. A. Turnock, *Drugs: Educ. Prev. Policy* (2023) (https://doi.org/10.1080/09687637.2023.2176286)
13. S. Kim, J. Chen, T. Cheng, A. Gindulyte, J. He, S. He, Q. Li, B. A. Shoemaker, P. A. Thiessen, B. Yu, L. Zaslavsky, J. Zhang, E. E. Bolton, *Nucl. Acids Res.* **49** (2021) D1388 (https://doi.org/10.1093/nar/gkaa971)
14. M. Abdollahi, M Pakzad. *Encyclopedia of Toxicology*, 3rd ed., 2014, p. 744 (http://dx.doi.org/10.1016/B978-0-12-386454-3.01150-7)
15. H. Yang, C. Lou, L. Sun, J. Li, Y. Cai, Z. Wang, W. Li, G. Liu, Y. Tang, *Bioinformatics* **35** (2019) 1067 (https://doi.org/10.1093/bioinformatics/bty707)
16. G. Xiong, Z. Wu, J. Yi, L. Fu, Z. Yang, C. Hsieh, M. Yin, X. Zeng, C. Wu, A. Lu, X. Chen, T. Hou, D. Cao, *Nucl. Acids Res.* **49** (2021) W5 (https://doi.org/10.1093/nar/gkab255)
17. K. Kolšek, J. Mavri, M. Sollner Dolenc, S. Gobec, S. Turk, *J. Chem. Inf. Model.* **54** (2014) 1254 (https://doi.org/10.1021/ci400649p)
18. V. M. Alves, R. C. Braga, E. Muratov, C. H. Andrade, *J. Braz. Chem. Soc.* **29** (2018) 982 (http://dx.doi.org/10.21577/0103-5053.20180013)
19. D. L. Roman, M. Roman, C. Som, M. Schmutz, E. Hernandez, P. Wick, T. Casalini, G. Perale, V. Ostafe, A. Isvoran, *Front. Bioeng. Biotechnol.* **7** (2019) 214 (https://doi.org/10.3389/fbioe.2019.00214)
20. B. V. Boros, D. Dascalu, V. Ostafe, A. Isvoran, *Molecules* **27** (2022) 6123 (https://doi.org/10.3390/molecules27186123)
21. A. Isvoran, A. Ciorsac, V. Ostafe, *ADMET & DMPK* **5** (2017) 192 (https://doi.org/10.5599/admet.5.3.423)
22. V. M. Alves, E. N. Muratov, A. Zakharov, N. N. Muratov, C. H. Andrade, A. Tropsha, *Food. Chem. Toxicol.* **112** (2018) 526 (https://doi.org/10.1016/j.fct.2017.04.008)
23. D. Craciun, D. Dascalu, A. Isvoran, *Studia UBB Chemia* **LXIV** (2019) 71 (https://doi.org/10.24193/subbchem.2019.4.06)
24. D. L. Roman, A. Isvoran, M. Filip, V. Ostafe, M. Zinn, *Front. Bioeng. Biotechnol.* **8** (2020) 584010 (https://doi.org/10.3389/fbioe.2020.584010)
25. D. Dascălu, D. L. Roman, M. Filip, A. Ciorsac, V. Ostafe, A. Isvoran, *ADMET & DMPK* **8** (2020) 425 (https://doi.org/10.5599/admet.843)
26. D. I. Voiculescu, V. Ostafe, A. Isvoran, *Farmacia* **69** (2021) 1032 (https://doi.org/10.31925/farmacia.2021.6.3)
27. I. M. Gridan, A. A. Ciorsac, A. Isvoran, *ADMET & DMPK* **7** (2019) 161 (https://doi.org/10.5599/admet.668)
28. D. I. Voiculescu, D. L. Roman, V. Ostafe, A. Isvoran, *Molecules* **27** (2022) 4682 (https://doi.org/10.3390/molecules27154682)
29. D. L. Roman, D. I. Voiculescu, M. A. Matica, V. Baerle, M. N. Filimon, V. Ostafe, A. Isvoran, *Molecules* **27** (2022) 6554 (https://doi.org/10.3390/molecules27196554)

30. D. Dascalu, A. Isvoran, N. Ianovici, *Molecules* **28** (2023) 4640. (https://doi.org/10.3390/molecules28124640)
31. C. A. Lipinski, F. Lombardo, B. W. Dominy, P. J. Feeney, *Adv. Drug. Deliv. Rev.* **46** (2001) 3 (https://doi.org/10.1016/S0169-409X(00)00129-0)
32. J. D. Hughes, J. Blagg, D. A. Price, S. Bailey, G. A. Decrescenzo, R. V. Devraj, E. Ellsworth, Y. M. Fobian, M. E. Gibbs, R. W. Gilles, N. Greene, E. Huang, T. Krieger--Burke, J. Loesel, T. Wager, L. Whiteley, Y. Zhang, *Bioorg. Med. Chem. Lett.* **18** (2008) 4872 (https://doi.org/10.1016/j.bmcl.2008.07.071)
33. D. Gadaleta, G. F. Mangiatordi, M. Catto, A. Carotti, O. Nicolotti, *Int. J. Quant. Struct. Prop. Relat.* **1** (2016) 45 (https://doi.org/10.4018/IJQSPR.2016010102)
34. K. Yano, S. Seto, H. Kamioka, K. Mizoi, T. Ogihara, *Biochem. Biophys. Res. Commun.* **520** (2019) 166 (https://doi.org/10.1016/j.bbrc.2019.09.067)
35. N. Okamoto, N. Yamanaka, *Curr. Biol.* **30** (2020) 359 (https://doi.org/10.1016/j.cub.2019.11.085)
36. G. L. Hammond, *J. Endocrinol.* **230** (2016) R13 (https://doi.org/10.1530/JOE-16-0070)
37. K. A. Usmani, J. Tang, *Curr. Protoc. Toxicol.* **4** (2004) Unit4.13. (https://doi.org/10.1002/0471140856.tx0413s20)
38. C. E. Wang, Y. F. Cao, H. Kurihara, Z. Z. Fang, R. R. He, *Lat. Am. J. Pharm.* **33** (2014) 1326 (http://www.latamjpharm.org/resumenes/33/8/LAJOP_33_8_1_13.pdf)
39. D. Davani-Davari, I. Karimzadeh, H. Khalili, *BMC Nephrol.* **20** (2019) 198. (https://doi.org/10.1186/s12882-019-1384-0)
40. K. Sakamoto, J. Kurokawa. *J. Pharmacol. Sci.* **139** (2019) 259 (https://doi.org/10.1016/j.jphs.2019.02.009)
41. Z. Wang, P. Zhao, X. Zhang, X. Xu, W. Li, G. Liu, Y. Tang, *Comput. Toxicol.* **18** (2021) 100155 (https://doi.org/10.1016/j.comtox.2021.100155)
42. H. S. Hvid-Jensen, F. Rasmussen, E. Bendstrup, *Respir. Med. Case. Rep.* **18** (2016) 45 (https://doi.org/10.1016/j.rmcr.2016.04.001)
43. R. Sever, C. K. Glass, *Cold Spring Harb Perspect Biol.* **5** (2013) a016709 (https://doi.org/10.1101/cshperspect.a016709)
44. L. Varticovski, D. A. Stavreva, A. McGowan, R. Raziuddin, G. L. Hager, *Mol. Cell. Endocrinol.* **539** (2022) 111415 (https://doi.org/10.1016/j.mce.2021.111415).

Journal of the Serbian Chemical Society
JSCS@tmf.bg.ac.rs • www.shd.org.rs/JSCS
J. Serb. Chem. Soc. 89 (3) S131–S133 (2024) *Supplementary material*

SUPPLEMENTARY MATERIAL TO

ADMET profiles of selected anabolic steroid derivatives

ANDREI BITANG[1], VIOREL BITANG[1], VLAD GROSU[2], ALECU CIORSAC[3] and ADRIANA ISVORAN[4]*

[1]*Department of Physical Education and Sports Performance, Faculty of Physical Education and Sport, "Aurel Vlaicu" University of Arad, Romania,* [2]*Mechatronics and Mechanical Engineering Department, Faculty of Automotive, Technical University of Cluj Napoca, Romania,* [3]*Department of Physical Education and Sport, University Politehnica Timisoara, Romania and* [4]*Department of Biology-Chemistry and Advanced Environmental Research Laboratories, West University of Timisoara, Romania*

J. Serb. Chem. Soc. 89 (3) (2024) 367–382

Table S-I. Fulfilment, by the investigated steroids, of the rules revealing oral bioavailability (Lipinski) and safety (Pfizer and GSK)

Steoid	Lipinski rule	Pfizer rule
methasterone	+	-
methyl-1-testosterone	+	-
4-hydroxytestosterone	+	+
methyldienolone	+	+
methyltrienolone	+	+
19-nor-5-androstenedione	+	+
oxymetholone	+	+

* Corresponding author. E-mail: adriana.isvoran@e-uvt.to

Table S-II. ADMETLab2.0 prediction of the probability that the investigated steroid derivatives are substrates/inhibitors of human cytochromes (CYPs) involved in xenobiotic metabolism.

Steroid name / cytochrome	substrate					inhibitor				
	CYP1A2	CYP2C19	CYP2C9	CYP2D6	CYP3A4	CYP1A2	CYP2C19	CYP2C9	CYP2D6	CYP3A4
methasterone	0.666	0.951	0.308	0.866	0.641	0.066	0.092	0.263	0.012	0.309
methyl-1-testosterone	0.561	0.923	0.180	0.471	0.869	0.060	0.415	0.249	0.095	0.740
4-hydroxy testosterone	0.585	0.732	0.161	0.845	0.269	0.105	0.085	0.240	0.013	0.056
Methyl dienolone	0.528	0.458	0.149	0.125	0.707	0.143	0.088	0.230	0.492	0.323
Methyl trienolone	0.404	0.730	0.161	0.066	0.726	0.229	0.165	0.210	0.572	0.844
19-nor-5-androstenedione	0.705	0.749	0.803	0.884	0.628	0.087	0.170	0.339	0.007	0.237
oxymtholone	0.665	0.891	0.164	0.617	0.598	0.024	0.045	0.175	0.014	0.439

Table S-III. admetSAR2.0 prediction of the probability that the investigated steroid derivatives to be substrates/inhibitors of the human cytochromes (CYP) involved in metabolism of xenobiotics.

Steroid name / cytochrome	substrate			inhibitor				
	CYP2C9s	CYP2D6s	CYP3A4s	CYP1A2i	CYP2C19i	CYP2C9i	CYP2D6i	CYP3A4i
methasterone	-0.827	-0.803	0.689	-0.500	-0.872	-0.690	-0.973	-0.858
methyl-1-testosterone	-1.000	-0.880	0.677	-0.598	-0.766	-0.810	-0.969	-0.844
4-hydroxy testosterone	-0.728	-0.852	0.751	-0.893	-0.860	-0.928	-0.936	-0.881
Methyl dienolone	-0.828	-0.892	0.686	-0.900	-0.666	-0.950	-0.945	-0.881
Methyl trienolone	-1.000	-0.900	0.671	-0.900	-0.666	-0.950	-0.945	-0.881
19-nor-5-androstenedione	-0.788	-0.788	0.544	-0.826	-0.790	-0.927	-0.940	-0.865
oxymetholone	-1.000	-0.871	0.688	-0.838	-0.863	-0.857	-0.964	-0.806

Table S-IV. Predicted values for the probabilities of the investigated steroids to produce toxicological effects

Steroid name/prediction tool toxicity	ADMETLab2.0				admetSAR2.0			
	Carc.	Ames mut.	Eye corr.	Eye irr.	Carc.	Ames mut.	Eye corr.	Eye irr.
methasterone	0.062	0.039	0.003	0.016	-0.900	-0.980	-0.988	-0.941
methyl-1-testosterone	0.499	0.011	0.004	0.021	-0.900	-0.910	-0.991	-0.978
4-hydroxytestosterone	0.058	0.049	0.003	0.012	-1.000	-0.830	-0.994	-0.939
methyldienolone	0.634	0.031	0.003	0.014	-0.971	-0.910	-0.994	-0.932
methyltrienolone	0.881	0.016	0.003	0.014	-0.914	-0.780	-0.994	-0.974
19-nor-5-androstenedione	0.874	0.017	0.003	0.031	-0.900	-0.930	-0.987	-0.920
oxymetholone	0.129	0.013	0.004	0.017	-0.970	-0.960	-0.995	-0.996

Carc. – Carcinogenicity: Ames mut. - Ames mutagenesis, Eye corr. - Eye corrosion; Eye irr. - Eye irritation

Table S-V. Predicted values for the probabilities of the investigated steroids to bind to nuclear receptors (NR): AR – androgen receptor, LBD – ligand binding domain, AhR – aryl hydrocarbon receptor, ER – estrogen receptor, PPAR gamma – peroxisome proliferator-activated receptor gamma.

Steroid name / effect on the nuclear receptors	NR-AR	NR-AR-LBD	NR-AhR	NR-ER	NR-ER-LBD	NR-PPAR-gamma
methasterone	0.092	0.239	0.001	0.323	0.833	0.015
methyl-1-testosterone	0.079	0.743	0.000	0.182	0.850	0.022
4-hydroxytestosterone	0.061	0.025	0.000	0.186	0.816	0.158
methyldienolone	0.766	0.940	0.058	0.619	0.735	0.633
methyltrienolone	0.843	0.979	0.064	0.739	0.821	0.871
19-nor-5-androstenedione	0.710	0.793	0.033	0.87	0.844	0.667
oxymetholone	0.459	0.691	0.001	0.119	0.553	0.732

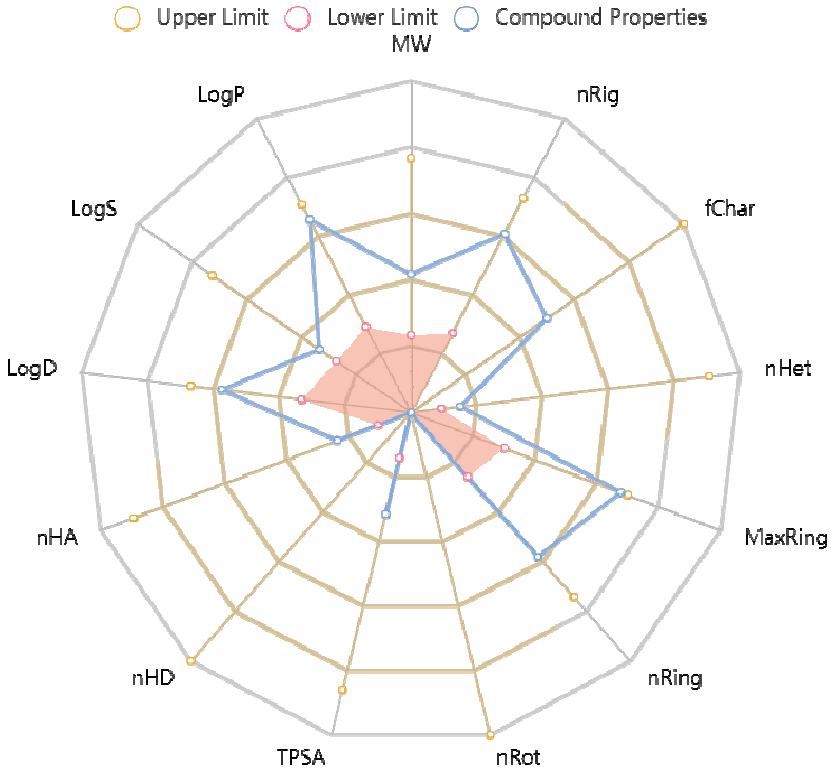

Figure S-1. The distribution of the properties of 19-nor-5-androstenedione (blue line) compared to the properties considered by the prediction models (yellow zone).

Journal of the Serbian Chemical Society
JSCS@tmf.bg.ac.rs • www.shd.org.rs/JSCS
J. Serb. Chem. Soc. *89* (3) 383–397 (2024)
JSCS–5727
Original scientific paper
Published 31 March 2024

An inverse gas chromatography study of the adsorption of organics on zeolite and zeolite/iron oxyhydroxide composite at the infinite and finite surface coverage

SLAVICA S. LAZAREVIĆ[1#]*, MARIJA T. MIHAJLOVIĆ-KOSTIĆ[2], IVONA M. JANKOVIĆ-ČASTVAN[1#], ĐORĐE T. JANAĆKOVIĆ[1#] and RADA D. PETROVIĆ[1#]

[1]*Faculty of Technology and Metallurgy, University of Belgrade, Karnegijeva 4, 11000 Belgrade, Serbia and* [2]*Belgrade Waterworks and Sewerage, Deligradska 28, 11000 Belgrade, Serbia*

(Received 8 September, revised 8 October, accepted 21 November 2023)

Abstract: The surfaces of natural (NZ) and zeolite/iron oxyhydroxide composite (ZFe) samples were analysed by means of inverse gas chromatography (IGC) using the adsorption data of organic non-polar and polar probes, in the infinite and finite-dilution regimes, in the temperature range 483–513 K. The dispersive components of the free energy of adsorption, γ_S, determined by the Gray method, decreased with increasing temperature for both zeolites. The specific interactions were characterised by the specific free adsorption energy change, ΔG_a^S, the specific enthalpy change of adsorption, ΔH_a^S, as well as the donor and acceptor interaction parameters (K_A, K_D) and the basic character of the NZ and ZFe was evidenced. The adsorption isotherms of *n*-hexane, benzene, chloroform and tetrahydrofuran (THF) were determined under finite surface coverage and used to estimate the specific surface area and the adsorption energy distribution. The adsorption capacity of the ZFe was higher than for NZ for all the investigated adsorbates. The specific surface areas and pore size distributions were also determined using nitrogen adsorption–desorption isotherms, *i.e.*, the BET method. It was observed that the nature of the adsorbate and the properties of the solid surface of the initial and modified samples governed the uptake of adsorbates.

Keywords: surface characteristics; electron donor–acceptor properties; specific surface area; adsorption energy distribution.

INTRODUCTION

Zeolites are microporous hydrated crystalline aluminosilicate minerals ($Mx / n[(AlO_2)_x(SiO_2)_y]\cdot zH_2O$, where M are alkali ($n = 1$) or alkaline ($n = 2$) earth metal

* Corresponding author. E-mail: slazarevic@tmf.bg.ac.rs
# Serbian Chemical Society member.
https://doi.org/10.2298/JSC230908093L

cation) consisting of three-dimensional structures of SiO_4 and AlO_4, tetrahedrally linked by oxygen atoms to form a structure which contains channels and cavities. Zeolites are various types of minerals that differ in their formula which generate variation in their Si/Al ratio, amount of cations, framework structure, porosity, surface area, and the surface properties (*e.g.*, hydrophobicity and acidity).[1] The isomorphous replacement of Si^{4+} by Al^{3+} results in a net negative charge that is compensated by alkali and alkaline earth metal cations within the framework. These frameworks are open so cations and water molecules have freedom of movement. As such, they are ideal molecular sieves and a high level of selectivity can be achieved in catalysis and ion-exchange. Due to their unique structure and properties (thermal stability, cage structure of molecule size, ion exchange, *etc*.) zeolites are widely used as adsorbents,[2–5] catalysts[6,7] and cation exchangers.[8,9]

The adsorption properties of natural zeolites have been improved by different physical and chemical modifications.[5] Many researchers reported that mixed systems synthesised from oxides and/or hydroxides of iron (also active adsorbents) and zeolites were able to adsorb high concentrations of inorganic species. The adsorption capacities for Mn^{2+},[10] Cu^{2+},[11] Zn^{2+},[12] and Pb^{2+},[13,14] Cd^{2+} and Zn^{2+},[15,16] As(V)[17] as well as dyes,[18,19] have been significantly increased. The desired impact of surface modification exists in the increase of specific surface area, better distribution of the particles of iron spices within the composite materials, presence of the new functional groups on the surface; ion exchange due to the presence of easily exchangeable ions; and hydroxide precipitation caused by the higher point of zero charge of the modified zeolite compared to natural zeolite.[16] But, the effect of chemical modification on their surface energy has been rarely reported.

Inverse gas chromatography (IGC) is a gas phase technique that provides information on the thermodynamic, surface energy, morphological parameters (such as, surface area and porosity), acid–base properties, glass transition temperatures, surface energy heterogeneity and reaction kinetics associated with gas––solid adsorption and catalytic reactions. In addition, the adsorption characteristics, such as isotherms and heats of adsorption, can be obtained from chromatographic experiments. The term “inverse” refers to reversal of the usual roles of the stationary and mobile phases used in conventional gas chromatography. In inverse gas chromatography, the stationary phase of the chromatographic column (solid material, such as a powder, fibre or film placed in a column) is of interest, in contrast to conventional gas chromatography when the mobile phase is the subject of interest. This stationary phase is then characterised by monitoring its interaction with volatile probe molecules of known properties as they are carried through the column *via* an inert gas. IGC has been widely used to study surface properties of various materials, such as synthetic and biological polymers, copolymers, polymer blends, adsorbents, foods, carbons, clays and catalysts.[20]

The present work was devoted to a detailed analysis of the interactions of natural and of iron oxyhydroxide modified zeolite with organic molecules from the gaseous phase at zero and finite surface coverage using inverse gas chromatography. The retentions of organic compounds of different chemical nature and polarity (non-polar, polar, donor or acceptor) were measured in the temperature range 483–513 K. The objectives of this study were to estimate and to compare: *i*) the thermodynamic parameters of adsorption (enthalpy and entropy), the dispersive and specific interactions of various organics with zeolite samples under infinite surface coverage, *ii*) the acid/base constants of zeolite samples, which describe the ability of a surface to act as electron acceptor or donor; *iii*) the adsorption isotherms and adsorption energy distributions for the adsorption of hexane, benzene, chloroform and tetrahydrofuran onto examined zeolites under finite surface coverage.

EXPERIMENTAL

Natural zeolite (NZ) from the Slanci locality, Serbia, and zeolite modified by iron(III) (ZFe) were used as adsorbents. The natural zeolite contained clinoptilolite as the dominant phase with lower contents of quartz and feldspar. The ZFe was prepared by the addition, under stirring, of 180 mL of 5 M KOH solution to a suspension of 20.0 g of natural zeolite and 100 mL of freshly prepared 1 M $FeCl_3$ solution, according to the method applied for synthesised pure goethite.[11,21] The suspension was diluted with deionized water to 2 L and held in a closed polyethylene flask at 70 °C for 60 h. The obtained brown–reddish precipitate was centrifuged, washed to remove Cl^- and dried at 105 °C. X-Ray diffraction analysis showed lower crystallinity of ZFe in comparison to the parent zeolite, and also that the ZFe contained an amorphous iron phase. According to the results of characterisation and properties, presented in the previous work,[15] it was assumed that an iron oxyhydroxide, phase similar to goethite, but not crystalline, was formed on the zeolite.

The specific surface areas and pore size distributions of the NZ and ZFe were estimated from nitrogen adsorption–desorption isotherms determined using a Micrometrics ASAP 2020 instrument. Before the measurements, the NZ and ZFe were degassed at 240 °C (the highest IGC experimental temperature) for 10 h under reduced pressure. The specific surface areas of samples (S_{BET}) were calculated according to the Brunauer, Emmett, Teller (BET) method from the linear part of the nitrogen adsorption isotherm.[22] The total pore volume (V_{tot}) was given at $p/p_0 = 0.998$. The volume of the mesopores and pore size distribution were analysed according to the Barrett, Joyner and Halenda method from the desorption isotherm.[23] The volume of the microspores was calculated according to *t*-plot analysis[24] using the Harkins–Jura thickness curve.

The following test compounds, purchased from various commercial suppliers, were used as IGC adsorbates: *n*-pentane, *n*-C_6H_{14}, *n*-heptane, *n*-octane, $CHCl_3$, diethyl ether (DEE), ethyl acetate (EtAc), THF, cyclohexane and C_6H_6. All test compounds were of HPLC grade.

IGC measurements were performed on a Perkin Elmer 8700 gas chromatograph equipped with a flame ionization detector (FID). Stainless steel columns with passivated inner walls (50 cm long and 30 cm long, internal diameter of 2.2 mm) were packed with 1.68 g of NZ (in the first series of experiments) and with 1.02 g of ZFe (in the second series of experiments). The two ends of the columns were plugged with silane-treated glass wool. Before the adsorption test of the probes, the columns were stabilised overnight on the GC system at the working

temperature under a nitrogen flow without connection to the detector in order to avoid detector contamination.

High purity nitrogen was used as the carrier gas at a flow rate of 3 cm^3min^{-1} for NZ and 6 $cm^3 min^{-1}$ for ZFe, measured with a soap bubble flowmeter and corrected for the pressure drop in the column using a pressure gradient correction factor (j). The measurements were performed in the temperature range 483–513 K. The injector and the detector temperature were set at 563 and 593 K, respectively.

For the IGC measurements under infinite dilution conditions, minor amounts of gaseous solutes were injected manually, at least in triplicate, which permitted the lateral interactions between adsorbed molecules to be neglected. The chromatograms were collected and the retention volumes determined as the difference between the peak maxima and the column "dead time", measured with methane as a non-interacting marker. In the case of finite surface coverage, amounts from 0.5 to 10 μl of n-C_6H_{14}, C_6H_6, $CHCl_3$ and THF were injected. The retention times and peak areas were based on the average of several injections of each sample.

RESULTS AND DISCUSSION

The specific surface area was measured by the conventional nitrogen adsorption–desorption technique. Adsorption–desorption isotherms at −196 °C on NZ and ZFe and pore volume and pore size distribution are presented in Fig. 1. The measured BET surface area, mesopores and micropores volume, the overall pore volume and D_{max} – the pore size at which the density of the pore size distribution achieves its maximum and D_{ave} – the average pore diameter are given in Table I.

The ZFe sample showed a hysteresis pattern, which was associated with the filling and emptying of the mesopores by capillary condensation, but did not show a plateau at high p/p_0 values. The hysteresis loop is of type H3. The type of hysteresis pattern indicates the presence of slit-like pores.[25] The shape of the nitrogen isotherm for ZFe is characteristic for Type IIb, indicating that the material contained both mesopores, which are responsible for the hysteresis, and macropores, which results in the absence of plateau-like mesoporous Type IV isotherms.[22] The obtained t-plot for ZFe indicates that no micropores were present. The NZ sample showed a low adsorbed volume at low and intermediate relative pressures, indicating a small contribution of micropores to the total pore volume (which was confirmed by t-plot analysis), but a high adsorbed volume and a hysteresis at higher relative pressures. According to Kuila and Prasad[25] the isotherm shape indicates that NZ had negligible micropores and fine mesopores but had a significant volume of larger mesopores and macropores.

The obtained chromatographic peaks for NZ and ZFe were symmetric and had maxima independent of the amount injected, which indicated that the adsorption occurred at zero surface coverage when the lateral interactions between the molecules adsorbed at the surface can be neglected. The net retention volumes, V_N, were calculated according to Eq. (S-1 of the Supplementary material to this paper) and used for the determination of the adsorption enthalpy change, ΔH_a, and adsorption entropy change, ΔS_a (Table II). Generally, more negative values of ΔH_a

correspond to stronger interactions between the adsorbate and adsorbent. As was expected, the ΔH_a values for the *n*-alkane homologous series increased with the chain length, the molecular weight, the boiling points, and the molar refraction for both zeolite samples, NZ and ZFe (Table II). It is evident from the data in Table II that C_6H_6 exhibited a more negative ΔH_a value than the corresponding values for the aliphatic and alicyclic hydrocarbons (*n*-C_6H_{14} and *c*-C_6H_{12}), probably because of the interactions occurring between the π-electrons in the aromatic rings and the surface functional groups. Similar results were found by Diaz *et al.*[26] for the adsorption of *c*-C_6H_{12}, C_6H_6 and *n*-C_6H_{14} onto zeolite 5A and zeolite 13X.

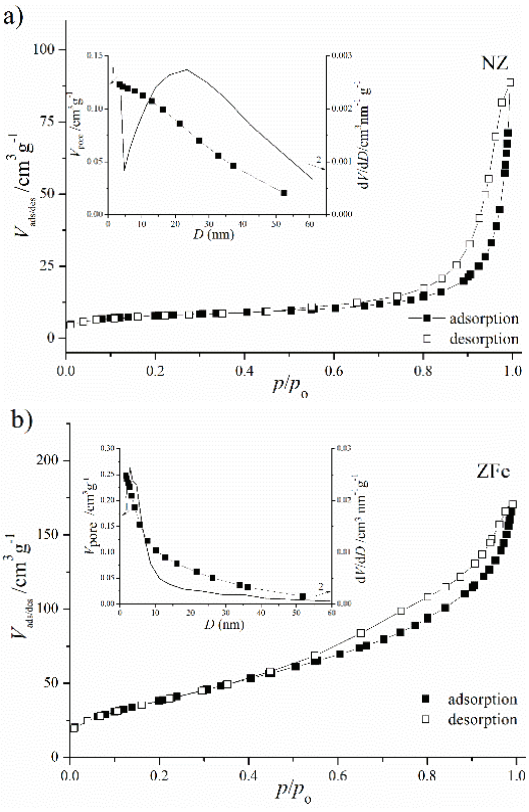

Fig. 1. Nitrogen adsorption/desorption isotherms, pore volume (1) and pore size distribution (2) of NZ (a) and ZFe (b).

The adsorption enthalpies for *n*-alkanes were higher in the case of the ZFe. According to the values of the adsorption enthalpies (Table II) the NZ sample exhibited some larger interactions with DEE, THF, C_6H_6 and *c*-C_6H_{12}, as a result of the presence of Lewis acid and Lewis base sites, whereas the ZFe samples showed stronger interactions with $CHCl_3$ and EtAc, suggesting an increase in donor properties by the formation of layers of iron oxyhydroxide on the surface and in the zeolite structural channels. During the modification, the dimensions of

the channels decreased and some acceptor sites were blocked, resulting in weaker interactions of cyclic and aromatic molecules with the ZFe.

TABLE I. The textural properties of the zeolites (240 °C)

Sample	S_{BET} $m^2 \cdot g^{-1}$	$V_{pore,total}$ $cm^3 \cdot g^{-1}$	$V_{micro,pore}$ $cm^3 \cdot g^{-1}$	$V_{meso,pore}$ $cm^3 \cdot g^{-1}$	D_{max} nm	D_{avg} nm
NZ	27.7	0.126	0.0054	0.123	23.3	20.9
ZFe	143	0.256	0.005	0.248	2.89	6.02

TABLE II. Enthalpy change of adsorption ΔH_a, and entropy change of adsorption ΔS_a, on the NZ and ZFe

Adsorbate	NZ		ZFe	
	$-\Delta H_a$ / kJ mol^{-1}	$-\Delta S_a$ / J mol^{-1} K^{-1}	$-\Delta H_a$ / kJ mol^{-1}	$-\Delta S_a$ / J mol^{-1} K^{-1}
n-C_5H_{12}	13.89	13.3±0.1	17.75	19.4±0.1
n-C_6H_{14}	18.48	19.5 ±0.1	22.97	24.1±0.1
n-C_7H_{16}	21.80	23.3±0.1	27.17	26.0±0.1
n-C_8H_{18}	26.89	30.2±0.1	33.43	32.4±0.1
$CHCl_3$	22.00	25.8±0.2	138.4	267±0.5
EtAc	27.63	21.6±0.1	45.40	56.8±0.2
DEE	33.01	32.3±0.1	20.58	6.70±0.1
THF	37.81	31.4±0.2	20.64	8.70±0.1
c-C_6H_{12}	18.43	18.7±0.1	15.00	8.20±0.1
C_6H_6	52.64	78.4±0.2	50.00	63.4±0.1

The data obtained from the interactions of the zeolite surfaces with *n*-alkanes were used to calculate the dispersive component of the surface free energy, γ_S^d, according to Eq. (S-5) of the Supplementary material. The values of ΔG_{CH2} for different temperatures were calculated as the slopes of the dependences of ΔG_a for *n*-alkanes, calculated according to Eq. (S-2), on the number of carbon atoms in the alkanes, n_C (Fig. 2). As expected, the values of ΔG_a for *n*-alkanes increased linearly with the chain length. The calculated γ_S^d values for NZ were 17.89 mJ m^{-2} at 513 K, 18.37 mJ m^{-2} at 503 K, 19.17 mJ m^{-2} at 493 K and 20.54 mJ m^{-2} at 483 K while for ZFe values were 76.73 mJ m^{-2} (513 K), 77.11 mJ m^{-2} (533 K), 77.18 mJ m^{-2} (493 K) and 77.24 mJ m^{-2} (483 K).

The γ_S^d values for both investigated samples gradually decreased with increasing temperature in the investigated range, whereby the influence of temperature was greater for NZ than for ZFe. This decrease was attributed to the entropic contribution to the surface free energy change. The γ_S^d values for the NZ sample were similar to those reported in the literature,[27,28] while the γ_S^d values for ZFe were higher than those obtained for NZ. As in the case of the ΔH_a values for *n*-alkanes, the higher values of γ_S^d for ZFe in comparison to those for NZ indicated stronger bonds between *n*-alkanes and the surface functional groups of ZFe than with surface of NZ. This could be the result of the existence of structural

heterogeneities on the lateral surface, into which linear alkanes are inserted, as well as the differences in structure, surface area and porosity due to the presence of iron oxyhydroxide in the modified sample.

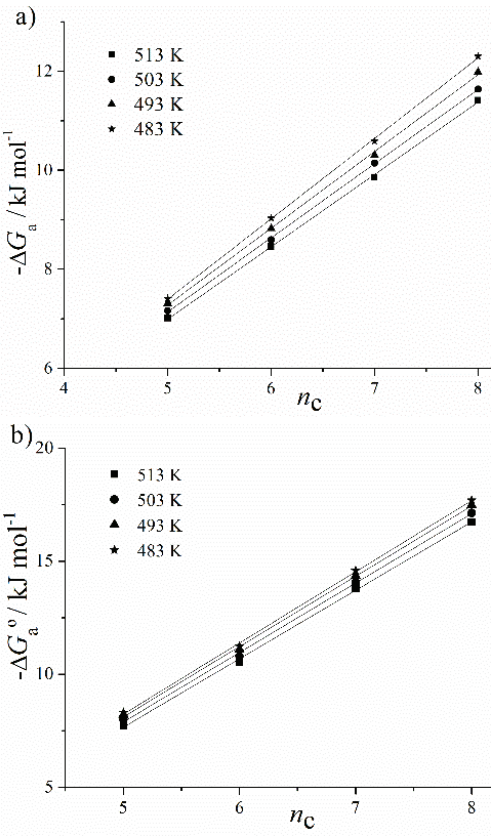

Fig. 2. Plots of ΔG_a *vs*. carbon number of *n*-alkanes for: a) NZ and b) ZFe.

The plot of $-\Delta G_a$ *versus* T_b in the case of *n*-alkanes is straight line, the "alkane line" (Figs. S-1 and S-2 of the Supplementary material). Due to specific interactions, the ΔG_a values for the polar probes are located off the alkane straight line in the dependence of ΔG_a on the adsorbate boiling point, T_b. The specific component of the free energy of adsorption (Table III) was determined from the difference between the free energy of adsorption for a polar probe and the free energy of adsorption for a real or hypothetical *n*-alkane with the same boiling point, T_b. The values presented in Fig. 3 and Table III indicate that the examined powders interact specifically with both a strong acid ($CHCl_3$) and a strong base (THF), exhibiting thereby both donor and acceptor character.

It is obvious that interactions of ZFe with polar probes are stronger than those of NZ, which indicates that the functional groups on the ZFe surface are more polar

than those on the NZ surface. Furthermore, the specific interactions are higher for the aromatic ring (C_6H_6) than for cycloalkanes. When benzene adsorbs on zeolites, there are two kinds of adsorption sites, *i.e.*, Lewis acid sites (hydroxyl protons covalently bonded to oxygen atoms bridging the framework silicon and aluminium atoms and cationic extra framework aluminium species Al^{3+}, $Al(OH)^{2+}$, and $Al(OH)^{2})^{29}$ interact with the benzene ring, and Lewis base sites, oxygen atoms in the zeolite structure, which have a very high interaction with benzene.

TABLE III. The specific free adsorption energy change ($-\Delta G_a^S$) at 513 K and $-\Delta H_a^S$ values of polar probes for NZ and ZFe

Adsorbate	NZ	ZFe	NZ	ZFe
	$-\Delta G_a^S$ /kJ mol^{-1}	$-\Delta G_a^S$ /kJ mol^{-1}	$-\Delta H_a^S$ /kJ mol^{-1}	$-\Delta H_a^S$ /kJ mol^{-1}
$CHCl_3$	6.12	19.0	25.9	34.7
EtAc	8.29	22.7	59.1	67.9
DEE	16.5	30.4	42.2	43.5
THF	15.5	27.3	42.0	40.0
c-C_6H_{12}	4.28	15.0	24.7	32.4
C_6H_6	8.04	21.9	59.0	67.5

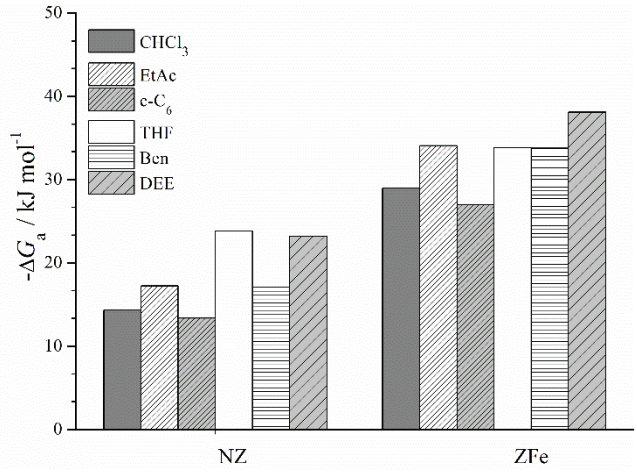

Fig. 3. The free energy change of adsorption (ΔG_a) of the polar probes on NZ and ZFe at 513 K.

The values of the specific enthalpy change of adsorption, ΔH_a^S for polar adsorbates (Table III) were obtained by plotting $\Delta G_a^S/T$ *versus* $1/T$ and used for the determination of the acid constant, K_A, and basic constant K_D according to Eq. (S-8) (Fig. 4). The determined values of K_D and K_A were 2.01 and 0.458 for NZ and 2.97 and 0.413 for ZFe.

The influence of the modification on surface properties of the NZ was confirmed by the values of K_D and K_A. The surface of the NZ exhibited predominantly

basic character with a K_D/K_A ratio of 4.39, but surface of the ZFe showed a higher basic character with the ratio of K_D/K_A = 7.20.

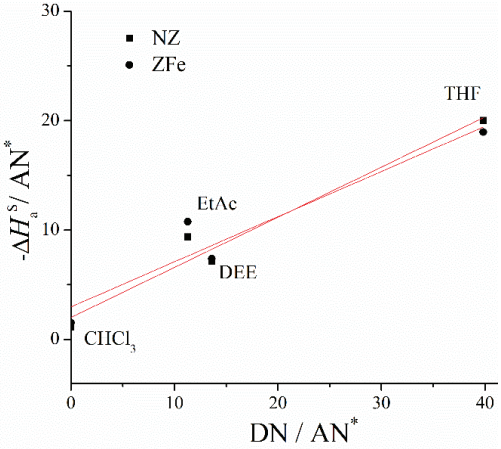

Fig. 4. Plot of $-\Delta H_a^S / AN*$ *versus* DN/ /AN* for the adsorption of polar probes onto NZ and ZFe.

Basic constant K_D is higher and acid constant is lower for ZFe than for NZ. This is the result of the presence of basic Fe–OH groups on ZFe surface due to deposition of Fe-oxyhydroxide during the modification. The acid–base properties of the natural zeolite was in good agreement with those reported for zeolites MgY (basic character, K_D/K_A = 3.50) and NH4Y (basic character, K_D/K_A = 2.61) reported by Bilgic.[27] It should emphasize that both samples interacted strongly with chloroform, which is both an electron donor and electron acceptor. This confirms that apart from having strong donor sites, there are some sites with acceptor properties on the surfaces of the zeolites.

The adsorption behaviour of the natural and modified zeolite samples as a function of both temperature and pressure was investigated by IGC under finite conditions. The adsorption isotherms for *n*-C_6H_{14}, C_6H_6, $CHCl_3$ and THF, plotted as α (mol kg^{-1}) *versus* p (kPa), obtained at the temperature 483, 493, 503 and 513 K, are presented in Figs. 5 and 6, for NZ and ZFe, respectively.

The experimental isotherms were interpreted using the BET equation and the BET fit is represented by dotted lines. The BET plots in the indicated range gave excellent linearity for each adsorbate and for both samples. Monolayer capacity α_m and the BET constant, C, were estimated using the slope and intercept of the corresponding straight lines and listed in Table IV. The α_m values were used for the calculation of the specific surface areas of the zeolites according to Eqs. (S-13) and (S-14) (Table IV).

The adsorption capacity of the ZFe increased for all investigated adsorbates. This was expected because of the higher surface area of ZFe in comparison to NZ

and stronger interactions of used organic molecules with the new functional groups on the ZFe surface, which was proven by ΔG_a determination at infinite coverage.

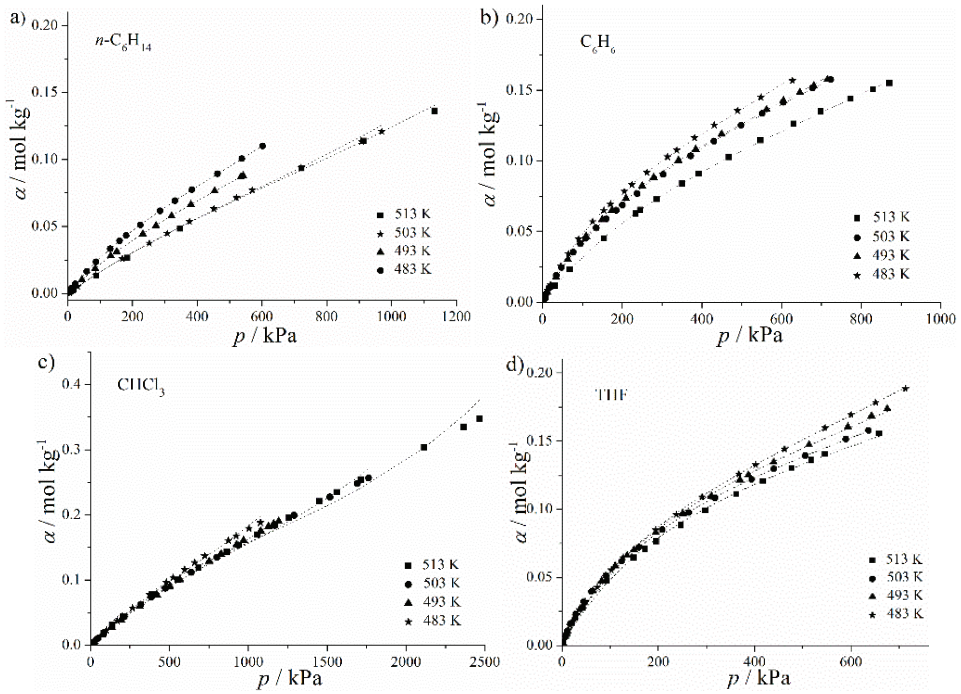

Fig. 5. Adsorption isotherms for: a) *n*-C_6H_{14}, b) C_6H_6, c) $CHCl_3$ and d) THF on the NZ at 483–513 K.

The adsorption capacity of the zeolite increased after modification for all investigated adsorbates. This was expected because of the higher surface area of ZFe in comparison to NZ and stronger interactions of used organic molecules with the new functional groups on the ZFe surface, which was proven by ΔG_a determination at infinite coverage.

According to the results presented in Table IV, the adsorption capacities of the NZ and ZFe decreased in the following order: $CHCl_3$, THF, C_6H_6 and *n*-C_6H_{14}. Previous IGC measurements at zero surface coverage showed the basic character of the NZ and ZFe. $CHCl_3$, as expected, had the greatest affinity towards the zeolites surfaces due to strong acid–base interactions and high values of the monolayer capacities were obtained. On the other hand, THF as a strong base is expected to establish repulsive forces with the zeolite surface. However, the values of monolayer capacity for THF adsorption were high for both the NZ and ZFe. Obviously, despite the fact that the surfaces of the NZ and ZFe have dominantly a basic character, there are also acid centers that interact with the strong base. A

similar conclusion was reached according to the determined acid/base properties of the NZ and ZFe at zero surface coverage.

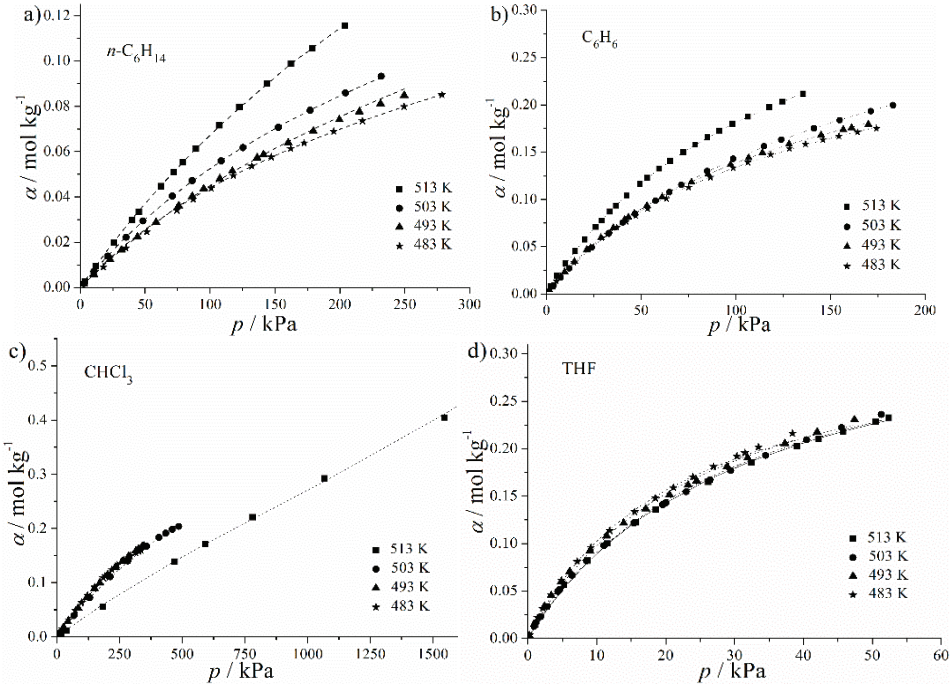

Fig. 6. Adsorption isotherms for: a) n-C_6H_{14}, b) C_6H_6, c) $CHCl_3$ and d) THF on the ZFe at 483–513 K.

Comparing the specific surface areas obtained by IGC and by the standard nitrogen adsorption method (Table I), it could be seen that the data for the NZ agree reasonably well. However, in the case of the ZFe sample, the specific surface area calculated from the IGC data obtained with n-C_6H_{14}, C_6H_6, THF and $CHCl_3$ were much lower than those obtained from nitrogen adsorption. This could be explained by differences in the molecular size. The nitrogen molecule, due to its smaller size (N_2 cross-sectional area is 0.162 nm^2), can penetrate into pores that are inaccessible to the larger molecules of n-C_6H_{14}, C_6H_6, THF and $CHCl_3$ (pore diameter of Fe–zeolite < diameter of molecule used). In the case of NZ, the mesopores were larger (the average pore diameter was 20.9 nm) and approachable for interaction with the organic probes.

The commonly accepted quantitative measure for the heterogeneity of the surface energetics, the adsorption energy distributions function, χ, that is related to the isotherm $\alpha(p,T)$, were determined using Eq. (S-15). The calculated distribution function was dependent on the choice of the local isotherm, as well as on the probe molecule.

TABLE IV. BET equation constant, C, monolayer capacity, α_m, and specific surface area of NZ and ZFe in the temperature range 483–513 K

Adsorbate	T / K	α_m / mol kg^{-1}		C		S_a /m^2 g^{-1}	
		NZ	ZFe	NZ	ZFe	NZ	ZFe
n-C_6H_{14}	513	0.121	0.268	4.30	9.34	28.7	64.0
	503	0.114	0.159	4.30	11.6	26.6	37.8
	493	0.110	0.153	5.20	8.74	26.2	36.4
	483	0.109	0.116	5.79	10.9	26.0	27.8
C_6H_6	513	0.146	0.350	7.87	29.3	26.9	64.1
	503	0.146	0.308	9.80	20.7	26.8	56.1
	493	0.135	0.258	9.90	23.6	24.8	47.2
	483	0.134	0.238	9.96	22.1	24.6	43.7
$CHCl_3$	513	0.170	0.372	7.73	3.98	28.9	63.5
	503	0.168	0.369	5.57	6.33	28.6	62.8
	493	0.167	0.357	4.40	6.25	28.5	60.8
	483	0.164	0.319	4.22	6.40	28.0	54.4
THF	513	0.163	0.352	13.86	117	28.3	61.0
	503	0.159	0.351	13.67	106	27.5	60.6
	493	0.159	0.331	12.31	112	27.5	57.2
	483	0.158	0.314	10.67	111	27.4	54.7

The distribution functions of the adsorption energy of the adsorption sites, relating the number of sites with a given energy to discrete adsorption energy values, measured with *n*-C_6H_{14}, C_6H_6, THF and $CHCl_3$ at 513 K are presented in Fig. 7a and b for the NZ and ZFe, respectively. Similar trends in the distribution functions of the adsorption sites were observed for both zeolite samples. As it could be seen from the plots that the number of adsorption sites with certain energy increased with decreasing ε_E. The obtained dependencies varied from one solid/ /adsorbate pair to another in terms of shape and the site number.

Similar values for the number of adsorption sites available on ZFe and on NZ were obtained for all four adsorbates, which suggest that number of sites on the zeolite surface did not change significantly during modification. The adsorption sites for the NZ and ZFe were also of similar energies.

The curve that describes the heterogeneity function for $CHCl_3$ was higher than that for the other adsorbates (see Fig. 6), indicating that a larger number of adsorption sites were involved in the interaction with $CHCl_3$. This is probably the result of the strong acid–base interactions of the hydroxyl groups of the adsorbate with the probe. Generally, χ is not only a characteristic of the solid itself but is also strongly dependent on the type of the solid/adsorbate combination.

The performed comparison of the adsorption energy distribution function, χ, for diverse sorbents enabled an evaluation of the heterogeneity of the surface energetics of these sorbents. The investigated samples, in spite of differences in porosity and sorption activity, were fairly similar in their degree of heterogeneity of the surface.

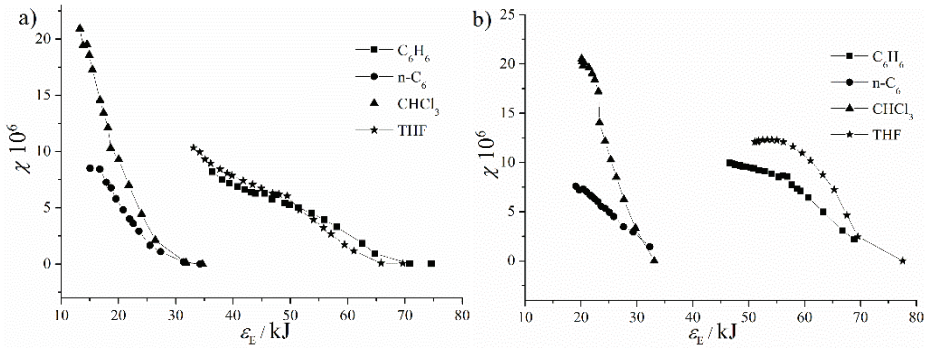

Fig. 7. Distribution functions of the adsorption sites measured with *n*-C_6H_{14}, $CHCl_3$, THF and C_6H_6 at 513 K for: a) NZ and b) ZFe.

CONCLUSION

Inverse gas chromatography under finite and infinite conditions was used to determine the surface properties of natural zeolite (NZ) and the influence of the modification with iron oxyhydroxide on the surface properties of the zeolite (sample ZFe).

Modification of the NZ considerably increased the dispersive component of its surface energy, specific interaction with polar probes, as well as the adsorption capacity for all investigated polar probes. Of the four adsorbates studied by finite coverage IGC, $CHCl_3$ had the greatest affinity towards the investigated zeolite surfaces due to strong acid–base interactions.

The NZ and ZFe strongly interacted with both the electron donor and the acceptor probes, as well as with the amphoteric probes. Based on the acceptor and donor interaction constants (K_D and K_A values), the NZ and ZFe were found to have a basic character.

The value of S_a for the NZ calculated from IGC data were in good agreement with those determined by the BET method. On the contrary, in the case of ZFe, these results did not correlated successfully due to the differences in the molecular sizes of the examined polar probes and nitrogen, as well as to the adsorbate–adsorbent interactions.

SUPPLEMENTARY MATERIAL

Additional data and information are available electronically at the pages of journal website: https://www.shd-pub.org.rs/index.php/JSCS/article/view/12579, or from the corresponding author on request.

Acknowledgment. This work was supported by the Ministry of Science, Technological Development and Innovation of the Republic of Serbia through the project contract No. 451--03-47/2023-01/200135.

ИЗВОД

ПРИМЕНА ИНВЕРЗНЕ ГАСНЕ ХРОМАТОГРАФИЈЕ ПРИ НУЛТОЈ И КОНАЧНОЈ ПРЕКРИВЕНОСТИ ЗА ИСПИТИВАЊЕ АДСОРПЦИЈЕ ОРГАНСКИХ МОЛЕКУЛА НА ЗЕОЛИТУ И КОМПОЗИТУ ЗЕОЛИТА И ГВОЖЂЕ-ОКСИХИДРОКСИДА

СЛАВИЦА С. ЛАЗАРЕВИЋ[1], МАРИЈА Т. МИХАЈЛОВИЋ-КОСТИЋ[2], ИВОНА М. ЈАНКОВИЋ-ЧАСТВАН[1], ЂОРЂЕ Т. ЈАНАЋКОВИЋ[1] и РАДА Д. ПЕТРОВИЋ[1]

[1]*Технолошко–металуршки факултет Универзитета у Београду, Карнегијева 4, 11 000 Београд и* [2]*Београдски водовод и канализација, Делиградска 28, 11000 Београд*

Применом инверзне гасне хроматографије, испитана су површинска својства природног зеолита (NZ) и композита зеолита и гвожђе-оксихидроксида (ZFe), коришћењем поларних и неполарних проба у условима нулте и коначне прекривености у температурном опсегу 483–513 K. Вредности дисперзивне компоненте слободне енергије адсорпције, γ_S, одређене методом Греја, опадају са порастом температуре за оба зеолита. Одређивањем промене специфичне слободне енергије адсорпције, ΔG_a^S, и промене специфичне енталпије адсорпције, ΔH_a^S, које одговарају кисело/базним интеракцијама на чврстој површини, одређени су и акцепторски и донорски параметри (K_A и K_D) на основу којих је утврђено да су површине узорака NZ и ZFe базног карактера. На основу добијених адсорпционих изотерми за *n*-хексан, бензен, хлороформ и тетрахидрофуран, применом инверзне гасне хроматографије у условима коначне прекривености, израчунате су вредности специфичне површине као и расподела адсорпционе енергије. Капацитет адсорпције узорка ZFe је био већи у односу на капацитета узорка NZ, за све испитане адсорбенте. Специфична површина узорака као и расподела величине мезопора одређени су применом адсорпционе/десорпционе изотерме за гасовити азот, односно применом BET методе. Закључено је да су природа адсорбата и површинска својства адсорбената главни фактори који одређују капацитет адсорпције.

(Примљено 8. септембра, ревидирано 8. октобра, прихваћено 21. новембра 2023)

REFERENCES

1. M.O. Daramola, E.F. Aransiola, T.V. Ojumu, *Materials* **5** (2012) 2101 (https://doi.org/10.3390/ma5112101)
2. N. Finish, P. Ramos, E. J.C. Borojovich, O. Zeiri, Y. Amar, M. Gottlieb, *J. Hazard. Mater.* **457** (2023) 131784 (https://doi.org/10.1016/j.jhazmat.2023.131784
3. D. Nibou, H. Mekatel, S. Amokrane, M. Barkat, M. Trari*, J. Hazard. Mater.* **173** (2010) 637 (https://doi.org/10.1016/j.jhazmat.2009.08.132)
4. V. Yadav, L. Kumar, N. Saini, M. Yadav, N. Singh, V. Murugasen, E. Varathan, *Water Air Soil Poll.* **234** (2023) 435 (https://doi.org/10.1007/s11270-023-06469-4)
5. S. Wang, Y. Peng, *Chem. Eng. J.* **156** (2010) (https://doi.org/10.1016/j.cej.2009.10.029)
6. K. Shikhaliyev, T. Onsree, A. H. Jaeschke, S. M. Ghoreishian, K. Shariati, A. Martinez, A. Katz, S. Hwang, A. Gaffney, J. M. Urban-Klaehn, J. Lauterbach, *Appl. Catal., B* **337** (2023) 122991 (https://doi.org/10.1016/j.apcatb.2023.122991)
7. M.A. Sadenova, S.A. Abdulina, S. A. Tungatarova, *Clean Technol. Environ.* **18** (2016) 449 (https://doi.org/10.1007/s10098-015-1018-6)
8. M. Kuronen, M. Weller, R. Townsend, R. Harjula, *React. Funct. Polym*. **66** (2006) 1350 (https://doi.org/10.1016/j.reactfunctpolym.2006.03.019)
9. I. Rodriguez-Iznaga, V. Petranovskii, G.Rodriguez-Fuentes, *J. Environ. Chem. Eng.* **2** (2014) 1221 (https://doi.org/10.1016/j.jece.2014.05.012)
10. M. Doula, *Water Res*. **40** (2006) 3167 (https://doi.org/10.1016/j.watres.2009.05.037)

11. M. Doula, A. Dimirkou, *J. Hazard. Mater.* **151** (2008) 738 (https://doi.org/10.1016/j.jhazmat.2007.06.047)
12. A. Dimirkou, *Water Res*. **41** (2007) 2763 (https://doi.org/10.1016/j.watres.2007.02.045)
13. M. Kragović, A. Daković, Ž. Sekulić, M. Trgo, M. Ugrina, J. Perić, G. D. Gatta, *Appl. Surf. Sci.* **258** (2012) 3667 (https://doi.org/10.1016/j.apsusc.2011.12.002)
14. P. Praipipat, S. Jangkorn, P. Ngamsurach, *Environ. Nanotechnol. Monit.* **20** (2023) 100812 (https://doi.org/10.1016/j.enmm.2023.100812)
15. M. T. Mihajlović, S. S. Lazarević, I. M. Janković-Častvan, B. M. Jokić, Đ. T. Janaćković, R. D. Petrović, *Chem. Ind. Chem. Eng. Q*. **20** (2014) 283 (https://doi.org/10.2298/CICEQ121017010M)
16. M. T. Mihajlović, S. S. Lazarević, I. M. Janković-Častvan, J. Kovač, B. M. Jokić, Đ. T. Janaćković, R. D. Petrović, *Clean Technol. Environ. Policy* **17** (2015) 407 (https://doi.org/10.1007/s10098-014-0794-8)
17. P. M. Nekhunguni, N. T. Tavengwa, H. Tutu, *J. Environ. Manage.* **197** (2017) 550 (https://doi.org/10.1016/j.jenvman.2017.04.038)
18. A. Badeenezhad, A. Azhdarpoor, S. Bahrami, S. Yousefinejad, *Mol. Simulat.* **45** (2019) 564 https://doi.org/10.1080/08927022.2018.1564077
19. N. J. Singh, B. Wareppam, A. Kumar, K. P. Singh, V. K. Garg, A. C. Oliveira, L. H. Singh, *J. Mater. Res.* **38** (2023) 1149 (https://doi.org/10.1557/s43578-022-00859-w)
20. S. Mohammadi-Jam, K.E. Waters, *Adv. Colloid Interf. Sci.* **212** (2014) 21 (https://doi.org/10.1016/j.cis.2014.07.002)
21. J. P. Jolivet, E. Tronc, Corinne Chaneac, *C. R. Geoscience* **338** (2006) 488 (https://doi.org/10.1016/j.crte.2006.04.014)
22. F. Rouquerol, J. Rouquerol, K. Sing, *Adsorption by Powders and Porous Solids*, Academic Press, London, 1999 (https://doi.org/10.1016/B978-0-12-598920-6.X5000-3)
23. E. P. Barrett, L. G. Joyner, P. P. Halenda, *J. Am. Chem. Soc.* **73** (1951) 373 (http://dx.doi.org/10.1021/ja01145a126)
24. B. C. Lippens, J. H. de Boer, *J. Catal.* **4** (1965) 319 (https://doi.org/10.1016/0021-9517(65)90307-6)
25. U. Kuila, M. Prasad, *Geophys. Prospec*. **61** (2013) 341 (https://doi.org/10.1111/1365-2478.12028)
26. E. Diaz, S. Ordonez, A. Vega, J. Coca, *J. Chromatogr., A* **1049** (2004) 139 (https://doi.org/10.1016/j.chroma.2004.07.061)
27. C. Bilgic, F.Tumsek, *J. Chromatogr., A* **1162** (2007) 83 (https://doi.org/10.1016/j.chroma.2007.04.003)
28. E. Diez, J.M Gomez, A. Rodriguez, A. Martinez, P. Saez, *Environ. Prog. Sustain.* **39** (2020) e13412 (https://doi.org/10.1002/ep.13412)
29. Y. J. Huang, Y. Jiang, V. R. R. Marthala, B. Thomas, E. Romanova, M. Hunger, *Phys. Chem., C* **112** (2008) 381 (https://doi.org/10.1021/jp7103616).

Journal of the Serbian Chemical Society
JSCS@tmf.bg.ac.rs • www.shd.org.rs/JSCS
J. Serb. Chem. Soc. 89 (3) S134–S138 (2024) *Supplementary material*

SUPPLEMENTARY MATERIAL TO

An inverse gas chromatography study of the adsorption of organics on zeolite and zeolite/iron oxyhydroxide composite at the infinite and finite surface coverage

SLAVICA S. LAZAREVIĆ[1]*, MARIJA T. MIHAJLOVIĆ-KOSTIĆ[2], IVONA M. JANKOVIĆ-ČASTVAN[1], ĐORĐE T. JANAĆKOVIĆ[1] and RADA D. PETROVIĆ[1]

[1]*Faculty of Technology and Metallurgy, University of Belgrade, Karnegijeva 4, 11000 Belgrade, Serbia and* [2] *Belgrade Waterworks and Sewerage, Deligradska 28, 11000 Belgrade, Serbia*

J. Serb. Chem. Soc. 89 (3) (2024) 383–397

THEORETICAL BACKGROUND – INVERSE GAS CHROMATOGRAPHY

Zero surface coverage

The primary experimental parameter measured in IGC, the net retention volume, V_N, in cm^3, can be calculated from the maxima of the chromatographic peaks and the dead time using the expression:[1]

$$V_N = jF_f \frac{(p_0 - p_w)}{p_o} \frac{T}{T_f} (t_R - t_o) \quad \text{(S-1)}$$

where t_R is the retention time (min), t_0 the dead time (min), T is column temperature (K), T_f is ambient temperature (K), p_0 is the outlet column pressure, p_w is the vapour pressure of water at T_f (Pa), F_f is the carrier gas flow rate (cm^3 min^{-1}) and j is the James–Martin compressibility factor.

The free energy change of adsorption, ΔG_a is related to V_N as follows:

$$\Delta G_a = -RT \ln\left(\frac{V_N \cdot p_{s,g}}{m \cdot S_a \cdot \Pi_S}\right) \quad \text{(S-2)}$$

where R is the gas constant, $p_{s,g}$ is the adsorbate vapour pressure in the gaseous standard state, equal to 101 kN m^{-2} (101 kPa), S_a is specific surface area of the adsorbent (m^2 g^{-1}), m is the mass of adsorbent in the column (g) and Π_S is the reference two-dimensional surface pressure, equal to 0.338 mN m^{-1}.[2]

The differential heat of adsorption of adsorbates at zero coverage, ΔH_a, was obtained from the temperature dependence of V_N according to Eq. (S-3):

$$\Delta H_a = -R \frac{d \ln V_N}{d(1/T)} \quad \text{(S-3)}$$

* Corresponding author. E-mail: slazarevic@tmf.bg.ac.rs

The entropy of adsorption of adsorbates, ΔS_a, is given by:

$$\Delta S_a = \frac{\Delta H_a^0 - \Delta G_a^0}{T} \quad \text{(S-4)}$$

The surface free energy of an adsorbent, γ_S (J/m^2), is expressed as the sum of the dispersive component, γ_S^d, and the specific component, γ_S^d, corresponding to the dispersive and specific interactions, respectively.[3] The dispersive properties of the solid surface are characterized by γ_S^d, while the specific properties can be described by the IGC-derived K_A and K_D parameters, characterising the ability of surface to acidic (acceptor of electrons) and basic (donor of electrons) interactions.

The dispersive component of the surface energy can be determined using the retention times of *n*-alkanes, because there are no acid–base interactions between alkanes and the stationary phase:

$$\gamma_S^d = \frac{\Delta G_{CH_2}^2}{4\gamma_{CH_2} \cdot N^2 \cdot a_{CH_2}^2} \quad \text{(S-5)}$$

where N is Avogadro's number, a_{CH_2} is the cross-section of a $-CH_2$ group (0.06 nm^2), and γ_{CH_2} (mJ m^{-2}) is the surface tension of a surface consisting of $-CH_2$ groups, given as a function of temperature (γ_{CH_2} = 35.6 + 0.058 (293–T)), while ΔG_{CH_2} represents the free energy of adsorption of a methylene group, defined as the energy difference between the adsorptions of two successive alkanes; ΔG_{CH_2} can be determined from the dependence of ΔG_a^S for alkanes on the carbon number, *i.e.*, as the slope of the straight line referred to as the "alkane line":

$$\Delta G_{CH_2} = -RT\, ln\left(\frac{V_{N,n}}{V_{N,n+1}}\right) \quad \text{(S-6)}$$

where $V_{N,n}$ and $V_{N,n+1}$ are the specific retention volumes of two consecutive *n*-alkanes having n and n+1 carbon atoms, respectively.

The specific interaction can be estimated from the retention data of polar probes. The probes used for to study the specific forces were chosen based on their acidic or basic character, as determined by Gutmann.[4] The polar probes interact more strongly with the solid than *n*-alkanes, as dispersive and specific forces are involved, and the values of ΔG_a for polar probes are situated above the "alkane line". The difference between the values of ΔG_a for polar probes and the values of ΔG_a for a real or hypothetical *n*-alkane with the same boiling point, T_b,[5] is equal to ΔG_a^S:

$$\Delta G_a^S = RT\, ln\left(\frac{V_N}{V_{N,ref}}\right) \quad \text{(S-7)}$$

where V_N is the net retention volume for the polar probe and $V_{N,ref}$ is the net retention volume for the *n*-alkane with the same boiling point, T_b.

The specific enthalpy of adsorption, ΔH_a^S, and the specific entropy of adsorption, ΔH_a^S, can be determined as the slope and the intercept, respectively, of the straight line obtained by plotting $\Delta G_a^S / T$ *versus* 1 / T.

Based on the values of ΔH_a^S for various polar molecules, Saint-Flour and Papirer[6] proposed an empirical relationship to characterize a solid with an acid constant K_A and a basic constant K_D:

$$-\frac{\Delta H_a^S}{AN*} = K_A \frac{DN}{AN*} + K_D \quad \text{(S-8)}$$

where *DN* and *AN** are the Gutmann donor and modified acceptor numbers,[4] respectively, corresponding to the polar probes used to determine the specific interactions with the solid. Values of constants K_A and K_D of the adsorbent can be obtained by plotting $\Delta H_a^S/AN^*$ as a function of DN/AN^*, according to Eq. (S-8).

The K_D/K_A ratio is a measure of the surface acidity and basicity. Thus, for a ratio $K_D/K_A > 1$, the surface is considered to be alkaline, but acidic for $K_D/K_A < 1$.

Finite surface coverage

At finite coverage, when high quantities of probe molecules are introduced into the chromatographic system, the surface adsorption results in non-linear isotherms and asymmetrical peak shapes. Assuming that the recorded peak height is proportional to the partial pressure, the quantity adsorbed onto an adsorbent, α, can be calculated using the following expressions (S-9, S-10):[1]

$$\alpha = \frac{1}{mRT}\int_0^p V_N dp \quad \text{(S-9)}$$

$$p = \frac{RTnh}{F_f S} \quad \text{(S-10)}$$

where p is the partial pressure of the adsorbate, n is the number of moles of probe injected, h is a height of the chromatographic peak and S is the area of the chromatographic peak. The definitions of R, T and m have been given previously.

The relationship between the amount of sample adsorbed in the column and the adsorbate vapour pressure is given by (S-11):[7]

$$\alpha = \frac{S_{ads} n}{mS} \quad \text{(S-11)}$$

where S_{ads} is the chart area bounded by the axis of the time t_0 of the non-retained specimen and the adsorption envelope of the peak maxima.

The experimental isotherms can be converted to the linear form of the well-known BET isotherm:[8,9]

$$\frac{p/p_0}{\alpha(1-p/p_0)} = \frac{1}{\alpha_m C} + \frac{(C-1)}{\alpha_m C}(p/p_0) \quad \text{(S-12)}$$

where C is a constant related to the heat of adsorption, α_m is the amount of adsorbate adsorbed in a monolayer and p_0 is the vapour pressure of the adsorbate at the temperature of the measurement. If $(p/p_0)/\alpha(1-p/p_0)$ is plotted in the narrow range of applicability of BET theory ($0.05 \leq p/p_0 \leq 0.3$), the slope and the intercept allow an estimation of α_m and C.

In this paper, the p_0 values were calculated according to the Antoine equation using the literature data for *n*-C_6H_{14},[10] $CHCl_3$,[11] benzene[11] and THF[12].

The area occupied by the adsorbate in the monolayer, σ, can be calculated by assuming that the adsorbed molecules have a spherical shape in hexagonal close packing, arranged on the solid surface in the same way as on a plane surface immersed into bulk liquid of the adsorbate (S-13):[13]

$$\sigma = 1.091 \left(\frac{M}{N\rho}\right)^{2/3} \quad \text{(S-13)}$$

where M is the molecular weight, ρ is the density of the probe, N is Avogadro's number and the constant 1.091 is a packing factor.

From σ and α_m data, the surface area of the adsorbent can be calculated using the following relation:

$$S_a = \alpha_m \sigma N \quad \text{(S-14)}$$

The surface energetic heterogeneity of a solid may be described by the energy distribution function, χ, relating the number of adsorption sites having a given adsorption energy to the adsorption energy of the molecule. The experimental isotherm $\alpha(p,T)$ as the sum of the partial isotherms corresponding to the homogeneous adsorption segments, is given by the equation:

$$\alpha(p,T) = \alpha_m \int_0^\infty \chi(\varepsilon_E)\, \theta(\varepsilon_E, p, T) d\varepsilon_E \quad \text{(S-15)}$$

where $\theta(\varepsilon_E,p,T)$ is the local isotherm of surface sites with the same ε_E.

To calculate χ, the terms derived by Rudzinski[14] can be used:

$$\chi = -\frac{\partial \alpha}{\partial \varepsilon_E} + \frac{3.14^2}{6} R^2 T^2 \frac{\partial^3 \alpha}{\partial {\varepsilon_E}^3} \quad \text{(S-16)}$$

where the ε_E function is estimated as:

$$\varepsilon_E = -RT\, ln \frac{p}{K} - zu \frac{\alpha}{\alpha_m} \quad \text{(S-17)}$$

using: $zu = H_L/4$,[15] and $K = p_0 \exp(H_L/RT)$[16], where z is the number of nearest neighbour adsorption sites, u is the interaction energy between molecules adsorbed on two neighbouring sites and H_L is the heat of evaporation of the probe.

REFERENCES

1. J. Conder, C. Young, Physicochemical Measurement by Gas Chromatography, Wiley-Interscience, New York, 1979
2. J. de Boer, The Dynamical Character of Adsorption, Clarendon, Oxford, 1953
3. F. Fowkes, J. Adhes. Sci. Technol. 1 (1987) 7 (https://doi.org/10.1163/156856187X00049)
4. V. Gutmann, The Donor-Acceptor Aproach to Molecular Interactions, Plenum Press, New York, 1978 (https://doi.org/10.1002/ange.19790910738)
5. D. Brookman, D. Sawyer, Anal. Chem. 40 (1968) 106 (https://doi.org/10.1021/ac60257a061)
6. C. Saint-Flour, E. Papirer, J. Colloid Interf. Sci. 91 (1983) 69 (https://doi.org/10.1016/0021-9797(83)90314-4)

7. A. Kiselev, Y. Yashin, Gas-Adsorption Chromatography, Plenum Press, New York, 1969.
8. S. Brunauer, P. H. Emmett, E Teller, J. Am. Chem. Soc. 60 (1938) 309 (https://pubs.acs.org/doi/epdf/10.1021/ja01269a023)
9. S. Brunauer, S. Deming, L. Deming, E. Teller, J. Am. Chem. Soc. 62 (1940) 1723 (https://pubs.acs.org/doi/pdf/10.1021/ja01864a025)
10. C. B. Willingham, W. J. Taylor, J. M. Pignocco, F. D. Rossini, J. Res. Natl. Bur. (U.S.) 35 (1945) 219 (https://nvlpubs.nist.gov/nistpubs/jres/35/jresv35n3p219_A1b.pdf)
11. D. R. Stull, Ind. Eng. Chem. 39 (1947) 517 (https://pubs.acs.org/doi/epdf/10.1021/ie50448a022)
12. D.W Scott, J. Chem. Thermodyn. 2 (1970) 833 (https://doi.org/10.1016/0021-9614(70)90026-1)
13. P. H. Emmett, S. Brunauer, J. Am. Chem. Soc. 59 (1937) 1553 (https://doi.org/10.1021/ja01287a041)
14. W. Rudzinski, J. Jagiello, Y. Grillet, J. Colloid Interf. Sci. 87 (1982) 478 (https://doi.org/10.1016/0021-9797(82)90345-9)
15. W. A. House, M. J. Jaycook, Colloid. Polym. Sci. 256 (1978) 52 (https://link.springer.com/article/10.1007/BF01746691)
16. M. Jaroniec, Surf. Sci. 50 (1975) 553 (https://chempap.org/file_access.php?file=294a512.pdf).

Journal of the Serbian Chemical Society
JSCS-info@shd.org.rs • www.shd.org.rs/JSCS
J. Serb. Chem. Soc. *89* (3) 399–413 (2024)
JSCS–5728
Original scientific paper
Published 31 March 2024

The influence of polyvinyl alcohol concentration toward conductivity and permeability of chitosan–montmorillonite composite membrane

ARIEF RAHMATULLOH*, MUTIA DEVI HIDAYATI and ANNISA NURIS FAJARIA

Department of Chemical Engineering, Politeknik Negeri Malang, Malang, East Java, Indonesia

(Received 19 September, revised 9 November 2023, accepted 19 February 2024)

Abstract: The composite membrane is synthesized using chitosan as a matrix membrane with montmorillonite (MMT) as a filler and modified using polyvinyl alcohol (PVA). The main aim of this study is to find out the influence of PVA concentration and the working temperature toward the permeability of chitosan–MMT/PVA composite membrane. Fourier transform infrared spectroscopy (FTIR) characterization is performed in order to identify the interaction between the chitosan matrix and the modified MMT with PVA. The presence of new absorption at 1116.82 and 619.17 cm^{-1} indicated the interaction between MMT and PVA. Further, the widening of OH absorption indicated the hydrogen bond which is formed between chitosan matrix and PVA. This interaction is also demonstrated by the evenly distributed surface on scanning electron microscope (SEM) topography analysis. The thermal stability of composite membrane is determined by thermal gravimetry analysis (TGA). In addition, the composite membrane containing PVA has four patterns decomposed. When the TVA is absent from the composite membrane, it has three decomposition patterns, which are shown by TGA analysis. Based on its tensile strength, the composite membrane has good mechanical properties. The proton conductivity of the composite membranes are directly proportional to the PVA concentration. On the other hand, the methanol permeability of composite membranes is inversely proportional with the PVA concentration. The highest proton conductivity was obtained with the addition of 2 % PVA of 2.94×10^{-4} S cm^{-1}. Further, it also has the lowest methanol permeability with the value of 5.05×10^{-6} cm^2 s^{-1}. As a result, the crosslinked composite membrane chitosan––MMT prepared by PVA-crosslinking technique has the potential to be exploited for the direct methanol fuel cell application.

Keywords: proton conductivity; methanol permeability; direct methanol fuel cell.

* Corresponding author. E-mail: arief1289@polinema.ac.id
https://doi.org/10.2298/JSC230919016R

INTRODUCTION

Currently, the expansion of the renewable energy sources has gained attention. Among the most prospective sources of the environmentally friendly, cheap and safe energy is hydrogen. The fuel cell is among many alternative devices that can tap and use the hydrogen energy. The fuel cell is capable of producing electrical energy by reacting hydrogen and oxygen with water as the product. Fuel cell is composed of two electrodes, namely the anode and the cathode, that are separated by polymer membrane. This membrane is known as polymer electrolyte membrane (PEM). It become the medium which transports the hydrogen ions produced by the reaction of the anode towards the cathode. Hence the cathode can generate electrical energy.[1]

The membranes for fuel cells are made from cheap materials that are resistant to high temperatures and high energy density. As a result, the permeability membrane and its ability to retain water or methanol can be achieved. The permeability membrane that is applied to the direct methanol fuel cell (DMFC) is one of the key components of DMFC performance, which results in the environmentally friendly and power efficient energy for a wide range of different applications.[2]

An alternative membrane material that can be used for PEM is chitosan. Chitosan is a well-known biopolymer waste, consisting of monomer *N*-acetyl glucosamine (GlcNAc) and also D-glucosamine (GlcN). Chitosan is a well-organized chemical structure material, inert and good ion conductive properties. Furthermore, the level of chitosan toxicity is relatively low. Therefore, the chitosan polymeric materials provide good properties for fuel cells. However, the low solubility of chitosan in water is a deficiency for PEM because chitosan can become waterless. Hence, cross-linking chitosan with other materials is necessary to improve the PEM properties.[3]

In this study, chitosan act as matrix membrane which was cross-linked with the inorganic filler montmorillonite (MMT) which is a hydrophobic material. MMT offers several advantages for being economical, environmentally friendly and high rate of SiO_2. Further, the SiO_2 plays an important role in the process of the cross-linking. Another reason for choosing MMT as inorganic filler are the hydrophobic properties of MMT curb methanol crossover, when it is in contact with methanol. However, MMT cannot interact with chitosan directly due to the weak interfacial interaction between the two surfaces.[4] Hence, it needs modifications with another material and polyvinyl alcohol (PVA) was used in this study. PVA was selected because of its hydrophilic properties and good chemical resistance. The additional reasons of choosing PVA are that it can interact with chitosan through hydrogen bond between hydroxyl group of PVA, and free amine group of chitosan and bind strongly with MMT.[5] PVA also presents the water-resistant bond between the inorganic filler and polymer matrix. Next, PVA can

form a strong bond which can provide high mechanical strength is also more resistant to the presence of methanol that can destruct the composite membrane's structure. Therefore, the modifications using PVA could decrease the permeability properties of the PEM.

This study is aimed to find out the effect of PVA concentration on the conductivity and permeability of chitosan–MMT/PVA composite membrane. The concentration percentages of PVA that we used in this study were 0, 1, 1.5 and 2 %.

EXPERIMENTAL

Materials

The composite membrane used in this study was synthesized from chitosan (Merck, Singapore), montmorillonite K-10 (97 % purity degree, Sigma Aldrich, Singapore), polyvinyl alcohol (98 % purity degree, Sigma Aldrich, Singapore). Other chemicals with pro analysis purity were CH_3COOH (97 % purity degree, Merck, Singapore), demineralized aqua, concentrated H_2SO_4 (98 % purity degree, Merck, Singapore), and methanol (96 % purity degree, Merck, Singapore).

Instrumentation

Several tools that used on this study such as scale, thermometer, electric heater, erlenmeyer, pH indicators, condenser, volume pipette, magnetic stirer, beaker glass, stirrer ultrasonic, an utensil of the permeability test, electrochemical impendance spectroscopy (EIS) of Autolab with FRA32M module, Fourier transform infra red (FTIR) 8400 Shimadzu, scaning electron microscopy (SEM) Hitachi TM3000, thermo gravimetry analysis (TGA) of Mettler Toledo and Stograph VG10-E.

The Fabrication of chitosan membrane

In this phase, 2 g of chitosan were dissolved in 2 vol. % of acetic acid and heated at 80 °C and stirred for 30 min. Then, the solution was treated with the ultrasonic bath for 30 min, left for 30 min, and treated again with the ultrasonic bath for 30 min. After the process, the solution was flattened on a glass plate and dried for 48 h. Further, the membrane was washed with aqua DM and dried at room temperature for 24 h.

Montmorillonite modification using polyvinyl alcohol

In this phase, 0.08 g of MMT was dissolved in 25 ml of 2 vol. % acetic acid. Then 1 g of polyvinyl alcohol was dissolved in 100 mL of aqua DM at 80 °C and stirred for 2 h. Further, the PVA solution mixed with MMT, it then stirred for 3 h at room temperature. The homogenized solution was modified MMT solution with PVA, 1 %, and referred to PVA concentration 0, 1.5 and 2 %. They were also modified using the same procedure.

The Preparation of composite membrane chitosan–montmorillonite/polyvinyl alcohol

In this part, 1.5 g of chitosan were dissolved in 37.5 mL of 2 vol. % acetic acid. The solution was then stirred and heated at 80 °C for 2 h. Next the solution was homogenized with the ultrasonic bath for 30 min. Further, the modified MMT solution at the concentration level of PVA 0, 1, 1.5 and 2 % was mixed with chitosan solution. Then the mixture was stirred and heated at 80 °C for 30 min. After that, the mixture was handled with the ultrasonic bath for 30 min, left for 30 min and handled again with the ultrasonic bath for 30 min. After the process of degasification, the mixture was flattened on a glass plate and dried for 48 h at room temperature. In the end, the membrane was saturated in a solution of 2 M H_2SO_4 for 24 h and

washed with aqua DM, and also dried at the room temperature for 24 h. The membranes were characterized with FTIR and SEM to find out the interaction between chitosan and MMT which is modified with PVA. The membrane conductivity measurement was carried out using EIS and permeability test was also conducted using the permeability tool test. TGA analysis was also conducted to find out the thermal stability of composite membrane.

Tensile strength

Tensile strength test of the composite membranes was conducted by making the membrane that measured 140 mm×25 mm in dry state. Next, the pull velocity of 10 mm/min and the pull strength of 10 N were applied to the membrane at room temperature.

RESULTS AND DISCUSSIONS

Modification of montmorillonite using polyvinyl alcohol

The initial stage of montmorillonite modification using polyvinyl alcohol was done by dissolving a number of MMT in acetic acid. The presence of acetic acid in this process is significant because it can perfectly modify MMT. Next in a different container, a certain amount of PVA concentrations (0, 1, 1.5 and 2 %) was dissolved in aqua DM. Then it was heated and stirred to form a homogeneous solution. Further, the PVA solutions were mixed with MMT solution and stirred for 3 h at room temperature to form the homogenous solution. This treatment is intended in order that PVA could coordinate with MMT through polysiloxane network between them.

Preparation of composite membrane chitosan–montmorillonite

Composite membranes were made from chitosan with montmorillonite integration. Chitosan acted as matrix membrane, while montmorillonite acted as a filler. MMT was modified with various PVA concentrations of 0, 1, 1.5 and 2 %. It was combined with the ratio of chitosan and MMT of 70:30. Monroy-Barreto *et al.* revealed that the filler reached the amount of the matrix at this ratio.[6] The pure chitosan membrane and the composite membrane were in the form of brownish yellow plastic sheets with varied concentration of PV, as shown in Fig. 1.

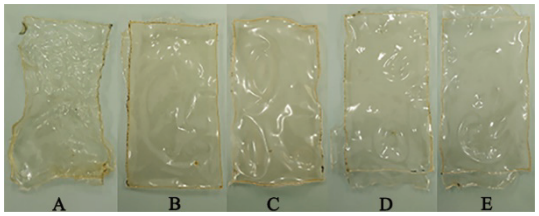

Fig. 1. A) Pure chitosan membrane; chitosan–MMT composite membrane with 0 (B), 1 (C), 1.5 (D) and 2 % (E) concentration.

In this research, fine composite membranes are made in the presence of acetic acid. The acid dissolved chitosan and modified the MMT perfectly. The

another advantage of acetic acid treatment is to render chitosan as a good proton conductor. When chitosan is solvable in acetic acid, both H^+ and CH_3COO^- of acetic acid are scattered in the chitosan and can be mobilized under an electric field. Further the mixed solution was heated at 80 °C and stirred. During this treatment the chitosan molecules were intercalated into the MMT to obtain a homogeneous solution mixture. The intercalation was caused by the hydrogen bond between the amine and the hydroxyl group of chitosan with the silica of MMT. Next, the ultrasonic treatment was conducted to make collision among the molecules and disperse the filler evenly on the membrane surface. Moreover, the repeated ultrasonic treatment is intended for the maximum interaction between the chitosan matrix and modified MMT. Hence, a perfect interaction can be formed between the two materials.[7,8] In addition, the interaction can also turn the solution into a gel form. Afterward, it was placed on flat glass for the membrane casting process. The cast membrane was dried at room temperature for 48 h to release the residue of acetic acid. Hence the bond, which was formed between chitosan matrix and modified MMT filler, became stronger. Further, the dry membrane was soaked in 2 M sulfuric acid solution. This treatment aimed to create the cross-linking process between chitosan and modified MMT. Thus, the interaction between them became optimal. The another objective of sulfuric acid handling was to make the chitosan polycationic. As a result, the chitosan matrix could donate its electron through the amine group.

As is shown in Fig. 1, the colour of the membrane is influenced by its composition. It is directly proportional to the concentration of PVA in the membrane. The pure chitosan membrane (see Fig. 1A) has the brightest colour among the others and it is wrinkled. The pure chitosan membrane is wrinkled due to its hydrophilic properties. The chitosan–MMT with 0 PVA (see Fig. 1B) has darker brownish yellow membrane surface among the other composite membranes. The MMT reacted successfully with chitosan and made the colour of the composite membrane mixed from chitosan and MMT 1 % PVA, which was found at MMT filler (see Fig. 1C), makes the colour of the membrane brighter and more plastic than the chitosan–MMT composite membrane with no PVA. When the concentration of PVA was 1.5 % in the composite membrane, the colour of the membrane was even brighter than the membrane with the concentration of PVA 0 and 1 %. It is also more plastic than hydrophobic, and consequently it is more resistant to breakage when soaked in water/methanol. Further, the membrane with the PVA concentration of 2 % had the brightest colour and the most plastic of all the others. Hence it is become more resistant to water/methanol.[9] Before the measurements and characterizations of the samples, the samples were dried at 60 °C by heated in vacuum oven.

Composite membrane characterization

Fourier transform infra red (FTIR). FTIR was conducted to find out the bond which had been formed in composite membrane. The result of the FTIR characterization can be seen at Fig. 2. While the various FTIR absorbances in the chitosan–MMT composite membrane can be seen in Table I.

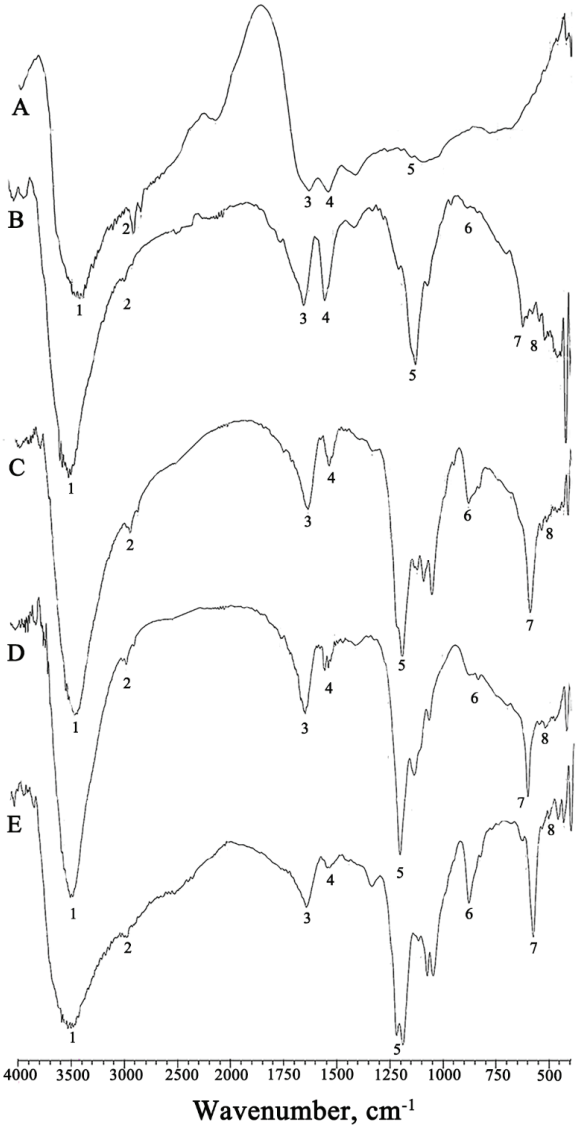

Fig. 2. FTIR spectra of chitosan membrane (A) and composite membranes with various PVA concentration: B) 0; C) 1; D) 1.5; E) 2 %.

TABLE I. Various wavenumber (cm^{-1}) of chitosan (CS)–montmorillonite (MMT) composite membrane FTIR absorption with various polyvinyl alcohol (PVA) concentration

No.	Vibration type	Membrane				
		CS	CS–MMT	CS–MMT/PVA 1 %	CS–MMT/PVA 1.5 %	CS–MMT/PVA 2 %
1	–OH	3435.34	3444.98	3435.34	3425.69	3433.41
2	$-CH_2$	2920.32	2931.90	2926.11	2928.04	2930.05
3	C–N	1635.69	1633.76	1633.76	1639.55	1635.69
4	$-NH_2$	1543.10	1537.32	1535.39	1543.10	1539.25
5	C–O	1263.42	1116.82	1193.98	1193.98	1220.98
6	Al–O	–	880.56	885.36	871.85	887.28
7	Si–O–Si	–	619.17	597.95	601.81	592.17
8	Si–O	–	542.02	543.94	549.73	551.66

The alteration of wave number of the absorption peaks and the emergence of the new absorption peaks, indicate the interaction between chitosan and MMT. Further, it also demonstrated that MMT had been successfully reacted with the chitosan matrix. Meanwhile, the wider and sharper of the –OH absorption indicate the interaction between chitosan and MMT (see Fig. 2B), and also between the chitosan matrix and PVA through the formed hydrogen bonds (see Fig. 2C, D and E).

The sharper of −CN vibration indicated the cross linking of chitosan and PVA.[10] Whereas, the interaction between MMT and PVA can be seen by the shifting wavenumber of Si−O–Si absorption from 619.17 to 592.17 cm^{-1}. This absorption shift occured because of the overlapping between Si−O vibration of MMT and C−O vibration of PVA. This condition is confirmed by the existence of strong enough the bend of Si−O which appeared in the wavenumbers 543.94, 549.73 and 551.66 cm^{-1} (Fig. 2B–E).[11]

Scanning electron microscopy (SEM). SEM characterization was carried out in order to determine the surface morphology of the membrane. The result of the SEM characterization can be seen at Fig. 3.

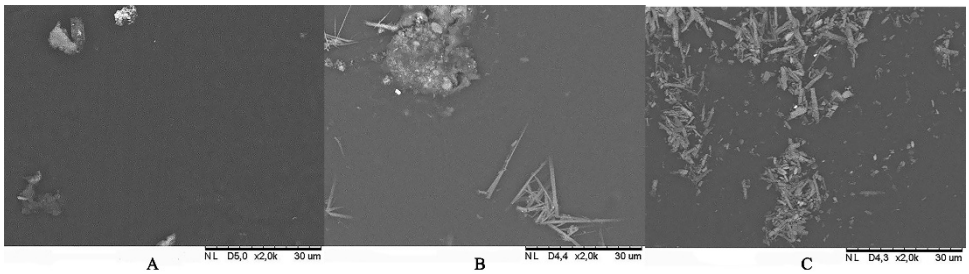

Fig. 3. SEM micrograph of surface membrane: A) pure chitosan; B) composite chitosan–MMT; C) chitosan–MMT / PVA 2 %.

Fig. 3 shows that pure chitosan membrane (see Fig. 3A) has more homogenous than that the surface of composite membrane chitosan–MMT modified PVA. This condition occurred because no fillers were added. Whereas, Fig. 3B illustrates that the surface of the membrane has uneven spots, which means that the filler particles are not evenly distributed on the chitosan matrix. The addition of MMT filler without PVA modification causes the uneven distribution of filler in the chitosan matrix. As a result, the membrane solution is not thoroughly mixed. Further, the intercalation between the chitosan matrix and the filler still occured, despite of the low efficiency. Meanwhile, the presence of PVA on the Fig. 3C caused the membrane surface to have even and uniform spots, which means that the filler particles were evenly distributed. A protective layer is formed over the chitosan surface, which could improve the chitosan polymer stability. This indicates that there was strong interaction not only between chitosan and PVA, but also between MMT and PVA. Further, the crosslinking among chitosan, MMT and PVA provides no phase separation. It also increases the compability and mechanical strength of the composite membrane. Nevertheless, it also provided the stable interface and inter-linking network of the composite membrane.[12]

A similar study reported on chitosan–polyvinyl alcohol composite membrane for the fuel cell applications.[13] The results of SEM analysis showed that the pure chitosan membrane has more even surface than the composite membrane. Further, the composite membrane was the uniform and free of any surface pores and cracks. The distributed particles could be oriented perpendicular to each other by the polymer chain, thanks to the electrostatic repulsion, thus, forming an inter-linking network.

Thermo gravimetry analysis. Thermo gravimetry analysis (TGA) characterization was conducted to determine the thermal stability of chitosan–MMT composite membrane. The result of TGA analysis of the composite membrane is shown in Fig. 4. Fig. 4 also illustrates that the presence of PVA on the composite membrane affected the decomposition pattern which can be seen at the thermogram spectra. It shows four decomposition patterns of the composite membrane with PVA while the composite membrane with the absence of PVA has three decomposition patterns. The first decomposition started at 60 °C and it was attributed to the evaporation of water molecules in the membrane for the composite membrane without PVA (Fig. 4A).[14] The first decomposition of the composite membrane with PVA (Fig. 4B) is also associated with the water evaporation, which is followed by the broken linkage between chitosan and PVA. The second decomposition of the composite membrane with PVA was related to the decomposition of polymer chain in chitosan, caused by dehydration, which triggered the formation of various different molecules with low molar mass that evaporates and it leads to the broken of hydrogen bonds between the amine groups of chit-

osan and the silica groups of MMT that occured at about 185 °C. The PVA caused the strong interaction between MMT and the chitosan matrix through hydrogen and covalent bonds. This condition is confirmed with Zawadzki and Kaczmarek, who conducted thermal analysis of chitosan at various temperatures. They state that the chitosan decomposition, which occurred above 180 °C, was related to the decomposition of pyranose rings through dehydration and deamination, further ring-opening reaction.[15]

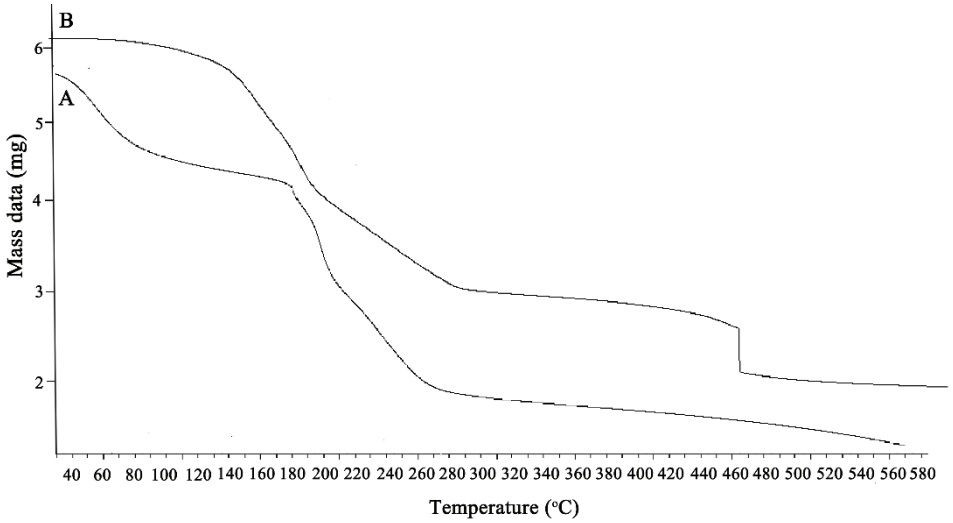

Fig. 4. Thermogram of composite membrane chitosan–MMT modified with PVA 0 % (A) and 2 % (B).

The third decomposition of the composite membrane with PVA and the second decomposition on membrane without PVA, occur at about 200 °C. For the composite membrane with PVA (Fig. 4B), the decomposition represented the broken chitosan and PVA bond on the membrane and also the disconnection of crosslinking between chitosan and MMT. The above fact was supported by Chen *et al*, who state that decomposition at the temperature of about 20–400 °C is related to the broken bond between chitosan polymer and PVA. Meanwhile, the composite membrane without PVA at the temperature for about 240–280 °C correspond to the disconnection bond between amine groups of chitosan and silica groups of MMT.[16]

The third decomposition of the composite membrane without PVA occurs around 310–340 °C. It is associated with the degradation and the decomposition polymer unit of chitosan and the decomposition of siloxane group from MMT. Next, the fourth thermal decomposition of the composite membrane with PVA related to chitosan polymer chain breakdown because of the dehydration at high temperatures. This phenomenon occurred at the temperature of about 290 °C. In

addition, this thermal decomposition is also represented by the decomposition of the residual organic substrate of PVA. Moreover, at 280–460 °C, this is also related to the elimination of the polysiloxane network between MMT and PVA, and disconnection of the crosslinking between chitosan and PVA. This is also endorsed by Lin *et al.*, who worked on the thermal analysis of hybrid membrane. Their study revealed that at the temperature above 250 °C, the decomposition was associated to the elimination of the siloxane group.[11] Meanwhile, the chitosan–MMT the decomposition in this temperature range was associated to the destruction of crosslinking between chitosan matrix and MMT. This fact is confirmed by Palani *et al*. They state that the temperature range of 350–500 °C is responsible for to the destruction of bond between chitosan and the filler of chitosan matrix.[17] To conclude, from Fig. 4 it can be seen that the composite membrane with PVA has better thermal stability than without one. It has a complex decomposition pattern and at the end of the process, the remaining mass of composite membrane with PVA is more than the mass of composite membrane without PV.

Tensile strength. Table II illustrates that in dry state, the composite membrane with PVA concentration of 2 % has the highest value of break elongation, and it also shows that break elongation value is directly proportional to the addition of PVA on the membrane. This is related with PVA characteristic which is has good mechanical properties and high flexibility. Thus, the addition of PVA on the composite membrane makes it more elastic with the significant increment of break elongation properties. On the other hand, the composite membrane without PVA addition has the lowest break elongation. This is because the hydrophobic characteristics of MMT increased the rigidity of the membrane. Further, the addition of PVA increases the tensile strength of composite membrane. This condition shows that the composite membrane chitosan–MMT modified with PVA is a quality material based on its mechanical properties. Consequently, these composite membranes had reasonable strength and could potentially be used for DMFC application.[18]

TABLE II. Tensile strength analysis of pure chitosan membrane and chitosan–MMT composite membrane with various concentrations of PVA in dry state

Membrane	Break elongation, %	Tensile strength, MPa
Pure chitosan	173.43	157.48
Chitosan–MMT	72.48	129.40
Chitosan–MMT/PVA 1 %	654	205.04
Chitosan–MMT/PVA 1.5 %	867.86	250.47
Chitosan–MMT/PVA 2 %	963	375.69

Proton conductivity. Proton conductivity is one of the main benchmark for the membrane, which can influence the fuel cell's performance directly. In this

study, it was measured by using EIS at room temperature which is shown in Table III.

TABLE III. Proton conductivity value of pure chitosan membrane and composite membrane chitosan–MMT with various PVA concentrations at room temperature; A = 1.0 cm^2

Membrane	Resistance, Ω	L / cm	σ / 10^{-4} S cm^{-1}
Pure chitosan	124.230	0.019	1.53
Chitosan–MMT	118.170	0.022	1.83
Chitosan–MMT/PVA 1 %	115.480	0.025	2.16
Chitosan–MMT/PVA 1.5 %	105.745	0.026	2.46
Chitosan–MMT/PVA 2 %	95.335	0.028	2.94

Table III illustrates the addition of PVA concentration effect on the membrane conductivity. The proton conductivity of the composite membranes rose from 1.83×10^{-4} to 2.94×10^{-4} S cm^{-1} as the PVA concentration, increased from 0 to 2 %. The composite membrane – 2 % PVA, has the highest conductivity among the others, because of the suitable amount of PVA to binding strongly the amine group of chitosan and it forms a polysiloxane network with MMT. Meanwhile, the pure chitosan membrane has the lowest value of conductivity among the others. This condition due to the hydrophility of chitosan, which makes the membrane soluble. As a consequence, the proton conductivity decreases significantly. Meanwhile, the composite membrane – 0 % PVA, has low conductivity because the absence of PVA makes the chitosan and MMT cannot bind strongly. Hence, proton conduction can't be conducted optimally. The composite membranes – 1 and 1.5 % PVA, have lower conductivity than the composite membrane – 2 % PVA. The addition of PVA concentration was not appropriate to the chitosan and MMT concentrations. Consequently, it cannot facilitate the conduction well and resulting poor proton conductivity value. On the system, chitosan––MMT composite membrane which is modified by PVA, have two factors that influence proton conductivity. These two factors are: *i*) the presence of polysiloxane network which can form a water-bound membrane layer to facilitate proton hopping. The proton hopping mechanism is the mechanism of transferring the proton across the membrane which determines the conductivity of membrane; *ii*) A strong hydrogen bond formed between the amine groups in chitosan and the epoxy on the silane ensures a high proton conduction.[2,8,19]

Those aforementioned is reinforced by Palani and co-workers, who also modified the chitosan membrane with polyvinyl alcohol for direct methanol fuel cell. They stated that the addition of PVA increase the proton conductivity of membrane. It is related with the amount of charge carrier (free functional groups) which is belongs to heterophasic morphology of PVA and influenced in protonic conduction. Moreover, PVA could make more flexible networks for the ionic transport.[17]

Methanol permeability. The methanol permeability is the parameter to find out the amount of methanol that passed through the membrane. The membrane of direct methanol fuel cell (DMFC) has too low methanol permeability to maintain optimum performance. Next, the methanol permeability is inversely proportional to the performance of membrane. The higher methanol permeability, the lower will be the performance.[2] The measurements of methanol permeability at room temperature is shown in Table IV. They indicate that the addition of PVA concentration influence on the methanol permeability. Table IV illustrates that the pure chitosan membrane has the highest value of methanol permeability. On the other hand, the composite membrane – 2 % PVA, has the lowest methanol permeability in comparison to the others, because the added amount of PVA is attributable to the strong hydrogen binding amine group of chitosan and formed a polysiloxane network with MMT. Moreover, the selectivity of PVA toward water–alcohol also affected the decrement of methanol permeability.[20,21] The addition of modified MMT filler to chitosan matrix affected the derivation of membrane permeability. Further, on the system chitosan–MMT composite membrane which is modified with PVA, has two factors that affect the membrane permeability. These two factors are: *i*) the dispersion of the anorganic particle on the composite membrane prolonged the path length and the tortuosity of methanol permeation. As a result, this made it difficult for the methanol molecule to pass through the membrane; *ii*) the presence of polysiloxane network on the composite membrane intensified the membrane ability to retain the structure when the methanol passed through. Next, the hydrophobicity of modified MMT on the composite membrane makes the rigidity of chitosan matrix and reduce the swelling ability of membrane.[2,19,22]

TABLE IV. Methanol permeability of pure chitosan membrane and composite membrane chitosan–MMT with various PVA concentrations at room temperature; A = 3.14 cm^2; V = 50 mL; C = 5 M

Membrane	Slope, M s^2	L / cm	Methanol permeability×10^6 cm^2 s^{-1}
Pure chitosan	0.0028	0.001	8.92
Chitosan–MMT	0.0019	0.0011	6.66
Chitosan–MMT/PVA 1 %	0.0008	0.0022	5.61
Chitosan–MMT/PVA 1.5 %	0.0007	0.0023	5.13
Chitosan–MMT/PVA 2 %	0.0006	0.0023	5.05

Table IV also shows that the existence of PVA on the composite membrane caused the lower membrane permeability. This is occurred because the hydroxyl group of PVA was dispersed well on the composite membrane and provided a strong crosslinking bond between the chitosan matrix and MMT modified with PVA.[5] Further, it enhanced the compatibility of MMT toward the chitosan matrix

and increased the ability of composite membrane to resist the methanol. Hence the membrane permeability against the methanol stayed low, which is good for the performance of the membrane.

This fact is reassured by Ayyubi and co-workers, who modified chitosan containing PVA using MMT. They revealed that the presence of PVA on the composite membrane makes methanol more difficult to pass through the membrane. Further, they also confirmed that the interaction between PVA and MMT narrowing the methanol pathway through the membrane.[23]

CONCLUSIONS

In this study, the composite membranes of chitosan–MMT modified PVA were prepared using varying PVA concentration and varying operating temperature to be used for DMFC application. Those composite membranes were made by the cross-linking technique. The interactions between chitosan–MMT with PVA was confirmed by the FTIR spectra through the widening and the sharpening of the OH absorption band and the existence of the new absorption at wave number 1116.82, 1193.98 and 1220.98 cm^{-1}. In the analysis using SEM, the interaction can be recognized by the surface, which has more even and uniforms spot. The thermal stability analysis via TGA illustrates that the composite membrane with PVA has good thermal stability. The tensile strength analysis shows that the composite membrane with various PVA concentrations have reasonable mechanical strength. Generally, the membrane conductivity value is directly proportional with the PVA concentration. When the PVA concentration increases, then it will escalate the membrane conductivity. On the contrary, the membrane permeability value is inversely proportional to the concentration of PVA. When the PVA concentration increases, it will decrease the membrane permeability. The composite membrane with the addition of 2 % PVA has the highest conductivity and the lowest permeability of all. Since the composite membrane chitosan––MMT prepared by PVA-crosslinking technique has good properties for the conductivity and the permeability, it is intended that this membrane will provide a particular performance for DMFC system.

ИЗВОД

УТИЦАЈ КОНЦЕНТРАЦИЈЕ ПОЛИ(ВИНИЛ-АЛКОХОЛА) НА ПРОВОДЉИВОСТ И ПЕРМЕАБИЛНОСТ ХИТОЗАН–МОНТМОРИЛОНИТ КОМПОЗИТНИХ МЕМБРАНА

ARIEF RAHMATULLOH, MUTIA DEVI HIDAYATI и ANNISA NURIS FAJARIA

Department of Chemical Engineering, Politeknik Negeri Malang, Malang, East Java, Indonesia

Композитна мембрана је синтетисана користећи хитосан као матрицу мембране са монтморилонитом (MMT) као пуниоцем и модификована коришћењем поливинил-алкохола (PVA). Главни циљ ове студије је да се сазна утицај PVA концентрације и температура на пермеабилност хитозана–MMT/PVA композитне мембране. Карактеризацијом FTIR се идентификује интеракција између хито-

санске матрице и MMT модификованог са PVA. Присуство нове апсорпције на 1116,82 и 619,17 cm^{-1} указује на интеракцију између MMT и PVA. Поред тога, ширење апсорпције OH указало је на водоничну везу која се формира између матрице хитосана и PVA. Ова интеракција је такође потврђена равномерно распоређеном површином у SEM. Термичка стабилност композитне мембране одређена је термогравиметријском анализом (TGA). Поред тога, у термограмима се виде четири ступња декомпозицију у присуству PVA. Без PVA постоје само три ступња декомпозиције. На основу јачине на кидање, композитна мембрана има добра механичка својства. Протонска проводљивост композитних мембрана је директно пропорционална PVA концентрацији. С друге стране, пермеабилност композитних мембрана метанолом је инверзно пропорционална PVA концентрацији. Највећа протонска проводљивост добијена је са додатком 2 % PVA од $2{,}94\times10^{-4}$ S cm^{-1}. Даље, мембрана тог састава такође има најнижу пермеабилност метанола са вредношћу од $5{,}05\times10^{-6}$ cm^2 s^{-1}. Као резултат тога, умрежена композитна хитозан–MMT мембрана добијена умрежавањем са PVA има потенцијал да буде искоришћена у директним горивним ћелијама са метанолом.

(Примљено 19. септембра, ревидирано 9. новембра 2023, прихваћено 19. фебруара 2024)

REFERENCES

1. K. Sopian, W. R. Wan Daud, *Renew. Energy* **31** (2006) 719 (http://dx.doi.org/10.1016/j.renene.2005.09.003)
2. V. Neburchilov, J. Martin, H. Wang, J. Zhang, *J. Power Sources* **169** (2007) 221 (http://dx.doi.org/10.1016/j.jpowsour.2007.03.044)
3. N. Shaari, S. K. Kamarudin, *J. Power Sources* **289** (2015) 71 (http://dx.doi.org/10.1016/j.jpowsour.2015.04.027)
4. S. Pricl, P. Posocco, G. Scocchi, M. Fermeglia, *Handb. Nanophysics Funct. Nanomater.* (2010) 3-1-3 (http://dx.doi.org/10.4325/seikeikakou.25.110)
5. P. G. Allison, R. D. Moser, M. Q. Chandler, J. A. Caminero-Rodriguez, K. Torres--Cancel, O. G. Rivera, J. R. Goodwin, E. R. Gore, C. A. Weiss, *J. Nanomater.* **2015** (2015) (http://dx.doi.org/10.1155/2015/291248)
6. M. Monroy-Barreto, J. C. Aguilar, E. Rodríguez de San Miguel, A. L. Ocampo, M. Muñoz, J. de Gyves, *J. Memb. Sci.* **344** (2009) 92 (http://dx.doi.org/10.1016/j.memsci.2009.07.039)
7. T. Fu, Z. Cui, S. Zhong, Y. Shi, C. Zhao, G. Zhang, K. Shao, H. Na, W. Xing, *J. Power Sources* **185** (2008) 32 (http://dx.doi.org/10.1016/j.jpowsour.2008.07.004)
8. A. Rahmatulloh, L. Atmadja, *J. Serbian Chem. Soc.* **86** (2021) 831 (http://dx.doi.org/10.2298/JSC201118043R)
9. Y. F. Yang, G. S. Gai, Z. F. Cai, Q. R. Chen, *J. Hazard. Mater.* **133** (2006) 276 (http://dx.doi.org/10.1016/j.jhazmat.2005.10.028)
10. G. Paradossi, R. Lisi, M. Paci, V. Crescenzi, *J. Polym. Sci., A* **34** (1996) 3417 (http://dx.doi.org/10.1002/pola.1996.874)
11. H. Lin, C. Zhao, W. Ma, K. Shao, H. Li, Y. Zhang, H. Na, *J. Power Sources* **195** (2010) 762 (http://dx.doi.org/10.1016/j.jpowsour.2009.08.020)
12. M. A. Abu-Saied, E. A. Soliman, E. A. A. Desouki, *Mater. Today Commun.* **25** (2020) 101536 (http://dx.doi.org/10.1016/j.mtcomm.2020.101536)

13. K. Hari Gopi, V. M. Dhavale, S. D. Bhat, *Mater. Sci. Energy Technol.* **2** (2019) 194 (http://dx.doi.org/10.1016/j.mset.2019.01.010)
14. M. Purwanto, L. Atmaja, M. T. Salleh, M. A. Mohamed, J. Jaafar, A. F. Ismail, M. Santoso, N. Widiastuti, *Malaysian J. Anal. Sci.* **21** (2017) 675 (http://dx.doi.org/10.17576/mjas-2017-2103-17)
15. J. Zawadzki, H. Kaczmarek, *Carbohydr. Polym.* **80** (2010) 394 (http://dx.doi.org/10.1016/j.carbpol.2009.11.037)
16. C. H. Chen, F. Y. Wang, C. F. Mao, W. T. Liao, C. D. Hsieh, *Int. J. Biol. Macromol.* **43** (2008) 37 (http://dx.doi.org/10.1016/j.ijbiomac.2007.09.005)
17. P. B. Palani, K. S. Abidin, R. Kannan, M. Sivakumar, F. M. Wang, S. Rajashabala, G. Velraj, *RSC Adv.* **4** (2014) 61781 (http://dx.doi.org/10.1039/c4ra10788h)
18. V. Vijayalekshmi, D. Khastgir, *J. Memb. Sci.* **523** (2017) 45 (http://dx.doi.org/10.1016/j.memsci.2016.09.058)
19. P. Pei, M. Wang, D. Chen, P. Ren, L. Zhang, *Prog. Nat. Sci. Mater. Int.* **30** (2020) 751 (http://dx.doi.org/10.1016/j.pnsc.2020.08.015)
20. J. Maiti, N. Kakati, S. H. Lee, S. H. Jee, B. Viswanathan, Y. S. Yoon, *J. Power Sources* **216** (2012) 48 (http://dx.doi.org/10.1016/j.jpowsour.2012.05.057)
21. T. Li, Y. Yang, *J. Power Sources* **187** (2009) 332 (http://dx.doi.org/10.1016/j.jpowsour.2008.11.035)
22. H. Wu, B. Zheng, X. Zheng, J. Wang, W. Yuan, Z. Jiang, *J. Power Sources* **173** (2007) 842 (http://dx.doi.org/10.1016/j.jpowsour.2007.08.020)
23. S. N. Ayyubi, L. Admaja, *Walisongo J. Chem.* **3** (2020) 1 (http://dx.doi.org/10.21580/wjc.v3i1.6018).

Journal of the Serbian Chemical Society
JSCS@tmf.bg.ac.rs • www.shd.org.rs/JSCS
J. Serb. Chem. Soc. *89* (3) 415–428 (2024)
JSCS–5729
Original scientific paper
Published 31 March 2024

Search for new apatite-like phases for lead utilization based on crystal structure and thermal expansion

EVGENY N. BULANOV*, ANASTASYYA A. VASILEVA, OXANA N. GOLITSYNA, ALYONA G. SHVAREVA and ALEXANDER V. KNYAZEV

Lobachevsky University, 23 Gagarin ave, Nizhny Novgorod 603022, Russia

(Received 24 July, revised 31 July, accepted 18 September 2023)

Abstract: Apatites, being one of the most numerous mineral-like families of compounds, are considered as a matrix for binding lead ions, which is dangerous for the biosphere. The crystal-chemical (composition, structure) and thermophysical aspects (thermal expansion) are considered as the basis for analysing the properties of this kind of material. It is suggested that substances of the composition $Pb_5(A^{IV}O_4)_2(B^{VI}O_4)$, $Pb_5(A^{IV}O_4)(C^{V}O_4)_2$ can be a perspective form of lead binding materials based on compounds with the structure of apatite (A^{IV} = Si, Ge; B^{VI} = S, Cr; C^{V} = P). Such compounds, as it was shown by DTA and HTXRD experiments, are distinguished by the absence of polymerphism and the abnormal ordering of structure. Also, they have relatively low values of thermophysical indicators (the rate of change of linear thermal expansion coefficients is $0.02–0.03\times10^6$ K^{-1}; values of the volume thermal expansion coefficients are $40–70\times10^6$ K^{-1}). Compounds $Pb_5(SiO_4)(PO_4)_2$ (a = 9.78782(16) Å, c = 7.31084(16) Å, V = 606.555(23) $Å^3$, R-bragg = 4.694 %) and $Pb_5(GeO_4)(PO_4)_2$ (a = 9.87697(12) Å, c = 7.33136(11) Å, V = 619.388(17) $Å^3$, R-bragg = 1.730 %) were obtained, identified and crystallographically characterised for the first time.

Keywords: lead; apatite; IR spectroscopy; Rietveld analysis; *in situ* HTXRD; thermal expansion.

INTRODUCTION

Environmental pollution is one of the global environmental problems of mankind. Soil pollution is particularly dangerous, since 90–95% of food products account for soil resources, from where 70–90% of toxins (including heavy metals) enter the body. It causes a chain reaction – the filtering capacity of the soil decreases, organic matter reserves and biodiversity decrease too; toxicants can enter groundwater from contaminated soil; then they accumulate in plant tissues and are transmitted to pasture animals, birds and finally to humans.[1]

* Corresponding author. E-mail: bulanoven@chem.unn.com
https://doi.org/10.2298/JSC230722069B

Particular attention should be paid to the problem of environmental pollution with lead, and its negative impact on the human body and animals. According to the provisions of the World Health Organization (WHO), lead is one of the 10 chemicals that cause the main concern from the point of view of public health and require action from Member States to protect workers, and children and women of childbearing age.

It should be noted that young children are particularly vulnerable to poisoning since 4–5 times more lead diffuses into their body compared to an adult organism.[2,3] Quite often, the symptoms of poisoning do not appear, and this makes lead exposure an underestimated threat to the most common neurocognitive disorders. Until 2012, the "dangerous blood lead level" for children of more than 10 mg/dL. However, in May 2012, the Advisory Committee on Childhood Lead Poisoning Prevention (ACIP) recommended a value of 5 mg/dL.[4] There is no "safe" concentration of lead in the blood; even such a low lead content in the blood can cause children to have a decrease in intelligence, behavioural disorders and learning difficulties.

The greatest impact on the environment is observed near local sources of pollution (for example, landfills of solid household waste, ore processing plants, metallurgical enterprises, as well as discarded sinkers and lead shot used for fishing or hunting). Natural emissions are also important sources of environmental lead pollution - the diffusion of natural lead from the earth's crust and mantle due to rock weathering and volcanic activity; the continued use of lead-containing paints in some countries (India, Vietnam, Mexico); the production and disposal of lead-acid batteries; products such as solder, pigments, jewellery, stained glass, ammunition, lead cable sheaths, *etc*.[5] Organic lead compounds, previously used as leaded gasoline anti-detonators for internal combustion engines (0.1–0.3 %) increase the octane number and save fuel consumption) are more toxic than inorganic forms of lead. Their use in 1922 became one of the most serious environmental threats. However, August 30, 2021 was a significant date, which means the end of the use of leaded gasoline in the world.[6]

But despite the elimination of the most prominent threat of lead pollution in 2021, this problem remains unresolved. Other sources of pollution (lead paints and pigments still used in some countries, toys, cosmetics, pipe corrosion, *etc*.) require great attention and urgent measures. For example, in the UK, phosphates are added to drinking water to minimize the incoming amount of lead from water pipes.[7]

One of the chain reactions of soil contamination with lead is the contamination of groundwater. Lead can also get into the water due to unauthorized landfills and corrosion of water pipes. To solve this problem, it is necessary to create permeable reaction barriers (PRB) or zones of destructible reaction treatment.[8]

Permeable reaction barriers are an actively developing technology in which a unique reactive material is installed directly on the migration path of the water stream, which makes it cost-effective. Groundwater flows through the barrier and reacts with the material in situ, resulting in toxic metals: Pb, Cd, Co, *etc*. They are delayed, and the water is neutralised. However, PRB materials are effective if they are permeable enough to saturate with groundwater; react with pollutants; retain reactivity and permeability for a long time, and are cost-effective.[9–11]

Apatite II™ – biogenic hydroxyapatite ($Ca_{10-x}Na_x(PO_4)_{6-x}(CO_3)_x(OH)_2$, $x < 1$) obtained from dried fish bones has been recommended as an alternative material for the removal of Zn(II), Pb (II), Mn (II) and Fe (II) from groundwater. Column tests were carried out in which apatite reacted with ground water with an increase in pH to 6.5–7.0 and the release of metal phosphates. Metals precipitated in the form of $Pb_5(PO_4)_3OH$, $Zn_3(PO_4)_2{\cdot}4H_2O$, $Mn_3(PO_4)_2{\cdot}4H_2O$, $Fe_3(PO_4)_2{\cdot}8H_2O$, while the activity of apatite increased with a decrease in the acidity of water. Thus, the concentration of metals in ground water dropped from 30–75 to 0.10 mg/L.[4,12,13]

An alternative way of binding lead is to directly precipitate it from the dissolved form, followed by the formation of compact ceramic materials for disposal.

However, both approaches raise questions about further work with the material: what to do with the substances, whether they are stable when ceramics are obtained from them, how stable the material is to temperature fluctuations in geological formations. It is assumed that the ceramics obtained from the interaction products will be stable for a long time and have good thermochemical properties due to the ability of apatite to encapsulate lead ions in its structure.

This work is devoted to the production of new lead compounds based on the aforementioned crystal-chemical type of apatite, as well as a systematic analysis of the crystal structure and thermal deformations accompanying the process of the final formation of the lead-recycling ceramic material on the example of new substances and a number of previously obtained and studied "classical" apatites ($Pb_5(PO_4)_3F$, $Pb_5(PO_4)_3Cl$, $Pb_5(PO_4)_3I$, $Pb_5(VO_4)_3F$, $Pb_5(VO_4)_3Cl$)[14,15] and solid solutions based on them in $Ca_5(PO_4)_3Cl$-$Pb_5(PO_4)_3Cl$[16] and $Ca_4Bi(PO_4)_3O$–$Pb_4Bi(PO_4)_3O$ systems.[17]

These compositions may be products of the interaction of the reaction material, apatite, with lead ions in ground water. Understanding the effect of the immobilization of lead in the structure of apatite on the solubility, crystallinity, surface activity and thermal stability of the reaction material is an urgent task.

EXPERIMENTAL

Sample preparation

In this paper, a number of compounds of the general composition $Pb_5(A^{IV}O_4)_2(B^{VI}O_4)$, $Pb_5(A^{IV}O_4)(C^{V}O_4)_2$ (A^{IV} = Si, Ge; B^{VI} = S, Cr; C^{V} = P) were considered.

These objects were chosen from the point of view of the high molar fraction of lead in the final compound, the absence of halogens that cause the binding of lead into phases of different composition, as well as from the point of view of the possibility of forming the crystal structure of apatite with a given chemical composition.

The synthesis was carried out by a solid-phase reaction using lead(II) nitrate $Pb(NO_3)_2$, silicon dioxide SiO_2, pre-calcined to 873 K, germanium dioxide GeO_2, diammonium hydrogen phosphate $(NH_4)_2HPO_4$, ammonium sulfate $(NH_4)_2SO_4$ and chromium trioxide (VI) CrO_3. All compounds were produced by "Khimreactive" (Russian Federation) and have *puriss. spec.* quality.

The stoichiometric mixture of reagents was calcined in an alundum crucible, observing the stepwise process: 150–300 °C (decomposition of lead nitrate and ammonium salts), 300––600 °C (conversion of silicon oxide into a more reactive polymorphic modification,[18] further, the heating was carried out in increments of 50 °C for 6 h until the monophase of the sample or the melting of the charge was reached. Dispersion was carried out every 2 h in an agate mortar using ethyl alcohol to create the additional wedging pressure and obtain a more finely dispersed product.

Sample characterization

The chemical purity and composition of the obtained samples were studied with Shimadzu XRF-1800 spectrometer using the fundamental parameters (FP) method with one standard sample. Kα lines intensities were measured three times at 40 kV, 50 mA on Rh anode.

Powder diffractograms were taken using a Shimadzu XRD-6000 X-ray diffractometer: CuKα radiation (λ = 1.5406 Å), Bregg–Brentano focusing, reflection shooting geometry, 2θ 10–60°, 0.02° step, scanning speed 2°/min.

Refinement of the crystal structure of compounds obtained for the first time ($Pb_5(SiO_4)(PO_4)_2$, $Pb_5(GeO_4)(PO_4)_2$) was carried out using the Rietveld method on the same diffractometer in the 2θ angle range 10–110°(120°), with 12 s signal dial time. Refinement of the crystal structure was carried out in the Topas 3.0 program.[19] The background was described by a Chebyshev polynomial of the fourth degree. The peak profile was described by the pseudo-Voigt PV_TCHZ function. The crystal structure from the research[20] (ICSD #65240) was used as a model.

Visualization of a fragment of the crystal structure according to the data of full-profile refinement of powder XRD patterns was carried out in the Atoms v. 6.1.2 program.[21]

High-temperature X-ray diffraction experiments in the range from 298 to 873 K were carried out on the same diffractometer with increments of 0.02° ranging from 10 to 60° using an HA-1001 Shimadzu attachment. To calculate the thermal expansion coefficients and plot the thermal expansion diagram TTT 2.0 software were used.[22]

The behaviour of individual compounds and composites in a wide range of temperature was investigated with thermoanalyser Shimadzu DTG-60H (heating rate 10 K/min, nitrogen atmosphere, alundum crucible).

The IR spectra of compounds were taken using a Shimadzu FTIR-8400s IR spectrometer to clarify the group structure and distortion of tetrahedral groups. The sample was prepared in the form of tablets d = 15 mm from a mixture with KBr (ω(substance) = 4 %), the interval of wave numbers was 4000–400 cm^{-1}, the number of scans was 30.

RESULTS AND DISCUSSION

Based on the data of powder XRD (Fig. 1) and X-ray fluorescence analysis (Table S-I of the Supplementary material to this paper), it was established that

only compounds whose stoichiometry corresponds to the compositions $Pb_5(SiO_4)(PO_4)_2$(PbSiP2), $Pb_5(GeO_4)(PO_4)_2$ (PbGeP2), $Pb_5(GeO_4)_2(CrO_4)$ (PbGe2Cr) and $Pb_5(GeO_4)_2(SO_4)$ (PbGe2S) were obtained, and phosphate derivatives were obtained and identified for the first time. In addition, the IR spectroscopy method shows the absence of various condensed tetrahedral groups, such as $P_2O_7^{4-}$ and $S_2O_6^{2-}$ (Table S-II, Supplementary material).[23]

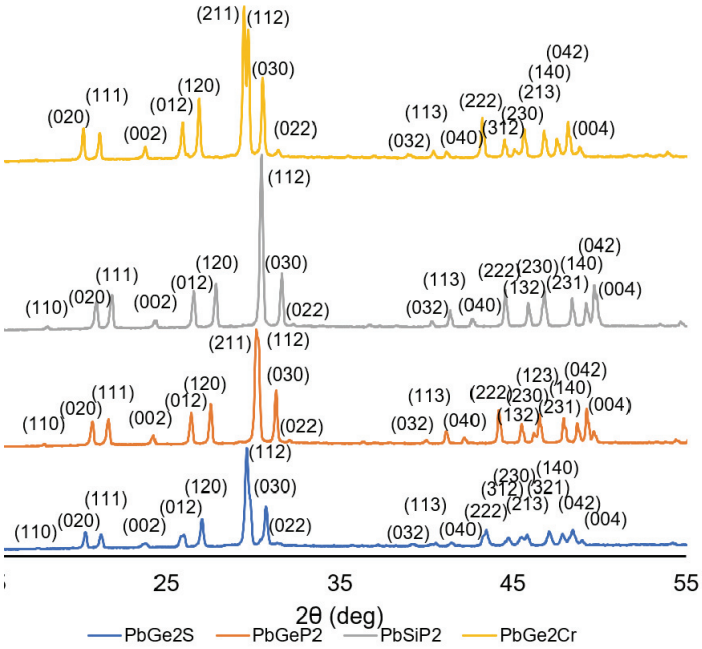

Fig. 1. XRD patterns of compounds under study

Results of the refinement of crystal structures of $Pb_5(SiO_4)(PO_4)_2$ and $Pb_5(GeO_4)(PO_4)_2$ are presented in Figs. 2 and 3 and in Tables I–III. Both compounds crystallise in the hexagonal syngony of the space group $P6_3/m$ and may be described in the framework of the classical crystal-chemical model of compounds with the structure of apatite.[24]

The crystal structure of such compounds is constructed from quasi-layers formed by tetrahedral groups and lead cations at position 6*h*. The layers, in turn, are connected by the polyhedra of lead at position 4*f* (Fig. 3).

The structure of tetrahedral groups is strongly distorted if compared to an ideal tetrahedron: an undistorted tetrahedron has 9 oscillations in the IR range, however, due to the energy degeneracy in its spectrum, only 4 will be observed. The real spectra of the compounds under study are saturated with oscillation bands of various tetrahedral groups (Fig. 4, Table S-II), which indicates not only

the “standard” causes of spectrum complications (difference bands, composite bands, overtones, Fermi resonance) but also a strong distortion of tetrahedra.

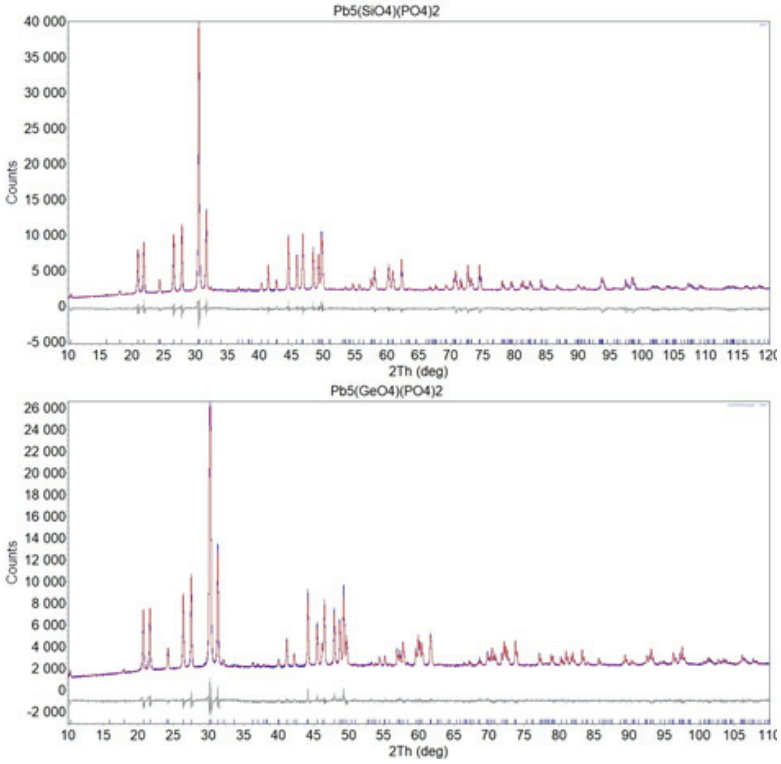

Fig. 2. Experimental, calculated, difference and stroke X-ray diffraction patterns of the new compounds.

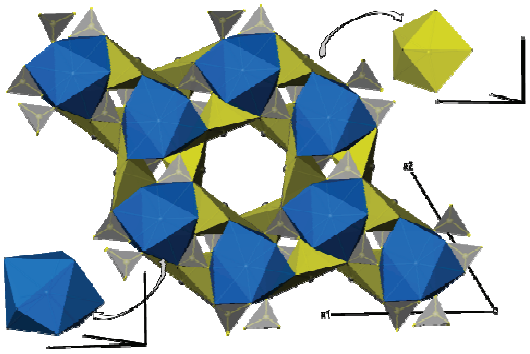

Fig. 3. Fragment of $Pb_5(SiO_4)(PO_4)_2$ crystal structure in projection along *c*-axis. $Pb^{4f}O_9$ polyhedron is shown in bottom left corner, $Pb^{6h}O_6$ polyhedron is in top right corner, $(Si/P)O_4$ tetrahedra are also shown.

Calculation of bond lengths and valence angles based on crystallographic data (Table II) also demonstrate a strong distortion of tetrahedral groups, but in this case, the main reason will be the statistical substitution in the centre of the

tetrahedron of various elements (Si, Ge, P, Cr, S), very different in size (0.26, 0.39, 0.17, 0.345 and 0.12 Å, respectively).[25]

TABLE I. Parameters and results of full-profile X-ray analysis of the crystal structures of the first-time-synthesized compounds

Parameter	$Pb_5(SiO_4)(PO4)_2$	$Pb_5(GeO_4)(PO4)_2$
Space group	$P6_3/m$	
a / Å	9.78782(16)	9.87697(12)
c / Å	7.31084(16)	7.33136(11)
V / Å^3	606.555(23)	619.388(17)
M / g·mol^{-1}	2636.066	2725.107
Crystal size, nm	148.3(73)	130.0(38)
Density, g·cm^{-3}	7.21665(28)	7.30584(21)
Coefficients of pseudo-Voight function		
U	0.1986(66)	–0.0583(23)
V	–0.2103(65)	0.0789(29)
Q	0.0508(15)	–0.02398(88)
Z	0	0
X	0.0001(60)	0.0001(31)
Y	0	0
Scale factor	0.00008708(38)	0.00007836(30)
R-Bragg, %	4.694	1.730
R_{exp} / %	1.94/6.55	1.95/6.76
R_{wp} / %	4.66/15.71	3.83/13.27
R_p / %	3.35/18.89	2.78/16.08
GOF	2.40	1.96
DW	0.49	0.64

TABLE II. Atomic coordinates and occupancies of positions of new synthesized apatites

Atom	Wycoff position	*x*	*y*	*z*	*Occ*	B_{eq} / Å^2
$Pb_5(SiO_4)(PO4)_2$						
Pb1	4f	1/3	2/3	0.9987(18)	1	0.461(31)
Pb2	6h	0.24952(50)	0.99860(89)	1/4	1	0.461(31)
P	6h	0.3805(25)	0.3950(21)	1/4	2/3	0.52(35)
Si					1/3	0.52(35)
O1	6h	0.4444(35)	0.3274(33)	1/4	1	0.46(38)
O2	6h	0.4778(30)	0.5619(29)	1/4	1	0.46(38)
O3	12i	0.2700(19)	0.3494(14)	0.0685(22)	1	0.46(38)
$Pb_5(GeO_4)(PO4)_2$						
Pb1	4f	1/3	2/3	0.9923(14)	1	0.538(28)
Pb2	6h	0.24943(37)	0.99694(63)	1/4	1	0.538(28)
P	6h	0.3824(17)	0.3906(15)	1/4	2/3	0.68(18)
Ge	6h				1/3	0.68(18)
O1	6h	0.4503(30)	0.3336(29)	1/4	1	1.16(36)
O2	6h	0.4946(24)	0.5730(24)	1/4	1	1.16(36)
O3	12i	0.2593(16)	0.3432(13)	0.0715(18)	1	1.16(36)

TABLE III. Parameters of the $Pb^{4f}O_9$ coordination polyhedron in the crystal structure of mixed-tetrahedral apatites under consideration

Distance and angle	$Pb_5(SiO_4)(PO_4)_2$	$Pb_5(GeO_4)(PO_4)_2$	$Pb_5(GeO_4)_2(SO_4)$	$Pb_5(GeO_4)_2(CrO_4)$
M^{4f}–O2×3, Å	2.807(28)	2.882(22)	2.833	2.833
M^{4f}–O1×3, Å	2.813(30)	2.802(25)	2.494	2.469
M^{4f}–O3×3, Å	2.892(15)	2.950(13)	2.956	2.972
φ / °	26.1	21.2	25.2	25.8

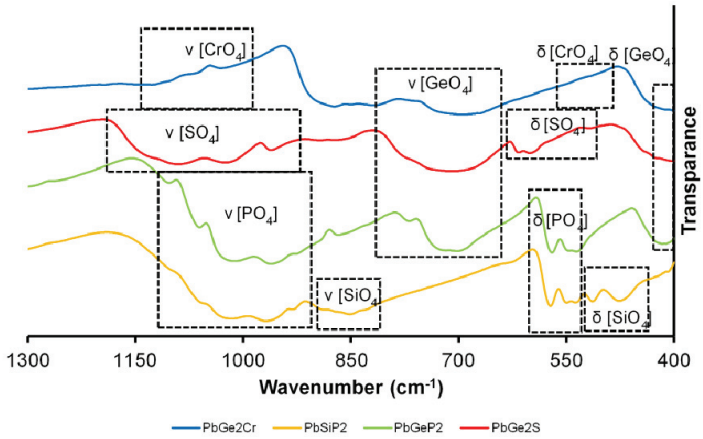

Fig. 4. IR spectra of synthesized mixed-tetrahedral apatites with line assignments.

The cations located in the crystallographic position 6*h*, as a rule, form coordination polyhedra with *CN* 7–9: pentagonal bipyramids, two- and three-cap trigonal prisms. In this case, as can be seen from the example of a fragment of the structure (Fig. 3), it is a pentagonal pyramid in question. However, this type of structural element is due to the specifics of the visualization software. The electronic structure of lead atoms has a fundamental difference from the numerous cations capable of forming the structure of apatite: being a p-element, lead has a stereochemically active electron 6s pair, which is located in the formally missing vertex of the pentagonal bipyramid, and directly in the structure is deployed in the area of a hexagonal channel running along the crystallographic axis *c*.

The cations in the crystallographic position 4*f* are always three-cap trigonal prisms of varying degrees of distortion. The distortion of this structural element is estimated by the twist angle.[26] As can be seen from the data in Table III, in the compounds under consideration, they are in a fairly narrow range of values characteristic of the structural type as a whole.

For the analysis of thermal expansion, the temperature dependences of the parameters of elementary cells are constructed, which are then approximated by linear or quadratic functions, according to the coefficients of which those of ther-

mal expansion are calculated in the TTT 2.0 software. A similar operation for compounds with the structure of apatite was given step by step in our previous works,[14,15] and here we would like to focus on specific results and conclusions.

First of all, it is worth noting that based on the results of the DSC (Fig. 5), it was decided to conduct high-temperature X-ray studies in the temperature range of 298–873 K, and the available data on other lead-containing apatites should be limited to a similar range (Fig. 6). It is also worth noting here that, unlike the vast majority of "classical" Pb-apatites, no anomalies were detected on the DSC curves of mixed-tetrahedral compounds and during the high-temperature X-ray experiment, suggesting the presence of polymorphic transformations.[14]

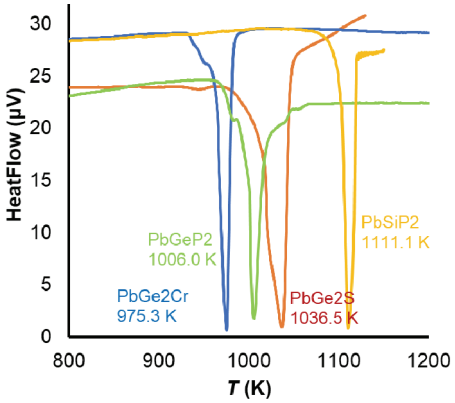

Fig. 5. DSC curves for synthesized mixed-tetrahedral apatites near melting points.

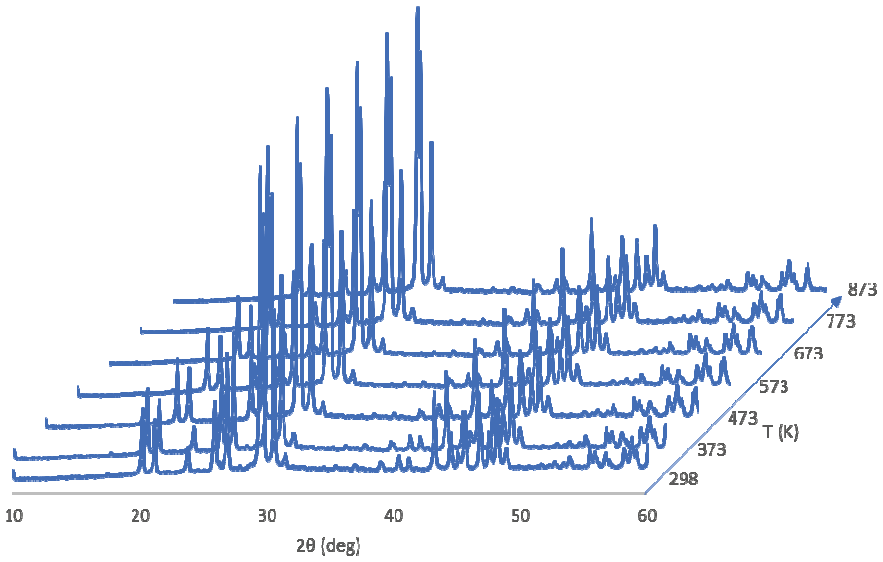

Fig. 6. HTXRD patterns of $Pb_5(GeO_4)_2(CrO_4)$.

Secondly, earlier we provided data on the values of the coefficients of thermal expansion exclusively along the crystallographic directions *a* and *c* and, thus, we obtained a characteristic of the crystal structure or of a single-crystal material. Of course, in the case of the hexagonal syngony under consideration, the main directions of the thermal expansion tensor and the crystallographic directions are strictly fixed relative to each other, and the values of the coefficients coincide. Therefore, for the completeness, Fig. 7 shows as an example a three-dimensional temperature surface of thermal expansion $Pb_5(SiO_4)(PO_4)_2$ at a temperature of 873 K, indicating the directions of the main directions of the tensor and the crystallographic axes. It is also worth noting that for the lead-containing apatites under consideration, the temperature dependencies of the linear coefficients of thermal expansion are shown in Table S-III of the Supplementary material, but for a potential material representing a ceramic polycrystalline sample, these data cannot be directly transferred due to the statistical orientation of microcrystals in space. However, the volumetric coefficient of thermal expansion (Table IV), as an integral quantity characterizing the behaviour of the material, can be used for analysis.

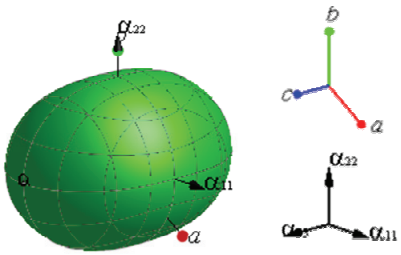

Fig. 7. Thermal expansion diagram $Pb_5(SiO_4)(PO_4)_2$ at 873 K, indicating the directions of the crystallographic axes and the main components of the thermal deformation tensor.

In the case of individual compounds with the apatite structure, it is seen that the nature of temperature dependencies (the rate of change is $0.02–0.03\times10^6$ K^{-1} per K) and the values of thermal expansion ($40–70\times10^6$ K^{-1}) converge, which confirms the previously stated assumption about the fundamental influence of metal cations in the composition of apatites on the nature of thermal deformations.[15] The abnormal behaviour of (rate of change $\sim0.1\times10^6$ K^{-1} per K; interval $1–66\times10^6$ K^{-1}) $Pb_5(PO_4)I$ compound is most likely due to the high defect of the structure, which was shown in a recent paper. The $Pb_5(PO_4)_3F$ compound also arouses similar suspicions (the rate of change is $\sim0.06\times10^6$ K^{-1} per K; the interval is $30–67\times10^6$ K^{-1}). The remaining "classical" and mixed-tetrahedral apatites behave without any anomalies.

Volumetric coefficients of thermal expansion of solid solutions of systems $(Ca_xPb_{1-x})_5(PO_4)_3Cl$ and $(Ca_xPb_{1-x})_4Bi_2(PO_4)_6O$ lie in a rather narrow range of values ($30–60\times10^6$ K^{-1}), and lower than in the case of individual substances, with the exception of the composition $Ca_{2.5}Pb_{2.5}(PO_4)_3Cl$, which differs both in

the anomalous values of the coefficient (interval 16–106×10^6 K^{-1}) and the angle of inclination of its temperature dependencies (the rate of change is ~0.16×10^6 K^{-1} per K). The only assumption about the reason for this effect is the formation of an internal ordering of the distribution of calcium and lead ions in the positions of the crystal structure, instead of the statistical distribution inherent in solid solutions.

TABLE IV. Temperature dependencies of volume (α_V) thermal expansion coefficients for "classical" apatites (column 1–5), mixed-tetrahedral apatites (column 6–9), solid solutions in $(Ca_xPb_{1-x})_5(PO_4)_3Cl$ (column 10–12) and $(Ca_xPb_{1-x})_4Bi_2(PO_4)_6O$ (column 13–15) systems; Standard uncertainties, u = 0.02 wt. %

T / K	1	2	3	4	5
	PbPF	PbPCl	PbPI	PbVF	PbVCl
298	30.0	39.1	1.0	40.5	46.5
373	34.8	41.6	9.6	42.5	48.1
473	41.2	45.0	20.9	45.2	50.2
573	47.6	48.3	32.3	47.8	52.2
673	53.9	51.6	43.6	50.5	54.3
773	60.2	54.9	54.8	53.1	56.3
873	66.5	58.1	66.0	55.7	58.4
T / K	6	7	8	9	10
	PbSiP2	PbGeP2	PbGe2S	PbGe2Cr	Ca3.5Pb1.5
298	46.4	43.8	49.0	54.1	35.6
373	48.6	45.9	51.9	56.3	38.3
473	51.5	48.6	55.8	59.1	41.9
573	54.4	51.4	59.6	61.9	45.5
673	57.3	54.1	63.5	64.7	49.0
773	60.2	56.8	67.3	67.5	52.6
873	63.0	59.5	71.0	70.2	56.1
T / K	11	12	13	14	15
	Ca2.5Pb2.5	Ca1.25Pb3.75	Ca6Pb2Bi2	Ca4Pb4Bi2	Ca2Pb6Bi2
298	16.1	34.5	32.1	35.0	38.0
373	28.0	37.0	34.6	37.9	40.7
473	43.8	40.3	37.9	42.2	44.2
573	59.5	43.6	41.2	46.6	47.7
673	75.2	46.8	44.4	50.9	51.2
773	90.7	50.0	47.7	55.2	54.7
873	106.1	53.2	50.9	59.5	58.1

From the point of view of binding lead for a long time into a ceramic matrix, its solid solutions with calcium look promising. Their advantages include lower values of thermal expansion coefficients, low rates of thermal deformation, and high melting temperatures. In addition, such a composition of the binding matrix has proven itself in the development of immobilizers of the Apatite II^{TM} type.[4,12,13] However, from the point of view of further compaction and binding,

there remains a high risk associated with the restructuring of the structure and the accompanying change in thermal deformations, as well as abnormal orderings in the crystal structure.

"Classical" apatites also raise concerns in terms of polymorphism. An additional limiting factor is the presence of halogen in their composition. A number of studies have demonstrated a low stability of halogen retention in the apatite matrix in leaching experiments,[27,28] which may lead to an increase in the defectiveness of the material up to its destruction.

Thus, among the remaining mixed tetrahedral compounds for further study, the most promising is the composition $Pb_5(SiO_4)(PO_4)_2$, which, in addition to relative thermal stability and the lowest level of thermal deformations among the analogues under consideration, has the advantage of simplicity and accessibility of the chemical composition.

CONCLUSION

This paper presents the results of the search for new phases to solve an urgent environmental problem – lead binding for long-term isolation from the environment, as well as an assessment of their prospects in terms of crystal chemical (composition, structure) and thermophysical (melting point, thermal expansion) data.

In the course of work it was not only possible to obtain two new mixed-tetrahedral compounds with apatite structure ($Pb_5(SiO_4)(PO_4)_2$ (a = 9.78782(16) Å, c = 7.31084(16) Å, V = 606.555(23) Å^3, R-bragg = 4.694 %) and $Pb_5(GeO_4)(PO_4)_2$ (a = 9.87697(12) Å, c = 7.33136(11) Å, V = 619.388(17) Å^3, R-bragg = 1.730 %) and characterize them in terms of crystal structure and thermal deformations, but also on the basis of thermal expansion analysis from the sample of lead-containing apatites extended due to earlier studies, to find a subclass characterised by low values of thermophysical parameters indicators (the rate of change of linear thermal expansion coefficients is $0.02–0.03\times10^6$ K^{-1}; values of the volume thermal expansion coefficients are $40–70\times10^6$ K^{-1}), which gives grounds to consider it as a potential chemical basis for the creation of materials for the lead immobilization for lead.

Of course, the above conclusions are not exhaustive and should be subsequently supplemented by a study of lead leaching rates from the proposed matrix under conditions as close as possible to real operating conditions. However, a non-trivial approach allowed us to detect a number of new compounds $Pb_5(SiO_4)(PO_4)_2$, $Pb_5(GeO_4)(PO_4)_2$ along with previously known $Pb_5(GeO_4)_2(CrO_4)$ and $Pb_5(GeO_4)_2(SO_4)$, but were out of sight, the use of which can solve the lead pollution problem faster.

SUPPLEMENTARY MATERIAL

Additional data and information are available electronically at the pages of journal website: https://www.shd-pub.org.rs/index.php/JSCS/article/view/12511, or from the corresponding author on request.

Acknowledgements. The authors are grateful to V.Zh. Korokin, Ph.D., for some of the syntheses carried out. The research was carried out with financial support *via* State assignment in Research scientific laboratory of "Chemistry of natural products and their synthetic analogues" of Scientific Educational Centre "Technoplatform 2035" (project FSWR-2021-014).

ИЗВОД

ПРОНАЛАЖЕЊЕ НОВИХ АПАТИТНИХ ФАЗА ЗА ИСКОРИШЋЕЊЕ ОЛОВА НА ОСНОВУ КРИСТАЛНЕ СТРУКТУРЕ И ТОПЛОТНОГ ШИРЕЊА

EVGENY N. BULANOV, ANASTASYYA A. VASILEVA, OXANA N. GOLITSYNA, ALYONA G. SHVAREVA и ALEXANDER V. KNYAZEV

Lobachevsky University, 23 Gagarin ave, Nizhny Novgorod 603022, Russia

Апатити, као једна од најзначајнијих група минералних структура, се разматрају као матрица за имобилизацију јона олова, који имају негативан утицај на биосферу. Кристално-хемијски (састав, структура) и термофизички аспект (топлотно ширење) се узимају као основа за анализу особина ове класе материјала. Сугерише се да су супстанце састава $Pb_5(A^{IV}O_4)_2(B^{VI}O_4)$ и $Pb_5(A^{IV}O_4)(C^{V}O_4)_2$ апатитне структуре одговарајућа форма за имобилизацију олова, при чему је A^{IV} = Si, Ge; B^{VI} = S, Cr и C^{V} = P. Ове компоненте, као што је показано помоћу диференцијално-термијске анализе (DTA) и високотемпературне рендгенске анализе (HTXRD), одликују се одсуством полиморфизма и абнормалног уређења структуре. Такође, имају релативно мале вредности термофизичких индикатора (брзина промене линеарног коефицијента топлотног ширења је 0.02–-0.03×10^6 K^{-1}, вредности запреминског коефицијента ширења су 40–70×10^6 K^{-1}). По први пут су добијене, идентификоване и кристалографски окарактерисане компоненте $Pb_5(SiO_4)(PO_4)_2$ (a = 9,78782(16) Å, c = 7,31084(16) Å, V = 606,555(23) Å^3, R-bragg = 4,694 %) и $Pb_5(GeO_4)(PO_4)_2$ (a = 9,87697(12) Å, c = 7,33136(11) Å, V = 619,388(17) Å^3, R-bragg = = 1,730 %).

(Примљено 24. јула, ревидирано 31. јула, прихваћено 18. септембра 2023)

REFERENCES

1. Food and Agriculture Organization of the United Nations, *Polluting our soils is polluting our future*, https://www.fao.org/fao-stories/article/en/c/1126974/ (accessed: July 22, 2023)
2. World Health Organization, *Lead poisoning*, https://www.who.int/news-room/fact-sheets/detail/lead-poisoning-and-health (accessed: July 22, 2023)
3. L. Chandran, R. Cataldo, *Pediatr. Rev.* **31** (2010) 399 (https://doi.org/10.1542/pir.31-10-399)
4. W. A. Martin, S. L. Larson, D. R. Felt, J. Wright, C. S. Griggs, M. Thompson, J. L. Conca, C. C. Nestler, *Appl. Geochem.* **23** (2008) 34 (https://doi.org/10.1016/j.apgeochem.2007.08.005)
5. United Nations Environment Programme, *Key scientific findings for lead: an excerpt from Final review of scientific information on lead*, https://wedocs.unep.org/bitstream/handle/20.500.11822/22871/Key_Scientific_Findings_Lead_RU.pdf?sequence=5&isAllowed=y (accessed: July 22, 2023)

6. United Nations Environment Programme, *Era of leaded petrol over, eliminating a major threat to human and planetary health*, https://www.unep.org/news-and-stories/press-release/era-leaded-petrol-over-eliminating-major-threat-human-and-planetary (accessed: July 22, 2023)
7. J. D. Hopwood, G. R. Derrick, D. R. Brown, C. D. Newman, J. Haley, R. Kershaw, M. Collinge, *J. Chem.* **2016** (2016) 9074062 (https://doi.org/10.1155/2016/9074062)
8. I. S. Kasimov, A. E. Vorob'ev, *Geochemical barriers in the hypergenesis zone*, MSU Publishing House, Moscow, 2002
9. J. Oliva, J. De Pablo, J. L. Cortina, J. Cama, & C. Ayora, *J. Hazard. Mater.* **194** (2011) 312 (https://doi.org/10.1016/j.jhazmat.2011.07.104)
10. M. Katoh, A. Makimura, T. Sato, *Environ. Technol. (UK)* **37** (2016) 3036 (https://doi.org/10.1080/09593330.2016.1174744)
11. S. Bailliez, A. Nzihou, E. Bèche, G. Flamant, *Process Saf. Environ. Prot.* **82** (2004) 175 (https://doi.org/10.1205/095758204322972816)
12. J. Oliva, J. De Pablo, J. L. Cortina, J. Cama, C. Ayora, *J. Hazard. Mater.* **184** (2010) 364 (https://doi.org/10.1016/j.jhazmat.2010.08.045)
13. J. Oliva, J. Cama, J. L. Cortina, C. Ayora, J. De Pablo, *J. Hazard. Mater.* **213**–**214** (2012) 7 (https://doi.org/10.1016/j.jhazmat.2012.01.027)
14. N. G. Chernorukov, A. V. Knyazev, E. N. Bulanov, *Inorg. Mater.* **47** (2011) 172 (https://doi.org/10.1134/S002016851101002X)
15. A. V. Knyazev, N. G. Chernorukov, E. N. Bulanov, *Mater. Chem. Phys.* **132** (2012) 773 (https://doi.org/10.1016/j.matchemphys.2011.12.011)
16. A. V. Knyazev, E. N. Bulanov, V. Z. Korokin, *Mater. Res. Bull.* **61** (2014) 47 (https://doi.org/10.1016/j.materresbull.2014.09.089)
17. E. N. Bulanov, K. S. Stasenko, O. N. Golitsyna, V. M. Kyashkin, A. V. Knyazev, *Ceram. Int.* **48** (2022) 9858 (https://doi.org/10.1016/j.ceramint.2021.12.188)
18. M. Mosesman, K. Pitzer, *J. Am. Chem. Soc.* **63** (1941) 2348 (https://doi.org/10.1021/ja01854a013)
19. A. A. Coelho, *J. Appl. Crystallogr.* **51** (2018) 210 (https://doi.org/10.1107/S1600576718000183)
20. G. Engel, B. Deppisch, *Z. anorg. allg. Chem.* **562** (1988) 131 (https://doi.org/10.1002/zaac.19885620116)
21. Atoms, V. 6.1.2, by Shape Software, 2006
22. R. S. Bubnova, V. A. Firsova, S. K. Filatov, *Glas. Phys. Chem.* **39** (2013) 347 (https://doi.org/10.1134/S108765961303005X)
23. K. Nakamoto, *Infrared and Raman Spectra of Inorganic and Coordination Compounds*, Fourth Edi John Wiley and Sons, Inc., New York, 1986
24. T. White, C. Ferraris, J. Kim, S. Madhavi, *Apatite - an adaptive framework structure*, 2018 (https://doi.org/10.2138/rmg.2005.57.10)
25. R. D. Shannon, *Acta Crystallogr., A* **32** (1976) 751767 (https://doi.org/10.1107/S0567739476001551)
26. S. C. Lim, T. Baikie, S. S. Pramana, R. Smith, T. J. White, *J. Solid State Chem.* **184** (2011) 2978 (https://doi.org/10.1016/j.jssc.2011.08.031)
27. M. Zhang, E. R. Maddrell, P. K. Abraitis, E. K. H. Salje, *Mater. Sci. Eng., B* **137** (2007) 149 (https://doi.org/10.1016/j.mseb.2006.11.003)
28. Z. Zhang, A. Heath, K. T. Valsaraj, W. L. Ebert, T. Yao, J. Lian, J. Wang, *RSC Adv.* **8** (2018) 3951 (https://doi.org/10.1039/c7ra11049a).

Journal of the Serbian Chemical Society
JSCS@tmf.bg.ac.rs • www.shd.org.rs/JSCS
J. Serb. Chem. Soc. 89 (3) S139–S142 (2024) *Supplementary material*

SUPPLEMENTARY MATERIAL TO

Search for new apatite-like phases for lead utilization based on crystal structure and thermal expansion

EVGENY N. BULANOV*, ANASTASYYA A. VASILEVA, OXANA N. GOLITSYNA, ALYONA G. SHVAREVA and ALEXANDER V. KNYAZEV

Lobachevsky University, 23 Gagarin ave, Nizhny Novgorod 603022, Russia

J. Serb. Chem. Soc. 89 (3) (2024) 415–428

* Corresponding author. E-mail: bulanoven@chem.unn.com

TABLE S-I. X-ray fluorescence analysis data for synthesized compounds.

Compound	PbO / wt%		SiO_2 / wt%		GeO_2 / wt%		P_2O_5 / wt%		SO_3 / wt%		CrO_3 / wt%	
	found	calc	found	calc	found	calc	found	calc	found	calc	found	calc
$Pb_5(SiO_4)(PO4)_2$	84.68	84.67	4.54	4.56			10.78	10.77				
$Pb_5(GeO_4)(PO4)_2$	81.92	81.91			7.66	7.68	10.42	10.42				
$Pb_5(GeO_4)_2(SO_4)$	79.42	79.41			14.82	14.89			5.76	5.70		
$Pb_5(GeO_4)_2(CrO_4)$	78.3	78.3			14.7	14.68					7.00	7.02

Standard uncertainties u are u(wt) = 0.02%.

TABLE S-II. Assignment of lines in IR spectra of mixed-tetrahedral apatites under study

Assignment	$Pb_5(SiO_4)(PO4)_2$	$Pb_5(GeO_4)(PO4)_2$	$Pb_5(GeO_4)_2(SO_4)$	$Pb_5(GeO_4)_2(CrO_4)$
ν (SiO_4)	850 s 827 m			
δ (SiO_4)	514 m 475 m			
ν (GeO_4)		724 m 703 m	730 m 708 sh	728 m 699 sh
δ (GeO_4)		416 m	411 m	412 m
ν (PO_4)	1097 sh 1056 sh 1021 s 970 s 932 sh 888 sh 870 sh 852 s 832 sh	1104 w 1061 sh 1015 s 964 s 932 sh 870 m 827 sh		
δ (PO_4)	572 s 550 m 538 m	570 s 549 m 538 m		
ν (SO_4)			1128 m 1026 m 963 m 896 w 876 w	
δ (SO_4)			617 m 602 m 520 w	
ν (CrO_4)				1126 m 1100 sh 1085 sh 1030 w
δ (CrO_4)				622 w 527 sh

s – strong, m – medium, w – weak, sh - shoulder

TABLE S-III. Temperature dependencies of linear thermal expansion coefficients for "classical" apatites (column 1-5), mixed-tetrahedral apatites (column 6-9), solid solutions in $(Ca_xPb_{1-x})_5(PO_4)_3Cl$ (column 10-12) and $(Ca_xPb_{1-x})_4Bi_2(PO_4)_6O$ (column 13-15) systems

	1	2	3	4	5	6	7	8	9	10	11	12	13	14	15
T (K)	**PbPF**	**PbPCl**	**PbPI**	**PbVF**	**PbVCl**	**PbSiP2**	**PbGeP2**	**PbGe2S**	**PbGe2Cr**	**Ca3.5Pb1.5**	**Ca2.5Pb2.5**	**Ca1.25Pb3.75**	**Ca6Pb2Bi2**	**Ca4Pb4Bi2**	**Ca2Pb6Bi2**
									α_a (K^{-1})·10^6						
298	9.7	13.5	-1.0	15.3	12.2	15.2	14.3	16.4	17.3	13.0	6.4	11.7	11.0	12.5	12.5
373	10.9	13.8	1.6	15.3	12.5	15.6	14.7	17.1	17.8	13.6	9.6	12.2	11.6	13.1	13.1
473	12.5	14.2	5.0	15.4	13.0	16.2	15.3	18.0	18.4	14.5	13.9	12.8	12.3	13.8	13.9
573	14.0	14.6	8.5	15.4	13.4	16.7	15.8	18.9	19.0	15.5	18.2	13.4	13.0	14.6	14.6
673	15.6	15.0	11.9	15.5	13.9	17.3	16.3	19.8	19.6	16.4	22.4	14.0	13.8	15.3	15.4
773	17.1	15.4	15.3	15.5	14.3	17.8	16.8	20.7	20.1	17.2	26.6	14.7	14.5	16.1	16.1
873	18.7	15.8	18.7	15.6	14.8	18.3	17.3	21.6	20.7	18.1	30.8	15.3	15.2	16.8	16.9
									α_c (K^{-1})·10^6						
298	10.5	12.0	3.1	9.9	22.1	16.0	15.1	16.3	19.5	9.7	3.3	11.2	10.1	9.6	13.0
373	13.0	13.9	6.4	11.8	23.0	17.4	16.4	17.8	20.7	11.0	8.8	12.7	11.4	11.7	14.5
473	16.3	16.5	10.9	14.4	24.2	19.2	18.1	19.8	22.4	12.8	16.0	14.7	13.3	14.6	16.5
573	19.5	19.0	15.4	16.9	25.3	21.0	19.8	21.9	24.0	14.6	23.2	16.7	15.1	17.4	18.5
673	22.8	21.5	19.8	19.5	26.5	22.8	21.5	23.9	25.6	16.3	30.4	18.7	16.9	20.2	20.4
773	26.0	24.0	24.2	22.0	27.6	24.6	23.2	25.9	27.2	18.1	37.5	20.7	18.7	23.0	22.4
873	29.2	26.5	28.6	24.5	28.8	26.3	24.9	27.9	28.8	19.8	44.5	22.7	20.5	25.8	24.3

Standard uncertainties u are u(wt) = 0.02%.

Journal of the Serbian Chemical Society
JSCS@tmf.bg.ac.rs • www.shd.org.rs/JSCS
J. Serb. Chem. Soc. *89* (3) 429–440 (2024)
JSCS–5730
Original scientific paper
Published 31 March 2024

Geochemistry of neutral mine drainage at sulfide deposits – Example of the „Grot“ Pb–Zn mine, south–eastern Serbia

SNEŽANA S. KRETIĆ*, JANA S. ŠTRBAČKI and NEBOJŠA B. ATANACKOVIĆ

University of Belgrade, Faculty of Mining and Geology, Department of Hydrogeology, Djusina 7, 11000 Belgrade, Serbia

(Received 11 August, revised 21 October 2023, accepted 19 February 2024)

Abstract: This study examines the chemistry of mine waters of the “Grot” Pb–Zn mine and identifies the hydrogeochemical factors that influence the formation of mine waters chemical composition. Eleven mine water samples were collected at six locations across the area of Kriva Feja in order to determine their chemical composition. Data analysis revealed that the waters belong to the HCO_3^-–SO_4^{2-}–Ca^{2+} and SO_4^{2-}–Ca^{2+} water types, with neutral pH values. The concentrations of metals in these waters (zinc, lead, barium, copper, chromium) are generally low, and most of the samples meet drinking water quality criteria (USEPA standards). Modelling using the PHREEQC software indicates that the dominant processes in the formation of the chemical composition of these waters are the dissolution of carbonate minerals and the oxidation of sulphide minerals. Carbonate minerals have a scarcer occurrence compared to sulphide minerals, such as galena, sphalerite and pyrite, which are dominantly distributed. The low intensity of sulphide mineral oxidation is interpreted to result from a rapid water exchange and reduced contact time between the water and the rock. The occurrence of this process is localized only in the ore body zone. This study highlights the importance of kinetics (in terms of the chemical reaction rate) as the main factor influencing the oxidation of sulphide minerals and, subsequently the quality of mine waters.

Keywords: groundwater; acid mine drainage; hydrogeochemical factors; metals; PHREEQC modelling; saturation index.

INTRODUCTION

Negative environmental effects occur when surface water or groundwater comes into contact with primary and secondary minerals from the ore deposit under oxidizing conditions.[1] The deposits containing sulphide minerals tend to generate acid mine drainage (AMD) during the oxidation process of these minerals (*e.g.*, pyrite, marcasite, and pyrrhotite).[2–4] The acid mine drainage refers to

* Corresponding author. E-mail: snezana.kretic@rgf.bg.ac.rs
https://doi.org/10.2298/JSC230811013K

water with low pH values (between 3.5 and 5), high sulphate concentrations, and elevated metal concentrations.[4,5] The oxidation of sulphide minerals, primarily pyrite, depends on physicochemical conditions, the type of oxidant (O_2 or Fe^{3+}), its concentration, activity, and the presence of microorganisms.[6–8] According to Lottermoser, several types of pyrite oxidation can be distinguished, including: abiotic oxidation by oxygen, biotic oxidation by oxygen, abiotic oxidation by oxygen and iron and biotic oxidation by oxygen and iron.[3] The formation of acid mine drainage is strongly influenced by the reaction rate (kinetics) and its duration.[9] The rate of biotic oxidation is always higher than abiotic, and pyrite oxidation in the presence of Fe^{3+} can be 2–3 times faster than in the presence of O_2 as the oxidant.[5] Depending on the geological environment in which groundwater circulates (*i.e.*, the type of ore and host rocks), acid mine drainage may not always form. Unlike pyrite, the oxidation of other sulphide minerals such as galena, sphalerite or arsenopyrite in the presence of oxygen does not directly produce acid mine drainage.[10–12] This is due to their lower reactivity, resulting from greater crystal structure stability, low concentrations of released iron and the formation of poorly soluble minerals.[13] The absence of sulphide mineral oxidation, in addition to kinetics, can also result from the presence of minerals that neutralize the acidity of mine drainage (carbonates, silicates, and hydroxides).[2,3] The neutralization process occurs under the same conditions as the sulphide mineral oxidation process and is independent of the oxygen concentration in the water.[3] Neutral mine drainage (NMD) will form in some sulphide deposits due to the previously mentioned processes. Neutral mine drainage refers to waters with a neutral pH value (between 6.5 and 7) and high metal concentrations (most commonly lead, zinc, copper and cadmium).[3] In these waters, sulphates and bicarbonates are the main anions, and calcium, magnesium and sodium content is elevated compared to acid mine drainage.[3] The occurrence of neutral pH and lower metal concentrations in some mine waters can be attributed to kinetic factors, *i.e.*, the slow dissolution and oxidation of sulphide minerals compared to rapid water exchange in mine waters.[2] Additionally, the surfaces of sulphide minerals can be covered with insoluble oxides or carbonates, which limits the oxidation.[2] Instances of neutral mine drainage have been found in Pb–Zn deposits throughout the United Kingdom and Italy.[14–17] These examples are characterized by neutral pH and increased concentrations of trace components such as lead, zinc, copper, arsenic and cadmium (depending on the specific locality where the mine waters are formed). The studies considering these occurrences as the most common reason for the formation of neutral mine drainage cite the neutralization process in the presence of carbonate minerals.[14–17]

The objectives of this study are to identify factors that could influence the formation of neutral mine drainage, determine the mineral phases being dissolved, and identify the dominant hydrogeochemical processes that affect the rel-

ease of trace elements into water. Such an approach could contribute to the adaptation of the mineral resource exploitation methods to reduce the negative impact on the environment and water resources.

EXPERIMENTAL

Study area

Details related to study area are given in Supplementary material to this paper.

Sampling and chemical analysis

Mine water samples were collected at eleven locations during the year's low flow period (September–November). During that period, 16 mine water samples were collected, while 11 samples were further considered in the study. The considered samples were taken at various locations across the exploitation field at discharge points from the adits before the sedimentation ponds, while the samples taken at locations after the ponds were omitted due to the possibility of the removal of certain components from the water. Mine water sampling was performed according to ISO 5667-1:2006, ISO 5667-3:2012 and ISO 5667-10:1992 standards at the adits discharge points.[18-20] Sampling and chemical analyses were carried out by the Institute of Public Health Vranje.

The determination of the pH was performed potentiometrically according to the ISO 10523:2008 standard.[21] The water mineralization was determined by the analytical procedure as the dry residue at 103–105 °C using the US EPA 160.3 method.[22] Main cation composition (Na^+, K^+, Mg^{2+}, Ca^{2+}) together with metals (zinc, lead, manganese, barium, copper, chromium) were determined by the induced coupled plasma with the atomic emission spectrometry ICP-AES (according to ISO 11885:2007 standard).[23] The content of arsenic in mine waters was determined by the atomic absorption spectrophotometry using the hydride technique (ISO 11969:1996).[24] The content of ammonium, nitrate, and nitrite ions was determined by spectrophotometric methods (ISO 7150-1:1984, ISO 7890-3:1988, ISO 6777:1984).[25-27] The content of sulphate ions was determined by the turbidimetric method (SRPS H.G8.115:1984), while the chloride content was determined volumetrically according to the ISO 9297:1989 standard.[29,29] Bicarbonate ions in water were determined by titration, in accordance with ISO 9963-1:1994.[30] The content of dissolved oxygen was determined by the volumetric method (ISO 5813:1983), while hydrogen sulfide was determined spectrophotometrically (SZZZ, 1990).[31,32]

Analysis and calculations

The degree of saturation of groundwater in relation to a certain mineral can be determined by comparing the product of ionic activity (*IAP*) of a real water sample and the solubility product of that mineral (*Ksp*), according to:[33]

$$SI = \log \frac{IAP}{Ksp} \tag{1}$$

where *SI* is the saturation index.

The obtained *SI* value can indicate oversaturation or undersaturation of the water sample with respect to a given mineral, with the possibility of precipitation ($SI > 0$) or dissolution ($SI < 0$) of the specific mineral.[33]

Saturation indices for specific mineral phases and the dissolved forms of inorganic substances in water were calculated using PHREEQC software (interactive version 3.7.3-15968).[34] This software is widely used in geochemical and mine water research for these types of cal-

culations.[15,35-37] When calculating *SI* for carbonate minerals, the MINTEQ database was used, as it covers a wide range of inorganic parameters (metals) and organic compounds.[38] The LLNL database was used for the calculation of *SI* for sulphur-bearing minerals because it has the most extensive dataset, making it more suitable for such calculations.[33,34] For example, it includes the reaction of pyrite with water.[34]

Excel workbook was used to determine statistical parameters (minimum, maximum, median) to determine the variations of certain parameters in mine waters. Also, this program was used for the graphical presentation of chemical parameters in the form of Box-Plot diagrams.

RESULTS AND DISCUSSION

Hydrochemistry of neutral mine drainage of the „Grot“ Pb–Zn mine

According to their physical properties, the examined mine waters are colourless and odourless. These waters belong to the category of cold waters. The water temperature ranges from 7.1 to 14.5 °C, depending on the air temperature. The mineralization (*TDS*) ranges from 163 to 719 mg L^{-1} (Tables I and S-I of the Supplementary material). These waters can be classified as low-mineralized, except for one sample with *TDS* > 500 mg L^{-1}.

TABLE I. Physical–chemical parameters and concentrations of macrocomponents in mine water samples from the exploration area

Parameter	Unit	Min	Median	Max	*N*	Criteria[18]
t	°C	7.1	9.5	14.5	11	–
TDS	mg L^{-1}	163	353	719	11	–
EC	µS cm^{-1}	180	431	632	11	<3000
pH	–	7.04	7.5	7.6	11	6-9
Dissolved O_2	mg L^{-1}	5.4	9.3	10.9	11	>0.4
Dissolved H_2S		0.006	0.048	0.351	11	≤1.0
Ca^{2+}		25.6	40.4	56.8	6	–
Mg^{2+}		1.2	3.65	4.2	6	–
Na^{+}		3.5	4.64	6.6	6	–
K^{+}		1	1	1.1	6	–
HCO_3^{-}		61	88.45	91.5	6	–
SO_4^{2-}		37.4	93.2	177.7	11	<300
Cl^{-}		4	6	18	11	<250
NO_3^{-}		0.83	1.7	12.09	11	<15
NO_2^{-}		0.005	0.041	0.333	11	–
NH_4^{+}		0.033	0.54	1.5	11	<1.5

The pH value of analysed waters ranges from 7.04 to 7.6, classifying them as neutral. According to the USEPA standards (2018), the pH of drinking water should be within the range of 6.5 to 8.5, which is met in all samples.[39]

The most dominant cation is Ca^{2+}, with 25.6 to 56.8 mg L^{-1} concentrations. Concentrations of Mg^{2+} range from 1.2 to 4.2 mg L^{-1}. The second most abundant cation in these waters is Na^{+}, with concentrations ranging from 3.5 to 6.6

mg L^{-1}. K^+ concentrations do not vary significantly in analysed samples (1 to 1.1 mg L^{-1}), having the lowest abundance among all cations in these waters.

The dominant anions in mine waters are bicarbonates and sulphates. HCO_3^- in mine waters occur in the range of 61 to 91.5 mg L^{-1}. SO_4^{2-} concentrations in these waters vary from 37.4 to 177.7 mg L^{-1}. Chlorides in these waters occur at low concentrations (4 to 18 mg L^{-1}). The content of NH_4^+, NO_2^- and NO_3^- in the water is also low.

Concentrations of dissolved oxygen (O_2) range from 5.4 to 10.9 mg L^{-1}, while the concentrations of dissolved hydrogen sulphide (H_2S) are relatively low (from 0.006 to 0.351 mg L^{-1}).

Based on the dominant anions and cations, the analysed mine waters can be classified into two hydrochemical groups: HCO_3^-–SO_4^{2-}–Ca^{2+} and SO_4^{2-}–Ca^{2+} waters (Fig. 1). The first group consists of mine waters that are not in direct contact with the rocks from the ore body (water that is pumped out before it reaches the active mining zone) and waters from sites where mining is currently not taking place. The second group consists of mine waters that are in direct contact with the rocks from the deposit, specifically the waters from the VI, VIII and IX horizons.

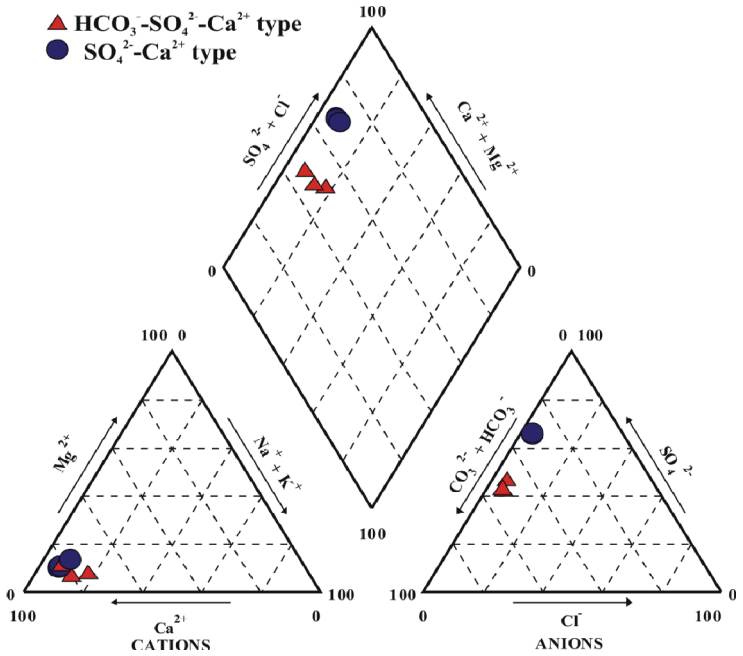

Fig. 1. Piper diagram of mine waters collected from six different locations within the exploration area.

Based on the results obtained from laboratory analysis, all water samples have met the prescribed criteria for wastewater (Table S-I).[40] A part of the mine water is used for the water supply of the Kriva Feja settlement and the mining complex,[41] indicating that some of the water samples also meet the criteria for drinking water.

Microelements in mine waters

According to the laboratory testing results, the concentrations of metals (zinc, barium, chromium, copper) in the mine waters are generally low (Table S-I and Fig. 2).[44] These results are not specific to sulphide deposit mine waters, which typically have low pH values and high metal concentrations, defined as the acid mine drainage (AMD).

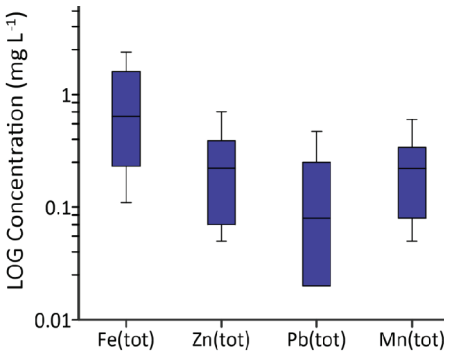

Fig. 2. Metal content in mine waters of the „Grot“ Pb–Zn mine in mg L^{-1}.

The iron concentrations in the tested waters range from 0.11 to 2.37 mg L^{-1}. The elevated concentrations of iron can be the indicator of the presence of oxidation of sulphide minerals.[2] Zinc concentrations in these waters are low (ranging from 0.05 to 0.7 mg L^{-1}), while lead concentrations vary from 0.02 to 0.47 mg L^{-1}. The concentrations of barium in the waters from this area are below 0.05 mg L^{-1}. Chromium and copper are present in trace amounts in these waters, with concentrations below 0.02 mg L^{-1} for chromium and below 0.03 mg L^{-1} for copper.

Manganese concentrations in mine waters range from 0.05 to 0.6 mg L^{-1}, while arsenic concentrations are below 0.05 mg L^{-1}.

Speciation modelling and saturation indices

The most of trace elements and many major elements in surface water and in groundwater exist in the form of complexes rather than free ions.[42] The presence of certain metals in water can indicate the reactions such as dissolution and precipitation of mineral phases.[5]

According to the modelling results in PHREEQC software, a list of the most prevalent ionic species in mine waters is provided (Table II). Me^{2+} and $MeSO_4$

represent the two dominant ionic species for calcium and magnesium, while trivalent iron is most commonly present as $Fe(OH)_2^+$ and $Fe(OH)_3$. Metals such as lead and copper are predominantly present as free ions and $MeCO_3$ ionic pair, while manganese is most commonly found as free ions or $MnSO_4$ ionic pair. Both types of mine waters have a similar distribution of ionic species. Only minor differences in the distribution of ionic species of zinc are observed. In both types of water, zinc predominantly occurs as free ions. Additionally, the presence of the $MeCO_3$ ionic pair is noticeable in the HCO_3^-–SO_4^{2-}–Ca^{2+} water type, while the $MeSO_4$ ionic pair is more dominant in the SO_4^{2-}–Ca^{2+} water type.

TABLE II. The distribution of ionic species in mine waters (presented in terms of median molalities and the median percentage distribution of ionic species relative to the total molality of metals)

Species	HCO_3^-–SO_4^{2-}–Ca^{2+}	SO_4^{2-}–Ca^{2+}	HCO_3^-–SO_4^{2-}–Ca^{2+}	SO_4^{2-}–Ca^{2+}
	Molality, mol/kg		%	
		Calcium		
Ca^{2+}	6.10×10^{-4}	1.16×10^{-3}	94.85	87.94
$CaSO_4$	2.94×10^{-5}	1.52×10^{-4}	4.60	11.38
		Iron		
$Fe(OH)_2^+$	3.19×10^{-6}	2.06×10^{-6}	68.46	76.85
$Fe(OH)_3$	1.11×10^{-6}	4.97×10^{-7}	23.48	18.60
		Magnesium		
Mg^{2+}	5.87×10^{-5}	1.53×10^{-4}	95.12	88.83
$MgSO_4$	2.51×10^{-6}	1.75×10^{-5}	4.06	10.15
		Sodium		
Na^+	2.03×10^{-4}	2.00×10^{-4}	99.83	99.51
		Lead		
$PbCO_3$	8.30×10^{-8}	8.07×10^{-8}	85.95	83.61
Pb^{2+}	7.89×10^{-9}	1.07×10^{-8}	6.64	7.00
$PbHCO_3^+$	3.34×10^{-9}	9.38×10^{-9}	3.30	3.71
		Zinc		
Zn^{2+}	8.49×10^{-7}	9.85×10^{-7}	77.28	67.26
$ZnCO_3$	1.01×10^{-7}	1.37×10^{-7}	11.57	9.94
$ZnHCO_3^+$	5.47×10^{-8}	8.39×10^{-8}	5.10	5.86
$ZnSO_4$	4.78×10^{-8}	2.08×10^{-7}	4.46	14.15
		Manganese		
Mn^{2+}	8.71×10^{-7}	1.38×10^{-6}	95.11	89.09
$MnSO_4$	3.52×10^{-8}	1.40×10^{-7}	3.87	9.61
		Copper		
$Cu(OH)_2$	2.84×10^{-7}	2.99×10^{-7}	60.16	63.25
$CuCO_3$	9.01×10^{-8}	1.02×10^{-7}	19.09	21.56
$Cu(HS)_3^-$	6.66×10^{-8}	3.96×10^{-8}	14.10	8.38

Based on the calculated *SI* values, the analysed waters are undersaturated ($SI < 0$) with the respect to minerals such as calcite, aragonite, cerussite, smithsonite, rhodochrosite, siderite and pyrolusite (Table III). The origin of Ca^{2+} and HCO_3^- in these waters could be linked to the dissolution of calcite and aragonite. The median *SI* values for calcite and aragonite are –0.80 and –0.95, respectively. Both minerals have similar saturation index values, implying that they can be dissolved relatively equally in the investigated area.

TABLE III. Saturation Index (*SI*) values for selected minerals; $N = 6$

Mineral	*SI* min	*SI* median	*SI* max
Aragonite	–1.20	–0.95	–0.66
Calcite	–1.05	–0.80	–0.51
Cerussite	–1.10	–1.00	–0.64
Smithsonite	–2.90	–2.41	–1.54
Rhodochrosite	–1.97	–1.79	–1.10
Siderite	–3.91	–3.6	–2.81
Barite	0.16	0.44	0.68
Galena	–4.37	–3.84	–2.82
Sphalerite	–6.81	–6.06	–5.17
Pyrite	–19.55	–19.24	–18.63

The *SI* values for minerals such as cerussite, smithsonite and rhodochrosite range from –1 to –2.9. The presence of Pb^{2+} in these waters can be attributed to the dissolution of cerussite. Since cerussite has a lower solubility product, this process occurs with lower intensity compared to the dissolution of calcium carbonates, resulting in lower concentrations of Pb^{2+} in the water.

The origin of Zn^{2+} and Mn^{2+} in mine waters may be associated with the dissolution of smithsonite and rhodochrosite. The occurrence of iron ions in these waters can be linked to the dissolution of siderite.

On the other hand, the saturation index values for mineral phases galena, sphalerite, pyrite, covellite and chalcopyrite are very low, indicating that the waters from this research area are undersaturated concerning the given minerals. The median *SI* value for the mineral phase pyrite is –19.24, while for galena it is around –3.84, and for sphalerite it is around –6.06. Although sulphides minerals dominate over carbonate minerals in the investigated area, it can be assumed that the oxidation process of sulphides minerals occurs to a low extent.

The origin of SO_4^{2-} may be from the oxidation processes of pyrite, galena and sphalerite. This process is specific to the ore deposit zone. Therefore, the origin of lead, zinc, manganese and iron can be twofold, as these metals can originate from sulphide minerals (such as galena, sphalerite, pyrite, *etc*.) and carbonate minerals. Most probably, the dissolution of carbonate minerals also takes place during the oxidation process of sulphide minerals. Additionally, the origin of barium may be from galena and sphalerite, where this metal is concentrated.[43] The

saturation index values for barite in these waters are slightly positive (median *SI* 0.44), indicating the precipitation of secondary barium sulphate, due to the presence of an abundance of sulphate ions.

All the minerals under consideration have been detected in the ore deposit, which is deposited in specific horizons within the schists.[43]

The origin of the mine waters is mainly atmospheric, with significant amounts of rainfall occurring in this area throughout the year. The low intensity of sulphide mineral oxidation may be attributed to the rapid exchange of these waters. Since the process of pyrite oxidation is low, this process is probably not dominant in shaping the chemical composition of these waters. The low concentrations of metals in the water are another indication of the low intensity of this process. Additionally, the sulphide minerals' solubility products are much lower than those of carbonate minerals. Therefore, the dissolution of carbonate minerals occurs before the dissolution of the sulphide minerals.

CONCLUSIONS

According to the results of chemical analysis, the mine waters of the "Grot" Pb–Zn underground mine have a neutral pH value and low concentrations of the trace elements except for manganese and iron. The analysed mine waters are classified into two groups based on their chemical composition. These differences can be attributed to the fact that the first group of waters of the HCO_3^-–SO_4^{2-}–Ca^{2+} type drains before contacting the ore body zone. On the other hand, the second group of waters of the SO_4^{2-}–Ca^{2+} type is in the direct contact with the ore body. However, it does not exhibit characteristics of acid mine drainage, probably due to the short water retention in the system. Modelling in PHREEQC software and the analysis of the obtained saturation index values revealed the two dominant processes in shaping the chemical composition of these waters: the dissolution of carbonate minerals and the oxidation of sulphide minerals. The intensity of sulphide mineral oxidation is low and localized to the ore zone. The lack of the intense sulphide mineral oxidation, despite their high occurrence in the study area, is due to the kinetics of this process. The longer rock-water contact is required to initiate this process, while the mine waters in this area are rapidly exchanged and have a short contact with the rock. Therefore, it can be concluded that the kinetic factor plays a crucial role in forming neutral, good-quality mine waters. At the same time, the neutralization in the presence of carbonate minerals is not a significant factor.

Since the acid mine drainage is a global issue, adapting some similar methods of the mineral resource exploitation and mine dewatering, where applicable, could further slow down this process. Finally, this study suggests that the mine drainage systems for mineral resource deposits should minimize the water retention in the system, ensuring a short contact time between water and rock.

SUPPLEMENTARY MATERIAL

Additional data and information are available electronically at the pages of journal website: https://www.shd-pub.org.rs/index.php/JSCS/article/view/12540, or from the corresponding author on request.

Acknowledgements. This research was funded by the Ministry of Science, Technological Development and Innovation of the Republic of Serbia. The authors are also grateful to the Geological Survey and the Environmental Protection Service of the Grot mine for their support.

И З В О Д

ГЕОХЕМИЈА НЕУТРАЛНИХ РУДНИЧКИХ ВОДА СУЛФИНИХ ЛЕЖИШТА НА ПРИМЕРУ Pb–Zn ЛЕЖИШТА “ГРОТ”

СНЕЖАНА С. КРЕТИЋ, ЈАНА С. ШТРБАЧКИ и НЕБОЈША Б. АТАНАЦКОВИЋ

Универзитет у Београду, Рударско–геолошки факултет, Департман за хидрогеологију, Ђушина 7, 11000 Београд

У овом раду проучаван је хемијски састав вода из рудника и издвојени су хидрогеохемијски фактори који утичу на његово формирање. Сакупљено је 11 узорака воде са 6 локација на подручју Криве Феје, како би се утврдио њихов хемијски састав. Анализом података утврђено је да су воде са овог подручја високог квалитета, HCO_3^--SO_4^{2-}-Ca^{2+} и SO_4^{2-}-Ca^{2+} типа, са неутралном pH вредношћу. Концентрације метала у овим водама (цинка, олова, баријума, бакра и хрома) генерално су ниске и већина узорака вода испуњава критеријуме воде за пиће (US EPA стандарде). Моделирање помоћу PHREEQC софтвера указује на то да су доминантни процеси у формирању хемијског састава ових вода растварање карбонатних минерала и оксидација сулфидних минерала. Карбонатни минерали имају мању заступљеност у односу на сулфидне минерале (попут галенита, сфалерита и пирита), који су доминантни на подручју истраживања. Слаб интензитет оксидације сулфидних минерала последица је брзе замене воде и смањеног контакта воде са стеном. Процес оксидације сулфидних минерала је локалног карактера и везује се само за зону лежишта. Ова студија указује на значај кинетике (тј. брзине хемијске реакције), као једног од главних фактора у процесу оксидације сулфидних минерала.

(Примљено 11. августа, ревидирано 21. октобра 2023, прихваћено 19. фебруар 2024)

REFERENCES

1. C. Wolkersdorfer, D.K. Nordstrom, R. Beckie, D.S. Cicerone, T. Elliot, M. Edraki, T. M. Valente, S. C. A. França, P. Kumar, R.A. Oyarzún Lucero, A. I. G. Soler, *Mine Water Environ.* **39** (2020) 204 (https://doi.org/10.1007/s10230-020-00666-x)
2. D. Banks, P. L. Younger, R. T. Arnesen, E. R. Iversen, S.B. Banks, *Environ Geol*. **32** (1997) 157 (https://doi.org/10.1007/s002540050204)
3. B.G. Lottermoser, *Mine Wastes: Characterization, Treatment and Environmental Impacts* Springer, Berlin, 2010, pp. 43–117 (https://doi.org/10.1007/978-3-642-12419-8)
4. D.K. Nordstrom, *Elements* **7** (2011) 393 (https://doi.org/10.2113/gselements.7.6.393)
5. D.K. Nordstrom, C.N. Alpers, In: *The environmental geochemistry of mineral deposits, part a: processes, methods, and health issues*, G.S. Plumlee, M.J. Logsdon, Eds., Rev Econ Geol, Littleton, 1999, pp. 133–160
6. A. Parbhakar-Fox, B.G. Lottermoser, *Minerals Eng.* **82** (2015) 107 (https://doi.org/10.1016/j.mineng.2015.03.015)

7. O. Guseva, A. K. B. Opitz, J. L. Broadhurst, S. T. L. Harrison, M. Becker, *Minerals Eng.* **163** (2021) 106750 (https://doi.org/10.1016/j.mineng.2020.106750)
8. R. Fan, G. Qian, Y. Li, M. D. Short, R. C. Schumann, M. Chen, R. C. Smart, A. R. Gerson, *Chem. Geol.* **588** (2022) 120653 (https://doi.org/10.1016/j.chemgeo.2021.120653)
9. N. Atanacković, *Risk assessment of water pollution caused by abandoned mining operations in Serbia*, Faculty of Mining and Geology, Belgrade, 2018, pp. 23–26 (https://nardus.mpn.gov.rs/handle/123456789/10186) (in Serbian)
10. S. R. Jennings, D. J. Dollhopf, W. P. Inskeep, *Appl. Geochem.* **15** (2000) 235 (https://doi.org/10.1016/S0883-2927(99)00041-4)
11. F. P. Walker, M. E. Schreibe, J. D. Rimstidt, *Geochim. Cosmochim. Acta* **70** (2006) 1668 (https://doi.org/10.1016/j.gca.2005.12.010)
12. Y. Yunmei, Z. Yongxuan, G. Zheinmin, H. G, Christopher, L. Denxian, *Environ. Sci. Tech.* **41** (2007) 6460 (https://doi.org/10.1021/es070788m)
13. G. S. Plumlee, In: *The environmental geochemistry of mineral deposits. Part A: Processes, techniques and health issues*, G. S. Plumlee, M. S. Logsdon, Eds., Society of Economic Geologists, Littleton, 1999, pp. 77-116
14. A. P. Jarvis, C. J. Gandy, J. A. Webb, *Minerals* **13** (2023) 592 (https://doi.org/10.3390/min13050592)
15. U. O. Chukwura, A. S. Hursthouse, *Environ. Earth Sci.* **79** (2020) 363 (https://doi.org/10.1007/s12665-020-09108-x)
16. R. Warrender, N. J. G. Pearce, W. T. Perkins, K. M. Florence, A. R. Brown, D. J. Sapsford, R. J. Bowell, M. Dey, *Mine Water Environ.* **30** (2011) 82 (https://doi.org/10.1007/s10230-011-0150-8)
17. N. Barago, E. Pavoni, F. Floreani, M. Crosera, G. Adami, D. Lenaz, S. Covelli, *J. Geochem. Explor.* **245** (2023) 107129 (https://doi.org/10.1016/j.gexplo.2022.107129)
18. ISO 5667-1: *Water quality - Sampling - Part 1: Guidance on the design of sampling programmes and sampling techniques* (2006)
19. ISO 5667-3: *Water quality - Sampling - Part 3: Preservation and handling of water samples* (2012)
20. ISO 5667-10: *Water quality — Sampling — Part 10: Guidance on sampling of waste waters* (1992)
21. ISO 10523: *Water quality - Determination of pH* (2008)
22. US EPA 160.3: *Total Residue by Drying Oven* (1983)
23. ISO 11885: *Water quality - Determination of selected elements by inductively coupled plasma optical emission spectrometry (ICP-OES)* (2007)
24. ISO 11969: *Water quality - Determination of arsenic - Atomic absorption spectrometric method (hydride technique)* (1996)
25. ISO 7150-1: *Water quality - Determination of ammonium - Part 1: Manual spectrometric method* (1984)
26. ISO 7890-3: *Water quality - Determination of nitrate - Part 3: Spectrometric method using sulfosalicylic acid* (1988)
27. ISO 6777: *Water quality - Determination of nitrite - Molecular absorption spectrometric method* (1984)
28. SRPS H.G8.115: *Reagents - Citric acid monohydrate - Determination of sulphate content - Turbidimetric method* (1984)
29. ISO 9297: *Water quality - Determination of chloride - Silver nitrate titration with chromate indicator (Mohr's method)* (1989)

30. ISO 9963-1: *Water quality - Determination of alkalinity - Part 1: Determination of total and composite alkalinity* (1994)
31. ISO 5813: *Water quality - Determination of dissolved oxygen - Iodometric method* (1983)
32. *Drinking Water - Standard Methods for Testing Hygienic Suitability*, Federal Institute for Health Protection, Belgrade, 1990 (in Serbian)
33. B. J. Merkel, B. Planer-Friedrich, *Groundwater Geochemistry*. Springer, Berlin, 2005, p. 20
34. D. L. Parkhurst, C. A. J. Appelo, *Description of input and examples for PHREEQC version 3–A computer program for speciation, batch-reaction, one-dimensional transport, and inverse geochemical calculations: U.S. Geological Survey Water-Resources Investigations,* Chapter 43 of Section A, Groundwater Book 6, 2013, Modeling Techniques: Techniques and Methods 6–A43
35. N. Durães, I. Bobos, E. Ferreira de Silva, *Environ. Sci. Pollut. Res.* **24** (2017) 4562 (https://doi.org/10.1007/s11356-016-8161-4)
36. J. S. Lee, H. T. Chon, *J. Geochem. Expl.* **88** (2006) 37 (https://doi.org/10.1016/j.gexplo.2005.08.012)
37. G. Madzivire, W. M. Gitari, V. R. Kumar Vadapalli, T. V. Ojumu, L. F. Petrik, *Min. Eng.* **24** (2011) 1467 (https://doi.org/10.1016/j.mineng.2011.07.009)
38. J. D. Allison, D. S. Brown, K. J. Novo-Gradac, *MINTEQA2/PRODEFA2--A geochemical assessment model for environmental systems--version 3.0 user's manual: Environmental Research Laboratory*, Office of Research and Development, U.S. Environmental Protection Agency, Athens, GA, 1990, p. 106
39. USEPA, *Drinking water standards and health advisories tables,* Office of Water U.S. Environmental Protection Agency Washington, DC, 2018
40. N. Lilić, D. Knežević, A. Cvjetić, D. Nišić, U. Pantelić, P. Lilić, *Environmental impact assessment study for the lead and zinc ore mining project "Vučkovo deposit" and "Kula deposit" within the "Grot" mining company A.D. - Kriva Feja*, Belgrade, Faculty of Mining and Geology, Belgrade, 2019, pp. 1–158 (in Serbian)
41. N. Atanacković, V. Dragišić, V. Živanović, I. Cvejić, S. Stojadinović, I. Jocić, In: *Proceedings of the 16th Serbian Symposium on Hydrogeology with International Participation*, Zlatibor, Serbia, 2022, Faculty of Mining and Geology, Belgrade, 2022
42. ID. Langmuir, *Aqueous environmental geochemistry*, Prentice Hall, Upper Saddle River, NJ, 1997, pp. 88–90
43. M. Babović, D. Cvetković, Č. Roglić, V. Avramović, S. Marić, *Explanatory book for the basic geologic map, scale 1:100 000, sheet "Trgovište sa Radomir" K 34-57*, Institute for Geological and Geophysical Research, Belgrade, 1977, pp. 1–59 (in Serbian).

Journal of the Serbian Chemical Society
JSCS@tmf.bg.ac.rs • www.shd.org.rs/JSCS
J. Serb. Chem. Soc. *89* (3) S143–S146 (2024) *Supplementary material*

SUPPLEMENTARY MATERIAL TO

Geochemistry of neutral mine drainage at sulfide deposits – Example of the „Grot“ Pb–Zn mine, south-eastern Serbia

SNEŽANA S. KRETIĆ*, JANA S. ŠTRBAČKI and NEBOJŠA B. ATANACKOVIĆ

University of Belgrade, Faculty of Mining and Geology, Department of Hydrogeology, Djusina 7, 11000 Belgrade, Serbia

J. Serb. Chem. Soc. *89* (3) (2024) 429–440

STUDY AREA

The Grot Mine is located in the southeastern part of Serbia, within the municipalities of Bosilegrad and Vranje. The mining area is characterized by mountainous terrain. In the central part of the mining field, there is the ridge of Besna Kobila, which is also the highest point in the relief (1923 m). Besna Kobila represents the watershed divide between the Black Sea basin (South Morava River basin) and Aegean Sea basin.[1] The river streams are characterized by a snow-rain regime, with peak flows occurring during snowmelt and spring rains. The area has a moderate continental climate with mountainous influences. The average annual air temperature ranges from 5 to 6 °C, with an average annual precipitation exceeding 1000 mm.[2] In geological terms, the ore field comprises older Paleozoic crystalline schists that are intruded by older granitoids, younger Tertiary granitoids, and the youngest volcanic rocks (quartz latites) (Fig. S-1). The ore deposit is hosted in the schists of the Lisina Series, accompanied by quartz-latite, calcschists, and marbles.[1,2] The formation of the mineral paragenesis is associated with several stages. The most important stage that led to mineralization (mesothermal phase) is characterized by the minerals such as galena, sphalerite, pyrite, chalcopyrite, arsenopyrite, molybdenite, tennantite, quartz, stibnite, rhodochrosite, calcite, manganese siderite, chalcedony, and aragonite.[3] During the supergene stage, minerals such as cerussite, smithsonite, pyrolusite, and limonite were formed through transformations.[3] From a hydrogeological perspective, the fractured aquifer has a predominant distribution in the exploration area. It is formed within the granitoid and quartzlatite rocks and crystalline schists (Lisina and Jerešnica Series).[2] The fracturing of the crystalline schist complex is significant. Groundwater accumulation is related to the fracture and fault systems of crystalline schists, marble, and quartz latite. The permeability of the rocks depends on the type of crystalline schist, with the Jerešnica-age crystalline schists being less permeable than the Lisina-age schists, representing a hydrogeological barrier for groundwater movement.[1] The mining works were carried out from 1290 m to 1720 m. Completing the main export adit (MEA) at the lowest mining horizon involved advancing through the entire massif of Besna Kobila, reducing the inflow of water into the mining works at higher elevations.[1] The drainage of mining operations is entirely gravity-based. All the water from the mine is discharged at

* Corresponding author. E-mail: snezana.kretic@rgf.bg.ac.rs

three levels: VI, VIII and IX horizons. In places where mine waters are discharged, sedimentation ponds have been installed at the outlets of mining horizons.[1] The majority of mine waters are drained through the MEA at the IX horizon, where the water flows in three directions (towards the flotation plant, towards the Hajdučki Osoj adit, and the outlet of the IX horizon at the Crna Reka site).[1]

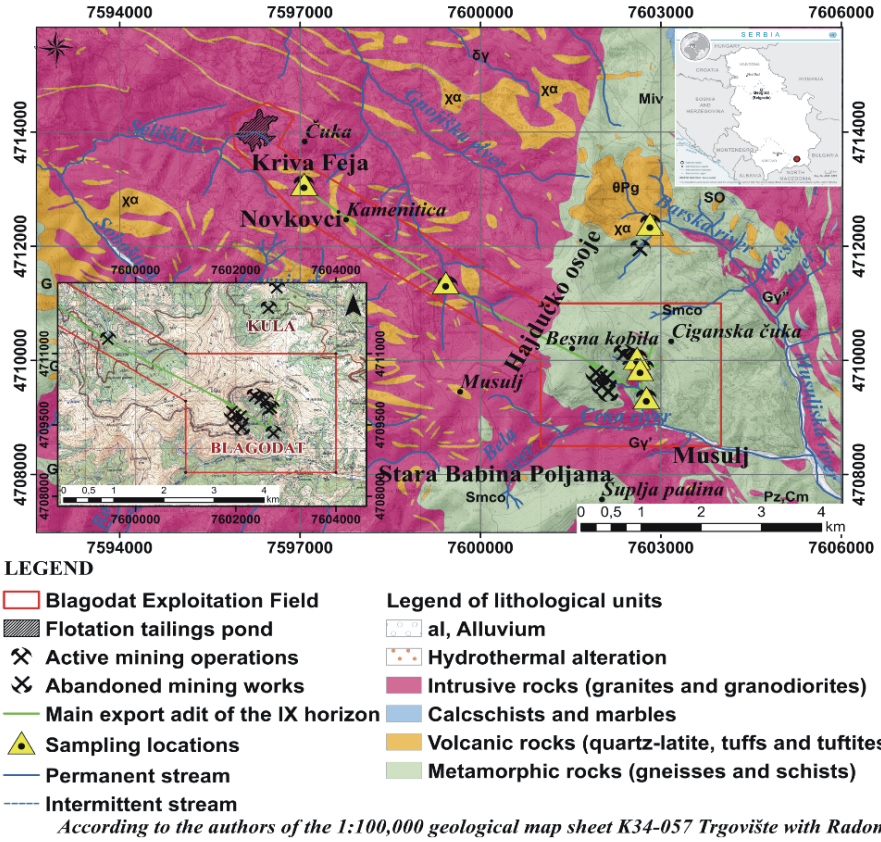

According to the authors of the 1:100,000 geological map sheet K34-057 Trgovište with Radomir.

Fig. S-1. Geological map of the study area (modified) with locations of mine water sampling points.[3-5]

Table S-I. Results of chemical analyses for the examined mine water samples relative to the USEPA standards for drinking water and emission limit values according to the Regulation on emission limit values for water pollutants and deadlines for their achievement (Official Gazeta RS 67/2011, 48/2012 and 1/2016)

Parameter	Unit	Sample											USEPA	Criteria for Wastewater
		1	2	3	4	5	6	7	8	9	10	11		
t	°C	7.1	7.5	7.2	14.5	14	10	9	9	10	10.5	9.5	/	/
TDS	mg L^{-1}	719	442	353	183	187	166	163	385	375	167	482	500	/
EC	µS cm^{-1}	610	608	569	249	262	197	180	431	433	225	632	/	<3000
pH	/	7.53	7.52	7.43	7.6	7.4	7.39	7.5	7.35	7.52	7.04	7.5	6.5-8.5	6-9
Dissolved O_2	mg O_2 L^{-1}	5.4	6	9.3	7	6.2	10	10.4	10.7	10.9	10.3	9	/	>0.4
Dissolved H_2S	mg L^{-1}	0.351	0.329	0.052	0.048	0.329	0.006	0.008	0.009	0.006	0.063	0.026	/	≤1.0
Ca^{2+}	mg L^{-1}	/	/	/	/	/	25.6	25.6	56.8	52.8	40.8	40	/	/
Mg^{2+}	mg L^{-1}	/	/	/	/	/	1.5	1.2	4.2	4.2	3.2	4.1	/	/
Na^{+}	mg L^{-1}	/	/	/	/	/	6.6	4.25	4.65	4.62	3.5	4.7	30-60	/
K^{+}	mg L^{-1}	/	/	/	/	/	1	1	1	1	1	1.1	/	/
HCO_3^{-}	mg L^{-1}	/	/	/	/	/	61	61	91.5	91.5	85.4	91.5	/	/
SO_4^{2-}	mg L^{-1}	177.7	116.1	93.2	90.5	41.7	44.4	37.4	153.4	152.8	53.8	154.4	250	<300
Cl^{-}	mg L^{-1}	18	12	8	10	8	4	4	6	6	5	6	250	<250
NO_3^{-}	mg L^{-1}	1	1	1.7	12.09	11.83	1.5	0.9	2.6	2.8	0.83	3.7	10	<15
NO_2^{-}	mg L^{-1}	0.333	0.298	0.197	0.041	0.035	0.005	0.009	0.06	0.03	0.006	0.061	1	/
NH_4^{+}	mg L^{-1}	0.93	0.86	0.91	0.86	1.5	0.18	0.33	0.43	0.39	0.033	0.54	/	<1.5
Fe total	mg L^{-1}	2.37	0.64	0.8	1.6	1.6	0.55	0.26	0.15	1.24	0.11	0.23	0.3	≤5
Cr total	mg L^{-1}	<0.02	<0.02	<0.02	<0.02	<0.02	<0.02	<0.02	<0.02	<0.02	<0.02	<0.02	0.1	≤0.25
Cu total	mg L^{-1}	<0.03	<0.03	<0.03	<0.03	<0.03	<0.03	<0.03	<0.03	<0.03	<0.03	<0.03	1.3	≤0.25
Zn total	mg L^{-1}	0.366	0.221	0.188	0.7	0.56	0.07	0.05	0.09	0.39	0.054	0.35	5	≤1
Pb total	mg L^{-1}	0.17	0.11	0.08	0.47	0.3	0.02	0.02	0.02	0.25	0.02	0.045	0.015	≤0.25

As total	mg L^{-1}	<0.05	<0.05	<0.05	<0.05	<0.05	<0.05	<0.05	<0.05	<0.05	<0.05	<0.05	0.01	≤0.05
Ba total	mg L^{-1}	<0.5	<0.5	<0.5	<0.05	<0.05	<0.05	<0.05	<0.05	<0.05	<0.05	<0.05	2	<1
Mn total	mg L^{-1}	0.6	0.25	0.29	0.34	0.36	0.05	0.05	0.08	0.22	0.08	0.12	0.05	<1

REFERENCES

N. Lilić, D. Knežević, A. Cvjetić, D. Nišić, U. Pantelić, P. Lilić, Environmental impact assessment study for the lead and zinc ore mining project “Vučkovo deposit” and “Kula deposit” within the “Grot” mining company A.D. - Kriva Feja, Belgrade, 2019, pp. 1-158, Faculty of Mining and Geology

N. Atanacković, V. Dragišić, V. Živanović, I. Cvejić, S. Stojadinović, I. Jocić, In: Proceedings of the 16th Serbian Symposium on Hydrogeology with International Participation, (2022), Zlatibor, Republic of Serbia, Faculty of Mining and Geology, Belgrade, 2022

M. Babović, D. Cvetković, Č. Roglić, V. Avramović, S. Marić, Explanatory book for the basic geologic map, scale 1:100 000, sheet "Trgovište sa Radomir" K 34-57, Belgrade, 1977, pp. 1-59, Institute for Geological and Geophysical Research, (in Serbian, English summary)

Military Geographic Institute, Topographic Map, 1:50,000, sheet Vlasotince 633_3_4, (Map), Belgrade, 1973, Federal Geological Institute

United Nations: Peace, dignity and equality on a healthy planet, https://www.un.org, (07.07.2023).

Journal of the Serbian Chemical Society
JSCS@tmf.bg.ac.rs • www.shd.org.rs/JSCS
J. Serb. Chem. Soc. *89* (3) 441–442 (2024)
JSCS–5731
Errata
Published 26 March 2024

ERRATUM

Correction of author's affiliation and acknowledgement in the article. Computer-aided approach for the identification of lead molecules as the inhibitors of cholinesterase's and monoamine oxidases: Novel target for the treatment of Alzheimer disease

SYEDA ABIDA EJAZ[1]*, MUBASHIR AZIZ[1], AMMARA FAYYAZ[1,4] TANVEER A. WANI[2] and SEEMA ZARGAR[3]

[1]Department of Pharmaceutical Chemistry, Faculty of Pharmacy, The Islamia University of Bahawalpur, Bahawalpur 63100, Pakistan, [2]Department of Pharmaceutical Chemistry, College of Pharmacy, King Saud Univeristy, P.O. Box 2457, Riyadh 11451, Saudi Arabia [3]Department of Biochemistry, College of Science, King Saud Univeristy, P.O. Box 22452, Riyadh 11451, Saudi Arabia and [4]School of Pharmaceutical Science and Technology, Tianjin University, 30072, Tianjin, China

This corrects the article "Computer-aided approach for the identification of lead molecules as the inhibitors of cholinesterase's and monoamine oxidases: Novel target for the treatment of Alzheimer disease" published in volume **89**, number 2, page 177 (https://doi.org/10.2298/JSC230307050E).

CONTENT OF THE CORRECTION

For author Ammara Fayyaz, additional affiliation is added.

Previous article affiliation was:

[1]Department of Pharmaceutical Chemistry, Faculty of Pharmacy, The Islamia University of Bahawalpur, Bahawalpur 63100, Pakistan, [2]Department of Pharmaceutical Chemistry, College of Pharmacy, King Saud University, P.O. Box 2457, Riyadh 11451, Saudi Arabia and [3]Department of Biochemistry, College of Science, King Saud University, P.O. Box 22452, Riyadh 11451, Saudi Arabia

Corrected affiliation is:

[1]Department of Pharmaceutical Chemistry, Faculty of Pharmacy, The Islamia University of Bahawalpur, Bahawalpur 63100, Pakistan, [2]Department of Pharmaceutical Chemistry, College of Pharmacy, King Saud Univeristy, P.O. Box 2457, Riyadh 11451, Saudi Arabia, [3]Department of Biochemistry, College of Science, King Saud Univeristy, P.O. Box 22452, Riyadh 11451, Saudi Arabia and [4]School of Pharmaceutical Science and Technology, Tianjin University, 30072, Tianjin, China

* Corresponding author. E-mail: abida.ejaz@iub.edu.pk; abidaejaz2010@gmail.com
https://doi.org/10.2298/JSC240325036E

In **Acknowledgement**, the supporting project number is changed.

Previous acknowledgement was:

Acknowledgement. The authors extend their appreciation to researchers supporting project number RSP-2023/357, King Saud University, Riyadh, Saudi Arabia, for funding this research.

Correct acknowledgement is:

Acknowledgement. The authors extend their appreciation to researchers supporting project number RSP2024R357, King Saud University, Riyadh, Saudi Arabia, for funding this research.